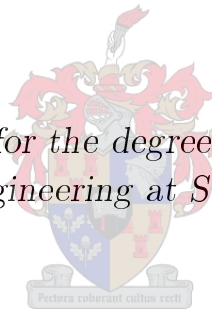


# Numerical and Experimental Investigation of One-way Fluid Structure Interaction of a Vertical Cantilever Beam in an Air Stream

by

Eugène Christiaan Joubert

*Dissertation presented for the degree of Doctor of Philosophy  
in the Faculty of Engineering at Stellenbosch University*



Supervisors:

Prof. T.M. Harms   Prof. G. Venter

December 2015

# Declaration

By submitting this dissertation electronically, I declare that the entirety of the work contained therein is my own, original work, that I am the sole author thereof (save to the extent explicitly otherwise stated), that reproduction and publication thereof by Stellenbosch University will not infringe any third party rights and that I have not previously in its entirety or in part submitted it for obtaining any qualification.

Signature: .....

E. C. Joubert

Date: .....December 2015.....

Copyright © 2015 Stellenbosch University  
All rights reserved.

# Abstract

## Numerical and Experimental Investigation of One-way Fluid Structure Interaction of a Vertical Cantilever Beam in an Air Stream

E. C. Joubert

Dissertation: PhD (Mech)

December 2015

This thesis uses open source software for simulating one-way fluid structure interaction (FSI) of a bluff-body geometry and validating the results with wind tunnel measurements. A vertical cantilever beam with a rectangular cross-section is used as main subject as it provides complex flow-induced structural loading conditions, stiffness for ensuring one-way FSI and facilitates the placement of sensors internally during wind tunnel measurements to prevent flow obstruction. The beam is orientated parallel to flow resulting in a streamwise cross-section ratio of  $L/D = 2.63$  and perpendicular to the flow to result in a cross-section ratio of  $D/L = 0.38$  where the cross-section length (long side) is  $L$  and the width (short side) is  $D$ . Two wind speeds are considered for each orientation causing the Reynolds number to vary between  $7.6 \times 10^4 < Re < 4 \times 10^5$ .

Laboratory measurements were done to provide boundary conditions, material properties, instrumentation calibration and validation data. Wind tunnel measurements were done for two wind speeds, two beam orientations and at various locations around and on the beam surface. This included velocity field measurements using particle image velocimetry (PIV), pressure, vibration and strain.

OpenFOAM is used for the computational fluid dynamics (CFD) work. The CFD simulations can be described as turbulent, incompressible, New-

tonian, three-dimensional and unsteady. In the near-wall region Spalding's "all- $y^+$ " wall function is used to provide some mesh flexibility and reduce computational requirements without compromising accuracy. The Realizable  $k$ - $\epsilon$ ,  $k$ - $\omega$  SST, Non-linear  $k$ - $\epsilon$  Shih and Spalart-Allmaras IDDES turbulence models are compared against measured time-averaged velocity and pressure results.

The time-averaged CFD results show that all turbulence models accurately reproduce measured flow fields in the upstream and side-wall regions. In the wake the IDDES turbulence model is the most accurate being able to reproduce a recirculation length of  $3D$  compared to the measured length of  $3.2D$ . The time-dependent results show that all models produce loading frequencies with Strouhal numbers between  $0.05 < St < 0.06$  which is comparable to literature with  $St \approx 0.06$  but the amplitudes vary. The IDDES model produces the most accurate results and is also second fastest after the  $k$ - $\omega$  SST model.

A segregated FSI method is employed and coupling is achieved using a combination of newly developed OpenFOAM utilities and Python programs which link the fluid and structural meshes. Code-Aster is used for the finite element methods (FEM) for structural analysis. A shell mesh is used with linear approach and a time-dependent load is applied to the structure as provided by the CFD results. Only the parallel beam at  $U = 30 \text{ m/s}$  shows significant oscillations. The results show that the FSI simulations accurately reproduce the strain of  $5.8 \mu\text{m}/\text{m}$  in the beam due to the flow drag loading of  $12.9 \text{ N}$ .

# Uittreksel

## Numeriese en Eksperimentele Studie van Een-rigting Vloeistof Struktuur Interaksie van 'n Vertikale Kantelbalk in 'n Lugstroom

*(“Numerical and Experimental Investigation of One-way Fluid Structure Interaction  
of a Vertical Cantilever Beam in an Air Stream”)*

E. C. Joubert

Proefskrif: PhD (Meg)

Desember 2015

Hierdie tesis gebruik vrylik beskikbare sagteware om een-rigting vloeistof-struktuur-interaksie (VSI) van 'n stomp geometrie te simuleer waarna die resultate met windtonnelmetings vergelyk word. 'n Vertikale kantelbalk met 'n reghoekige deursnit is die geometrie wat ondersoek word. Hierdie geometrie verskaf die styfheid benodig vir een-rigting VSI en maak dit moontlik om instrumentasie te huisves tydens windtonneltoetse om sodoende nie die vloei te beïnvloed nie. Die balk word parallel tot die vloei geplaas wat 'n deursnit stroomrigting-verhouding veroorsaak van  $L/D = 2.63$ , asook loodreg tot die vloei om 'n stroomrigtings-verhouding van  $D/L = 0.38$  te gee. Twee windsnelhede word ondersoek vir elke oriëntasie wat gevolglik Reynolds getalle van  $7.6 \times 10^4 < Re < 4 \times 10^5$  gee.

Labratorium toetse is gedoen om die simulاسies se randwaardes, materiaal eienskappe, instrumentasie kalibrasie en validasie data te voorsien. Windtonnel toetse is gedoen vir twee windsnelhede en twee balk oriëntاسies. Dit sluit in vloeiveld-, druk-, vibrاسie- en vervormingsmeetings.

OpenFOAM word gebruik vir die numeriese vloeidinamika (NVD) simulاسies. Hierdie simulاسies kan beskryf word as turbulent, onsamedrukbaar,

Newtonies, drie-dimensioneel en tyd-afhanklik. Naby die wand word Spalding se “alle- $y^+$ ” funksie gebruik wat die simulاسie minder sensitief maak vir rooster-vernfyning in die gebied sonder om die akkuraatheid te verminder. Die Realizable  $k-\epsilon$ ,  $k-\omega$  SST, Nie-lineêre  $k-\epsilon$  Shih en Spalart-Allmaras IDDES turbulensie-modelle word vergelyk met gemete snelheid en druk data.

Die resultate wys dat die gemete snelhede goed vergelyk met die numeries berekende snelhede vir al die turbulensie-modelle wat oorweeg is, maar slegs die IDDES model gee ’n vergelykbare voorspelling van die stroom-af hersikulasie lengte voorspel as  $3D$  in vergelyking met die  $3.2D$  gemete waarde. Die tyd-afhanklike simulاسies van alle modelle bepaal ’n sleur frekwensies met die Strouhal getal tussen  $0.05 < St < 0.06$  wat vergelykbaar is met die literatuur wat ’n Strouhal getal van  $St \approx 0.06$  verskaf. Die berekende hefkrag-amplitudes verskil egter tussen die turbulensie modelle. Die IDDES-model verskaf die mees akkurate resultate en is ook die tweede vinnigste na die  $k-\omega$  SST model.

’n Verdeelde VSI metode word gebruik en die koppelling word gedoen deur ’n kombinasie van nuwe kode in OpenFOAM en Python. Code-Aster word gebruik vir die eindige-element metodes om die struktuur te analiseer. Plaat-elemente en lineêre modellering word gebruik waarvoor die NVD resultate die tyd-afhanklike kragte verskaf. Slegs die parallelle balk by  $U = 30$  m/s toon tyd-afhanklike gedrag. ’n Vervorming van  $5.8 \mu\text{m}/\text{m}$  op die balk word akkuraat bereken deur die VSI-simulاسies, wanneer die balk onderwerp word aan ’n ekwivalente sleurkrag van 12.9 N.

# Acknowledgements

I would like to express my sincere gratitude to the following people and organisations:

- The most important thanks goes to my wife, Thia Joubert, and two daughters, Nichola and Sophia Joubert. Thank you for sacrificing precious family hours, carrying extra burdens and, even though it was difficult at times, continuing to encourage me to finish what I had started.
- I would like to thank Eugène and Trudie Joubert, my parents, for their faith in me and assisting my wife when I was not available. Also parents-in-law Kosie and Martha Nel for their encouragement and support.
- Professors Thomas Harms and Gerhard Venter, my supervisors, for insight, guidance and knowledge impartation.
- The Harry Crossley Foundation for partly funding this project.
- Mechanical and Mechatronic Engineering laboratory staff for assistance during manufacturing and testing. Especially thank you to Brendan Boule for his assistance in the vibration and strain gauge measurements.
- Throughout this project extensive simulations were run on the Stellenbosch University high performance computing cluster. This required the support of cluster administrator Charl Moller for installing software, creating run scripts, making backups and more. For his support, quick response and patience I am very grateful.
- I would also like to thank Professor Wikus van Niekerk, my employer towards the end of the PhD, for motivating me to finish and allowed me some time to do the last work.

# Dedications

*Let the words of my mouth and the meditation of my heart be acceptable in  
your sight, O Lord, my rock and my redeemer. ESV Psalm 19:14*



# Contents

<b>Declaration</b>	<b>i</b>
<b>Abstract</b>	<b>ii</b>
<b>Uittreksel</b>	<b>iv</b>
<b>Acknowledgements</b>	<b>vi</b>
<b>Dedications</b>	<b>vii</b>
<b>Contents</b>	<b>viii</b>
<b>List of Figures</b>	<b>xii</b>
<b>List of Tables</b>	<b>xvii</b>
<b>Nomenclature</b>	<b>xix</b>
<b>1 Introduction</b>	<b>1</b>
1.1 Background and Motivation . . . . .	1
1.2 Research Objectives . . . . .	5
1.3 Dissertation Outline . . . . .	7
1.4 Contributions and Accomplishments . . . . .	8
<b>2 Mechanics of Fluid Structure Interaction</b>	<b>10</b>
2.1 Viscous Fluid Flow . . . . .	10
2.1.1 Cylinder aerodynamics . . . . .	11
2.1.2 Rectangular cross-sectioned prism aerodynamics . . . . .	12
2.2 Mechanics of Turbulence . . . . .	15
2.3 Near-wall Velocity Profile . . . . .	17

2.4	Aeroelasticity . . . . .	19
2.5	Vortex-induced Vibrations . . . . .	21
<b>3</b>	<b>Numerical Methods</b>	<b>23</b>
3.1	Simulating Bluff-body Aerodynamics . . . . .	23
3.2	Fluid Structure Interaction Modelling . . . . .	26
3.3	Discretisation Methods . . . . .	27
3.3.1	Finite difference method . . . . .	28
3.3.2	Finite volume method . . . . .	28
3.3.3	Finite element method . . . . .	28
3.4	Software . . . . .	29
3.5	Turbulence Modelling . . . . .	30
3.5.1	RANS turbulence modelling . . . . .	31
3.5.2	LES turbulence modelling . . . . .	37
3.5.3	DES turbulence modelling . . . . .	40
3.5.4	Summary of turbulence models . . . . .	46
3.6	Interpolation Schemes . . . . .	47
3.7	Three-dimensional Simulation . . . . .	52
3.8	Unstructured Meshing . . . . .	52
3.9	Near-wall Treatment . . . . .	53
<b>4</b>	<b>Methodology</b>	<b>56</b>
4.1	Geometry Selection . . . . .	56
4.2	Wind Tunnel Set-up . . . . .	58
4.3	Fluid Structure Interaction Approach . . . . .	62
4.4	Flow Modelling . . . . .	63
4.4.1	Domain and boundary conditions . . . . .	63
4.4.2	Meshing considerations . . . . .	65
4.4.3	Turbulence and numerical schemes . . . . .	65
4.5	Coupling Modelling . . . . .	68
4.6	Structural Modelling . . . . .	73
4.7	Computational Resources . . . . .	76
4.8	Experimental Set-up and Procedure . . . . .	78
4.8.1	Pressure measurement set-up . . . . .	79
4.8.2	PIV measurement set-up . . . . .	80
4.8.3	Strain measurement set-up . . . . .	84

4.8.4	Vibration measurement set-up . . . . .	86
<b>5</b>	<b>Sensitivity Studies</b>	<b>88</b>
5.1	Convergence Considerations . . . . .	88
5.2	Fluid Domain Boundary Distance Effects . . . . .	89
5.3	Fluid Mesh Refinement Sensitivity . . . . .	91
5.4	Near-wall Treatment Effects . . . . .	94
5.5	Boundary Layer Development Investigation . . . . .	97
5.6	Load Confirmation . . . . .	97
5.7	Structural Model Parameters Sensitivity . . . . .	99
5.8	Structural Mesh Resolution Effects . . . . .	100
5.9	Point Load Strain Verification . . . . .	101
5.10	Modal Analysis and Comparison with Measurements . . . . .	102
5.11	Ramp Time Sensitivity . . . . .	104
<b>6</b>	<b>Turbulence Model Comparisons</b>	<b>106</b>
6.1	Vortex Shedding Frequency Compared to Literature Data . . . . .	112
6.2	Flow-induced Loading Amplitude Comparison . . . . .	113
6.3	Computational Time . . . . .	114
<b>7</b>	<b>Data Comparison</b>	<b>115</b>
7.1	Parallel Beam Velocity Data Comparison With Measurements . . . . .	115
7.2	Perpendicular Beam Velocity Data Comparison with Measure- ments . . . . .	118
7.3	Fluid Simulation Results Compared to Pressure Data . . . . .	121
<b>8</b>	<b>General Case Results</b>	<b>123</b>
8.1	Global Flow Features . . . . .	123
8.2	Strain Response . . . . .	125
<b>9</b>	<b>Detailed Case Analysis</b>	<b>132</b>
9.1	Global Flow Features . . . . .	132
9.2	Flow-induced Loading . . . . .	136
9.3	Vortex Structures . . . . .	139
9.4	Vortex Stretching . . . . .	141
9.5	Time-dependent Structural Response . . . . .	142

<b>10 Conclusion</b>	<b>147</b>
10.1 Summary of Results . . . . .	147
10.2 Future Work . . . . .	149
<b>Appendices</b>	<b>152</b>
<b>A Instrumentation Calibrations and Specifications</b>	<b>153</b>
A.1 Particle Image Velocimetry . . . . .	153
A.2 Pressure Transducers . . . . .	154
A.3 Strain Gauge Specifications . . . . .	155
A.4 Displacement Tests . . . . .	157
<b>B Structural Model Parameters Sensitivity Analysis</b>	<b>159</b>
<b>C Structural Drawings</b>	<b>162</b>
<b>D Code</b>	<b>165</b>
<b>E PIV Guidelines</b>	<b>168</b>
<b>F Vibration Data</b>	<b>171</b>
<b>List of References</b>	<b>174</b>

# List of Figures

1.1	Tacoma Narrows bridge collapse of 1940 (Elliott, 1940) . . . . .	2
1.2	Vesleskarvet including the SANAE IV base and other structures in surrounding area looking north (Hofmeyr, 2015) . . . . .	3
1.3	SANAE IV base situated on the Southern Buttress looking south (Hofmeyr, 2015) . . . . .	4
1.4	South facade of the SANAE IV Base in Antarctica . . . . .	5
1.5	Wind tunnel PIV measurements of a small scale SANAE IV base model ( $Re = UD/\nu = 1 \times 10^4$ ) (Kretzschmar, 2010) . . . . .	6
2.1	Flow regimes around a cylinder for various Reynolds numbers (Lienhard, 1966) . . . . .	13
2.2	Classes of vortex formations due to lengthening of the afterbody (Morgenthal, 2000; Deniz and Staubli, 1997) . . . . .	14
2.3	Turbulence Energy Spectrum (De Villiers, 2006) . . . . .	16
2.4	Dimensionless near-wall velocity profile (Adapted from White (2006))	18
2.5	Contributing components of flow-induced structural loading . . . . .	20
2.6	Lock-in phenomena (Simiu and Scanlan, 1996) . . . . .	22
3.1	Flow patterns characteristic of a finite height, square cross-section geometry (Wang, 2004; Uffinger <i>et al.</i> , 2013) . . . . .	25
3.2	Graphical representation of Reynolds decomposition for the velocity signal (Mockett, 2009) . . . . .	32
3.3	Hierarchy of complexity for various types of RANS turbulence models (Mockett, 2009; Rung, 2000) . . . . .	36
3.4	LES filtering of the velocity signal (Mockett, 2009) . . . . .	37
3.5	Various wall-bounded grid spacing possibilities (adapted from Spalart <i>et al.</i> (2006)) . . . . .	43

3.6	Turbulence modelling strategies for the various turbulence scales (adapted from Bagleito (2009)) . . . . .	46
3.7	One-dimensional flow domain discretisation . . . . .	50
3.8	$r - \psi(r)$ digram for TVD criteria . . . . .	51
4.1	Mounted beam assembly (showing parallel beam) . . . . .	57
4.2	Wind tunnel test section set-up and components (adapted from Joubert <i>et al.</i> (2015)) . . . . .	59
4.3	Measured inlet velocity and turbulence intensity profiles (Deacon, 2009) . . . . .	61
4.4	FSI domain decomposition and information transfer . . . . .	62
4.5	Parallel beam fluid simulation domain dimensions, layout and bound- aries ( $L = 100$ mm, $D = 38$ mm and $H = 500$ mm) . . . . .	64
4.6	Perpendicular beam fluid simulation domain dimensions, layout and boundaries ( $L = 100$ mm, $D = 38$ mm and $H = 500$ mm) . . . . .	64
4.7	Parallel beam CFD mesh . . . . .	66
4.8	Perpendicular beam CFD mesh . . . . .	67
4.9	Mesh linking . . . . .	70
4.10	Simplified pressure function for a single shell element in the struc- ture mesh . . . . .	71
4.11	Load simplification through the linking procedure due to differences in mesh resolution . . . . .	72
4.12	Effect of mesh resolution on linking distances . . . . .	72
4.13	Shell meshes for structural analysis . . . . .	74
4.14	Structural model shell offsets and boundary conditions . . . . .	75
4.15	Modelling the channel with shell elements with varying thickness . . . . .	76
4.16	Connection modelling showing the channel and bracket . . . . .	76
4.17	Pressure pipes assembly . . . . .	80
4.18	Wind tunnel set-up for PIV measurements . . . . .	82
4.19	Strain gauge photos of the parallel beam . . . . .	84
4.20	Strain gauge measurement locations (units are mm) . . . . .	85
4.21	Modal tests accelerometer locations . . . . .	87
5.1	Time step residuals for the parallel beam and $U = 30$ m/s . . . . .	89
5.2	Lift coefficient over time at height $y = H/2$ . . . . .	90

5.3	Grid sensitivity comparison for the parallel beam with $U = 30$ m/s using the time-averaged pressure on the beam surface ( $x^*$ is the distance along the half perimeter of the beam cross-section) . . . .	92
5.4	Effect of mesh refinement on vortex structures for $Q = 1.5 \times 10^{-5}$ (see table 5.1 for mesh details) . . . . .	93
5.5	Near beam meshing strategies ( $y = H/2$ ) . . . . .	95
5.6	Wall-normal refinement sensitivity study meshes ( $z = 0, y = H/2$ ) .	96
5.7	Wall-normal refinement pressure results . . . . .	96
5.8	Upstream domain velocity profile comparisons (Joubert <i>et al.</i> , 2015)	98
5.9	Forces at nodes at fully loaded condition . . . . .	99
5.10	Point load strain verification set-up . . . . .	102
5.11	First three measured NF's of the parallel beam set-up . . . . .	103
5.12	First three measured NF's of the perpendicular beam set-up . . . .	103
5.13	Applied loads for different ramp times . . . . .	105
5.14	Tip displacement response to various ramp times . . . . .	105
6.1	Turbulence model comparison of time-averaged pressure along the half perimeter of the beam cross-section at various heights . . . . .	107
6.2	Turbulence model comparison of time-averaged velocity profiles of the side-wall recirculation zone . . . . .	108
6.3	Turbulence model comparison of time-averaged velocity profiles of the wake region . . . . .	109
6.4	Time-averaged velocity profiles at $y = H/2$ . . . . .	111
6.5	Vortex structure comparison for various turbulence models ( $Q = 5 \times 10^{-5}$ ) . . . . .	112
6.6	Vortex shedding frequency comparison with literature . . . . .	113
6.7	Flow-induced loading comparison for various turbulence models . .	114
7.1	Parallel beam velocity profile comparison positions . . . . .	116
7.2	Parallel beam validation results at $y = 0.5H$ . . . . .	117
7.4	Parallel beam validation results at $y = 0.94H$ . . . . .	117
7.3	Parallel beam validation results at $y = 0.72H$ . . . . .	118
7.5	Perpendicular beam velocity profile comparison positions . . . . .	119
7.6	Perpendicular beam validation results at $y = 0.5H$ . . . . .	119
7.7	Perpendicular beam validation results at $y = 0.72H$ . . . . .	120
7.8	Perpendicular beam validation results at $y = 0.94H$ . . . . .	120

7.9	Parallel beam pressure validation results . . . . .	121
7.10	Perpendicular beam pressure validation results . . . . .	122
8.1	Velocity magnitude and pressure coefficient plot of the parallel beam with $U = 30$ m/s . . . . .	124
8.2	Velocity magnitude and pressure coefficient plot of the perpendicular beam with $U = 30$ m/s . . . . .	124
8.3	Wake vortex structure top view comparison for the four case studies ( $Q = 5 \times 10^{-5}$ ) . . . . .	125
8.4	Wake vortex structure side view comparison for the four case studies ( $Q = 5 \times 10^{-5}$ ) . . . . .	126
8.5	Parallel beam strain gauge measurements for various speeds . . . . .	127
8.6	Perpendicular beam strain gauge measurements for various speeds . . . . .	128
8.7	Time-averaged flow-induced strain on the parallel beam at various flow speeds (strain modulus results on the middle plane of the shell elements) . . . . .	129
8.8	Time-averaged flow-induced strain on the perpendicular beam at various flow speeds (strain modulus results on the middle plane of the shell elements) . . . . .	130
9.1	Time-averaged three-dimensional global flow features represented by the streamlines (Joubert <i>et al.</i> , 2015) . . . . .	133
9.2	Time-averaged cross-section flow features (Joubert <i>et al.</i> , 2015) . . . . .	134
9.3	Time-averaged velocity profiles in the wake for $u_x$ and $u_y$ (Joubert <i>et al.</i> , 2015) . . . . .	135
9.4	Time-averaged horizontal velocity profiles on the side-wall region for $u_y$ and $u_z$ (Joubert <i>et al.</i> , 2015) . . . . .	136
9.5	Instantaneous velocity and pressure for the points of maximum and minimum lift during the vortex shedding cycle (Joubert <i>et al.</i> , 2015)	137
9.6	Identifying key points in the vortex shedding cycle using the lift coefficient (adapted from Joubert <i>et al.</i> (2015)) . . . . .	138
9.7	The time-averaged lift coefficient distribution over the height of the beam for the point of a) maximum and b) minimum lift during the vortex shedding cycle with standard deviations (Joubert <i>et al.</i> , 2015)	139



9.8	The time-averaged pressure coefficient distribution over the half perimeter of the beam cross-section for the point of a) maximum and b) minimum lift during the vortex shedding cycle (Joubert <i>et al.</i> , 2015) . . . . .	140
9.9	Iso-surfaces ( $Q = 5 \times 10^{-5}$ ) (Joubert <i>et al.</i> , 2015) . . . . .	141
9.10	Vortex stretching in the wake region . . . . .	142
9.11	Time-dependent a) surface pressure, b) lift and c) tip displacement (where points A and B are the time instances of minimum and maximum tip displacement which used for further discussion) . . .	143
9.12	Mesh deformation at times of minimum and maximum displacement	144
9.13	Tip displacement frequency . . . . .	145
9.14	Tip displacement trace . . . . .	146
A.1	PIV calibration target . . . . .	153
A.2	Pressure transducer calibration curves (S/N: DB07820109D) . . . .	154
A.3	Pressure transducer calibrations curves (S/N: DB07830109D) . . . .	154
A.4	Parallel beam strain gauge calibration curves . . . . .	156
A.5	Perpendicular beam strain gauge calibration curves . . . . .	157
A.6	Displacement test set-up . . . . .	158
C.1	Mounted beam assembly (showing parallel beam) . . . . .	162
C.2	Brackets dimensions . . . . .	163
C.3	Channel side view dimensions . . . . .	163
C.4	Channel top view dimensions . . . . .	164
D.1	Extract fluid mesh (OpenFOAM utility) . . . . .	165
D.2	Extract fluid pressure (OpenFOAM utility) . . . . .	165
D.3	Extract fluid shear stresses (OpenFOAM utility) . . . . .	166
D.4	Extract structural mesh (Code-Aster command file) . . . . .	166
D.5	Find mesh face centre nearest neighbours (Python file) . . . . .	166
D.6	Defining time-dependent structural analysis (Code-Aster command file) . . . . .	167
F.1	Vibration results for parallel beam at $U = 30$ m/s . . . . .	171
F.2	Vibration results for parallel beam at $U = 60$ m/s . . . . .	172
F.3	Vibration results for perpendicular beam at $U = 30$ m/s . . . . .	173
F.4	Vibration results for perpendicular beam at $U = 60$ m/s . . . . .	173

# List of Tables

1.1	SANAE IV base dimensions . . . . .	2
2.1	Properties of turbulence scales . . . . .	17
3.1	SGS stress terms . . . . .	39
3.2	RANS length scales . . . . .	42
3.3	IDDES blending function, $f_B$ , modes of operation . . . . .	45
3.4	Turbulence modelling methods and readiness (Adapted from Spalart (2000)) . . . . .	47
3.5	Blending factor functions for various schemes (Versteeg and Malalasekera, 2007) . . . . .	50
4.1	Fluid domain simulation boundary conditions . . . . .	63
4.2	Parallel beam fluid mesh refinement distances . . . . .	65
4.3	Perpendicular beam fluid mesh refinement distances . . . . .	68
4.4	Structure mesh elements, materials and offsets (see also figures 4.14 and 4.15) . . . . .	77
4.5	PIV post-processing (top view, downstream camera) . . . . .	83
5.1	Mesh sensitivity study refinement levels and mesh sizes . . . . .	91
5.2	Comparison of drag measured, reproduced by CFD and applied to the structure for the parallel beam and $U = 30$ m/s . . . . .	99
5.3	Structure mesh refinement sensitivity . . . . .	100
5.4	Comparison of simulated and measured strain for the parallel beam subjected to a drag equivalent point load . . . . .	101
5.5	Natural frequency prediction accuracy . . . . .	103
6.1	Comparison of performance for various turbulence models (* = from literature) . . . . .	110

*LIST OF TABLES*

xviii

8.1	Comparison of time-averaged simulated and measured strain values (at gauge no. 2 and 6) . . . . .	131
A.1	Strain gauge specifications . . . . .	155
A.2	Displacement test results comparison . . . . .	158
B.1	Free beam sensitivity study . . . . .	160
B.2	Mounted beam sensitivity study . . . . .	161

# Nomenclature

## Abbreviations

CBC	Convective boundedness criteria
CFD	Computational fluid dynamics
CPU	Central processing unit
DDES	Delayed detached eddy simulation
DES	Detached eddy simulation
DoF	Degree-of-freedom
FDM	Finite difference method
FEM	Finite element method
FSI	Fluid structure interaction
FVM	Finite volume method
GPU	Graphical processing unit
HPC	High performance computing
IDDES	Improved delayed DES
LES	Large eddy simulation
LLM	Log-layer mismatch
NF	Natural frequency 1/s
NRF	National Research Foundation
NVD	Normalised variable diagram
NVF	Normalised variable formulation
FOAM	Field Operation And Manipulation
PDE	Partial differential equation
QUICK	Quadratic Upstream Interpolation for Convective Kinematics
RAM	Random access memory

RANS	Reynolds Averaged Navier-Stokes
RNG	Renormalized group
RMS	Root mean square
RSM	Reynolds Stress Model
S-A	Spalart-Allmaras
SANAE	South African National Antarctic Expedition
SANAP	South African National Antarctic Program
SGS	Sub-grid scale
SST	Shear Stress Transport
TKE	Turbulence kinetic energy . . . . . [ m <sup>2</sup> /s <sup>2</sup> ]
TVD	Total variation diminishing
WMLES	Wall-modelled LES
URANS	Unsteady Reynolds Averaged Navier-Stokes

**Roman Symbols**

$C$	Damping matrix . . . . . [ kg/s ] Coefficient
$d_w$	Wall distance . . . . . [ m ]
$D$	Beam cross-section width . . . . . [ m ]
$E$	Energy density . . . . . [ m <sup>2</sup> /s <sup>2</sup> ]
$f$	Function Frequency . . . . . [ 1/s ]
$f_i$	Specific fluid body forces (gravity and centrifugal) [ m/s <sup>2</sup> ]
$G$	Spacial filtering kernel
$H$	Beam height . . . . . [ m ]
$k$	Turbulence kinetic energy . . . . . [ m <sup>2</sup> /s <sup>2</sup> ]
$K$	Stiffness matrix . . . . . [ kg/s <sup>2</sup> ]
$l$	Turbulence length scale . . . . . [ m ]
$L$	Beam cross-section length . . . . . [ m ]
$M$	Mass matrix . . . . . [ kg ]
$p$	Pressure variable . . . . . [ Pa/æ ]

$P$	Inlet pressure boundary value . . . . .	[Pa/æ]
$P_k$	Turbulence production term . . . . .	[m <sup>2</sup> /s <sup>3</sup> ]
$Q$	Second invariant of the velocity gradient tensor	
$\rho$	Density . . . . .	[kg/m <sup>3</sup> ]
$r$	Differencing ratio	
$\tilde{S}$	Modified vorticity	
$t$	Time . . . . .	[s]
$T_i$	Turbulence intensity	
$U$	Inlet velocity . . . . .	[m/s]
$u, v, w$	Velocities . . . . .	[m/s]
$x$	Distance in the streamwise direction . . . . .	[m]
$\ddot{x}$	Acceleration . . . . .	[m/s <sup>2</sup> ]
$y$	Distance in the vertical direction or distance from the wall . . . . .	[m]
$z$	Distance in the transverse direction . . . . .	[m]

### Greek Symbols

$\alpha$	Generic parameter	
$\delta$	Boundary layer thickness . . . . .	[m]
$\delta_{ij}$	Kronecker delta	
$\Delta$	Grid spacing or filter width . . . . .	[m]
$\epsilon$	Turbulence dissipation rate . . . . .	[m <sup>2</sup> /s <sup>3</sup> ]
$\theta$	Angle . . . . .	[°]
$\kappa$	Von Karman constant	
$\mu$	Dynamic viscosity . . . . .	[kg/ms]
$\nu$	Kinematic viscosity . . . . .	[m <sup>2</sup> /s]
$\nu_t$	Turbulence viscosity or eddy-viscosity . . . . .	[m <sup>2</sup> /s]
$\tilde{\nu}$	Spalart-Allmaras turbulence field variable . . . . .	[m <sup>2</sup> /s]
$\phi$	Flow variable	
$\rho$	Density . . . . .	[kg/m <sup>3</sup> ]
$\tau$	Shear stress . . . . .	[kg/ms]

$\psi$	Blending factor
$\Psi$	Limiter function
$\omega$	Specific turbulence dissipation rate . . . . . [m <sup>2</sup> /s <sup>3</sup> ]

**Vectors and Tensors**

$C_{ij}$	Clark stress tensor . . . . . [kg/ms <sup>2</sup> ]
$L_{ij}$	Leonard stress tensor . . . . . [kg/ms <sup>2</sup> ]
$R_{ij}$	Reynolds stress tensor . . . . . [kg/ms <sup>2</sup> ]
$S_{ij}$	Strain rate tensor . . . . . [m/ms]

**Subscripts**

$\parallel$	Parallel
$d$	Dissipative scales
$d$	Wall values
$D$	Diameter
$i$	Inertia driven scales
	Intensity
	Inlet
	Spacial or summation index
$k$	Turbulence kinetic energy
$l$	Lift
$m$	Molecular
$p$	Cell centre point
$p$	Pressure
$t$	Turbulence
$w$	Wall
$x, y, z$	Direction indicators
$\infty$	Free-stream or inlet values

**Superscripts**

'	Fluctuating component
---	-----------------------

+	Wall units
*	Different from the norm (for example: $x^*$ distance along half perimeter)

**Oversymbols**

–	Averaged component
	Filtered term
~	Test filter
∧	Filtered variable

**Dimensionless Groups**

$C_p$	Pressure coefficient . . . . .	$[(p_x - P)/(\frac{1}{2}\rho U^2)]$
$C_l$	Lift coefficient . . . . .	$[(p_z - P)/(\frac{1}{2}\rho U^2)]$
$Re$	Reynolds number . . . . .	$[UL/\nu]$
$Re_D$	Reynolds number (diameter) . . . . .	$[UD/\nu]$
$Re_y$	Reynolds number (wall distance) . . . . .	$[Uy/\nu]$
$St$	Strouhal number . . . . .	$[fD/U]$
$u^+$	Dimensionless velocity . . . . .	$[u/u_\phi]$
$y^+$	Dimensionless wall distance . . . . .	$[yu_\phi/\nu]$



# Chapter 1

## Introduction

### 1.1 Background and Motivation

Structures encounter flow-induced loading when in contact with a fluid that has a different speed, pressure or temperature. It plays a key role in almost every energy conversion technology in use today and is most recognisable in cases where engineering structures are subjected to harsh environments. Some examples are wind loading on buildings, ocean vessel hydrodynamics, aircraft wing flutter, vehicle aerodynamic drag, wind turbine blade vibrations and many more. The complex relationship between the fluid and structure is often referred to as fluid structure interaction (FSI). If the FSI effects are neglected in the design of engineering structures it can have catastrophic effects. One well known example of the destructive power of FSI is highlighted in the collapse of the first Tacoma Narrows Bridge in 1940 shown in figure 1.1.

At the time, designers had to rely on experience and experimentation to determine flow-induced loading and structural response since numerical or analytical methods for prediction of flow induced oscillations were not yet developed. The disaster highlighted the importance of accounting for unsteady wind loading on bridges. Since the incident occurred significant research has been done to study FSI which highlights the importance of this field in modern engineering and design. For example, it has been observed that aerodynamic loading can be the determining factor for stiffness in long-span bridges even in areas susceptible to earthquakes (Morgenthal, 2000).

This particular study was motivated by structural vibrations observed in the South African National Antarctic Expedition (SANAE) IV base in Antarc-

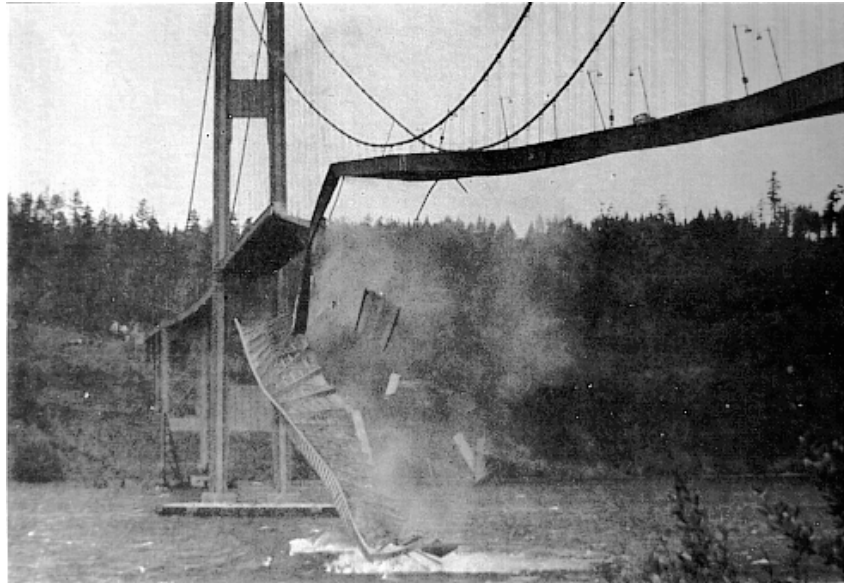


Figure 1.1: Tacoma Narrows bridge collapse of 1940 (Elliott, 1940)

tica during strong wind conditions. The SANAE IV base is situated entirely above ground on a rocky outcrop named Vesleskarvet (see figures 1.2 and 1.3). It consists of three interlinking block sections orientated from north to south and was specifically designed to reduce snow build-up by allowing the predominantly easterly wind to blow underneath the base and then transport snow over a nearby cliff. The base structure consists of a shell which is stiffened by an underlying steel rib network. The structure is mounted 3 m above ground on steel poles which are secured to the bedrock with rock bolts.

The base consists of sections, named block *A*, *B* and *C*, which have the dimensions listed in table 1.1. Block *A* houses the sleeping quarters and science equipment and has a rectangular cross-section with rounded edges. The cross-section is characterised by a length parallel to the flow,  $L$ , of 12.32 m and width perpendicular to the flow,  $D$ , of 6.53 m resulting in a  $L/D$  ratio of 1.89 (see figure 1.4).

Table 1.1: SANAE IV base dimensions

Block	$H$	$L$	$D$	$L/D$
<i>A</i>	44.97	12.32	6.53	1.89
<i>B</i>	44.97	14.82	6.53	2.27
<i>C</i>	44.97	15.27	7.12	2.14

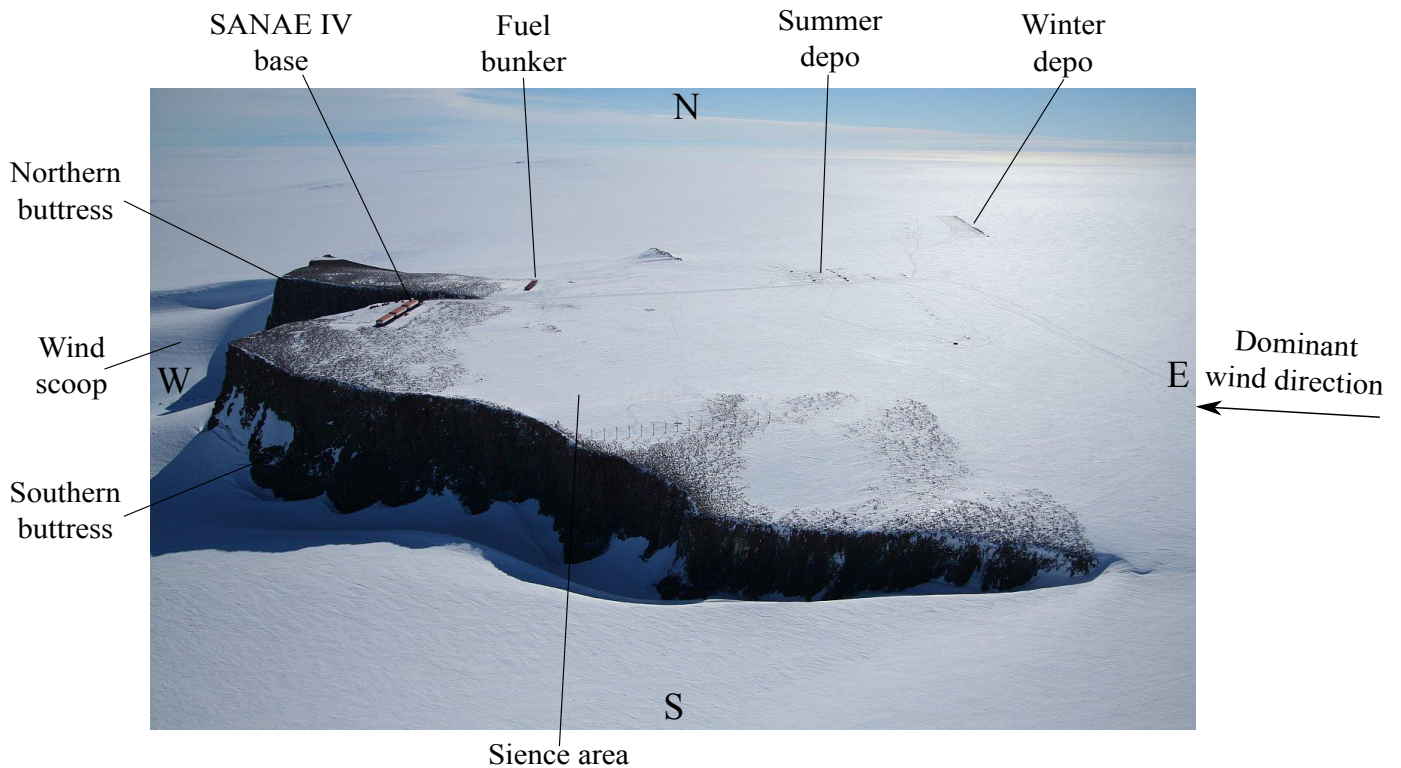


Figure 1.2: Vesleskarvet including the SANAE IV base and other structures in surrounding area looking north (Hofmeyr, 2015)

It has been observed many times that at medium to high wind speeds flow-induced structural loading results in high levels of noise and vibration of objects inside the base. This was experienced first hand when the author had the privilege of visiting the base during the summer takeover expedition of December 2010. The vibrations and noise reduce the human comfort of the occupants and especially the overwintering team who are confined to the base during the winter months. The structural vibrations are most extreme during winter storms when the wind speed at the base regularly exceeds 100 km/h and even sometimes exceed 200 km/h.

Structural vibrations also have an effect on the sensitive measurement equipment mounted within the base by affecting its accuracy and life. Lastly the base itself is starting to show signs of fatigue. This includes cracks, shell panel separation and loosening of rock bolts. Separation of the insulating shell panels results in heat loss and consequently, more fuel consumption especially in the winter months. The result is that the base has to constantly be maintained by the overwintering team with limited tools and resources as well as a

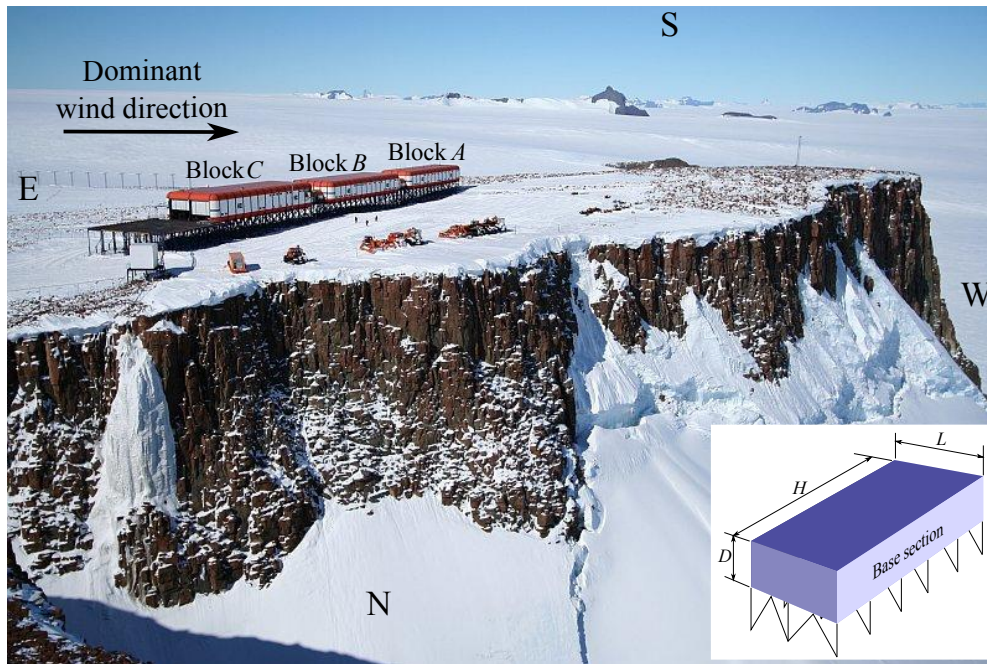


Figure 1.3: SANAE IV base situated on the Southern Buttress looking south (Hofmeyr, 2015)

summer takeover maintenance team who addresses the most significant issues during the one month stay at the base.

Although structural failure is not an immediate concern, it is important to understand all factors which have an effect on the human comfort and base life expectancy especially since the base, which is already more than 15 years old, is nearing the end of its designed life of 20 years and funding for a new base is limited. Therefore, the origin and implications of the flow-induced structural loading should be investigated so that human comfort, energy efficiency and base life expectancy can be improved.

From experience with bluff-body aerodynamics and commonly associated flow features such as separation and vortex shedding the hypothesis is that the aerodynamics around the base is expected to cause a steady drag loading, occasional buffeting from wind gusts and unsteady loading on the outer shell due to vortex shedding originating at the upstream base edges. This flow separation, was confirmed in preliminary wind tunnel studies of the base aerodynamics with the help of particle image velocimetry (PIV) measurements as shown in figure 1.5.

The most important factors summarising the SANAE IV base problem are

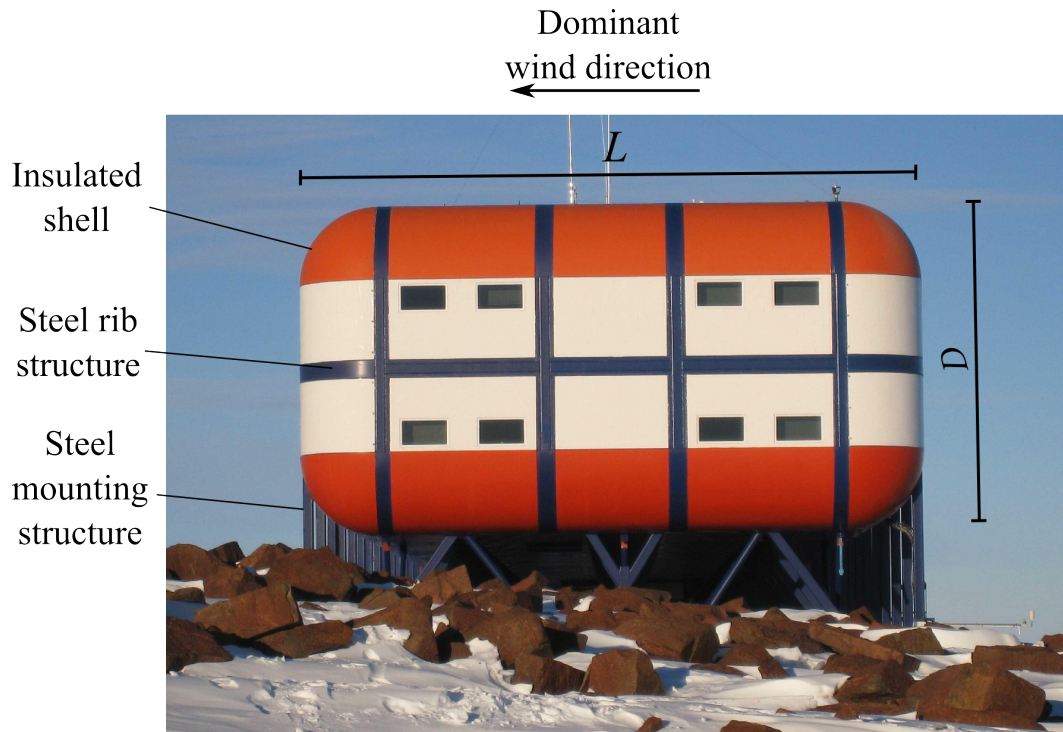


Figure 1.4: South facade of the SANAE IV Base in Antarctica

as follows:

- The base shape is simple, more aerodynamic than most buildings, can be considered a bluff-body and has some characteristics related to circular and rectangular prism geometries.
- Structurally the base is quite complex, it is very stiff, consists of a metal frame structure with a double shell for thermal insulation and has numerous internal objects of unknown weight.
- The vibrations observed result in very small displacements, has a relatively low frequency and is associated with medium to high wind speeds.

## 1.2 Research Objectives

The author visited the SANAE IV base during the December 2010 summer takeover expedition and subsequently conducted a preliminary literature review. After this it was decided that a detailed study of the base would not be the best approach. This is because of the size of the base and uncertain-

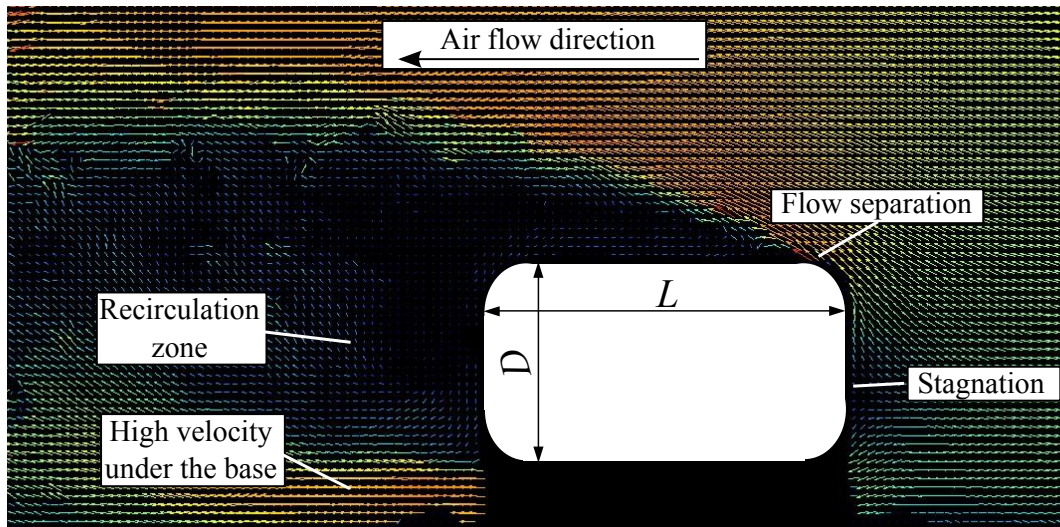


Figure 1.5: Wind tunnel PIV measurements of a small scale SANAE IV base model ( $Re = UD/\nu = 1 \times 10^4$ ) (Kretzschmar, 2010)

ties regarding the structure and content due to restricted access and outdated construction blueprints. Additionally, funding limitations prevented further access to the base itself to do on-site wind and structural measurements.

Instead it was decided to focus on the fundamental mechanics of this type of FSI, to develop a suitable one-way FSI coupling methodology and to test it on a simple geometry. In this way the methodology could then later be applied to the SANAE IV base or similar structures in the future. This work, therefore, simplifies the subject geometry but delves into understanding the bluff-body aerodynamics, flow-induced structural loading, developing the numerical method and validating the models.

Additionally, one of the goals of this study was to make use of open source software as far as possible. This is because the free licences makes larger simulations needing parallel computing more affordable and the availability of the source code makes it possible to use, modify and expand existing code.

In more detail the objectives can be listed as follows:

- Identify, design and manufacture a suitable bluff-body structure which could act as the subject for developing, testing and validating the one-way FSI coupling method.
- Take measurements of the mechanical properties, aerodynamics and structural response to characterise boundary conditions and test the accuracy

of the applied methodology.

- Review commonly used turbulence models by comparing it to measurements and identify an appropriate model for bluff-body aerodynamics.
- Identify and describe the key bluff-body flow characteristics of the chosen geometry in detail.
- Develop a coupling model to transfer the flow data to the structural grid.
- Simulate and analyse structural dynamics.
- Quantify the accuracy of the flow and structural simulation results by comparing it to the measured data.

### 1.3 Dissertation Outline

This dissertation starts with a review of the underlying mechanisms involved in bluff-body aerodynamics and FSI. Following this is a review of various numerical methods to find an accurate and efficient way for simulating the aerodynamics, structural loading and response.

In the methodology chapter a cantilever beam structure is selected as the subject geometry for this investigation. This chapter describes the methods and procedures used for the simulations and measurements. The methodology chapter is then followed by the sensitivity studies where the methodology is put to the test.

After the sensitivity studies one chapter is dedicated to the review of a number of turbulence models and comparing it to measured data. After this the next chapter provides a detailed data comparison for the chosen turbulence model against measured data for various speeds and orientations.

The subsequent chapter gives an overview of the flow and structural loading of different beam orientations and flow speeds using the developed FSI methodology explained in previous chapters. In the next chapter one case is selected for further investigation due to its transient flow and structural response.

Lastly, a summary of the findings is given as well as the conclusions and recommendations derived from the investigation.

## 1.4 Contributions and Accomplishments

In this project the following contributions were made:

- The fundamental underlying phenomena and resulting bluff-body aerodynamics of a finite height rectangular prism with cross-section ratios of  $L/D = 2.63$  and  $D/L = 0.38$  and Reynolds number varying between  $7.6 \times 10^4 < Re < 4 \times 10^5$  has been investigated in detail (see also published work (Joubert *et al.*, 2015)).
- Accurate wind tunnel measurements for fluid dynamics and structural loading of a cantilever beam have been provided and used to show the accuracy of the implemented numerical models. This data can now be used in future studies for validation and benchmarking of highly separated flow solvers and models. The measured data include velocity (using PIV), pressure, strain and vibration values.
- A large part of this project involved the new PIV system set-up and measurements for which the author was responsible as part-time laboratory engineer. The work with the PIV system lead to a number of improvements of the existing infrastructure and testing methods for which a guideline is provided in this report. These contributions allow new users to do more accurate PIV measurements based on the experience gained through numerous projects.
- The state-of-the-art Spallart-Allmaras improved, delayed, detached eddy simulation (IDDES) turbulence model for computational fluid dynamics (CFD) has been reviewed, implemented and shown to be accurate and computationally efficient despite the complexity of the aerodynamics.
- The “all- $y^+$ ” wall function was implemented in the CFD and shown to be accurate and computationally efficient. This wall treatment makes meshing significantly less strict and it has been shown to work effectively with the detached eddy simulation (DES) turbulence model even though it was mostly used for Reynolds-averaged Navier Stokes (RANS) models in the past.
- A one-way FSI coupling method was developed and implemented. This made it possible to analyse the flow-induced structural loading which was



shown to be accurate when compared to measured strain and vibration values. This methodology and initial results were also presented at the SACAM 2014 international conference (Joubert *et al.*, 2014).

- The author was one of the first researchers to use the open source software OpenFOAM and Code-Aster extensively at Stellenbosch University. Since then, as a direct consequence of this study, the user base and expertise has grown significantly. Additionally, this study contributed towards the implementation of OpenFOAM on the high performance cluster (HPC) at Stellenbosch University's Engineering Faculty as well as on one of the first high performance graphical processing unit (GPU) computers at the faculty which was also presented at th SACAM 2014 conference (Van Zyl *et al.*, 2014).

## Chapter 2

# Mechanics of Fluid Structure Interaction

This chapter is the first part of the literature review and discusses the fundamental mechanics describing the underlying phenomena contributing to fluid structure interaction (FSI). The content includes topics such as viscous fluid flows, bluff-body aerodynamics, turbulence, near-wall flow patterns, aeroelasticity and vortex-induced vibrations.

### 2.1 Viscous Fluid Flow

The starting point for investigating the complex mechanics of FSI is to consider the effects of viscous shear stresses on the fluid dynamics. Viscous fluids moving along surfaces will result in boundary layers that develop due to the no-slip condition along the surface and the viscous shear forces that slows down the near-wall fluid particles. The greater the fluid viscosity, the greater the shear forces acting on the neighbouring fluid particles will be and, consequently, the larger the boundary layer that develops. A greater viscosity, therefore, means more of the bulk flow is affected by the no-slip condition.

The boundary layer represents the section of fluid affected by the no-slip condition and is characterised by velocity gradients starting from very large at the wall to zero at the boundary layer outer limits. Fluid pockets within the boundary layer, that are subjected to the inherent velocity gradients, will experience driving shear forces from the free-stream on one side and retarding shear forces from the no-slip condition on the other side resulting in rotational

flow in the near-wall region.

The free stream flow is, however, not always parallel to the wall. In cases where the wall boundary curves away from the mean flow direction separation can occur. The phenomena of separation can be explained considering flow around a cylinder. A fluid parcel approaching a cylinder will experience a deceleration as it nears the stagnation point high pressure zone. As the flow is redirected around the cylinder the fluid parcel experiences an accelerating force due to a favourable (negative) pressure gradient until the maximum velocity is reached at the midpoint around the cylinder circumference. When the parcel moves towards the downstream side of the cylinder it experiences a adverse (positive) pressure gradient and consequently decelerates. If a fluid parcel is was not affected by the no-slip condition on the wall then the downstream velocity will be the same as the upstream velocity. On the other hand, if the fluid parcel is slowed down by the wall shear stresses as it moves passed the cylinder in close proximity then it will not have enough momentum to overcome the adverse pressure gradient on the downstream side. The adverse pressure gradient will slow down the fluid parcel and reverse its direction causing it to block other fluid parcels which will have to separate from the wall to move passed the obstruction and maintain momentum balance.

The phenomena of separation and vortex formation, as explained above, can be said to be strongly influenced by the free stream momentum and the viscous stresses of the fluid. This relation of inertia forces and viscous effects is expressed by the Reynolds number ( $Re = UD/\nu$ ) where the characteristic length,  $D$ , represents the size of the flow obstruction. Using the Reynolds number it is possible to represent the flow characteristic in a dimensionless form allowing for effective comparison with previous studies reported in literature, as well as scaling. But vortex shedding around simple and common geometries is very complex. It can occur in many different regimes which are highly dependent on the Reynolds number, therefore, making it very challenging to predict analytically or reproduce numerically (Morgenthal, 2000).

### 2.1.1 Cylinder aerodynamics

Flow around a cylinder is one of the most widely studied bluff body cases. It is considered here because of the rounded edges of the SANAE IV base, because of its wide use in engineering applications and also because it presents

an opportunity to investigate the effects of complex fluid dynamics related to vortex shedding using a relatively simple geometry. Common examples of cylinders in engineering structures are antennas, bridge stay cables, pipelines and risers used in deep sea drilling operations.

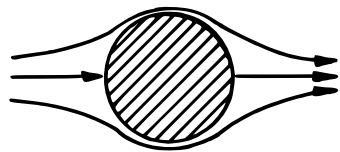
Reviewing previous work it quickly becomes clear that the effects of Reynolds number on the vortex shedding around a cylinder is highly complex, difficult to predict numerically and even challenging to measure experimentally. For example, Kravchenko and Moin (2000) summarised the findings of various authors who found that the separating shear layer around a cylinder is highly sensitive to various experimental parameters such as the free-stream inlet turbulence (Bloor, 1964), acoustic noise (Cardell, 1993), cylinder vibrations (Chyu and Rockwell, 1996), boundary conditions (Prasad and Williamson, 1996, 1997) and aspect ratio (Norberg, 1994).

Despite the challenges, it has become one of the most widely documented topics in bluff-body aerodynamics, vortex shedding and also FSI due to the simple geometry, rich variety of flow phenomena, high dependency on the Reynolds number, numerical calibration potential and different vortex shedding regimes. A summary of the known flow regimes for cylinders is shown in figure 2.1.

### 2.1.2 Rectangular cross-sectioned prism aerodynamics

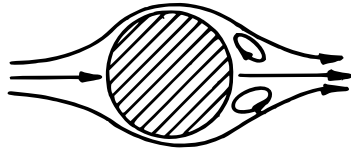
Research related to the fluid dynamics around cylinders and their associated structural loading is extensively documented. However, although it provides insight for a rich variation in fluid phenomena dependent on the Reynolds number, it is still only applicable to certain engineering cases. Rectangular cross-sectioned structures, on the other hand, are very common. Some examples are, buildings, bridges, walls, trains and even some large ships and barges.

Rectangular cross-sectioned prisms present a different set of challenges due to their high degree of bluntness (sharp edges) which causes flow characteristics such as high pressure gradients, relatively fixed position of separation and vortex-induced loading on the afterbody (the section of the geometry downstream of separation point). Parkinson (1989), as one example, highlighted that the size and shape of the afterbody is one of the most important parameters for a two-dimensional body exhibiting vortex-induced excitations since this



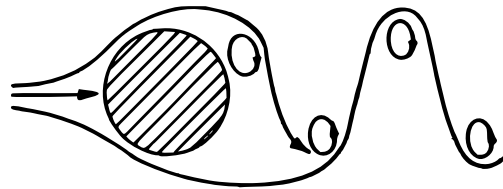
**$Re < 5$**

Regime of unseparated flow.



**$5 \text{ to } 15 < Re < 40$**

A fixed pair of Föppl vortices in the wake.

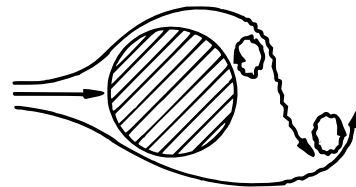


**$40 \leq Re < 90$  and  $90 \leq Re < 150$**

Two regimes in which vortex street is laminar.

Periodically governed in low Re range by wake instability.

Periodically governed in high Re range by vortex shedding

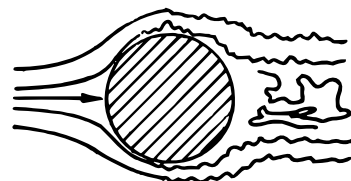


**$150 \leq Re < 300$**

Transition range to turbulence in vortex.

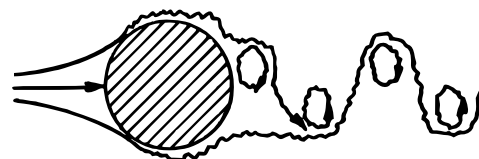
**$300 \leq Re < 3 \times 10^5$**

Vortex street is fully turbulent.



**$3 \times 10^5 \leq Re < 3.5 \times 10^6$**

Laminar boundary layer has undergone turbulent transition. The wake is narrower and disorganised. No vortex street is apparent.



**$3.5 \times 10^6 \leq Re < \infty (?)$**

Re-establishment of the turbulent vortex street that was evident in  $300 \leq Re < 3 \times 10^5$ . This time the boundary layer is turbulent and the wake thinner.

Figure 2.1: Flow regimes around a cylinder for various Reynolds numbers (Lienhard, 1966)

is where the pressure loading occurs. This means that a geometry orientated perpendicular to the flow is likely to encounter very little excitation compared to the same geometry orientated parallel to the flow (Parkinson, 1974). This almost seems like the opposite of what is expected in practice since structures orientated parallel to the flow are more streamline and, therefore, considered

to have smaller drag loading.

The influence of the afterbody is highlighted when considering rectangular cross-sectioned prisms of different  $L/D$  ratios and the resulting vortex shedding phenomena. Deniz and Staubli (1997) presented the findings of various authors that relate the effect of the  $L/D$  ratio of a rectangular cross-sectioned prisms to the vortex shedding frequency (represented by the Strouhal number ( $St = fD/U$ )). This relation is shown in figure 2.2.

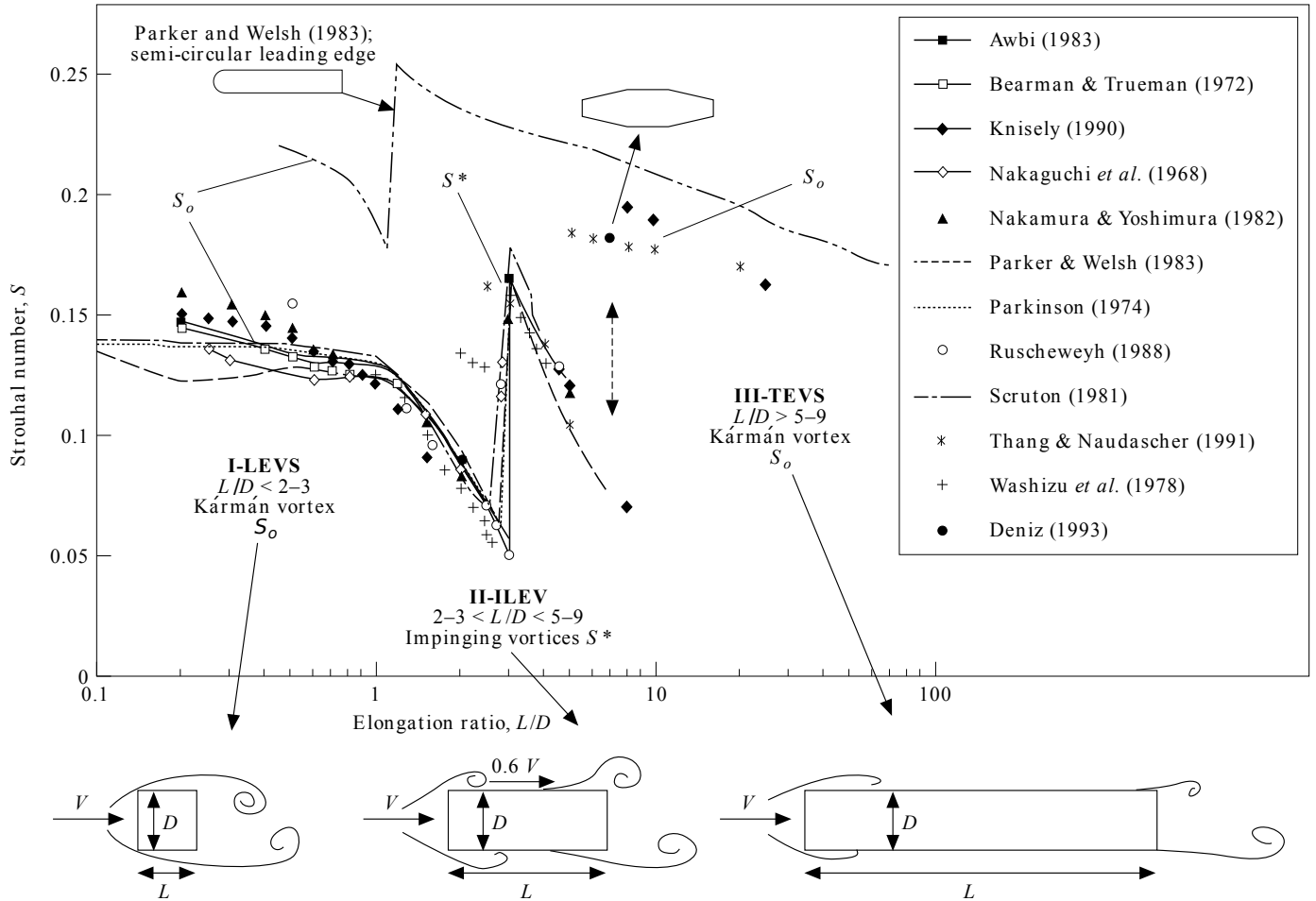


Figure 2.2: Classes of vortex formations due to lengthening of the afterbody (Morgenthal, 2000; Deniz and Staubli, 1997)

For  $L/D < 2 - 3$ , such as for the widely studied infinite square cross-sectioned prism, the afterbody (length of geometry after separation point) is short and the upstream edge vortex shedding dominates without impinging on the side-wall. The next regime is for  $2 - 3 < L/D < 5 - 9$  where upstream

edge vortex shedding impinges on the side-wall but without reattachment taking place. Lastly, for  $L/D > 5 - 9$  the upstream edge vortices attach to the side-wall and trailing edge vortex shedding dominates.

## 2.2 Mechanics of Turbulence

The mechanics of turbulence and predicting its effect on the flow is one of the most widely studied topics in computational fluid dynamics due to its importance and wide applicability to engineering applications. This section looks at the origin of turbulence as well as the effects of various scales of turbulence on the flow. In section 3.5 the numerical methods for modelling turbulence are discussed in more detail.

It has been observed that flow becomes unstable, or turbulent, when the inertia forces exceed the viscous forces by a certain ratio which, as previously mentioned, are effectively expressed by the Reynolds number. Turbulence can be described as rotational flow structures characterised as being random, chaotic, unsteady and three-dimensional. These rotational flow structures, also called turbulent eddies, cause effective mixing by bringing particles close together which were initially separated by some distance and so allowing the exchange of all flow properties including mass, momentum and heat. Furthermore, turbulence can only exist in the presence of viscous shear (De Villiers, 2006) which prevents the uncontrolled growth of turbulence by dissipating energy through the conversion of momentum into heat.

An important, and often overlooked, characteristic of turbulence is that eddies have a wide range of length scales which becomes important when developing mathematical approximations. For the purpose of this discussion turbulent eddies are categorised into large, medium and small scales each with different characteristic and energy content. De Villiers (2006) describes the various scales of turbulence using the idealized turbulence energy spectrum as shown in figure 2.3.

**Large eddies** have a more permanent and predictable nature. They are dominated by inertia effects, which are independent of the viscosity, and introduce turbulence kinetic energy (TKE) into the system by extracting energy from the mean flow. Since the large eddies contain the most TKE they are often referred to as the energetic scales. These large eddies are also anisotropic

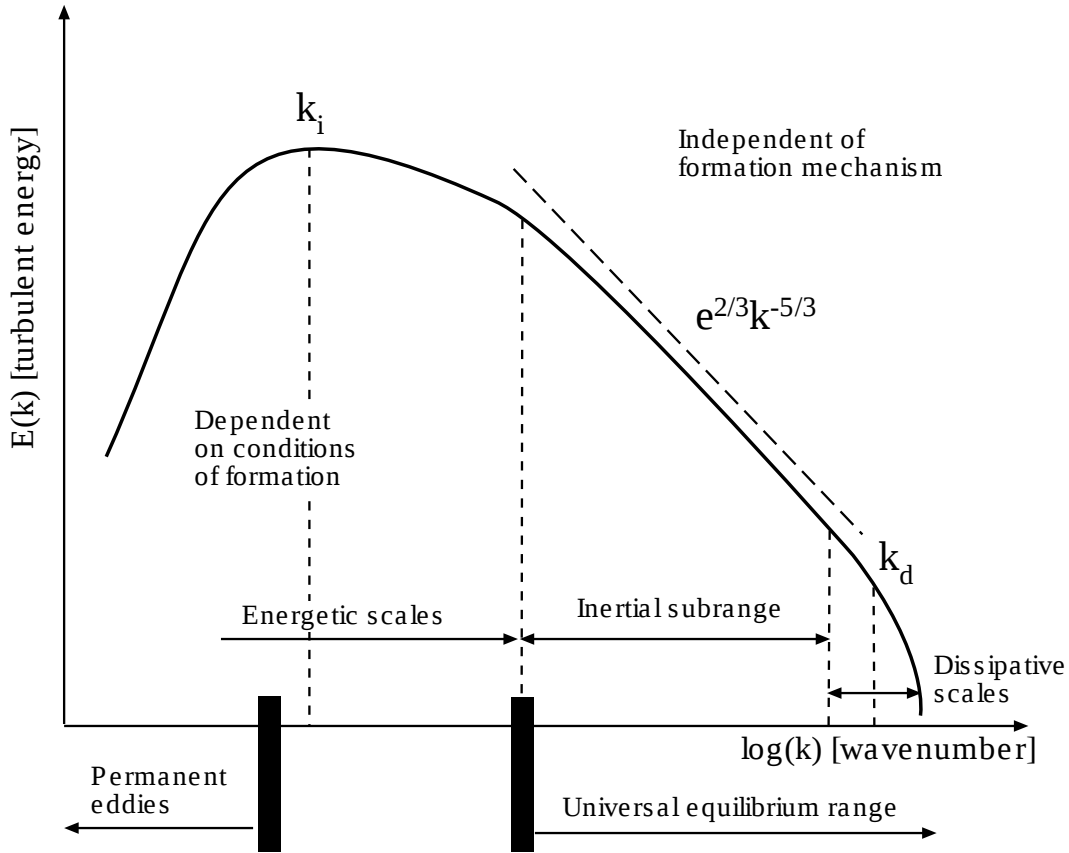


Figure 2.3: Turbulence Energy Spectrum (De Villiers, 2006)

(or directional which means angular momentum is preserved) and can be affected by the boundary conditions.

When larger eddies break down through a sequence of complex instabilities they form **medium eddies** also referred to as the transitive scales or inertial sub-range. These eddies are still dominated by inertia rather than viscous effects but contain very little, and dissipate insignificant amounts of, TKE. Instead the medium scales have the purpose of transporting energy from the larger energetic scales to the smaller dissipative scales (De Villiers, 2006). The medium scale eddies are more isotropic (non-directional or invariant under rotation) and obey the Kolmogorov (1991) theory expressed in equation 2.2.1:

$$E(k) = C_k \epsilon^{2/3} k^{-5/3} \quad (2.2.1)$$

The last category, or **small eddies**, are dominated by viscous effects. These eddies are independent of mean flow forcing effects or boundary con-



ditions as is the case with the large eddies. Small eddies fulfil the role of converting the momentum energy, handed down through the transitive scales (medium eddies), into heat and can be identified in the turbulence energy spectrum by an almost exponential drop-off in turbulence energy (see figure 2.3). Therefore, these eddies are often referred to as the dissipative scales.

This section showed the following important characteristics of turbulence:

- It is very effective at mixing flow properties.
- Different scales of turbulence exist with very different characteristics which are listed in table 2.1.
- To model all scales of turbulence in the same way will be too simplistic.

Table 2.1: Properties of turbulence scales

Large eddies	Medium eddies	Small eddies
Energetic scales	Transitive scales	Dissipative scales
Introduces TKE	Transfers TKE	Drains TKE
Dominated by inertia effects	Independent of inertia effects	Independent of inertia effects
Independent of viscous effects	Independent of viscous effects	Dominated by viscous effects
Anisotropic	Isotropic	Isotropic
Affected by boundaries	Independent of boundaries	Independent of boundaries

## 2.3 Near-wall Velocity Profile

Having a closer look at the near-wall velocity profile for turbulent flows it is possible to see that the effects of turbulence differs significantly from free flows due to the presence of the wall boundary. Using the Reynolds number (ratio of inertia and viscous forces) with the length scale based on wall distance,  $Re_y = Uy/\nu$ , it is possible to see that far from the wall (large  $y$ ) inertia forces will dominate ( $Re_y > 1$ ) and very close to the wall (small  $y$ ) viscous

forces will dominate ( $Re_y < 1$ ). This is confirmed through measurements, which are presented in figure 2.4, showing a thin linear region where the viscous forces dominate, a logarithmic region where both inertia and viscous forces are important and a wake region where inertia forces dominate.

A dimensional analysis of the measured velocity profiles for attached turbulent boundary layers can be done using the so called friction velocity,  $u_\tau = \sqrt{\tau_w/\rho}$ . This procedure produces two new dimensionless groups  $u^+ = U/u_\tau$  (dimensionless velocity) and  $y^+ = u_\tau y/\nu$  (dimensionless wall distance) for which the velocity profiles of various Reynolds numbers correlate to a high degree (see figure 2.4).

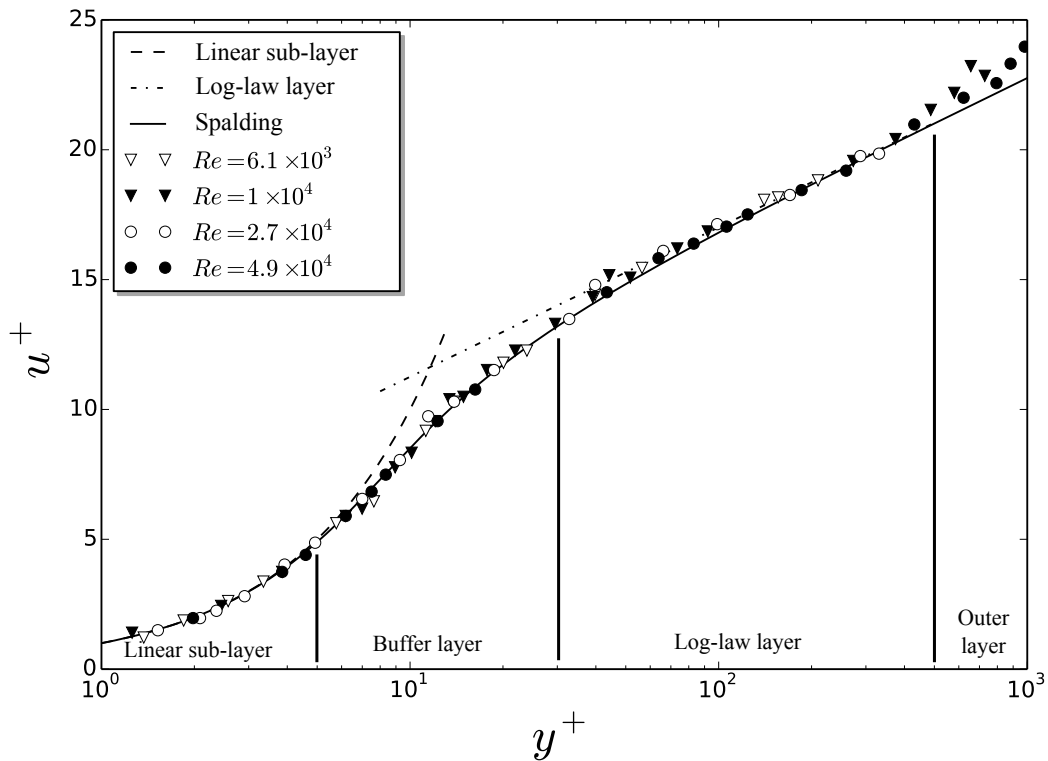


Figure 2.4: Dimensionless near-wall velocity profile (Adapted from White (2006))

This dimensionless profile can be divided into various regions:

- The **linear sub-layer** is the region attached to the wall where turbulence structures are very small and viscous forces dominate. In this region the dimensionless velocity profile is simply defined by  $u^+ = y^+$  and is usually valid for  $y^+ < 5$ .

- The **buffer layer** represents the region where the viscous and inertia are more or less equal ( $Re_y \approx 1$ ). This layer is found for  $5 < y^+ < 30$ . In the buffer layer the velocity profile is neither linear nor logarithmic but rather a transition from the linear to logarithmic layers.
- The **log-law layer** can be defined by  $u^+ = \frac{1}{\kappa} \ln(y^+) + B$  which is usually valid for  $30 < y^+ < 500$ . The log-law layer is also often referred to as the inner layer or overlap region between the viscous sub-layer and the outer layer. In this region viscous and inertia forces are both important.
- The **outer layer** is the region farthest from the wall where the velocity profile deviates from the inner (log-law) layer to various degrees due to, for example, an adverse pressure gradient. The stronger the adverse pressure gradient the greater the deviation from the inner layer. This layer, being far from the wall is independent of viscous stresses, therefore, the inertia forces dominate. This layer can be defined by the so-called law-of-the-wake  $\frac{U_{max} - U}{u_\tau} = -\frac{1}{\kappa} \ln\left(\frac{y}{\delta}\right) + A$ .

Spalding (1961) provided an equation for the dimensionless near-wall velocity profile that includes the linear sub-layer, buffer layer and log-law layer. For this reason it is often referred to as an "universal" velocity profile which is convenient in near-wall numerical modelling (see section 3.9). The equation is as follows:

$$y^+ = u^+ + 1/E \left[ e^{\kappa u^+} - 1 - \kappa u^+ - (\kappa u^+)^2/2 - (\kappa u^+)^3/6 \right] \quad (2.3.1)$$

## 2.4 Aeroelasticity

Engineering structures such as buildings, vehicles or bridges, for example, often experience dynamic structural loading through FSI. This is because engineering structures are usually not streamline but rather bluff-bodies and, therefore, experience related fluid phenomena (Morgenthal, 2000) (see also section 3.1). The SANAE IV base, which initially sparked interest in this field of study, has attributes that motivate special interest in aerodynamics around cylinders,

rectangular cross-sectioned prisms and finite length (and height) bluff-bodies such as surface mounted cubes or cantilever beams.

Flow-induced loading resulting from bluff-body aerodynamics consists of a number of contributing factors shown in figure 2.5. The main contributors in wind loading are mean flow, fluctuations originating upstream of the structure, vortices generated from the shape of the geometry itself and excitation due to the fluid forces arising from structural dynamics.

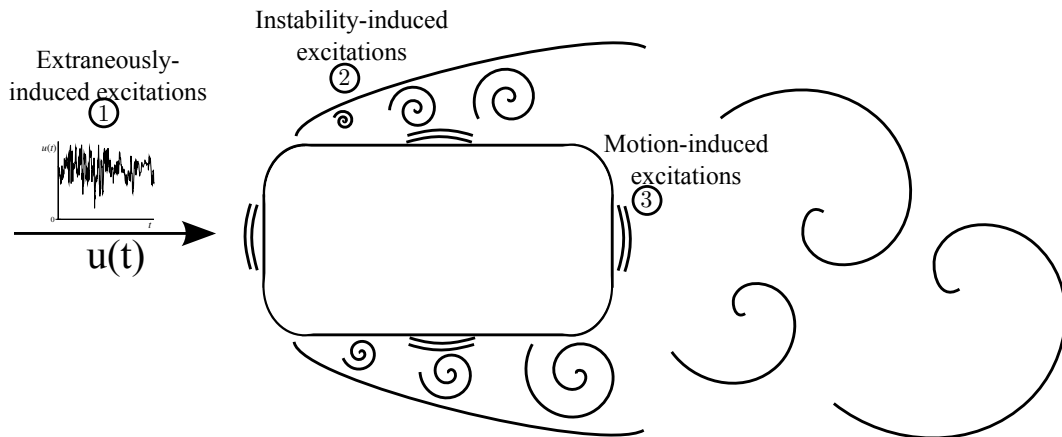


Figure 2.5: Contributing components of flow-induced structural loading

Naudascher and Rockwell (2005) categorised flow-induced excitations into the following:

- Extraneously-induced excitation (originating upstream)
- Instability-induced excitation (originating from the shape of the structure)
- Movement-induced excitation (originating from the movement of the structure)

**Extraneously-induced excitation** refers to the oncoming flow and the superimposed velocity fluctuations. This category includes flow phenomena such as gusts or even eddy structures resulting from upstream obstacles. Wind loading of this nature is usually referred to as buffeting. Generally structures, that are not in the wake of a vortex shedding structure upstream of it, will experience periodic pulsations that are random. Although these excitations

can sometimes cause significant structural movement they usually result in temporary oscillations decaying due to structural damping.

**Instability-induced excitations** are caused by bluff-bodies in viscous moving fluid. Vortex shedding usually cause relatively small structural vibrations but can have a significant impact when this loading frequency reaches the structure's natural frequency in which case resonance will occur. Some examples of structures where vortex-induced vibrations have caused problems are cylinder shaped structures such as chimneys, pipes, towers, risers and antennas (Morgenthal, 2000). The vortex shedding frequency is determined by the viscosity, velocity and density of the fluid as well as the shape of the structure in the fluid stream.

Lastly, **movement-induced excitation** refers to cases where significant structural displacement takes place as in the case of galloping of stay cables of bridges. Another example of wind induced structural excitations with large displacements is flutter of airfoils. Flutter, unlike vortex induced vibrations and galloping, does not require flow separation to result in structural excitation. Instead the aerodynamic forces feed the structure oscillations with more and more energy as the flow velocity is increased (Morgenthal, 2000).

Countering of aerodynamic excitation of structures has been widely investigated but usually involves increasing the stiffness and damping (active or passive) or altering the vortex shedding aerodynamics of the structure.

For the SANAE IV base very small structural displacements were observed. This means that the effects of movement-induced excitations, usually associated with large displacements such as galloping and flutter, are considered negligible. Instead, instability-induced excitations (vortex-induced vibrations), are suspected to be the major contributor apart from the occasional buffeting. Therefore, the next section looks at vortex-induced vibrations in more detail.

## 2.5 Vortex-induced Vibrations

From the descriptions of flows around cylindrical and rectangular cross-sectioned prisms it is clear that flow around bluff-bodies results in complex flow patterns that usually involves separation and vortex shedding. Additionally, these flows are accompanied by flow-induced, time-dependent pressure forces that mostly act on the afterbody of the structure. Since the pressure oscillations are di-

rectly related to the vortex shedding phenomena a suspended bluff-body will experience forces perpendicular at the same rate and forces parallel to the flow at twice the vortex shedding frequency (Morgenthal, 2000).

In cases where the vortex-induced vibrations occur close to the structure's natural frequency large oscillation amplitudes can result. In most cases these oscillations will be limited by structural damping and will, therefore, usually not pose a immediate threat. It can, however, cause fatigue failure, reduce human comfort and deteriorate operating performance for high accuracy devices such as heliostats for example making it an important design consideration.

Usually the vortex shedding frequency will increase with an increase of the flow velocity. Once the vortex shedding frequency reaches the structure's natural frequency resonance occurs and vortex shedding is dominated by the structural oscillations. Even with further increases in flow velocity the vortex shedding frequency remains at the resonance frequency. This phenomena is called lock-in and is shown in figure 2.6.

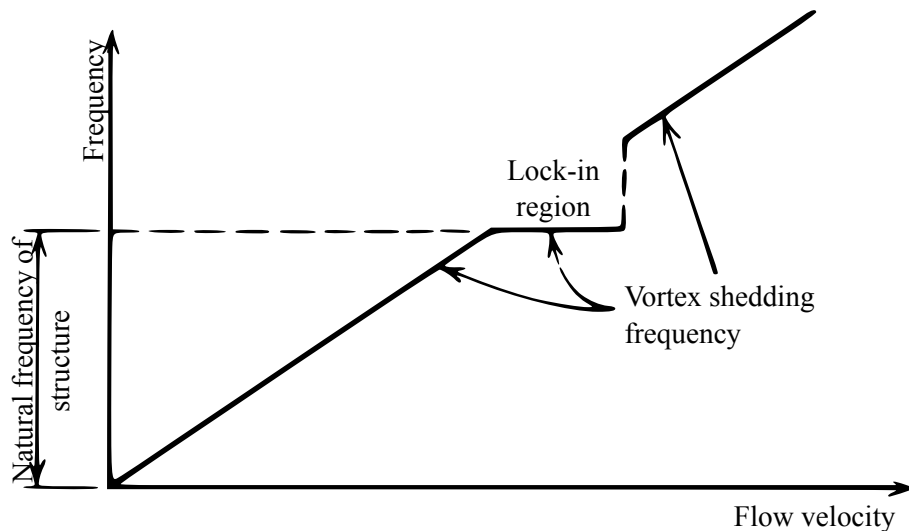


Figure 2.6: Lock-in phenomena (Simiu and Scanlan, 1996)

# Chapter 3

## Numerical Methods

With increases in computational resources in recent years, numerical methods such as computational fluid dynamics (CFD) and finite element methods (FEM) for structural analysis have gained popularity. Numerical methods divides a region of interest into a large number of small but manageable parts and makes use of vast amounts of computational resources to do iterative calculations in an attempt to predict physical phenomena. Alternatively, analytical methods are either too complex to solve or too simplified to capture the physical behaviour of the multi-physics problems that are involved in fluid structure interaction (FSI). Furthermore, wind tunnel measurements suffer from scaling limitations, are expensive and also time consuming for parameter studies but even so continues to play an important role in the validation of new methodologies.

Now that the fundamental mechanics of viscous fluid flow and vortex-induced structural loading phenomena have been considered it is of interest to look at the various methods available for accurately predicting and analysing these phenomena. This chapter focusses on the numerical methods needed to simulate FSI. This chapter starts with previous accomplishments with simulating bluff-body flows then moves on to discuss topics such as software, turbulence models and interpolation schemes.

### 3.1 Simulating Bluff-body Aerodynamics

Numerical modelling and measurements of bluff-body aerodynamics has found significant interest in engineering sciences. This is due to the shape of engi-

neering structures, the vast number of bluff-body structures and the effects of aerodynamic forces on these structures. Examples are houses, bridges, buildings to name only a few. Flow around bluff bodies are very complicated and especially challenging since they are highly three-dimensional and usually associated with a wide range of flow regimes such as stagnation, separation, rapid acceleration, recirculation, strong shear layers, high streamline curvature, reattachment and unsteady vortex shedding.

A number of studies have investigated two and three-dimensional flows around infinite prisms with circular, square and rectangular cross-sections (Williamson, 1996; Zdravkovich, 1997; Matsumoto, 1999; Wissink and Rodi, 2008; Lübcke *et al.*, 2001; Wang *et al.*, 2001; Lee, 1997; Bruno *et al.*, 2010; Mannini *et al.*, 2010*a*) to better understand the related fluid dynamics and accuracy of various numerical modelling strategies. Although these studies shed light on the underlying causes of the flow phenomena as well as the strengths and limitations of available numerical models when applied to infinite geometries, finite height geometries (including wall mounted cubes), on the other hand, cannot be treated in the same way. Finite height geometries introduce additional three-dimensional flow phenomena due to the effects of the wall mounting and free tip which interact with the wake dynamics typically understood to originate from the cross-section shape of infinite prisms (Lim *et al.*, 2009; Yakhov *et al.*, 2006; Iaccarino *et al.*, 2003; Rodi, 1997; Wang and Zhou, 2009; Wang *et al.*, 2009; Becker *et al.*, 2008; Uffinger *et al.*, 2008; Kawai *et al.*, 2009; Uffinger *et al.*, 2010, 2013). One example is the study by Kawai *et al.* (2009), who conducted detailed PIV measurements of flow around a finite height building structure and elaborated on the complexity of the unsteady three-dimensional interaction of the side-wall vortex shedding and the arc vortex originating from the top of the column.

Wang (2004) presented a conceptual schematic of the basic flow features that have been identified for finite height columns with square cross-sections (see figure 3.1). This highlights the three-dimensional effects that are involved and, although it is not the same geometry as the beam in this study, it does provide a overview of the general flow features to be expected and discussed. The flow features around the geometry include the horseshoe vortex upstream of the column, the base vortex, side-wall vertical vortices and tip vortices.

The horseshoe vortex upstream of the flow seems to have little effect on



the rest of the flow (Sau *et al.*, 2003; Bourgeois *et al.*, 2011). The base vortex originates from the upstream tip of the column side edge at the base and is characterised by an upward flow at the column side-wall. At mid-height, with little influence from the base and tip, vortices originate from the side-wall upstream edges. These side-wall vortices are closely related to the observed flow phenomena of infinite columns. The existence of tip vortices were proposed by a number of investigations (Etzold and Fiedler, 1976; Kawamura *et al.*, 1984; Sumner *et al.*, 2004) as well as the existence of an overarching vortex structure connecting the side-wall vortices (Sakamoto and Arie, 1983; Wang and Zhou, 2009). Investigations of the phase shift of vortices over the height of the column further suggests that a bent shape vortex structure (reaching further downstream at the mid-height than at the top and base) exists in the wake region.

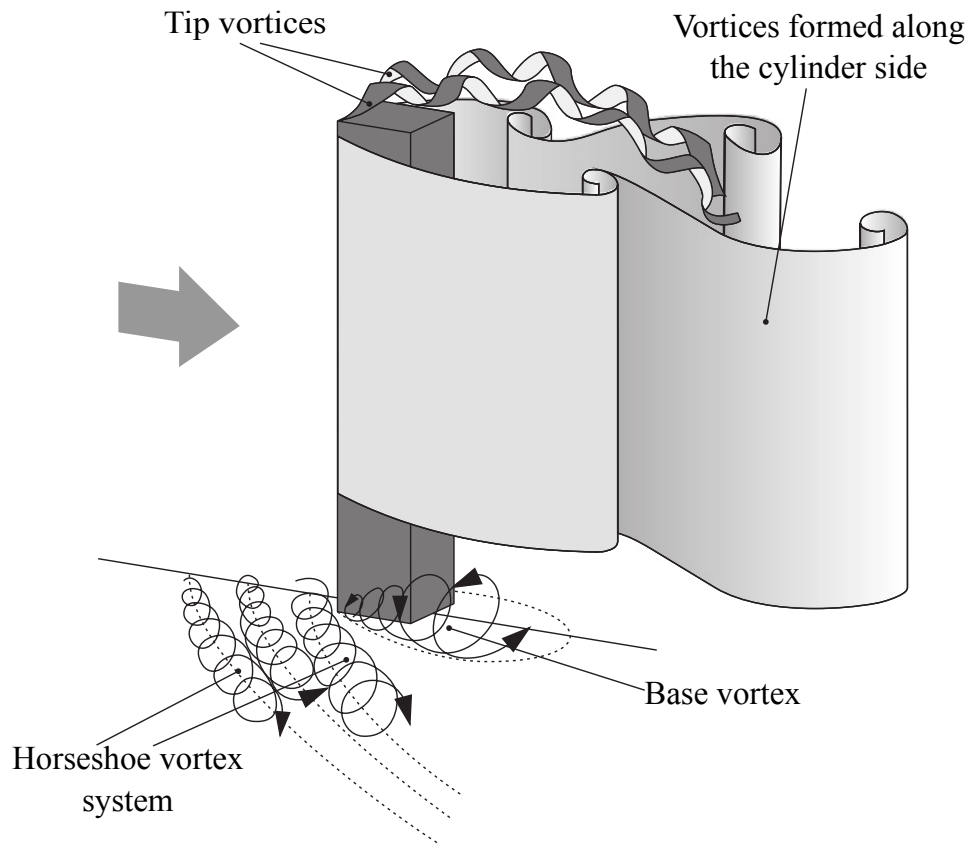


Figure 3.1: Flow patterns characteristic of a finite height, square cross-section geometry (Wang, 2004; Uffinger *et al.*, 2013)

## 3.2 Fluid Structure Interaction Modelling

Numerical methods for solving FSI can be regarded as a newer field compared to CFD and FEM for structural analysis. Although it a very common phenomena, the complexity of FSI required some maturing of the individual fields of numerical methods for analysing fluids and structures as well as advances in computational resources before it could be used successfully.

In recent years, with the above mentioned advances becoming a reality, FSI has drawn a great deal of attention and remains a very active area of research. Two reasons can be indicated here: Firstly modern materials such as composites as well as new structural optimisation techniques lead to new challenges in structural analysis, which also require more accurate loading information. Secondly, the mostly turbulent usually separating boundary layer flows with time-dependent vortex shedding remain challenging to correctly simulate and thus analyse with numerical methods.

FSI occurs when the fluid properties, such as heat and momentum, are transferred to the structure. In the case of isothermal bluff-body aerodynamics fluid dynamics around a geometry induces time-varying structural loading. In general there are two types of FSI modelling. One-way FSI refers to the case where there is negligible feedback from the structure to the flow and it is, therefore, possible to solve the two domains separately. For two-way FSI, on the other hand, the structural displacements are significant enough to influence the fluid dynamics and, therefore, the fluid and structural dynamics have to be solved iteratively through continuous feedback.

Small structural vibrations, such as were observed in the SANAE IV base, are not significant enough to influence the overall aerodynamics and the FSI is, therefore, considered one-way only. That does not, however, mean these small structural vibrations are negligible since small excitations in one part of a structure can often result in significant structural movement in another part of the structure away from the source of excitation. It can also have a significant impact on sensitive equipment as well as human comfort. Additionally, the mean flow structural loading can cause significant stresses in a structure even with small displacements. This one-way coupling is the focus of this study.

The complex multi-physics involved in FSI means that the solvers and case studies are usually simplified in some way or other. For studies with an

advanced two-way coupling scheme geometries are usually straight forward, with only two-dimensional meshes and simplified turbulence modelling if any. These simplifications are put into place because of the challenges associated with structural motion and fluid dynamics in the vicinity of moving boundaries which results in problems for solution stability, mesh motion and transient simulation turnover time. But these simplifications also mean that is not possible to look at complex structures and aerodynamics. On the other hand, more complex geometries and three-dimensional FSI simulations are possible when simpler, one-way FSI is present, such as in the case of the SANA E IV base.

Numerical methods for solving FSI can be divided into two categories:

- Monolithic - A single solver is used to simultaneously resolve the governing equations of the fluid and structure physics.
- Partitioned - Two separate solvers are used to resolve the governing equations of the fluid and structure physics independently.

The monolithic method has the advantage of not needing any coupling method or interpolation scheme which can increase computational time and resources. On the other hand, this method has the disadvantage that it is not possible to apply an ideally suited solver to each of the physic domains. Very few software exist that use the monolithic method and these are usually very limited in their application which means that solvers will often have to be written for a specific case study. The partitioned method, on the other hand, can use more efficient independent solvers for fluid and structure physics equations but a coupling method will then be required.

### 3.3 Discretisation Methods

As was mentioned previously, numerical methods divide the domain of interest into smaller parts forming a mesh. Consequently, the governing equations need to be discretised accordingly. The three main methods of interest for discretisation are the finite difference method (FDM), finite volume method (FVM) and FEM.

### 3.3.1 Finite difference method

The FDM, is based on the differential form of the partial differential equations (PDE) that describe the governing equations. This means that all the derivatives in the PDE's are substituted by difference formulations usually obtained from a local Taylor series expansion. The discretisation is based on structured grids where variables are stored at the nodal points. This method, therefore, is not appropriate for complex geometries where structured grids are impossible or not practical. Furthermore, accuracy limitations occur by neglecting the higher order terms of the Taylor series expansion.

### 3.3.2 Finite volume method

The FVM is based on representing the governing conservation equations, e.g. the Navier-Stokes or Euler equations expressing conservation of momentum, in integral form. The integrals are usually solved over finite volumes with variables stored at the centre of these volumes. Each volume is surrounded by boundary faces that are either shared with neighbouring cells or with the domain boundary. Domain boundary conditions, therefore, have to be defined and the values between neighbouring volumes can be determined through interpolation schemes. The FVM is, firstly, convenient to apply to three-dimensional applications due to the volume integrals, secondly, it allows for strict conservation of the governing equations by monitoring what crosses the boundaries of each volume and, thirdly, provides a framework for unstructured meshes and, therefore, simulation of complex geometries. This method also provides a discrete solution and is preferred for fluid dynamics due its strict conservation of quantities such as mass, momentum and energy for example.

### 3.3.3 Finite element method

The FEM originated from numerically solving linear algebra problems related to structural analysis. For this reason all major structural analysis codes continue to employ this method. The domain would usually be divided into different elements for which the approximate solution is represented by an expansion basis of shape functions. Because this method does not allow for strict conservation it is not the preferred method for fluid dynamics, although, some codes do use it for this purpose. Furthermore, the FEM often makes

use of the weighted residual method and, therefore, is not ideally suited for non-linear problems although many examples of such codes exist.

In summary, the FVM is preferred for fluid dynamics and the FEM for structural analysis. Therefore, employing either of these methods for both fluid and structural analysis will significantly reduce the complexity that can be modelled and force the application of a method to a field for which it was not intended.

### 3.4 Software

In this study one of the objectives was to use open source software instead of the commercial codes such as Fluent and Star-CCM+, both of which were initially developed for fluid dynamics and expanded to include FSI capabilities. Open source software has the benefit of being free and, therefore, essentially provides unlimited licences. This allows for large simulations through parallel computing which would be very expensive with commercial codes. Since this method is intended for larger applications such as building aerodynamics and flow induced loading, large computational capabilities are essential.

Another important benefit of open source software is that the source code is available. Access to the source code helps the user to know exactly how the code functions, therefore, providing a learning platform between experts in the field and new users all over the world. Access to the source code allows for expandability and modification which are necessary for new code development and research on this fundamental level.

At the start of this study in 2010 the author reviewed what software was available and it was found that limited open source FSI software existed at the time that provided the full functionality to simulate the complex fluid dynamics around bluff-bodies and the abilities to accurately model connections in structural assemblies. Even though more and more software became available throughout the course of this project the original view has not changed. Some CFD software codes employing the FVM have introduced simplified structural solvers and, in other cases, structural analysis software constructed using the FEM has made fluid dynamics solvers available too but the capabilities are still very restricted. The restrictions include limited solvers and meshing capabilities. Furthermore, these solvers are usually limited to only simplified

geometries and simple flow conditions.

The nature of the FSI in this project allows for using two separate software codes, each established in its own field, and to develop a link between them to transfer the load information from the fluid to the structural solver. For this purpose OpenFOAM (OpenFOAM, 2015) was chosen for CFD simulations and Code-Aster (Code-Aster, 2011) for structural analysis. OpenFOAM stands for open field operation and manipulation, uses the FVM and is written in C++. On the other hand, Code-Aster uses the FEM and is written in Python and Fortran. In this project Code-Aster was used within the framework of Salome-Meca (Code-Aster, 2011) which is an essential tool for the pre- and post-processing.

Each code contains a wide-variety of models making it possible to apply this method to more complex flow regimes and more detailed structures. However, this also means a coupling method would be required for a partitioned solution. The two codes chosen are open source which means that the source code is accessible. They, therefore, provide a suitable foundation for developing a useful tool for one-way FSI. Since the codes are used separately fluid and structural analysis can be conducted independently if needed, such as for preliminary simulations or validation. Keeping the codes separate also means that the software can be individually updated when needed.

For the interested reader a comprehensive list of open source software can be found online (iMechanica, 2014).

### 3.5 Turbulence Modelling

Turbulence and the accurate modelling thereof is one of the central themes in this dissertation. This is because it is such a common phenomena in engineering applications and because it continues to pose a challenge to accurately model numerically. For these reasons turbulence modelling is discussed in detail in this section. Various models are considered along with their reported performance for bluff-body aerodynamics.

In CFD resolving the Navier-Stokes equations up to the small scales of turbulence, such as in direct numerical simulation (DNS), requires large amounts of computational resources. Even with substantial progress in high performance computing technology DNS continues to be too computationally in-

tensive and, therefore, impractical for highly turbulent and large case studies which is often the case with engineering applications (Lee, 1997).

To reduce computational requirements simplified numerical approximations are introduced to account for the effects of turbulence. However, due to the complexity of the turbulence phenomena and the varying characteristic of the scales of turbulence, models often struggle to reproduce the complex flow around bluff-bodies (Versteeg and Malalasekera, 2007; Kim and Boysan, 1999).

Turbulence models are usually highly flow regime specific and vary significantly in complexity and grid resolution requirements. This raises the question: Which turbulence model, currently available, can be accurately and efficiently applied to reproduce the flow around a bluff-body for the purpose of FSI? The rest of this section briefly discusses different groups of turbulence models with their advantages and disadvantages.

### 3.5.1 RANS turbulence modelling

The incompressible Navier-Stokes equations of motion in conservation form can be expressed as:

$$\frac{\partial u_i}{\partial x_i} = 0 \quad (3.5.1)$$

$$\frac{\partial u_i}{\partial t} + u_j \frac{\partial u_i}{\partial x_j} = f_i - \frac{1}{\rho} \frac{\partial p}{\partial x_i} + \nu \frac{\partial^2 u_i}{\partial x_j \partial x_j} \quad (3.5.2)$$

In this case  $f_i$  represents the fluid body forces such as gravity and centrifugal forces when present. These forces are, however, not present in the simulations conducted in this project.

It is possible to separate the mean and fluctuating components of fluid properties through Reynolds decomposition as shown in equations 3.5.3 for which  $\overline{u'_i} = 0$  and  $\overline{p'} = 0$ . This is also shown in figure 3.2.

$$u_i = \overline{u}_i + u'_i, \quad p = \overline{p} + p' \quad (3.5.3)$$

This is convenient since velocity fluctuations can be quantified through

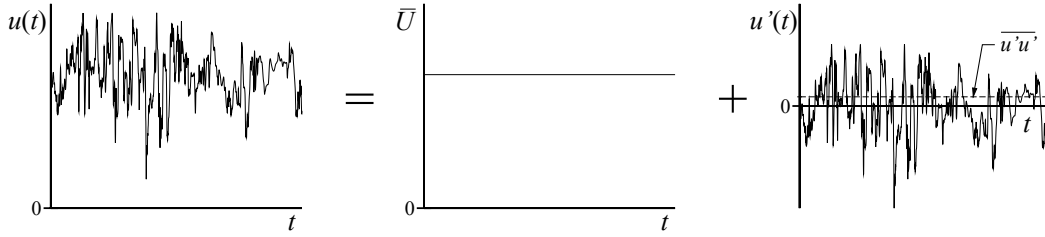


Figure 3.2: Graphical representation of Reynolds decomposition for the velocity signal (Mockett, 2009)

measurements such as with holt-wire or hot-film probes. TKE, or  $k$ , is introduced in this process defined as the sum of the average magnitude of the velocity fluctuations as in equation 3.5.4. Furthermore, turbulence intensity,  $T_i$ , is defined as the average root mean square (RMS) velocity divided by the mean velocity and is related to TKE as expressed in equation 3.5.5.

$$k = \frac{1}{2} \overline{u'_i u'_i} \quad \text{or} \quad k = \frac{1}{2} (\overline{u'^2} + \overline{v'^2} + \overline{w'^2}) \quad (3.5.4)$$

$$T_i = \frac{(\frac{2}{3}k)^{1/2}}{U_{ref}} \quad (3.5.5)$$

Applying Reynolds decomposition (shown in figure 3.2 and equations 3.5.3) to the incompressible Navier-Stokes equations (represented by equations 3.5.1 and 3.5.2) and completing time-averaging produces the so called Reynolds-averaged Navier-Stokes (RANS) equations as

$$\frac{\partial \bar{u}_i}{\partial x_i} = 0 \quad (3.5.6)$$

$$\frac{\partial \bar{u}_i}{\partial t} + \bar{u}_j \frac{\partial \bar{u}_i}{\partial x_j} = \bar{f}_i - \frac{1}{\rho} \frac{\partial \bar{p}}{\partial x_i} + \nu \frac{\partial^2 \bar{u}_i}{\partial x_j \partial x_j} - \frac{\partial \overline{u'_i u'_j}}{\partial x_j} \quad (3.5.7)$$

With further manipulation equation 3.5.7 becomes

$$\rho \frac{\partial \bar{u}_i}{\partial t} + \rho \bar{u}_j \frac{\partial \bar{u}_i}{\partial x_j} = \rho \bar{f}_i + \frac{\partial}{\partial x_j} [-\bar{p} \delta_{ij} + 2\mu \bar{S}_{ij} - \rho \overline{u'_i u'_j}] \quad (3.5.8)$$

In equation 3.5.8  $\delta_{ij}$  is the Kronecker delta ( $\delta_{ij} = 1$  if  $i = j$  and  $\delta_{ij} = 0$  if



$i \neq j$ ) and the strain-rate tensor,  $\overline{S}_{ij}$ , is

$$\overline{S}_{ij} = \frac{1}{2} \left( \frac{\partial \overline{u}_i}{\partial x_j} + \frac{\partial \overline{u}_j}{\partial x_i} \right) \quad (3.5.9)$$

The last term in equation 3.5.8 is referred to as the shear stress tensor (see equation 3.5.10). To achieve closure RANS turbulence models predict the effects of these Reynolds stresses,  $\tau_{ij}$ , through various statistical approximations.

$$\tau_{ij} = -\overline{\rho u'_i u'_j} \quad (3.5.10)$$

The Boussinesq approximations was one of the first methods of modelling the Reynolds stresses by introducing the concept of the eddy, or turbulence, viscosity,  $\nu_t$ . The Boussinesq approximation is presented in equation 3.5.11. RANS models that use the Boussinesq assumption are often referred to as eddy-viscosity models since the Reynolds stresses are expressed by algebraic equations based on an eddy-viscosity. One such an example is given in equation 3.5.12 for the well known  $k$ - $\epsilon$  model.

$$-\overline{u'_i u'_j} = 2\nu_t \overline{S}_{ij} - \frac{2}{3} k \delta_{ij} \quad (3.5.11)$$

$$\nu_t = C_\mu \frac{k^2}{\epsilon} \quad (3.5.12)$$

The original  $k$ - $\epsilon$  model, proposed by Launder and Spalding (1974), was one of the first turbulence models to be introduced and has been widely used for its simplicity and robustness (Kim and Boysan, 1999; Paterson and Apelt, 1990). For this model two new constitutive relations were introduced. One for the TKE,  $k$ , and one for its dissipation rate,  $\epsilon$ , as shown in equations 3.5.13 and 3.5.14. The calibration coefficients can be found in the original paper by Launder and Spalding (1974).

$$\frac{\partial k}{\partial t} + \overline{u}_j \frac{\partial k}{\partial x_j} = \frac{\partial}{\partial x_j} \left[ \left( \nu + \frac{\nu_t}{\sigma_k} \right) \frac{\partial k}{\partial x_j} \right] - \overline{u'_i u'_j} \frac{\partial \overline{u}_i}{\partial x_j} - \epsilon \quad (3.5.13)$$

$$\frac{\partial \epsilon}{\partial t} + \bar{u}_j \frac{\partial \epsilon}{\partial x_j} = \frac{\partial}{\partial x_j} \left[ \left( \nu + \frac{\nu_t}{\sigma_\epsilon} \right) \frac{\partial \epsilon}{\partial x_j} \right] - C_1 \frac{\epsilon}{k} \overline{u'_i u'_j} \frac{\partial \bar{u}_i}{\partial x_j} - C_2 \frac{\epsilon^2}{k} \quad (3.5.14)$$

In turbulence modelling the length scale,  $l$ , is a physical quantity describing the size of the largest energy-containing eddies in turbulent flow. This length scale provides a convenient way of defining the inlet turbulence by making it equal to the characteristic length of the channel or the largest obstacle upstream of the simulated domain. For wind tunnel simulations, for example, the length scale can be defined by the turbulence grid wire dimensions if present or the tunnel hydraulic diameter. In more sophisticated turbulence models the transport equations can be rearranged to reveal the length scale in different terms as well as for  $\nu_t$ . In the case of the  $k$ - $\epsilon$  model, the length scale can be shown to be  $l = C_\mu k^{2/3} / \epsilon$ .

The underlying Boussinesq eddy-viscosity hypothesis, which treats all scales of turbulence as isotropic, however, limits the accuracy of this model to account for the interaction effects of Reynolds stresses and mean velocity field (Mannini *et al.*, 2010a) especially flows associated with strong streamline curvature as is the case with bluff bodies (Lübcke *et al.*, 2001).

Typical limitations of the original  $k$ - $\epsilon$  model are related to the overproduction of TKE and consequently too large turbulence viscosity in stagnation regions which often leads to reduction or even complete suppression of flow separation and unsteady vortex shedding downstream of the stagnation region (Kim and Boysan, 1999; Li *et al.*, 1998; Rodi, 1997; Lee, 1997; Mannini *et al.*, 2010a). It has also been found that, although the overproduction of TKE often results in smaller or even totally suppressed separation on the side walls of rectangular prisms, it can also lead to an over-predicted downstream recirculation length (Huang *et al.*, 2007).

Since then, a number of alternative RANS eddy-viscosity models have been proposed to address some of the limitations of the original  $k$ - $\epsilon$  model. Some examples are the LK model proposed by Launder and Kato (1993), the MMK model by Murakami *et al.* (1998), the realizable  $k$ - $\epsilon$  variation proposed by Shih *et al.* (1995a) and the renormalized group (RNG) model by Yakhot *et al.* (1992).

Validation of these turbulence models are extensive. Rodi (1997), for example, compared various turbulence models for flows around bluff bodies in-

cluding a square prism and a surface mounted cube and found that the Kato and Launder (1993) modification improved the results. Similarly Huang *et al.* (2007) compared results for various turbulence models for flow around a tall building and reported that the MMK model performed the best of the RANS models tested. In other studies, Lee (1997) as well as Kim and Boysan (1999) reported that the RNG model produces better results than the original  $k$ - $\epsilon$  model.

However, models built on the Boussinesq approximation are still limited by the isotropic treatment of all scales of turbulence which, as discussed in section 2.2, are too simplistic and consequently introduces errors. Additionally, considering equations 3.5.10 and 3.5.11 it can be seen that the Reynolds stresses,  $\tau_{ij}(\bar{S}_{ij}, k, \epsilon, \rho)$ , adjust themselves based on local fluid properties such as the mean strain,  $\bar{S}_{ij}$ , and so does not account for the transport effects of the Reynolds stresses (Versteeg and Malalasekera, 2007).

More sophisticated models were, therefore, introduced that make use of higher order algebraic equations to account for anisotropic behaviour of turbulence. The models in this group are, subsequently, referred to as anisotropic, non-linear or algebraic eddy-viscosity models. Examples of algebraic models are the ones by Gatski and Speziale (1993) and Shih *et al.* (1995*b*). These models have received noteworthy interest since the efficiency of the eddy-viscosity hypothesis is retained while at the same time anisotropic flow behaviour is introduced resulting in these models significantly outperforming the isotropic eddy-viscosity models (Lübcke *et al.*, 2001; Ratnam and Vengadesan, 2008; Ramesh *et al.*, 2006; Mannini *et al.*, 2010*a*).

Apart from the RANS eddy-viscosity models, Reynolds stress models (RSM) were also developed to solve the transport equations for the Reynolds stresses (equation 3.5.9) and in so doing account for the history and transport effects of the Reynolds stresses. The RSM models have been reported to perform better than the eddy-viscosity based models due to the more realistic representation of the Reynolds stresses (Lee, 1997; Rodi, 1997; Kim and Boysan, 1999). In the work by Lee (1997) on turbulent flow around a square prism RSM models were reported to give better results than eddy-viscosity based RANS models but at the same time require a significant increase in computational resources due to the seven extra partial differential equations (PDE's) that have to be solved along with the regular transport equations. This decreases the popular-

ity of RSM models for large scale engineering studies. A complexity hierarchy of the various RANS models is presented in figure 3.3.

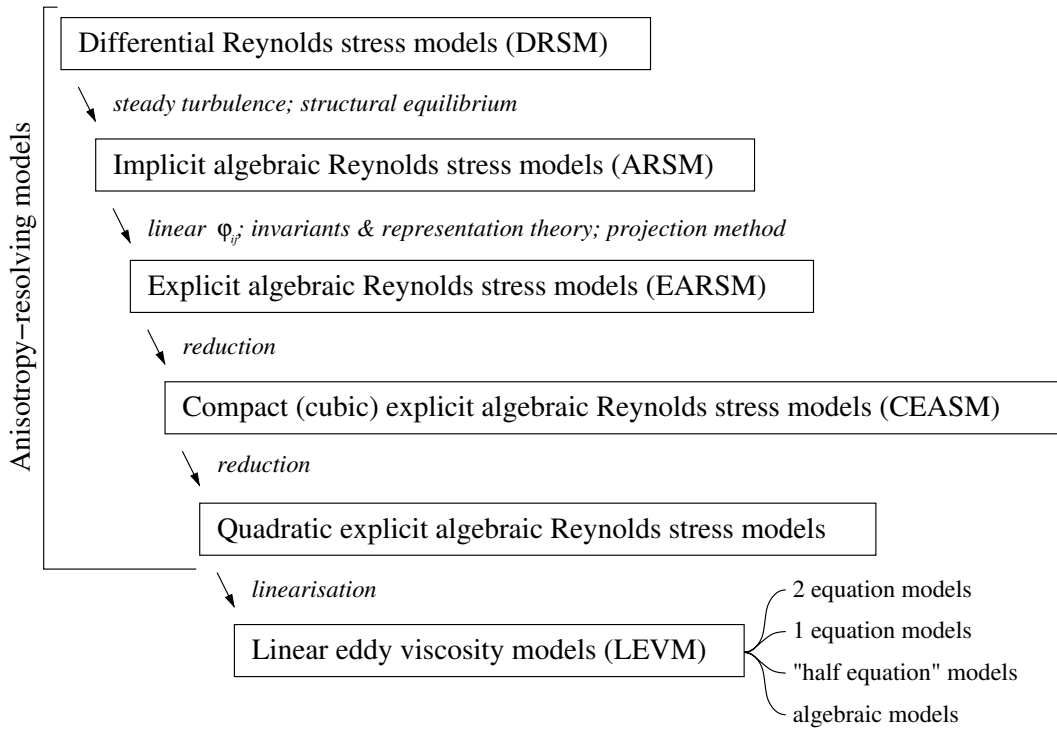


Figure 3.3: Hierarchy of complexity for various types of RANS turbulence models (Mockett, 2009; Rung, 2000)

The near-wall treatment of RANS models can be generally divided into high-Re and low-Re methods. High-Re near-wall treatment has no built-in functionality to account for the near-wall damping effects in the turbulence model but instead uses the wall-functions as boundary conditions and larger grid spacing to correctly calculate the wall shear stress.  $y^+$  values for high-Re wall treatment, therefore, have to be between 30 and 500 to place the first grid cell within the log-law region where wall damping effects are negligible. Low-Re models, on the other hand, usually have built-in damping functions to account for the near-wall effects and, therefore, do not need wall-functions to determine the wall shear stress if sufficiently small wall normal grid refinement is used. In this case the  $y^+$  values have to be smaller than 5 with the aim to place the first few cells within the linear sub-layer.

Successful near-wall treatment using RANS models can be a tedious process. High-Re and low-Re methods have very different requirements and are

very grid specific. Violation of these requirements will result in incorrect boundary condition and often significant errors in the solution. Additionally, since the wall treatment is dependent on the flow solution, prior knowledge of the flow is needed to set-up the simulation correctly which often results in an iterative process. Furthermore, the computational efficiency of the high-Re wall treatment is more desirable than the computationally expensive low-Re wall treatment but since the wall-functions were developed for attached boundary layers, their applicability to highly separated flows is questionable.

The inlet conditions for RANS models are more straight forward since the TKE can usually be measured. Furthermore, relations exist which relate TKE to the dissipative variable specific to each turbulence model, such as  $\epsilon$  and  $\omega$ .

### 3.5.2 LES turbulence modelling

The vastly different characteristics between the various scales of turbulence eddies as well as the restriction of computational resources which continues to prevent numerically resolving all scales of turbulence motivated the development of large eddy simulation (LES). LES rests on the basis of resolving the large, energy carrying, anisotropic eddies and modelling the small isotropic, energy dissipating eddies in a RANS like closure method. To do this it is assumed that a flow variable,  $\phi$ , is the sum of a small,  $\phi'$ , and large scale,  $\bar{\phi}$ , contribution. A spacial filtering kernel,  $G(x, x'; \Delta)$ , is applied to separate the large and smaller scales as in equation 3.5.15 which is depicted in figure 3.4 for the velocity signal.

$$\bar{\phi}(x) = \oint G(x, x'; \Delta) \phi(x') dx' \quad (3.5.15)$$

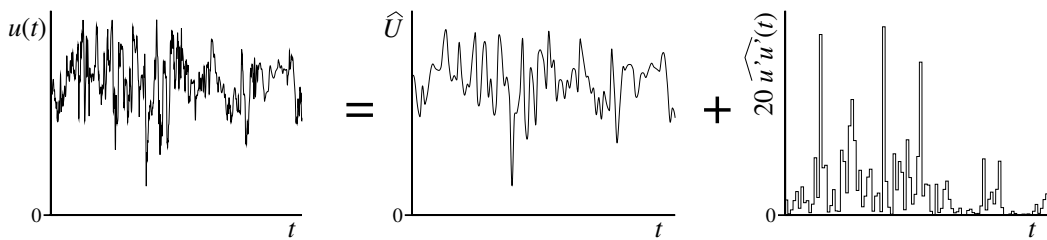


Figure 3.4: LES filtering of the velocity signal (Mockett, 2009)

where  $\Delta$  is the filter width used to distinguish between the wavelength of eddies that will be resolved or modelled. Generally the filter width is taken as the cube root of the grid cell volume,  $\Delta = \sqrt[3]{\Delta_x \Delta_y \Delta_z}$ , which provides a good overall indication of the length scale but the maximum cell width,  $\Delta = \max[\Delta_x, \Delta_y, \Delta_z]$ , can also be used and would be more appropriate in cases where high aspect ratios are present such as near walls. Various filter functions are possible of which the most common are the Gaussian, box (or top-hat) and Fourier cut-off filters. Small eddies are, therefore, referred to as the sub-grid scale (SGS) contributions and large eddies are referred to as the grid scale contributions.

Applying this filtering to the incompressible Navier-Stokes equations (without body forces) we get the following:

$$\frac{\partial \bar{u}_i}{\partial x_i} = 0 \quad (3.5.16)$$

$$\frac{\partial \bar{u}_i}{\partial t} + \frac{\partial}{\partial x_j} (\bar{u}_i \bar{u}_j) = -\frac{1}{\rho} \frac{\partial \bar{p}}{\partial x_i} + 2\nu \frac{\partial}{\partial x_j} \bar{S}_{ij} \quad (3.5.17)$$

In this case  $\bar{u}_i \bar{u}_j$  is the filtered advection term where the LES turbulence modelling is introduced,  $\bar{p}$  is the filtered pressure and  $\bar{S}_{ij}$  is the strain rate tensor. The filtered advective term can be split up as follows:

$$\rho \bar{u}_i \bar{u}_j = \tau_{ij} + \rho \bar{u}_i \bar{u}_j \quad \text{or} \quad \tau_{ij} = \rho \bar{u}_i \bar{u}_j - \rho \bar{u}_i \bar{u}_j \quad (3.5.18)$$

where  $\tau_{ij}$  in this case represents the SGS stress with the characteristics that  $|\tau_{ij}|$  becomes zero as the filter width,  $\Delta$ , (or grid spacing in most cases) tends towards zero. Applying equation 3.5.18 to the filtered Navier-Stokes equations produces

$$\frac{\partial \bar{u}_i}{\partial t} + \frac{\partial}{\partial x_j} (\bar{u}_i \bar{u}_j) = -\frac{1}{\rho} \frac{\partial \bar{p}}{\partial x_i} + 2\nu \frac{\partial}{\partial x_j} \bar{S}_{ij} - \frac{1}{\rho} \frac{\partial \tau_{ij}}{\partial x_j} \quad (3.5.19)$$

Performing Reynolds decomposition, as with the RANS equations, the SGS stress can also be shown to consist of three terms as follows:

$$\tau_{ij} = L_{ij} + C_{ij} + R_{ij} \quad (3.5.20)$$

Table 3.1: SGS stress terms

Term	Name	Description
$L_{ij} = \rho \overline{\overline{u_i u_j}} - \rho \overline{u_i} \overline{u_j}$	Leonard stress tensor	Interaction between the large, resolved scales
$C_{ij} = \rho \overline{\overline{u_i u'_j}} + \rho \overline{u'_i \overline{u_j}}$	Clark stress tensor	Interactions between the resolved and modelled scales
$R_{ij} = \rho \overline{u'_i u'_j}$	LES Reynolds stress tensor	Interactions among the sub-grid, modelled scales

As with the RANS models, the SGS stresses,  $\tau_{ij}$ , must be modelled. The SGS model has the primary function to dissipate all energy passed down from the larger scales. One example of such a SGS model is the Smagorinsky-Lilly model which uses the Boussinesq hypothesis to model the stresses. The SGS kinematic viscosity,  $\nu_{SGS}$ , is similar to the turbulence viscosity,  $\nu_t$ , in RANS models but just much smaller since with LES it does not include the energy of the larger scales.  $\nu_{SGS}$  is introduced as follows:

$$\tau_{ij} = -2\rho\nu_{SGS}\overline{S_{ij}} + \frac{1}{3}\tau_{ii}\delta_{ij} \quad (3.5.21)$$

$$\frac{\partial \overline{u_i}}{\partial t} + \frac{\partial}{\partial x_j}(\overline{u_i u_j}) = -\frac{1}{\rho} \frac{\partial \overline{p}}{\partial x_i} + 2 \frac{\partial}{\partial x_j} [(\nu + \nu_{SGS})\overline{S_{ij}}] \quad (3.5.22)$$

Through numerous comparative investigations it has been found that LES turbulence modelling produces more accurate simulation results when compared to the RANS counterpart (Murakami *et al.*, 1992; Lübcke *et al.*, 2001; Rodi, 1997; Huang *et al.*, 2007). However, although LES is significantly less computational intensive compared to DNS, computational requirements are still the main drawback of these models, making LES often too expensive for large scale studies of highly turbulent flows (Rodi, 1997; Huang *et al.*, 2007). LES becomes especially expensive in highly turbulent flows where thin boundary layers occur at walls. For example, for flow around a cylinder Lübcke *et al.*

(2001) reported that LES simulations took 20 times longer to solve compared to RANS models. Furthermore, Rodi (1997) reported that LES simulations took more than 36 times longer than RANS simulations for flow around a square prism and surface mounted cube.

The near-wall treatment of wall-resolved LES generally requires that  $y^+ \leq 1$ . The inlet conditions are more challenging. A summary of options available for defining the inlet conditions for LES are as follows (adapted from Versteeg and Malalasekera (2007)):

- Superimpose random Gaussian perturbations onto the mean velocity profile with the correct turbulence intensity for which auxiliary RANS simulations can be used to calculate the Reynolds stresses, and therefore, more accurate turbulence content.
- Use turbulence-free inlet conditions and extend the inlet domain further upstream to allow the flow turbulence to develop up to the point of interest.
- Specifying fully developed flow at the inlet by using preliminary LES simulation with either long domains or cyclic boundaries. Some new developments make it possible to introduce mapped fields onto the inlet from downstream thereby allowing turbulence content to be introduced during the simulation instead of with auxiliary simulations.
- Specifying profiles with superimposed perturbations of developing boundary layers from auxiliary LES simulations.

### 3.5.3 DES turbulence modelling

RANS models continue to be the workhorse of engineering aerodynamics because of its efficiency, robustness, widely reported performance validation and fairly good results obtained. But the limitations of these models are also widely reported especially for the excessive production of turbulence shear stresses in the presence of adverse pressure gradients and overproduction of TKE at impingement zones. These drawbacks originate from the "local-homogeneity" treatment of turbulence as well as the Reynolds averaging over the entire turbulence spectrum (Haase *et al.*, 2009). LES, on the other hand, has been shown to produce very accurate results for separated flows. But LES is still



too computationally expensive for highly turbulent engineering flow applications. Since these computational expenses usually arise from the high resolution needed in the boundary layers and wakes it means that LES would continue to be unaffordable for the near future (Haase *et al.*, 2009).

In order to find a middle ground between the efficiency of RANS models and the accuracy of LES, detached eddy simulation (DES) was first introduced by Spalart *et al.* (1997) as a hybrid RANS/LES turbulence model (based on the Spalart-Allmaras RANS model (Spalart and Allmaras, 1992)) and specifically for the purpose of highly separated flows. DES combines the favourable aspects of RANS, which is efficient and accurate at calculating attached boundary layers (thin shear layers), and LES, which is more accurate in highly separated flows.

To see how DES is implemented we consider the Spalart-Allmaras (S-A) RANS model (equations from the original publication of Spalart and Allmaras (1992) but also available online at NASA (2015)). The S-A model, often referred to as an one-equation model, does not calculate the TKE and, therefore, ignores the last term ( $-2/3k\delta_{ij}$ ) in the Boussinesq hypothesis which then becomes

$$-\overline{u'_i u'_j} = 2\nu_t \overline{S}_{ij} \quad (3.5.23)$$

The new transport equation in the S-A model is based on the newly introduced  $\tilde{\nu}$  variable as follows:

$$\begin{aligned} \frac{\partial \tilde{\nu}}{\partial t} + u_j \frac{\partial \tilde{\nu}}{\partial x_j} = & c_{b1}(1 - f_{t2})\tilde{S}\tilde{\nu} - \left[ c_{w1}f_w - \frac{c_{b1}}{\kappa^2}f_{t2} \right] \left( \frac{\tilde{\nu}}{d_w} \right)^2 \\ & + \frac{1}{\sigma} \left[ \frac{\partial}{\partial x_j} \left( (\nu + \tilde{\nu}) \frac{\partial \tilde{\nu}}{\partial x_j} \right) + c_{b2} \frac{\partial \tilde{\nu}}{\partial x_j} \frac{\partial \tilde{\nu}}{\partial x_j} \right] \end{aligned} \quad (3.5.24)$$

where equation 3.5.24,  $d_w$ , is the distance to the nearest wall. The closure relations and coefficient values can be found in the original paper by Spalart and Allmaras (1992).

The boundary conditions for  $\tilde{\nu}$  are

$$\tilde{\nu}_w = 0, \quad 3\nu_\infty \leq \tilde{\nu}_\infty \leq 5\nu_\infty \quad (3.5.25)$$

for which the values of  $\tilde{\nu}$  correspond to  $\nu_t$  values of

$$\nu_{t,w} = 0, \quad 0.210438\nu_\infty \leq \nu_{t,\infty} \leq 1.29423\nu_\infty \quad (3.5.26)$$

DES can be implemented in any RANS model, in a relatively simple way, by modifying the relevant transport equations so that the length scale is revealed and then selecting the appropriate length scale depending on which turbulence model should be active. Travin *et al.* (2002) was the first to propose a DES formulation for a two-equation turbulence model and defined the DES length scale,  $l_{DES}$  as

$$l_{DES} = \min [l_{RANS}, l_{LES}] \quad (3.5.27)$$

where  $l_{LES} = C_{DES}\Delta$  and  $l_{RANS}$  depends on the RANS model used to create the DES model. In this case the filter width  $\Delta = \max [\Delta_x, \Delta_y, \Delta_z]$  and  $C_{DES}$  is a constant with the value calibrated to be 0.65. Here are a few common RANS model length scales:

Table 3.2: RANS length scales

Turbulence model	$l_{RANS}$
Spalart-Allmaras	$d_w$
$k-\epsilon$	$C_\mu k^{2/3}/\epsilon$
$k-\omega$	$k^{1/3}/(C_\mu\omega)$

This means that if the RANS model transport equations are manipulated to reveal the length scale and this is then replaced by equation 3.5.27 it will allow the model to switch between the RANS and LES versions. For the S-A model at near-wall regions  $d_w < C_{DES}\Delta$  which means the RANS model will be implemented. For the far-field  $d_w > C_{DES}\Delta$  and, therefore, the SGS model will be used.

The original DES model was, however, found to be sensitive to grid spacing in the near-wall region where boundary layers are present. Different possibilities for near-wall grid spacing is shown in figure 3.5. The original DES model works well with thin boundary layers and flat cells which relates to large grid spacing parallel to the wall or high aspect ratios ( $\Delta_{||} > \delta$ ). The problem

occurs when the original DES formulation is used in cases where the grid spacing parallel to the wall becomes smaller than the boundary layer thickness ( $\Delta_{\parallel} < \delta$ ). In this case the LES branch of the model will be activated, incorrectly, within the boundary layer. This leads to very small turbulence viscosity and grid-induced separation because the resolved scales in the LES branch do not reproduce the needed Reynolds stresses (Spalart, 2009; Mockett *et al.*, 2012).

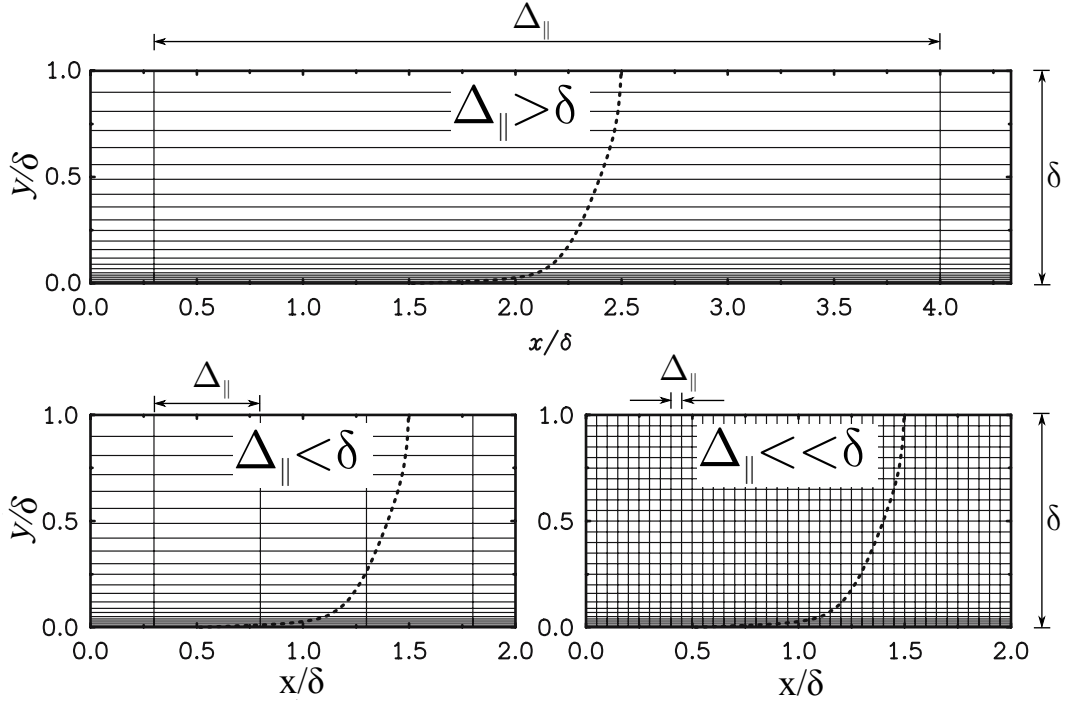


Figure 3.5: Various wall-bounded grid spacing possibilities (adapted from Spalart *et al.* (2006))

A number of remedies were proposed including delayed DES (DDES) where the model was shielded against this occurrence (Spalart *et al.*, 2006). The remedy involves adding functions to detect the boundary layer, similar to the  $F_1$  and  $F_2$  functions of the  $k$ - $\omega$  model, which prevent the switch to LES within it. The functions are

$$r_d = \frac{\nu + \nu_t}{\sqrt{\overline{u_i u_j}} \kappa^2 d_w^2} \quad (3.5.28)$$

$$f_d = 1 - \tanh[(8r_d)^3] \quad (3.5.29)$$

$$l_{DDES} = l_{RANS} - f_d \max[0, l_{RANS} - l_{LES}] \quad (3.5.30)$$

for which the values of the  $f_d$  function are 1 in the LES regions and 0 for the rest. In the case of the S-A model the DDES length scale becomes  $l_{DDES} = d_w - f_d \max[0, d_w - C_{DES}\Delta]$ . The new length scale definition can in this way prevent use of the LES branch if  $r_d$  indicates it is within a boundary layer.

Another group of hybrid RANS-LES models have been proposed with the common feature of offering wall-modelling in LES (WMLES). WMLES employs a much smaller RANS layer with the objective to resolve the larger outer boundary layer with LES (Mockett *et al.*, 2012). WMLES reduces the computational requirements of LES and so makes it an useful extension for DES. Early combinations of the two methodologies showed successful results for channel flows but also produced a log-layer mismatch (LLM) which resulted in reduced skin-friction (Nikitin *et al.*, 2000). Shur *et al.* (2008) then developed the "improved" DDES (IDDES) model which successfully includes the WMLES branch and addresses the LLM issues.

To include the WMLES branch a new sub-grid length scale,  $\Delta$ , was proposed to not only rely on the grid spacing ( $\Delta_x, \Delta_y, \Delta_z$ ) but also on the wall distance,  $d_w$ .

$$l_{LES} = \Delta = \min\{\max[C_w d_w, C_w \Delta_{max}, \Delta_{wn}], \Delta_{max}\} \quad (3.5.31)$$

where  $C_w$  is a constant equal to 0.15,  $\Delta_{max} = \max[\Delta_x, \Delta_y, \Delta_z]$  and  $\Delta_{wn}$  is the wall-normal grid resolution. Function 3.5.31 means that the sub-grid length scale,  $\Delta$ , will be  $\Delta_{max}$  far from the wall,  $C_w \Delta_{max}$  close to the wall and a linear blend in between. The WMLES length scale is a blend of the RANS and LES length scales as

$$l_{WMLES} = f_B(1 + f_e)l_{RANS} + (1 - f_B)l_{LES} \quad (3.5.32)$$

This new length scale contains two new empirical functions  $f_B$  and  $f_e$ . The blending function,  $f_B$ , as defined in equation 3.5.33, causes the switch between RANS and LES according to table 3.3.

$$f_B = \min \left[ 2e^{-9\alpha^2}, 1 \right], \quad \alpha = 0.25 - \frac{d_w}{\Delta_{max}} \quad (3.5.33)$$

Table 3.3: IDDES blending function,  $f_B$ , modes of operation

$d_w/\Delta_{max}$	$f_B$	Mode
0 $\rightarrow$ 0.53	1	RANS
0.53 $\rightarrow$ 1	1 $\rightarrow$ 0	Blend
1 $\rightarrow$ $\infty$	0	LES

The elevating function,  $f_e$ , prevents log-layer mismatch and is defined as

$$f_e = \max[(f_{e1} - 1), 0] \Psi f_{e2}, \quad (3.5.34)$$

With these new blending functions it is possible to define the IDDES length scale as

$$l_{IDDES} = \tilde{f}_d(1 + f_e)l_{RANS} + (1 - \tilde{f}_d)l_{LES} \quad (3.5.35)$$

where

$$\tilde{f}_d = \max[(1 - f_{dt}), f_B], \quad f_{dt} = 1 - \tanh[(8r_{dt})^3] \quad (3.5.36)$$

The interested reader may refer to the original paper for closing relations and constants of the IDDES model in the paper by Shur *et al.* (2008).

DES models have been shown to provide superior results compared to RANS models and often similar accuracy as LES models but with significantly less computational expenses. For example, extensive reviews can be found in the DESider project (Haase *et al.*, 2009) as well as studies by Mockett (2009), Mockett *et al.* (2012) and Strelets (2001).

Although DES is more commonly used in combination with low-Reynolds number wall treatment (see section 2.3 and 3.9) studies such as the DESider project have shown that DES using classic wall-functions work surprisingly well (Haase *et al.*, 2009). The classic wall functions were, however, developed for

attached flows and, therefore, significant errors can be expected when applied to separated flows (Mockett, 2009). Even so, Mockett *et al.* (2012) investigated the use of IDDES with an “all- $y^+$ ” wall treatment for attached and separated flows and concluded that it improved the robustness.

### 3.5.4 Summary of turbulence models

The level of modelling of the different scales of turbulence is shown in figure 3.6 for various turbulence model groups. RANS models all scales of turbulence and treats them as isotropic. LES filters out and resolves large eddies which contain the most energy and then only models the smaller dissipative scales. DNS resolves all scales of turbulence but due to the fine grid resolution required is limited to small applications with low turbulence. DES combines the use of RANS near the walls and LES in separated regions.

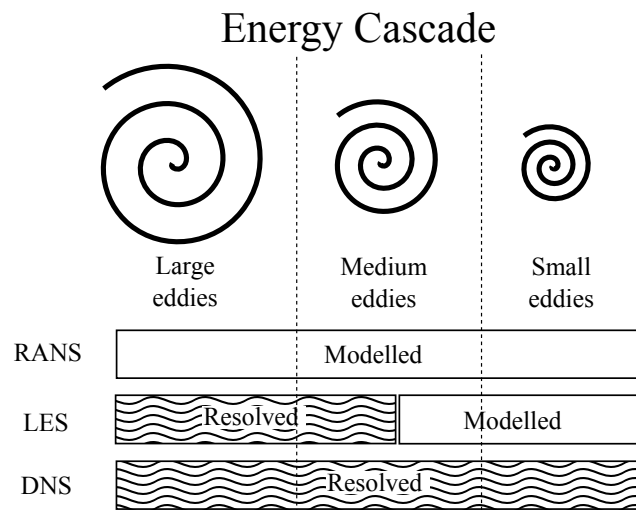


Figure 3.6: Turbulence modelling strategies for the various turbulence scales (adapted from Bagleito (2009))

The turbulence modelling methods and their estimated readiness is summarised in table 3.4. RANS models have been in use for a while and are extensively validated but this group also has its limitations which consequently motivated the development of numerous improvements and adaptations. LES, on the other hand, provides high accuracy advantages for separated flows but requires significant computational resources. Although these models are in use today, their applicability to highly turbulent flows is often impractical due to

computational constraints and, therefore, they are expected to be ready when the necessary advances in computational technology has been made. DES, making use of the best of LES and RANS modelling, is highly accurate and currently computationally affordable providing an attractive solution for the simulations envisaged in this study with respect to resource availability.

Table 3.4: Turbulence modelling methods and readiness (Adapted from Spalart (2000))

Method	Description	Readiness
RANS	Model all scales of turbulence	1995
DES	RANS near walls and LES for detached eddies	2000
LES	Model small scales and resolve large scales of turbulence	2045
DNS	Resolve all scales of turbulence	2080

Since this study involves bluff-body aerodynamics including high degree of separation, DES turbulence models seem to be the most suitable for this study. It provides an attractive middle ground promising accuracy and computational efficiency and with the two improvements implemented in IDDES makes this model applicable to a wide range of flow simulations.

### 3.6 Interpolation Schemes

Interpolation schemes are generally used in the discretisation of the governing equations to interpolate fluid properties from cell centres to face centres which is necessary when using the FVM. Interpolation schemes, sometimes also referred to as differencing schemes, should be carefully considered since they can have significant impact on the accuracy and stability of the simulation. The accuracy and stability requirements are different when discretising different terms in the transport equations. For example, discretisation of the diffusion term is straightforward but the convection terms require special attention to ensure stability of the simulation (Versteeg and Malalasekera, 2007).

Convection-specific schemes are a category of interpolation schemes used to determine the convection flux values on cell faces. Differencing schemes will calculate the exact solution if the domain can be discretised into an infinite amount of cells. Since this is not possible due to limited computational power,

errors and instability are introduced in the simplified differencing formulations. There are generally four properties of a differencing scheme to consider that influence its accuracy and stability:

- **Conservativeness** means that the flux leaving one cell must be equal to the flux entering another cell. The transport of the flux must, therefore, be represented in a consistent manner.
- **Boundedness** has two main requirements. The first is that the discretised equation matrix should be diagonally dominant. Secondly, boundedness requires that all the discretised equation coefficients have the same sign. Boundedness prevents unrealistic oscillations from being introduced due to the discretisation process.
- **Transportiveness** means that a discretisation scheme takes into account the direction and strength of the flow. With no flow, convection will be negligible and diffusion will cause fluid properties to spread evenly. With a fluid in motion a cell will be influenced more by its upwind neighbour than downwind neighbour due to convection. The dimensionless Péclet number,  $P_e$ , is often used to determine the point where transportiveness becomes important since it relates the relative strength of convection over diffusion. At high  $P_e$  the convection dominates and downstream cells are more influenced by the properties of upwind cells than downwind cells and, therefore, the up- and downwind influence cannot be regarded as equal. Transportiveness generally improves the stability of a scheme by using upwind quantities and therefore improves the convergence.
- **Accuracy** of a differencing scheme generally refers to the truncation of higher order terms in the Taylor series expansion during discretisation. The order of accuracy of the difference approximation is determined by the highest power term that was not truncated. Only truncation of the first order terms in the Taylor series expansion preserves boundedness but the resulting first order accuracy is unsatisfactory. Lee (1997), for example, highlighted the importance of higher order convection schemes and pointed out that lower order convection schemes tend to under-predict force coefficients. Higher order schemes generally are affected by more



neighbouring cells improving the interpolation or extrapolation accuracy but tend to introduce unrealistic oscillations under certain conditions. Even though higher order schemes generally produce greater accuracy the drawback, however, is that it also comes at a cost of additional computational expense.

Two of the most well known differencing schemes are upwind and central (linear) differencing. It can be shown that the upwind scheme is conservative, bounded and accounts for transportiveness but is only first order accurate since all 2<sup>nd</sup> and higher order terms in the Taylor series expansion are neglected. The upwind scheme is stable and, due to its simplicity, has been widely used in CFD. However, this scheme is less accurate in coarse grids especially when flow is not aligned with the grid which results in numerical diffusion errors sometimes also referred to as false diffusion. The central differencing scheme is also conservative but neither bounded nor accounts for transportiveness. This scheme is, consequently, often unstable for coarse grids producing spurious oscillations or 'wiggles' at high Péclet numbers when transportiveness becomes important. Even so, more accurate results are achieved on finer or non-flow aligned grids than with the upwind scheme.

The trade-off between stability and accuracy is common for interpolation schemes and motivated the development of more advanced schemes to achieve favourable characteristics. One way to find the middle ground between the stability and accuracy is to use blended schemes that combine the effects of two schemes through a blending factor,  $\psi$ . The blending factor is a fraction that will result in full upwind differencing if  $\psi = 0$ , full central differencing for  $\psi = 1$  and a blend of the two for  $0 < \psi < 1$ .

Figure 3.7 shows a simple one-dimensional flow domain for a cell,  $P$ , with an east,  $E$ , and west,  $W$ , neighbour. Notice centroids are denoted with upper-case letters and face values with lower-case letters. Using figure 3.7 as reference, a general form of the upwind biased scheme (flow direction from left to right) for calculating the east face flux,  $\phi_e$ , value is expressed in equation 3.6.1.

$$\phi_e = \phi_P + \frac{1}{2}\psi(r)(\phi_P - \phi_E) \quad (3.6.1)$$

where  $\phi_P$ ,  $\phi_E$  and  $\phi_W$  are the fluid properties at the cell centroids and  $\phi_e$  is the fluid property at the east face. In this formulation the blending factor,

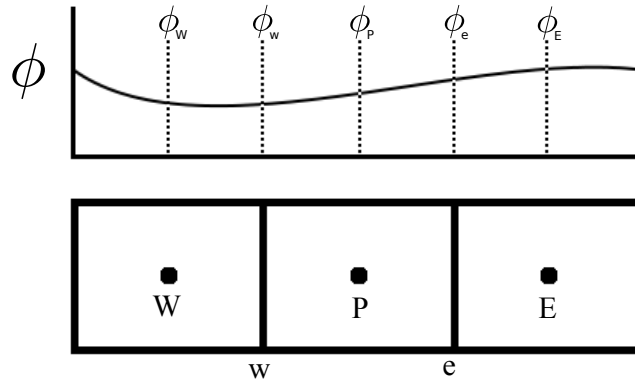


Figure 3.7: One-dimensional flow domain discretisation

$\psi(r)$ , is a function of the ratio of the fluid properties of a cell of interest and its east and west neighbours as expressed in equation 3.6.2.

$$r = \frac{(\phi_P - \phi_W)}{(\phi_E - \phi_P)} \quad (3.6.2)$$

It is possible to express  $\psi(r)$  for various interpolation schemes in terms of  $r$  as displayed in table 3.5.

Table 3.5: Blending factor functions for various schemes (Versteeg and Malalasekera, 2007)

Scheme	$\psi(r)$
Upwind	0
Central	1
Linear upwind	$r$
QUICK	$(3+r)/4$

To address the instability problems related to oscillations produced by higher order schemes more advanced methods have been introduced that adjust the discretisation method locally based on the flow conditions (Jasak *et al.*, 1998). One example is the total variation diminishing (TVD) schemes which introduce artificial diffusion sources or weighting methods to produce upwind-biased schemes (Versteeg and Malalasekera, 2007). TVD refers to the objective of preserving monotonicity by neither introducing new extremes or promoting local minima or maxima to counter the effects of overshoots produced by for

example the central and QUICK schemes. For TVD schemes  $\psi(r)$  is referred to as the limiter function for which Sweby (1984) introduced the criteria for 2<sup>nd</sup> order TVD schemes as follows:

- To classify as a TVD scheme  $\psi(r) \leq 2r$  and  $\psi(r) \leq 2$
- To be second order accurate  $r \leq \psi(r) \leq 1$  and  $1 \leq \psi(r) \leq r$
- To be symmetric  $\psi(r)/r = \psi(1/r)$

These criteria can effectively be presented in the  $r - \psi$  diagram as in figure 3.8.

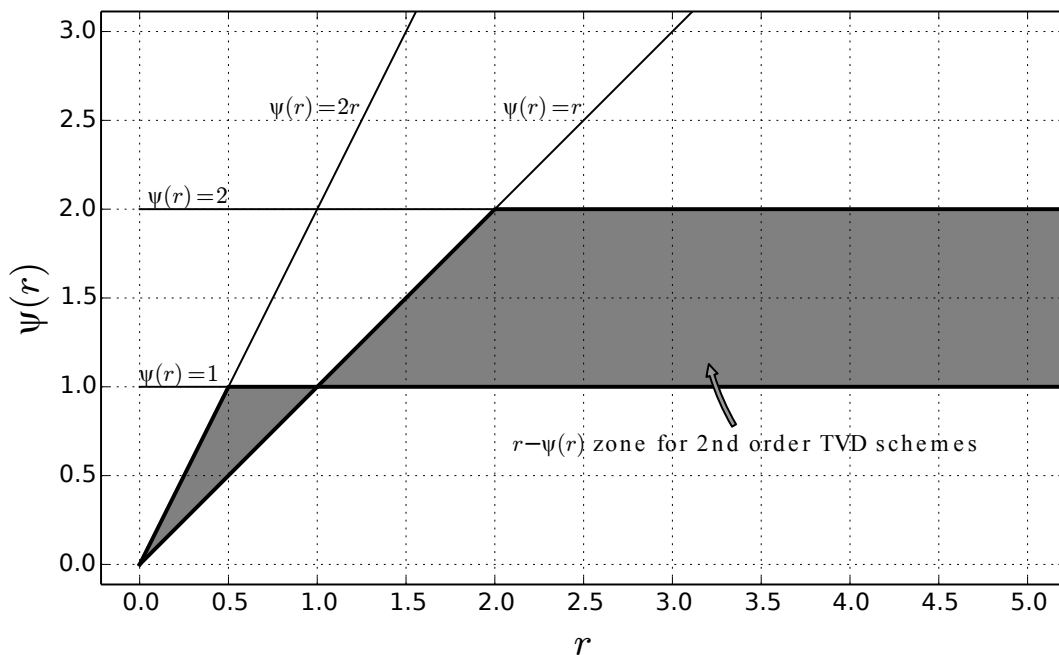


Figure 3.8:  $r - \psi(r)$  digram for TVD criteria

Many TVD schemes have since been proposed (see, for example, Van Leer (1974); Van Albada *et al.* (1982); Roe (1985); Sweby (1984); Leonard (1988); Lien and Leschziner (1993) for TVD schemes). These schemes are mostly second order accurate and adhere to the basic requirements of boundedness, conservativeness and transportiveness. The drawback is that higher complexity limiter functions require more computational resources. The gains in accuracy and stability, however, outweigh the drawback especially when considering the cost of increasing grid resolution that would be required in the absence of

higher order schemes. Therefore, these TVD schemes will be strongly considered in this project.

Other scheme groups include the normalised variable diagram (NVD) schemes and normalised variable formulation (NVF) schemes but these do not play a major role in this project so will not be discussed here in detail.

### 3.7 Three-dimensional Simulation

It is also important to notice that all flows are inherently three-dimensional. Although, in some cases, it is possible to produce accurate flow patterns using simplified two-dimensional analysis, more than often engineering applications involve non-streamline finite height bluff-body geometries that produce significantly three-dimensional flows that cannot be reproduced through two-dimensional simulations. Bruno *et al.* (2010) evaluated the flow around a rectangular prism with a  $L/D$  ratio of 5 using a LES turbulence model and highlighted the presence of three-dimensional flow features around a nominally two-dimensional structure. It was concluded that although the aerodynamic force is mainly driven by the two-dimensional flow features, the three-dimensional flow features are not negligible. The importance of three-dimensional simulations is also supported by work by Murakami *et al.* (1992) who reported that the two-dimensional simulations fail to accurately predict the surface pressures on the structures which are strongly influenced by the three-dimensional flow features.

### 3.8 Unstructured Meshing

Using structured meshes for complex flow domains is usually very difficult resulting in either overrefined meshes in simple flow regions or too coarse meshes in complex flow regions (Kim and Boysan, 1999). Unstructured meshes, on the other hand, allow for use of arbitrarily shaped cells and, therefore, reduce meshing time while at the same time allowing for more complex body fitted meshes. Unstructured meshes also allow for local mesh refinement such as in the boundary layer, high shear regions as well as separation and recirculation regions (Kim and Boysan, 1999). The drawbacks of unstructured grids are, however, that frequently flow flux discretisation is more diffusive than in struc-

tured grids. Furthermore, unstructured meshes often demand finer spacial discretisation to obtain grid-independent solutions (Mannini *et al.*, 2010b). It is also difficult to conduct a grid-convergence study such as with the Richardson extrapolation in unstructured meshes.

### 3.9 Near-wall Treatment

The near-wall treatment generally refers to the selection of boundary conditions, meshing strategy and turbulence models to accurately predict the wall shear stress and turbulence content due to the presence of a no-slip wall boundary (see section 2.3). For each turbulence model group in section 3.5 the near-wall treatment was briefly described. In this section a more general overview is presented.

Due to the impact of the wall boundary on the mean flow, the small turbulence scales as well as the complex interaction of the viscous and inertia forces in the near-wall region usually means that this region requires careful consideration with regards to computational efficiency and accuracy. The main considerations to take into account when selecting a near-wall treatment are the following:

- Boundary conditions needed for the specific near-wall approach. For example, would wall functions be used or not?
- Applicability of the near-wall treatment and boundary conditions in the expected flow conditions. For example, are wall functions applicable to separated flows?
- Turbulence model near-wall capabilities. For example, when using a low-Re wall treatment, does the turbulence model have the necessary near-wall damping terms?
- Near-wall meshing requirements for the chosen boundary condition. For example, what are the appropriate  $y^+$  values?

Traditionally RANS near-wall treatment strategies can be divided into low and high-Reynolds number approaches. Low-Reynolds number wall treatment calculates the flow up to the wall (viscous sub-layer) and, therefore, requires

very fine boundary layer cells with  $y^+ < 5$ . Since it is generally recommended to have a number of mesh nodes within the viscous sub-layer this means that using the low-Reynolds number method usually demands high computational resources. The wall shear stress is simple to determine being within the viscous sub-layer but the turbulence model must have built-in near-wall damping terms.

High-Reynolds number wall treatment, on the other hand, requires that the first meshing node fall within the log-law region ( $30 < y^+ < 500$ ). This approach models the near-wall region by making use of wall functions as boundary conditions to determine the correct wall shear stress. Since meshing within the viscous sub-layer is not required these models have significant computational resource savings.

Of the two approaches, the low-Reynolds number computations have been reported to produce better results but at the cost of 10 times more CPU time than the high-Reynolds number counterpart forming the stumbling block for the practical application of low-Reynolds number approaches in engineering applications (Lee, 1997).

One of the difficulties with near-wall modelling, as is briefly discussed in section 3.5, is that it is often impossible to create a mesh that will adhere to the near-wall treatment strategy requirements. This is because flow around complex geometries can change substantially over a short distance thereby changing the meshing requirements for the near-wall model but not allowing gradual mesh adaptation. Additionally, flow is often transient resulting in near-wall velocity fluctuations that are difficult to predict and mesh appropriately without placing too high demand on computational resources. The result being too large grid spacing for low-Re wall treatment or too small grid spacing for high-Re wall treatment leading to incorrect calculation of the wall shear stress and turbulence.

Using the "universal" velocity profile by Spalding (1961) (see equation 2.3.1) has the advantage of allowing a wider range of wall-normal computational grid spacing without compromising accuracy. By employing the "universal" velocity profile in the wall functions the stringent meshing criteria of  $y^+$  imposed by other common wall treatments is alleviated since these partitioned wall treatments require adherence to either the viscous sub-layer or log-layer. This is often difficult to achieve without prior knowledge of the near-wall flow.

Since a wider range of  $y^+$  is allowed it is often referred to as an “all- $y^+$ ” wall treatment.

It should, however, be noted that even though an “all- $y^+$ ” wall treatment allows for some flexibility with regard to the wall-normal grid refinement it still requires the applied turbulence model to have near-wall damping terms if the meshing is fine enough to place the first grid cell within the viscous sub-layer. If the turbulence model does not have built-in near-wall damping terms then the shear stress will not be calculated correctly. Turbulence models with the a "low-Re" in the name usually have these near-wall damping terms included. Some other examples of regular turbulence models with near-wall damping terms are the  $k$ - $\omega$  SST and Spalart-Allmaras turbulence models.

Another important consideration is that Spalding’s wall function was developed for smooth walls and attached boundary layers. Its applicability to separated flow is, therefore, questionable suggesting significant errors can be expected when applied to separated flows (Mockett, 2009). Even so, in the DESider project it was reported that DES using classic wall-functions work surprisingly well (Haase *et al.*, 2009). Mockett *et al.* (2012) also investigated the use of IDDES with an “all- $y^+$ ” wall treatment for attached and separated flows and concluded that it improved the robustness. These reports as well as the additional benefit of significantly reducing the computational demands of the near-wall region motivates further investigation of the use of an “all- $y^+$ ” wall treatment.

# Chapter 4

## Methodology

In this chapter the details regarding the numerical modelling and experimental set-up are explained. This chapter starts with selecting the appropriate geometry for achieving one-way FSI. This is followed by the wind tunnel description and the FSI simulation methodology. The chapter then continues with detailed descriptions of the computational fluid dynamics (CFD), coupling and finite element method (FEM) structural models. Lastly, the wind tunnel measurements are described.

### 4.1 Geometry Selection

Inspired by the rectangular shape of the SANAE IV base as well as the documented studies on bluff-bodies it was decided to use a vertical cantilever beam with rectangular cross-section as the subject for this investigation. This beam is subjected to an air stream in a wind tunnel to create the aerodynamics and flow-induced structural loading which could be measured and reproduced through simulations.

In figure 4.1 the structural assembly can be seen. The cantilever beam is a standard aluminium extrusion with a cross-section length,  $L$ , of 100 mm, a width,  $D$  of 38 mm and a shell thickness of 2 mm. A 740 mm long piece of the beam is used of which a height,  $H$ , of 500 mm is subjected to wind loading. At the top the beam it is sealed with a 8 mm thick aluminium plate (in the pressure measurements a wooden plate was used instead) and at the base is welded to a 8 mm plate with bolt holes for mounting purposes. The cantilever beam is mounted on a steel channel underneath the wind tunnel test section



which is connected to the wind-tunnel substructure using two 6 mm thick steel brackets and bolts.

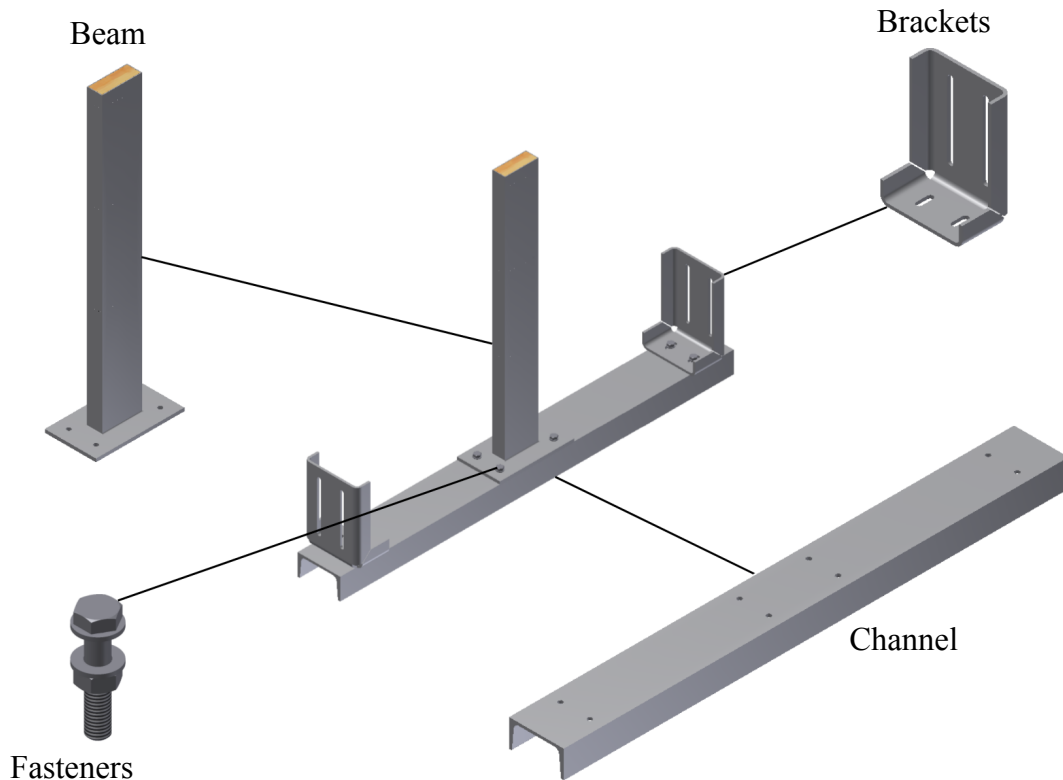


Figure 4.1: Mounted beam assembly (showing parallel beam)

The beam geometry was selected for the following reasons:

- Inexpensive and easily obtainable materials which allow for simplified manufacturing.
- Stiff structure due to rectangular tube extrusion allows for measurable but one-way FSI.
- Bluff-body profile due to rectangular cross-section creates the desired time-dependent vortex shedding.
- It provides the option to choose between a very short or long afterbody which will change the degree of FSI.
- Sharp edges allow for simpler separation point control, fluid domain meshing and simulation as opposed to rounded edges.

- Homogeneity in the extrusion material and profile helps for accurate structural modelling and experimental validation.
- Size of the internal cavity allows for internal placement of accelerometers and pressure tubing without influencing the aerodynamics of the structure during testing.

Four beams were constructed in total. Two parallel beams (the long,  $L$ , side is orientated parallel to the flow) resulting in a stream-wise cross-section ratio of  $L/D = 2.63$  and two perpendicular beams (the long,  $L$ , side is orientated perpendicular to the flow) with a stream-wise cross-section ratio of  $D/L = 0.38$ . The stream-wise cross-section ratio is usually referred to in literature as  $L/D$  ratios which may be misleading if the perpendicular beam is considered for comparison since the correct ratio is  $D/L = 0.38$ . The stream-wise cross-section ratios makes it possible to compare results to the findings of previous studies.

For each orientation, one beam was used for pressure measurements which required structural alterations such as pressure taps and access holes (sealed with wooden blocks during measurement). The other beams were kept intact and unaltered to ensure accurate structural response. The unaltered beams were used for measurements such as particle image velocimetry (PIV), vibration and strain.

The mounted parallel beam assembly, shown in figure 4.1, is the main focus of investigation in this dissertation due to the expected vortex shedding, time-dependent pressure loading and longer afterbody (the area after separation) on which the vortex induced loading will impact. The perpendicular beam orientation was subjected to the same flow conditions, and underwent the same measurements and simulations as the parallel beam but post-processing and flow features were not analysed in the same detail.

## 4.2 Wind Tunnel Set-up

Wind tunnel measurements were carried out to provide reference data for validation purposes. The wind tunnel is an open loop, sub-sonic wind tunnel with a test section that is  $2H$  high,  $14L$  wide and  $3.8H$  long (relative to the beam dimensions). The wind tunnel has a flow range of approximately

$10 < U < 90$  m/s in the test section where  $U$  refers to the bulk flow velocity entering the test section. The wind tunnel has viewing ports on the top and sides which allows for quick access to the models inside and facilitates optical measurements such as PIV. The wind tunnel test section and parallel beam components can be seen in figure 4.2.

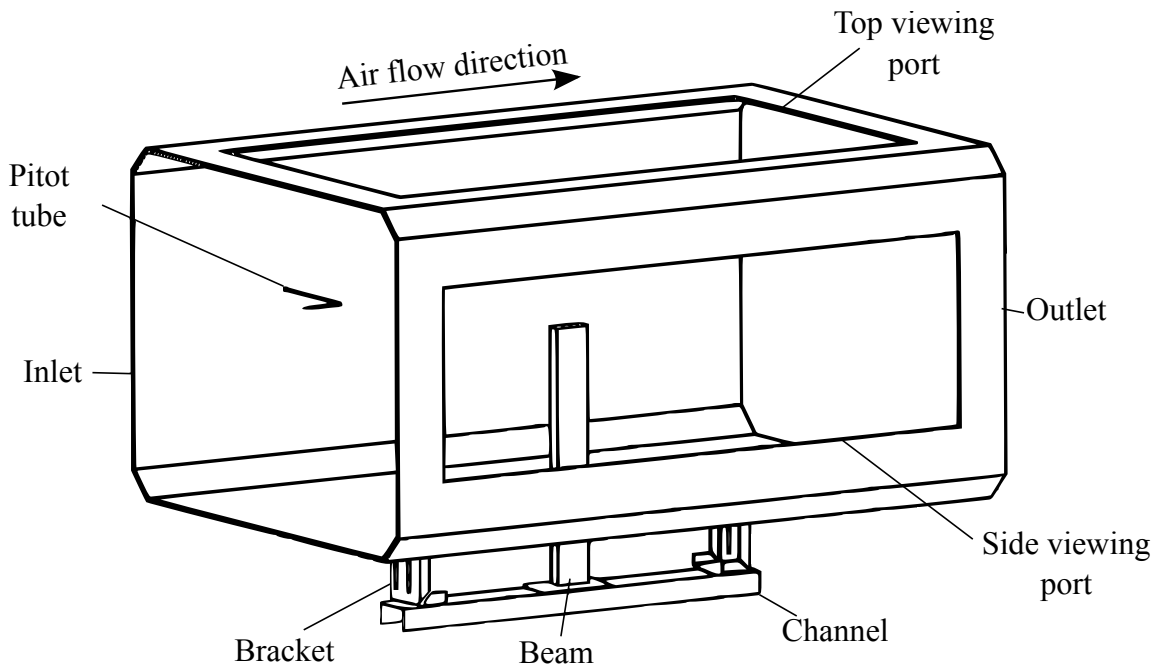


Figure 4.2: Wind tunnel test section set-up and components (adapted from Joubert *et al.* (2015))

The wind tunnel has the following limitations:

- The open-loop configuration means that tests are dependent on atmospheric conditions such as temperature and humidity which can have an affect on measurements.
- The open-loop configuration also means that seeding density for PIV tests is limited (see section 4.8.2) since the seeding introduced at the inlet cannot be recycled though the tunnel but is instead lost to the atmosphere.
- The viewing port in the wind tunnel test section prevents PIV measurements near the base of the beam by either blocking the laser or cameras through the side window line of sight.

- Wind tunnel vibrations can interfere with vibration measurements when connected to the test section structure.

The chosen geometry and mounting orientations result in a blockage ratios of 1.4 % for the parallel beam set-up and 3.6 % for the perpendicular beam set-up which is considered negligible. Furthermore, the parallel beam only occupies 2.7 % of the test-section width and the perpendicular beam only 7.1 %. From previous tests by Deacon (2009) it was shown that boundary layer thickness of the wind tunnel is less than  $0.2H$  for all walls at the speeds considered in this study. Since the beam is situated in the centre of the test section it is more than  $17D$  away from the wind tunnel walls for both the parallel and perpendicular set-ups. This suggest that the wind tunnel side-wall boundary layer has little effect on the near beam aerodynamics and consequently, only the vertical velocity profiles were considered in the simulations of this study (see section 4.4.1 for more detail). This means that only the top and bottom boundary layers were considered since the beam is directly influenced by these but not the test section side wall boundary layers.

Reference velocity measurements were conducted using a pitot tube which was positioned outside the boundary layer at approximately  $0.57H$  from the side wall (see figure 4.18). The inlet conditions for the wind tunnel is described by the vertical profiles of velocity and turbulence intensity shown in figure 4.3 as measured by Deacon (2009).

When conducting wind tunnel measurements it is often desired to avoid the wall boundary layers. However, in this study finding a set-up for a rigid structure for one-way only FSI that would suspend a bluff-body geometry in the free-stream while avoiding the boundary layer proved unsuccessful. Mounting the beam on the wind tunnel structure directly was intentionally avoided due to the presence of wind tunnel vibrations during operation which may interfere with measured vibrations. Furthermore, if the beam does not provide acceptable vibration response it would be advantageous to be able to change the wind loading height or even beam length if needed. Therefore, it was decided to mount the beam so that a part of it will protrude through the wind tunnel floor and so get subjected to wind loading. This beam is then mounted on a steel channel and connected to an independent steel sub-structure that is available under the wind tunnel test section through the use of two steel brackets. Because the steel sub-structure is considered rigid the structural model

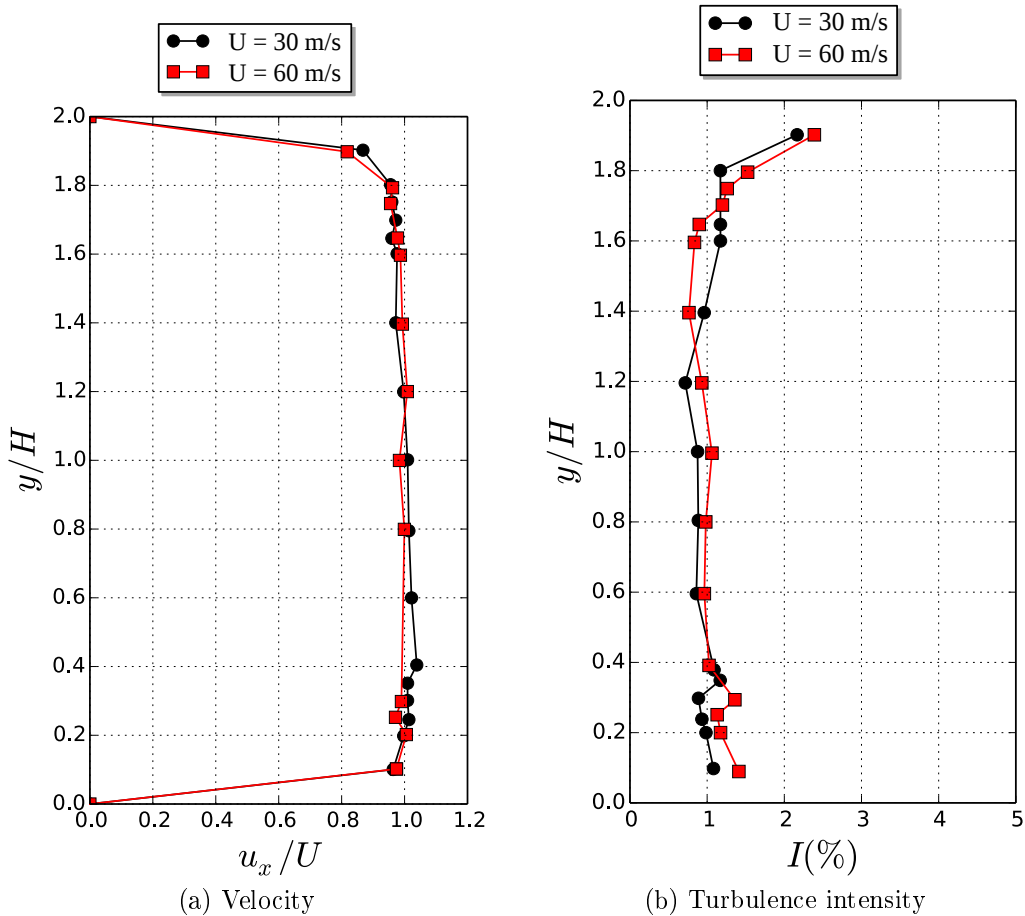


Figure 4.3: Measured inlet velocity and turbulence intensity profiles (Deacon, 2009)

only included the beam, channel and brackets. The connection between the brackets and the wind tunnel sub-structure was modelled as a rigid boundary condition.

The entry hole through the wind tunnel floor was cut slightly larger than the beam so that the beam never made contact with the wind tunnel structure during wind loading. A space of 2 mm between the wind tunnel and beam structure was found to be sufficient. The gap was sealed with tape to prevent air flow into the wind tunnel. The tape was applied in such a way to prevent any structural dampening. The impact of the tape on the structure was checked with modal tests by comparing two sets of data with and without the tape. It was found that the tape did not change the results.

### 4.3 Fluid Structure Interaction Approach

To simulate one-way FSI a segregated solution method is employed where the case is decomposed into fluid and structural domains as displayed in figure 4.4. This is possible due to the small displacements expected from the FSI given the boundary conditions. The fluid domain is solved first, using OpenFOAM (2015) to produce the transient bluff-body aerodynamics and resulting structural loading. The pressure and shear forces are then extracted from the fluid results and assigned to the structural domain as lists of time-dependant pressure and shear loads. The structural domain is then solved for the linear transient response.

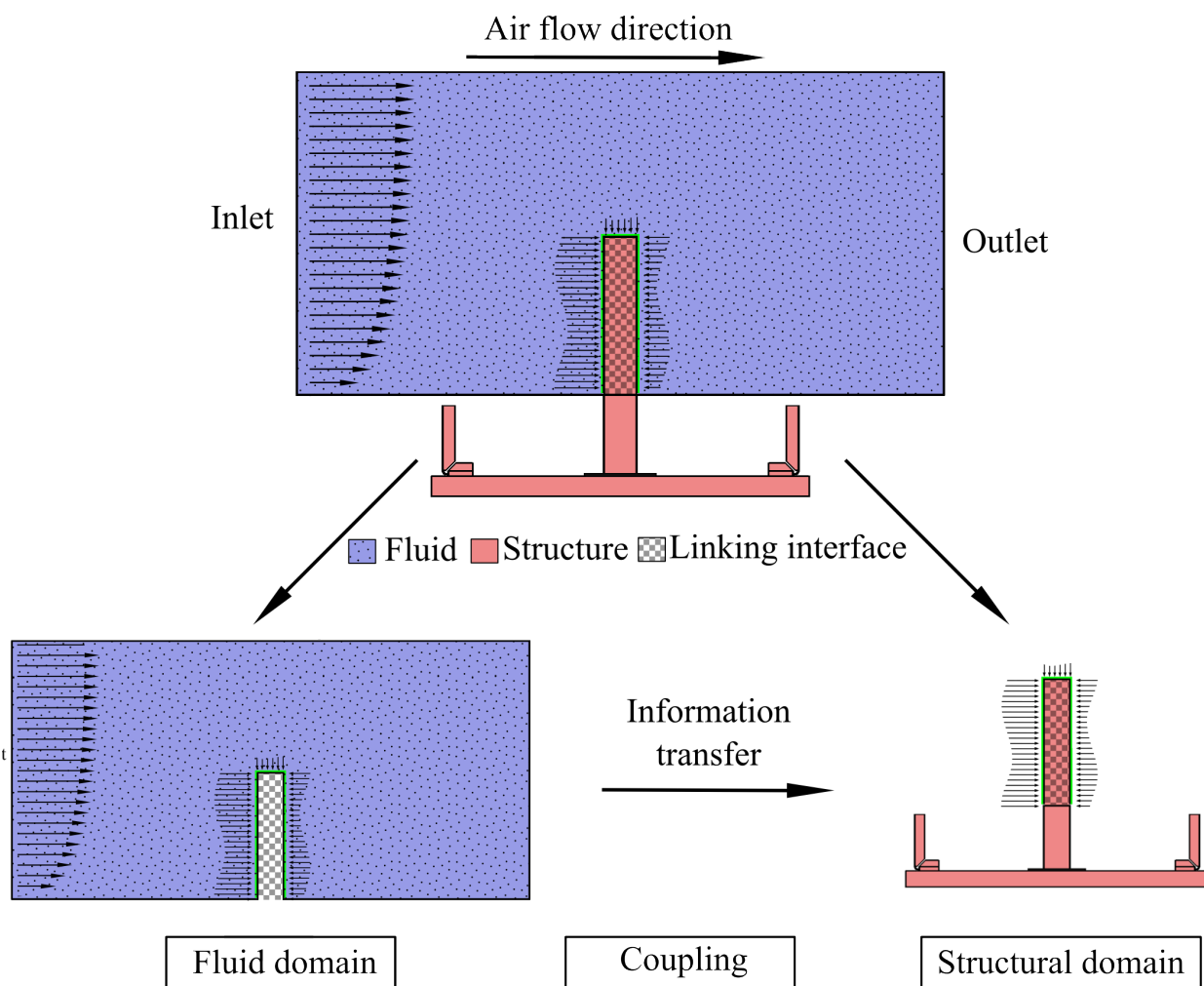


Figure 4.4: FSI domain decomposition and information transfer

With this modelling decomposition there is effectively three parts to con-

sider namely: Firstly, the fluid model, secondly, the coupling model and thirdly, the structural model. The methodologies followed for each of these parts are discussed in more detail in the next three sections.

## 4.4 Flow Modelling

The air stream in the simulations is modelled according to the wind tunnel conditions and can be described as being three-dimensional, turbulent, incompressible, isothermal air at atmospheric conditions (temperature and pressure). This simplifies the governing equations to the continuity equation and classic time-dependant filtered Navier-Stokes equations expressed in equations 3.5.16 and 3.5.17 respectively.

### 4.4.1 Domain and boundary conditions

The fluid domains and boundary condition labels can be seen in figures 4.5 and 4.6. The boundary conditions for the simulations are outlined in table 4.1. The inlet velocities were set according to the measured vertical velocity profiles shown in figure 4.3 while the horizontal velocity profiles at the inlet were considered uniform. Due to the low level of turbulence the value for  $\tilde{\nu}$  was set as zero but higher turbulence inlet conditions ( $\tilde{\nu}=5\nu_\infty$ ) were also investigated with negligible difference in the results.

Table 4.1: Fluid domain simulation boundary conditions

Parameter	Inlet	Outlet	Walls
$U$	$U_x = f(y)$ and $U_y = U_z = 0$	zero-gradient	zero
$p$	zero	zero-gradient	zero-gradient
$\nu_{sgs}$	zero-gradient	zero-gradient	wall-function
$\tilde{\nu}$	zero	zero-gradient	zero-gradient

The front, back, top and bottom boundaries in figures 4.5 and 4.6 are modelled as walls. At the walls the "universal" velocity profile suggested by Spalding (1961) is used to account for the effects of wall shear stress on the bulk flow without the need for high resolution near wall grid spacing. The computational grid produces a wall normal cell thickness of  $D/32$  which results

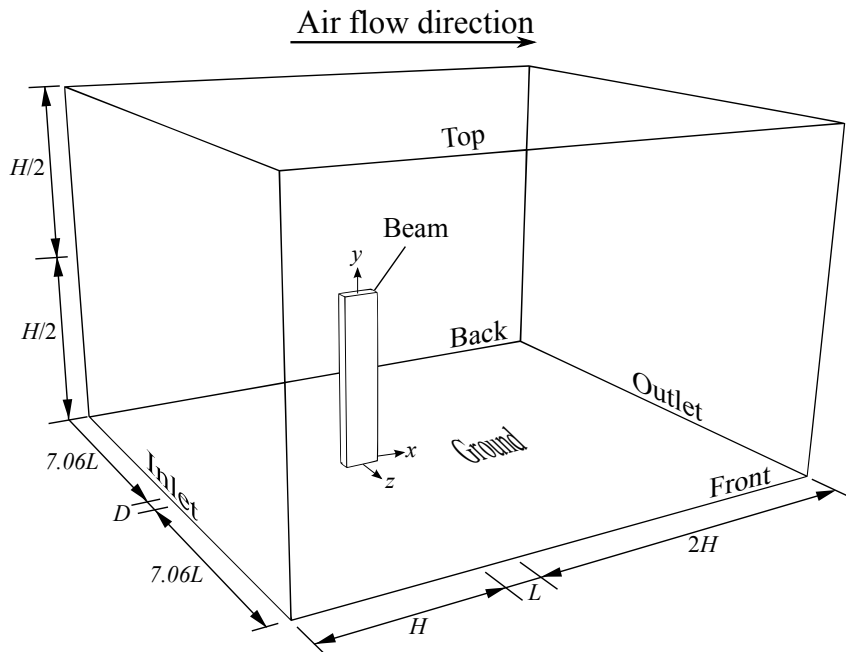


Figure 4.5: Parallel beam fluid simulation domain dimensions, layout and boundaries ( $L = 100$  mm,  $D = 38$  mm and  $H = 500$  mm)

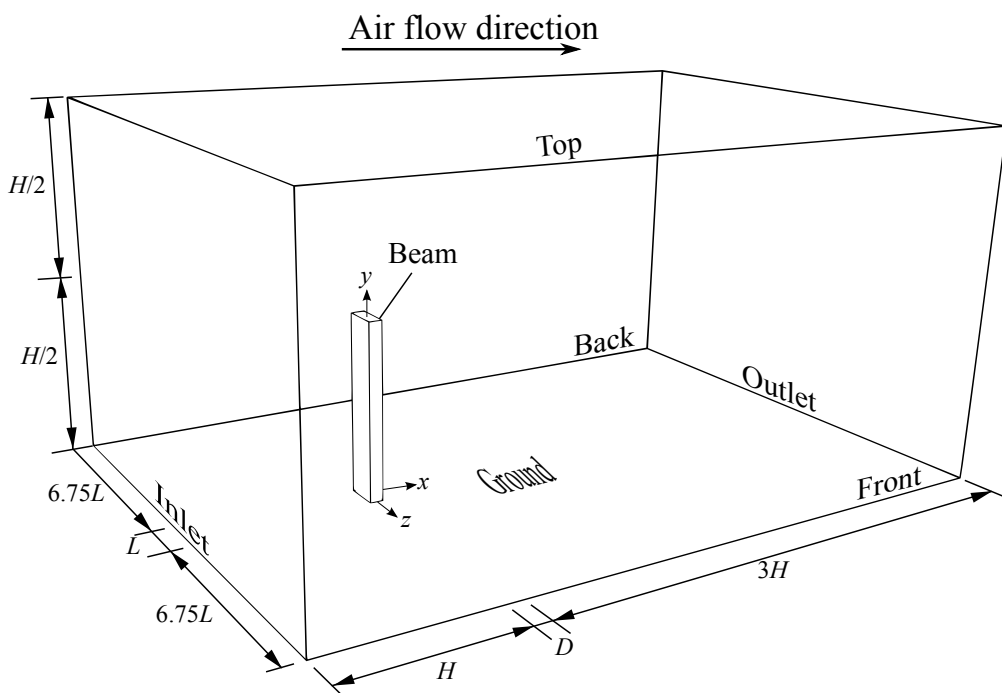


Figure 4.6: Perpendicular beam fluid simulation domain dimensions, layout and boundaries ( $L = 100$  mm,  $D = 38$  mm and  $H = 500$  mm)

in  $8 < y^+ < 40$  over the majority of the beam with the exception of the



upstream edge producing a maximum of 60.

#### 4.4.2 Meshing considerations

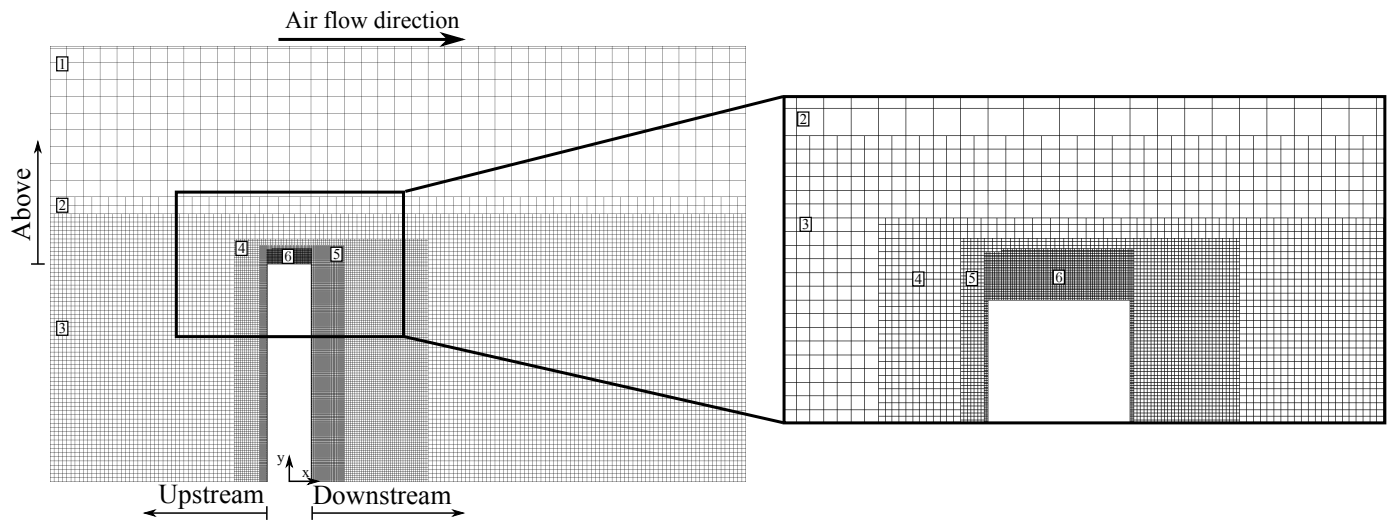
The computational meshes are shown in figures 4.7 and 4.8 for which the refinement details are provided in tables 4.2 and 4.3. Spacial discretization is done with the help of a predominantly structured mesh with some unstructured mesh features such as local refinement (increased grid density) as shown in figure 4.7. All cells are of the computationally efficient hexahedral kind and cubic shaped. Local mesh refinement is applied in regions where high velocity gradients are expected *i.e.* near walls and also in recirculation regions. However, to limit computational requirements, grid refinement is mainly introduced around the beam since this region is the focus of this study as opposed to the far field and downstream part of the wake. Refinement of the upstream part of the domain was also considered necessary to sustain the inlet velocity profile. The mesh refinement also helps to reduce the effects of numerical diffusion, although this is countered more efficiently with higher order differencing schemes. Lastly, the edges of the beam are modelled as sharp edges.

Table 4.2: Parallel beam fluid mesh refinement distances

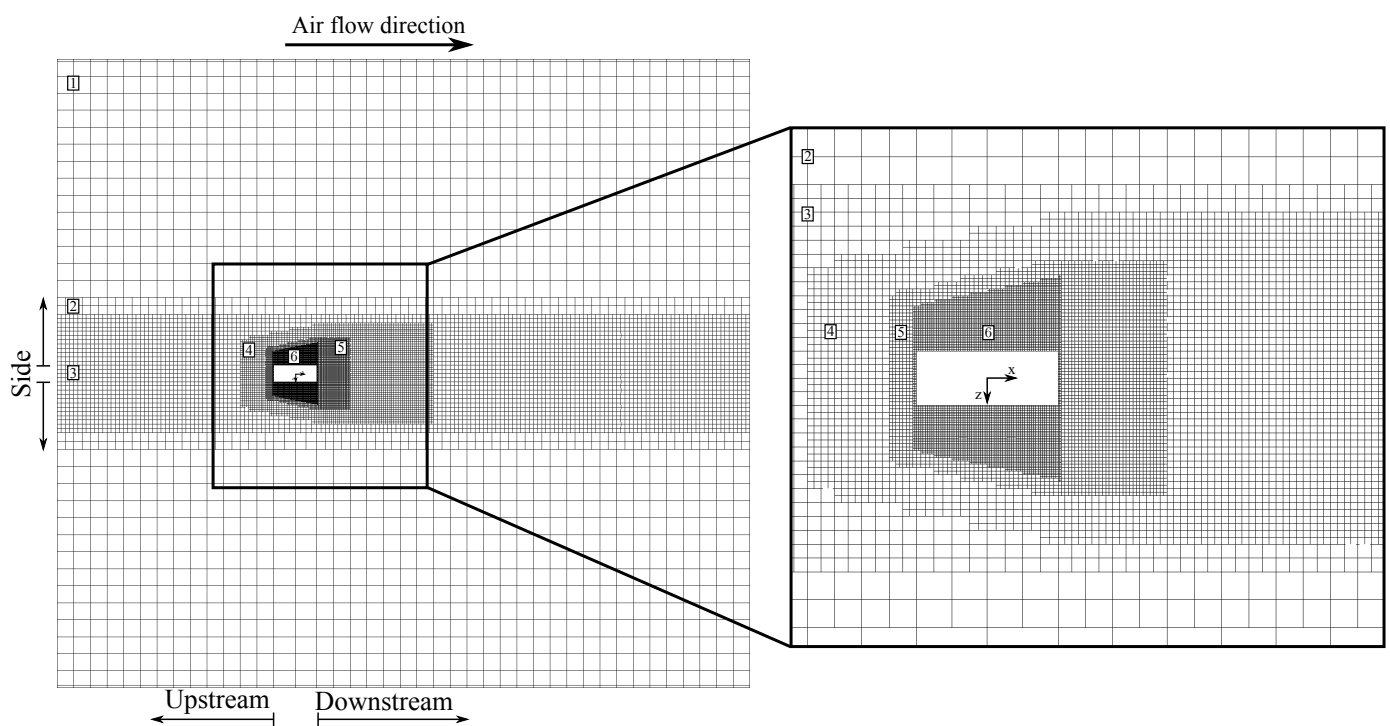
Zone	$\Delta_x$	Upstream	Downstream	Side	Above
1	$D$	$H$	$2H$	$7.06L$	$H$
2	$D/2$	$H$	$2H$	$4D$	$4D$
3	$D/4$	$H$	$2H$	$3D$	$3D$
4	$D/8$	$2D$	$7D$	$3D$	$3D$
5	$D/16$	$0.5D$	$2D$	$2.2D$	$2.2D$
6	$D/32$	$0.05D$	$0.05D$	$1.9D$	$1.9D$

#### 4.4.3 Turbulence and numerical schemes

The complex flow features introduced by a finite height bluff-body along with time and computational restrictions motivates the use of detached eddy simulation (DES) turbulence modelling. More specifically, the Spalart Almaras



(a) Side view ( $z = 0$ )



(b) Top view ( $y = H/2$ )

Figure 4.7: Parallel beam CFD mesh

improved delayed DES (IDDES) turbulence model (Shur *et al.*, 2008) is implemented since it includes the latest developments and improvements in this particular category of turbulence models (see section 3.5).

For the time advancement the Crank-Nicholson second order, bounded and implicit scheme was used, although, using the first order implicit and bounded

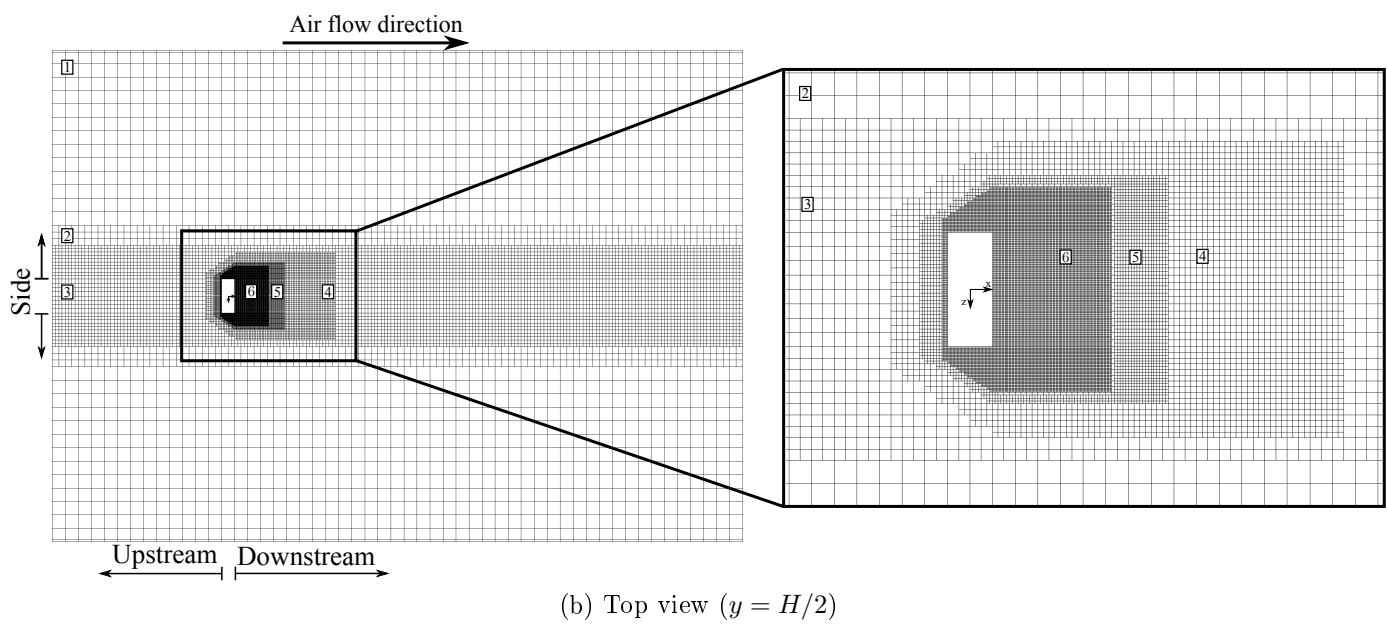
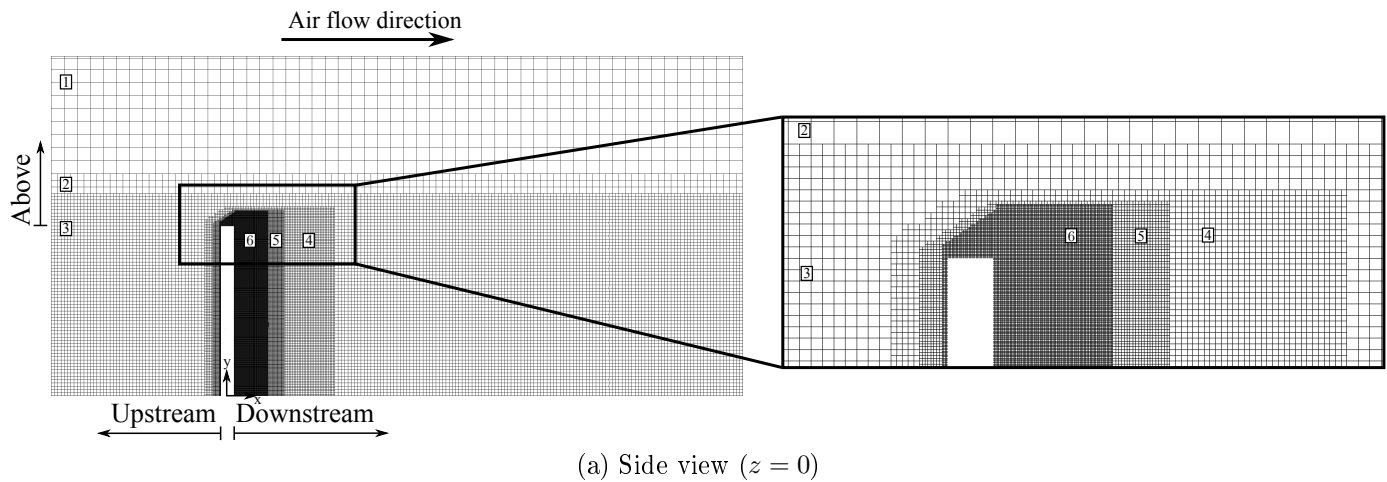


Figure 4.8: Perpendicular beam CFD mesh

Euler scheme showed negligible difference in results. Time advancement is done through a dimensionless time step size of  $tU/D = 7.89 \times 10^{-3}$  which kept the mean Courant number at 0.011 and the maximum Courant number at 0.5 allowing stable simulations.

For the parallel beam with  $U = 30$  m/s (considered the main focus of this study) this resulted in  $2.2 \times 10^3$  time steps per vortex shedding cycle providing a high resolution of the time-dependent solution. The simulation solved  $TU/D = 1579$  non-dimensional time units, which excludes the initial transient, and allows for 90 vortex shedding cycles and comprehensive analysis

Table 4.3: Perpendicular beam fluid mesh refinement distances

Zone	$\Delta_x$	Upstream	Downstream	Side	Above
1	$D$	$H$	$3H$	$6.75L$	$H$
2	$D/2$	$H$	$3H$	$1.5L$	$1.5L$
3	$D/4$	$H$	$3H$	$L$	$L$
4	$D/8$	$0.5L$	$3L$	$0.8L$	$0.8L$
5	$D/16$	$0.25L$	$1.5L$	$0.5L$	$0.5L$
6	$D/32$	$0.05L$	$1L$	$0.4L$	$0.4L$

and time dependent flow features.

The advection (divergence) terms are solved with the help of a limited-linear second order accurate, bounded, total variation diminishing (TVD) scheme. All other terms are solved with the linear (central differencing) scheme which is second order accurate. Lastly, mass conservation is imposed through the pressure-velocity coupling method which uses the pressure implicit with splitting operators (PISO) algorithm proposed by Issa (1986).

## 4.5 Coupling Modelling

Coupling refers to the transfer of information from the fluid domain to the structure domain through the linking interface (see figure 4.4). The prerequisites for the coupling are a) a completed fluid simulation and b) a prepared FEM structural mesh. Coupling is achieved in the following way (see appendix D for the most important code segments):

- Fluid and structural mesh information is extracted at the linking interface by cycling through all the faces and writing the face centre indexes and coordinates to a file. For the fluid mesh this is done through a custom utility developed in OpenFOAM and for the structure domain the mesh is extracted using the Code-Aster simulation command file. Loading full meshes can be time consuming but due to the simplified coupling this step would be done only once. Even so, one way to reduce the linking time is to sample data only on the points of interest (structure face centres).

- Flow-induced pressure and shear loads at the linking interface are extracted in OpenFOAM by cycling through the faces and writing the load components to relevant files. In the case of the beam, the shear stress was found to be small compared to the pressure for the chosen geometry and flow conditions but it was still included since it might play a more important role in future studies. In this project it was found easier to link pressures and stresses instead of forces since the normal vector information and areas do not have to be linked as long as the normal vectors are correctly defined on the structural mesh. Additionally no force balancing is needed at shared nodes since Code-Aster automatically calculates this if pressures are used.
- The fluid and structure meshes are linked through a Python program that cycles through all the faces in the structure mesh and searches for the nearest fluid mesh face centre. This method is referred to as the nearest neighbour method. The indexes of the paired faces are then written to a "link" file. This procedure is illustrated in figure 4.9 where the fluid and structure meshes are shown and the linked face centres are represented by the coloured lines. Typically the fluid mesh has a higher resolution due to the detail needed for bluff-body aerodynamics and turbulence modelling. For example, in the final FSI simulation the structural mesh face centres are 8 times further apart than the fluid mesh centres. In this step off-sets in the meshes are accounted for but overall orientations should be the same. It should be noted that structure elements are QUAD4 elements and have no actual face centre nodes. The face centre coordinates are calculated and used during the linking process.
- The load linking is done using a Python program which cycles through the faces on the structure mesh and assigns to it the transient pressure and shear loads from the corresponding fluid mesh face it is linked to. In this linking process a load file is written in Code-Aster format which serves as an input for the structural simulation. The loads are in the form of discrete functions of pressure and shear values over time for each structural node, which are discussed further below.

The pressure loads in Code-Aster are applied in the opposite direction as the surface normal vector and over the face area. The shear stresses, on

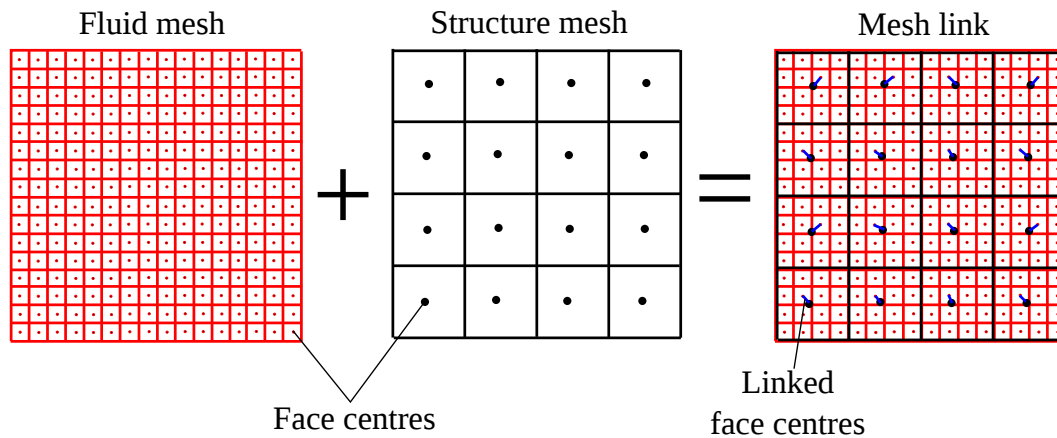


Figure 4.9: Mesh linking

the other hand, are extracted from OpenFOAM in global coordinates and applied in the same way. Both pressure and shear are multiplied by air density to get the correct units for Code-Aster since incompressible simulations in OpenFOAM record pressure as  $P/\rho$ .

The OpenFOAM load data available for the FSI simulations do not include the initial transient data but rather data from periods of the simulations where equilibrium (or converged) status has been reached. This means that the fluid domain beam is under full loading condition from the first time step that can be linked for the FSI simulations. Therefore, direct application of the fluid loads on the structure from the no-load condition will result in a step loading profile (or discontinuous loading profile similar to an impact) and induce unrealistic and, therefore, unwanted oscillations. To prevent these unwanted oscillations it was decided to introduce two modifications to the load profiles. Firstly, a smooth ramp (partial sinusoidal) function is added before the data to gradually transition the beam from no-load to a fully loaded but steady state condition. Secondly, a part of the extracted flow-induced loads is dampened so that load oscillations smoothly grow to take the load profile from steady state to full time-dependent loading. In figure 4.10 the applied time-dependent pressure load for a single structural element is shown.

This coupling strategy has a number of accuracy considerations to take into account. Firstly, the method is based on the assumption that only small structural displacements occur in which case the structural movement has negligible effect on the flow. If the flow-induced loading results in significant displacements a more strongly coupled methodology needs to be followed. Secondly,

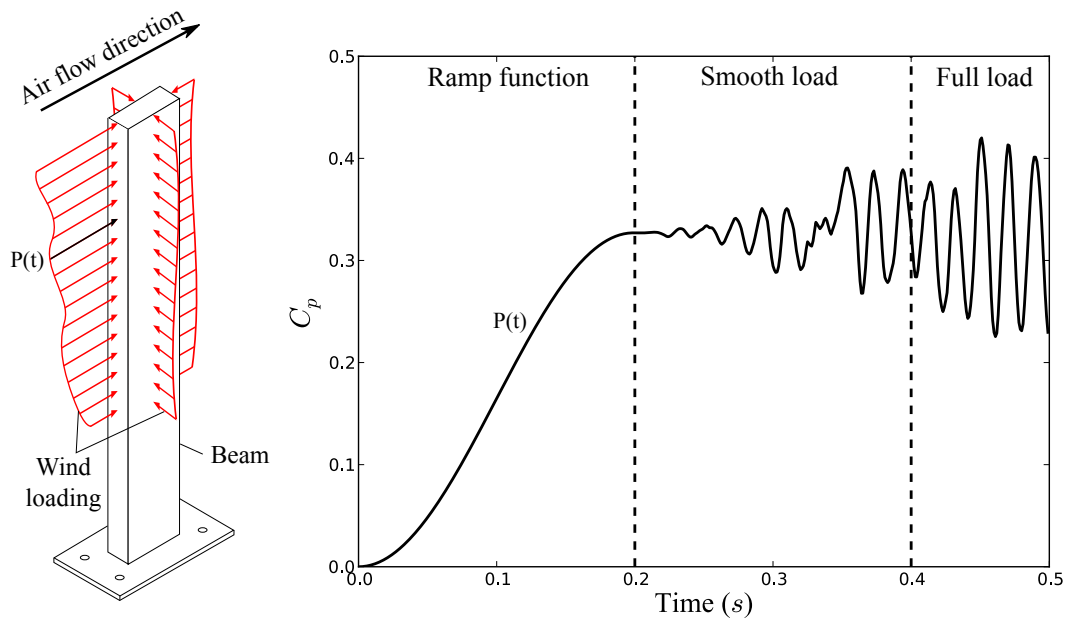


Figure 4.10: Simplified pressure function for a single shell element in the structure mesh

each structural mesh element is subjected to the pressure and shear loads of the fluid node it is linked to but it applies this load over the entire area of the structural element regardless of the resolution difference to the fluid domain. This is illustrated in figure 4.11 which shows how the pressure load along outer perimeter of the cross-section of the beam at the height of  $y = H/2$  is simplified due to the lower resolution of the structural mesh.

This means that inaccuracies may occur if the lined fluid and structural elements are far apart or if the fluid node loads are not representative of the average load over the area covered by the structural element. The effect of mesh resolution differences on the linking distances is illustrated in figure 4.12. These problems can easily be mitigated by increasing the structural mesh resolution which is usually not as costly as refinement of the fluid mesh would be. Lastly, the structural simulation time resolution can only be as fine as the fluid time resolution after which the solution will resort to linear interpolation between time steps. This is not considered a problem since the fluid domain time steps are usually very small.

The limitations of the nearest neighbour linking method can be reduced by involving more than one fluid mesh face centre to determine the loading on the structural face centre. Two options are, for example, using an interpolation

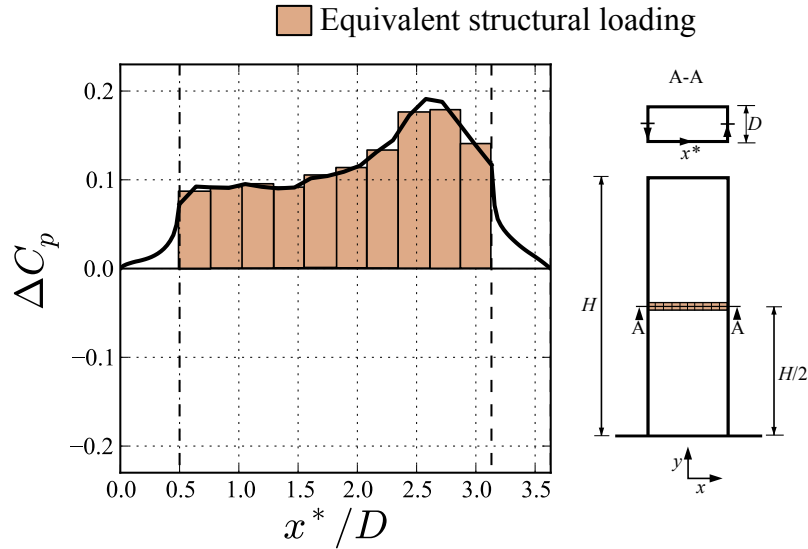


Figure 4.11: Load simplification through the linking procedure due to differences in mesh resolution

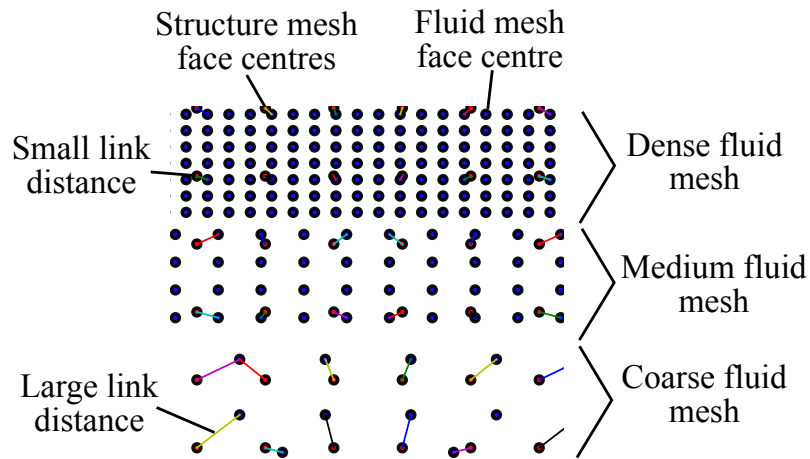


Figure 4.12: Effect of mesh resolution on linking distances

to determine the loads at the position of the structure mesh face centres or by using the average load of the face centres covered by the structure mesh element. However, both methods would significantly increase the linking time and memory requirements since it would require the collection of more fluid mesh element data and intermediate calculations for each structure mesh element to determine the average or interpolation.



## 4.6 Structural Modelling

The structural simulations were completed using Code-Aster (2011) version 10. The motivation for using Code-Aster in this project was discussed in section 3.4.

The structural model solves the transient response of the assembly which includes the beam, channel and brackets shown in figure 4.1. Supplementary structural drawings are also provided in appendix C. The model can be described as mechanical and the solution is linear. This does, however, limit the modelling accuracy of boundary conditions since non-linear response due to contact interaction between components is not accounted for.

The governing equations for the structural analysis can be seen in equation 4.6.1 where  $M$ ,  $C$  and  $K$  are the mass, damping and stiffness matrices respectively. The  $\alpha_i(t)$  are functions of time and  $F_i(x)$  are force vectors resulting from the combined loading of the various boundary conditions.

$$M\ddot{x} + C\dot{x} + Kx = \sum_i \alpha_i(t)F_i(x) \quad (4.6.1)$$

The structure consists of four main components namely: beam, channel and two brackets which are all connected through nuts and bolt fasteners. The structural domain consists primarily of QUAD4 shell elements with limited TRIA3 elements to facilitate the meshing around curved edges. The entire mesh was modelled with discrete Kirchof elements (also referred to as DKT elements). Higher order elements such as QUAD8/TRIA6 and QUAD9/TRIA7 were also investigated but these had a negligible effect on the results. The total number of equations solved for the structural model was  $1.74 \times 10^5$  of which the meshes can be seen in figures 4.13.

The structural domain boundaries and shell element offsets can be seen in figure 4.14. The time-dependent loading is applied to the upper 500 mm part of the beam which includes pressure and shear stresses. Shell elements are used throughout due to the thin wall thickness of all components which saves some computational requirements. The shells were modelled in such a way to limit material overlapping and facilitate assembly of the system. The channel was divided into different shell elements with varying thickness as shown in figure 4.15. These were connected with rigid body elements.

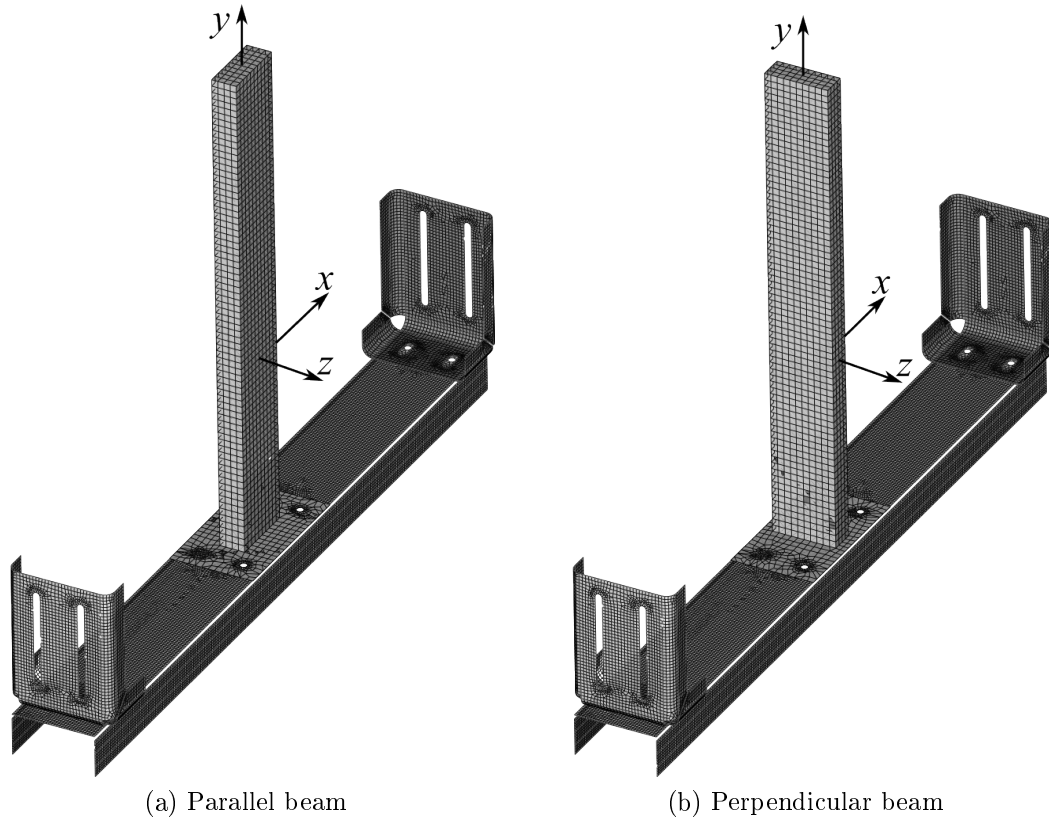


Figure 4.13: Shell meshes for structural analysis

The bracket sides are fixed at bolt hole locations where it is connected to the wind tunnel sub-structure as shown in figure 4.16. Each bolt is represented by connecting 4 nodes on each component with rigid body elements. Additionally, the masses of each bolt were measured to be 41.2 g and these were added as point masses to the closest node to the bolt centre.

The structural assembly components and material properties are given in table 4.4. The beam material is modelled as aluminium with a density of  $2702 \text{ kg/m}^3$  which was determined using the Archimedes Method using 10 samples of the beam wall material ( $20 \times 20 \text{ mm}$  and  $2 \text{ mm}$  thick). The Young's modulus was set as  $70.89 \text{ GPa}$  and a Poisson's ratio of  $0.33$  was used.

The Young's modulus was determined using cantilever beam displacement measurements and simulations (see appendix A section A.4 for more details). In both cases solid aluminium strips of the beam material of  $2 \text{ mm}$  thickness and various lengths was used. In these tests the tip displacement was measured and an optimiser coupled with Code-Aster FEM simulations was used to calculate the Young's modulus. In this case the optimiser changes the Young's

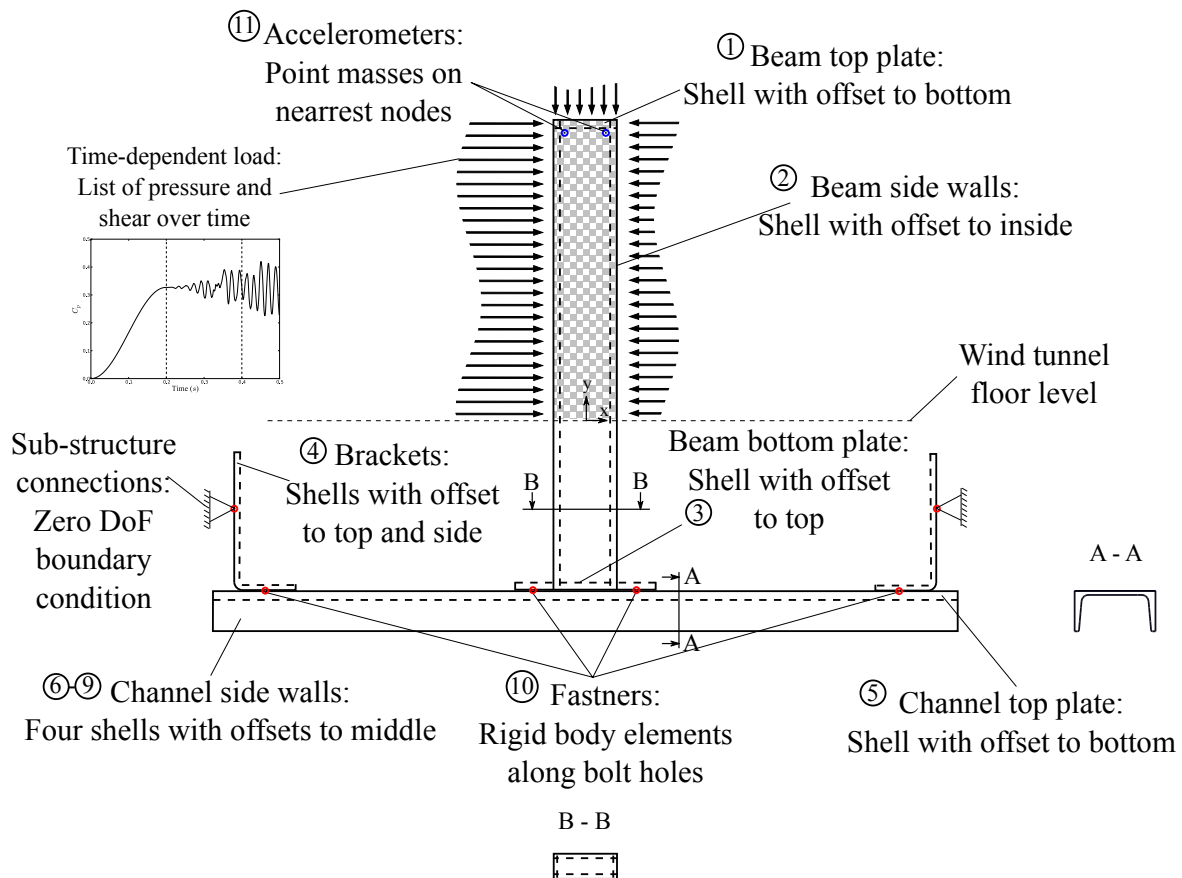


Figure 4.14: Structural model shell offsets and boundary conditions

modulus until the tip displacement becomes equal to the measured displacement. Due to the simplicity of the beam geometry and boundary conditions, the reliability of the FEM codes for simple cases such as these and the repeatability of the results for various lengths produces an accurate representation of the Young's modulus. Using this method the tests produced a maximum variation in Young's modulus calculation of 0.18 % which is considered negligible.

The steel components were modelled with a density of  $7870 \text{ kg/m}^3$ , a Young's modulus of 200 GPa and Poisson's ratio of 0.3 which are considered typical values for mild steel. Typical values were used instead of measured values because it was not possible to take samples of the channel and bracket material without changing the component structural characteristics. Furthermore, due to the air flow loading on the beam as well as its lower stiffness and mass, it is suspected that the structural response will be more dependent on the beam characteristics than on the channel and brackets.

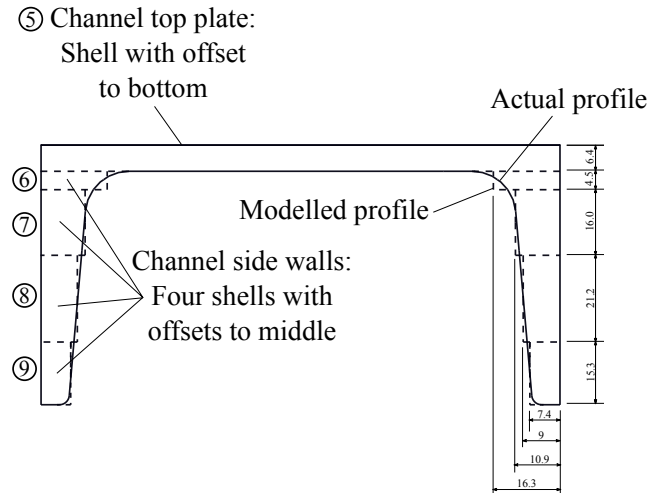


Figure 4.15: Modelling the channel with shell elements with varying thickness

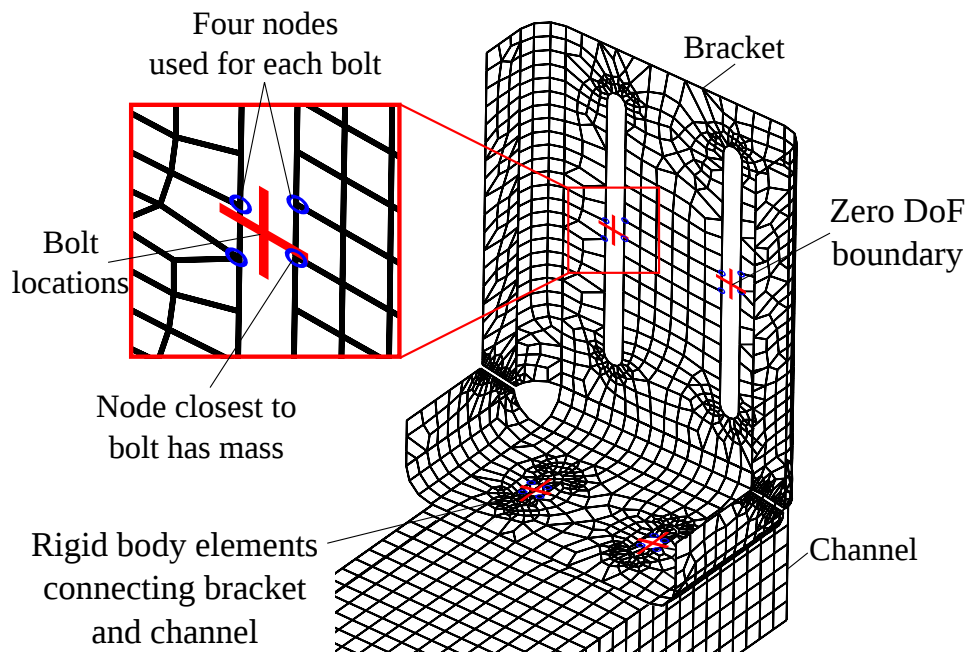


Figure 4.16: Connection modelling showing the channel and bracket

## 4.7 Computational Resources

The CFD simulations were run on the Stellenbosch University high performance computing (HPC) cluster using 24 cores on a 48-core AMD Opteron 6172 processor with an infiniband interconnect. A typical simulation with 3.5 million cells used approximately 4.6 GB RAM and took 5 weeks to complete 2 seconds of a transient simulation. It should also be noted that simulations were started from previous results to improve stability, convergence and

Table 4.4: Structure mesh elements, materials and offsets (see also figures 4.14 and 4.15)

Nb	Name	Type	Material	$th$ [mm]	Offset [mm]	$m$ [kg]
1	Beam top	Shell	Alum.	8	$dy = -th/2$	Calc.
2	Beam side	Shell	Alum.	2	$dz = dx = 0$	Calc.
3	Beam bottom	Shell	Alum.	8	$dy = th/2$	Calc.
4	Brackets	Shell	Steel	5.7	$dz = dx = dy = th/2$	Calc.
5	Channel top	Shell	Steel	6.4	$dy = -th/2$	Calc.
6	Channel side	Shell	Steel	16.3	$dz = \pm th/2$	Calc.
7	Channel side	Shell	Steel	10.9	$dz = \pm th/2$	Calc.
8	Channel side	Shell	Steel	9	$dz = \pm th/2$	Calc.
9	Channel side	Shell	Steel	7.4	$dz = \pm th/2$	Calc.
10	Fasteners	Point mass	Steel	N/A	N/A	0.0495
11	Accelerometers	Point mass	Ceramic	N/A	N/A	0.004

reduce simulation time.

Larger simulations (for the finest mesh) were also done using up to 32 cores at once. The finest mesh consisted of more than 14 million cells and took almost 6 weeks to complete only 0.45 seconds of the transient simulation. The simulation was terminated due to time and space limitations before a large enough statistical representation could be achieved. The total time needed to complete 2 seconds of the finest mesh simulation is estimated to be 26 weeks and the total disk space would exceed 3 TB even when using a compressed format which is more than the HPC disk space allowance. Even if 1 simulation of the finest mesh was completed there would not be enough time using the same mesh for simulating other velocities or orientations. Lastly, it would also require a dedicated 4 TB hard drive for each new simulation to get the data from the cluster and then take weeks for each post-processing operation. Therefore, large simulations such as these were not pursued further.

The Post-processing, linking and FEM simulations, being significantly less computationally intensive than the CFD simulations, were done on a Dell Optiplex 990 Workstation with one Intel Core i7-2600K CPU with 4 true processing cores and permitting 8 threads to be executed simultaneously providing a maximum processor speed of 3.8 GHz. This desktop has 16 GB of RAM. The post-processing and linking of the data for large simulations took approx-

imately 4-5 days and FEA structural simulations took approximately 1.5 days to complete.

This project was also instrumental in the set-up, operation and testing of a new GPU system for CFD simulations at Stellenbosch University Mechanical and Mechatronic Engineering (Van Zyl *et al.*, 2014). The system consists of a Dell Precision T7600 Workstation with two Intel Xeon E5-2630 CPUs with maximum operating capabilities of 2.8 GHz, two Nvidia Tesla C2075 GPGPUs and 32 GB of RAM. Each of the two GPUs contain 448 cores with maximum operating capability of 1.15 GHz, allow 515 Gflops of double precision floating point calculations or 1.03 Tflops of single precision floating point calculations (Van Zyl *et al.*, 2014). Furthermore, each card is limited to 6 GB of on-board GDDR5 memory with a maximum bandwidth of  $144 \text{ GB s}^{-1}$ .

This system was used extensively throughout this project for CFD simulations of total cell count  $< 5$  million due to the 6 GB RAM limitation of the GPU Nvidia Tesla cards. Before the HPC cluster had the infiniband interconnect, transient simulations using multiple processors on different nodes were highly unstable. Additionally, the HPC cluster was heavily utilised during periods of this study resulting in long waiting times for simulations especially of larger size. The GPU system was, therefore, obtained to meet the need for high performance computations that was not possible at the time with the HPC cluster and had a significant advantage over the high-end desktops in processing power. At the time OpenFOAM was also the only CFD software code that provided the needed solvers, unlimited free licences and could make use of GPU processors using linear precision. It was found in initial investigations that for simulations of total cell count  $> 300\,000$  cells the GPU system performed better than the desktop (Dell Optiplex 990 Workstation) using CPUs. With simulations of 1.2 million cells the GPU already performed 3 times faster with the performance gap growing with larger and larger simulations (Van Zyl *et al.*, 2014).

## 4.8 Experimental Set-up and Procedure

In this project numerous experiments were conducted to shed further light on the underlying dynamics as well as to provide boundary conditions, material specifications and validation data. The experiments included pressure, PIV,

strain and vibration measurements for which the set-ups are discussed in the following sections in more detail.

### 4.8.1 Pressure measurement set-up

The beam in the air stream creates complex turbulent aerodynamics which induces pressure and shear loads on the structure surface. The pressure loads result in forces normal to the face it acts upon while the shear stresses, on the other hand, results in tangential forces. In this project pressure measurements were carried out to measure the pressure on the beam outer surface since this would be an important indicator of the accuracy of the simulations to reproduce the loading conditions.

To measure the pressure two beams were constructed, including one for each orientation (parallel to the flow and perpendicular to the flow). The parallel beam pressure taps are displayed in figure 4.17. Pressure taps were drilled with 0.5 mm diameter starting from the centre of the upstream face of the beam continuing on a horizontal plane around the cross-section half perimeter to the side wall and then to the centre of the downstream face. In later tests, 1 mm diameter holes were found to have negligible effect on the flow as well and provided an additional benefit of stabilizing the pressure in the transducer pipe more quickly than the 0.5 mm holes. The pressure taps were slightly off-set vertically to limit the effect of a pressure tap on the downstream ones but this was not taken into account in the validation results due to the negligible offset distances.

The pressure measurements were conducted in the medium speed wind tunnel with the beam assembly mounted below the tunnel and the beam protruding through the test section floor as shown in figure 4.2. On the inside of the beam all the pressure taps were connected to pipes leading to pressure transducers via a pressure channel scanner. This makes it possible to measure up to 40 pressure points with one transducer without having to reconnect piping in-between measurements. The pressure transducers were calibrated three times in total using a Betz anemometer. It was found that the pressure transducer measurement drift was negligible even when calibrations were one year apart. The calibration curves for the pressure transducers are provided in appendix A.

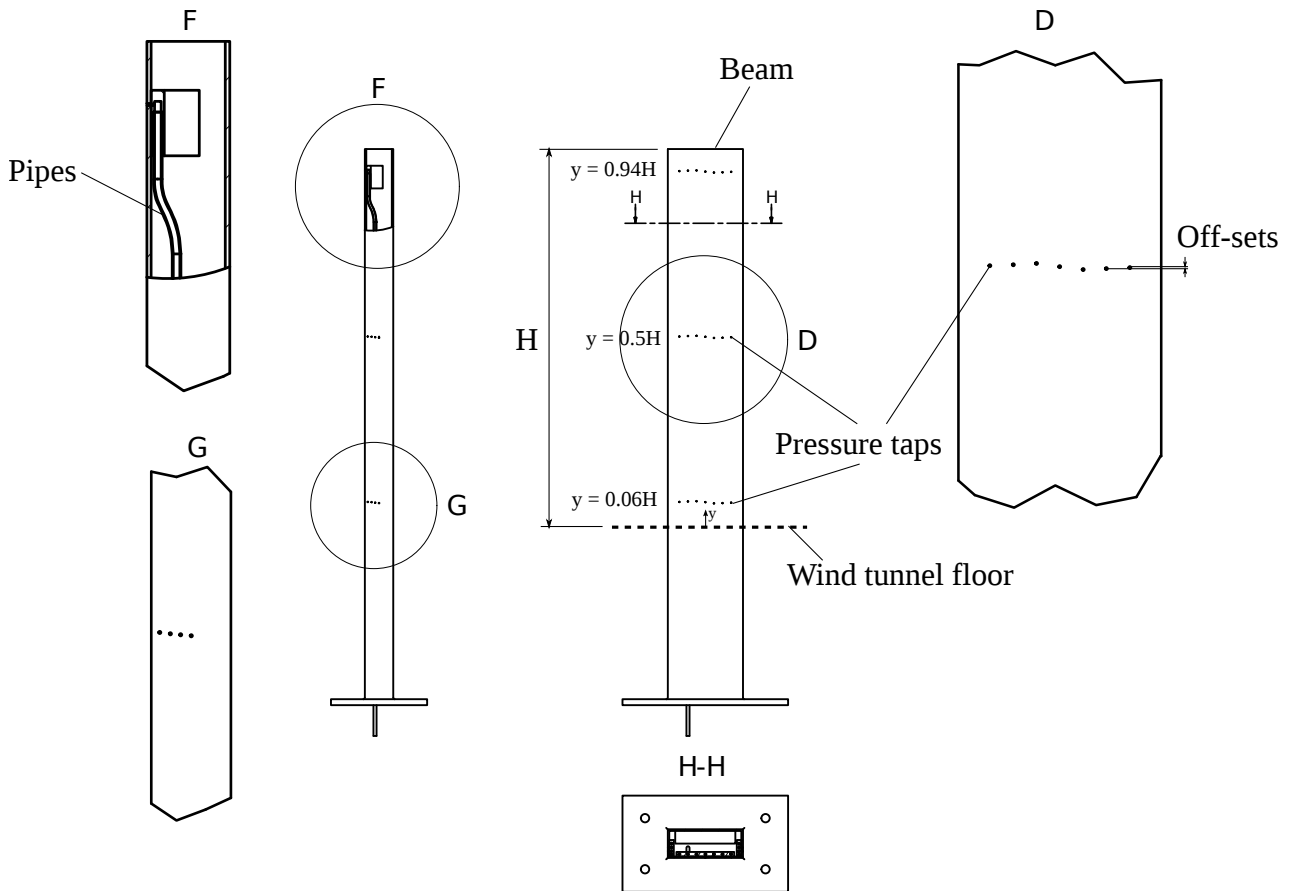


Figure 4.17: Pressure pipes assembly

Time-averaged pressure was measured at  $y = 0.06H$ ,  $0.5H$  and  $0.94H$  with  $y$  measured from the wind tunnel floor and  $H = 0.5$  m. Each beam was tested at 2 wind tunnel speeds ( $U = 30$  and  $60$  m/s) resulting in a total of 12 data sets with each set including approximately 15 pressure taps on each height. The pressure was measured for at least 10 seconds after equilibrium was reached to obtain to eliminate the initial transient effects while the pressure stabilizes in the pipes. The dynamic pressure ( $p = 1/2\rho U$ ), used to calculate the pressure and lift coefficients, was obtained using a reference velocity measurement from a pitot tube which was positioned outside the boundary layer at approximately  $0.57H$  from the side wall (see figure 4.18).

#### 4.8.2 PIV measurement set-up

Time-averaged velocity field measurements were taken using a PIV system. PIV makes use of a laser, two cameras and particles in the flow to measure



velocity vectors on a plane. The system is calibrated using a calibration target which provides a reference grid providing spacial calibration as well as an axis system to be used in the velocity calculations. The calibration is discussed in appendix A.1.

The PIV system takes two consecutive images 10 to 70  $\mu\text{s}$  apart (depending on the flow speed) which is referred to as an image set and is considered by the software as a single unit. These image sets are used to calculate the velocity by dividing them into square correlation areas (usually 32 x 32 or 64 x 64). In a process called adaptive correlation the particle cloud movement in each correlation area is calculated by comparing the two images in an image pair. With the distance, direction and time known the velocity vector for each correlation area can be calculated.

The resolution of the correlation areas is important since only a single vector will be created in each correlation area. Dividing the photos into many correlation areas will result in more vectors and better representation of velocity gradients but smaller particle clouds will be used to calculate the velocity vectors so it may introduce more errors. Coarser correlation area resolution includes larger particle clouds and, therefore, less incorrect vectors but it also introduces smoothing that could misrepresent areas that have high velocity gradients.

The PIV experiments were conducted in the medium speed wind-tunnel in the dark to reduce data interference. Small oil droplets were sprayed into the wind tunnel inlet to act as flow tracers (or seeding) for the PIV system. Oil droplets are preferred over water or smoke since oil does not evaporate and has a high light reflectivity making it easier to detect. The laser was directed through the side window and the cameras positioned on top of the wind-tunnel to measure the flow on a horizontal plane as it moves around the geometry. This can be seen in figure 4.18.

The PIV measurements were carried out for the upper part of the beam at heights  $y = 0.5H$ ,  $0.72H$  and  $0.94H$  (see figure 4.18 for  $y = 0.5H$  position set-up). The maximum sampling frequency was limited to 7.5 Hz, therefore, allowing only one measurement every 6 vortex shedding cycles for the parallel beam and  $U = 30$  m/s. For this reason only time-averaged data comparison is possible with the available PIV system. The PIV system was manufactured by Dantec Dynamics (2012) and consists of two cameras, a q-switch NdYag

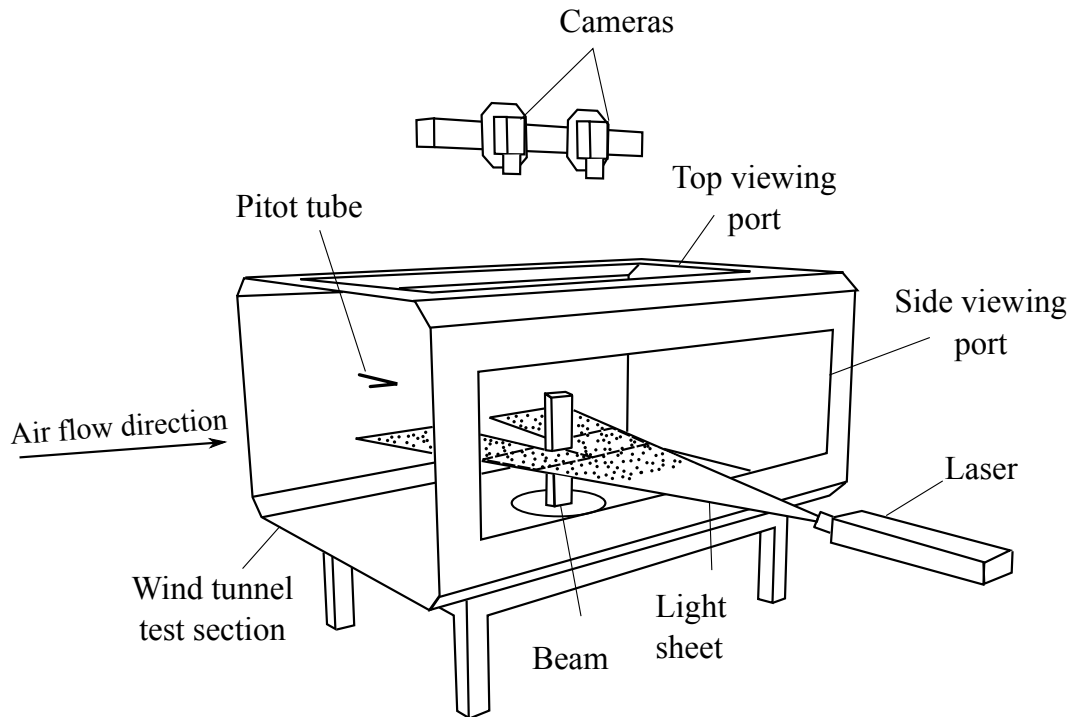
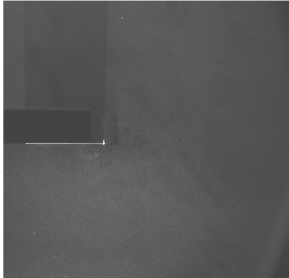

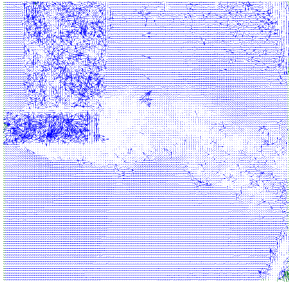
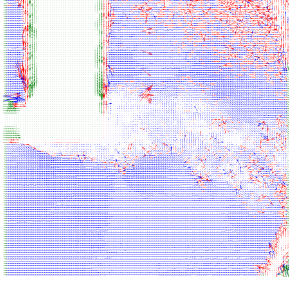
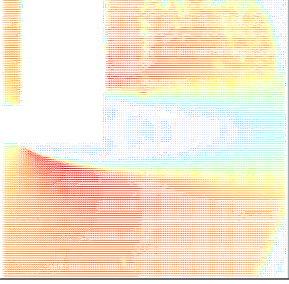


Figure 4.18: Wind tunnel set-up for PIV measurements

LASER, a synchroniser box, data acquisition cards and Dynamic Studio version 3.41.38 operating software. The cameras were positioned so that one camera focusses on the upstream edge and side-wall region of the beam and the other one on the downstream edge and wake region. The measurements were done with a dimensionless time between pulses of  $30 < dt < 50 \mu s$ . 150 photo pairs were used to create the time-averaged results.

Even with very good calibration incorrect vectors will always appear in the data where: firstly, particles moved through the plane instead of along the plane of measurement, secondly, where the laser light sheet is weak, thirdly, where cameras are out of focus, fourthly, where overexposure occurs and, lastly, where stationary components or reflections are visible. Limited post-processing filters were applied with the main objective to delete inaccurate data without replacing it with new interpolated data. These filters include masking of shadow areas, peak height validation (using correlation peak filter ratios set to 1.2), moving average validation, and time-averaging (also called vector statistics). The data processing steps are shown in table 4.5. The data used in table 4.5 is specifically selected from a case with bad data to demonstrate the post processing steps.

Table 4.5: PIV post-processing (top view, downstream camera)

Image	Description
	<b>Raw image:</b> The raw image shows the beam, the laser shadow, some overexposure around the beam edges and the seeding particles in the flow. Overexposure should be avoided since it reduces the amount of data near surfaces and may damage the cameras. However, larger apertures are necessary to detect more particles in the darker areas.
	<b>Masking:</b> Masking is used to black out areas not usable in the post processing. This will typically be areas occupied by an object, where there is overexposure or too little particles visible. Image masking is preferred over vector masking since it eliminates bad data before any vectors are calculated.
	<b>Adaptive correlation:</b> Velocity vectors are created through adaptive correlation (shown without the image masking). In this study 64 x 64 correlation areas were mostly used since these were found to provide the best trade-off between resolution and accuracy. The highest intensity of the laser and also the best focus is positioned around the beam downwind face.
	<b>Mean and peak validation:</b> Post-processing filters are used to only remove incorrect vectors and not to modify vectors. A moving average validation with a 3 x 3 averaging area and peak height ratio of 1.2 was used. The deleted vectors are shown in red.
	<b>Vector statistics:</b> Lastly, the software calculates the time-average of 150 images using the vector statistics filter. This time-averaged data is then used for validation and other purposes.

### 4.8.3 Strain measurement set-up

Strain gauge measurements were conducted to give an indication of the vibration as well as the strain in the beam. Since the beam is a hollow tube a 1/4 bridge set-up was used with a total of 8 strain gauges for each beam orientation. These were positioned at the base of the beams with 2 gauges placed on each of the beam faces as shown in figures 4.19 and 4.20. The strain gauge specifications are provided in section A.3.

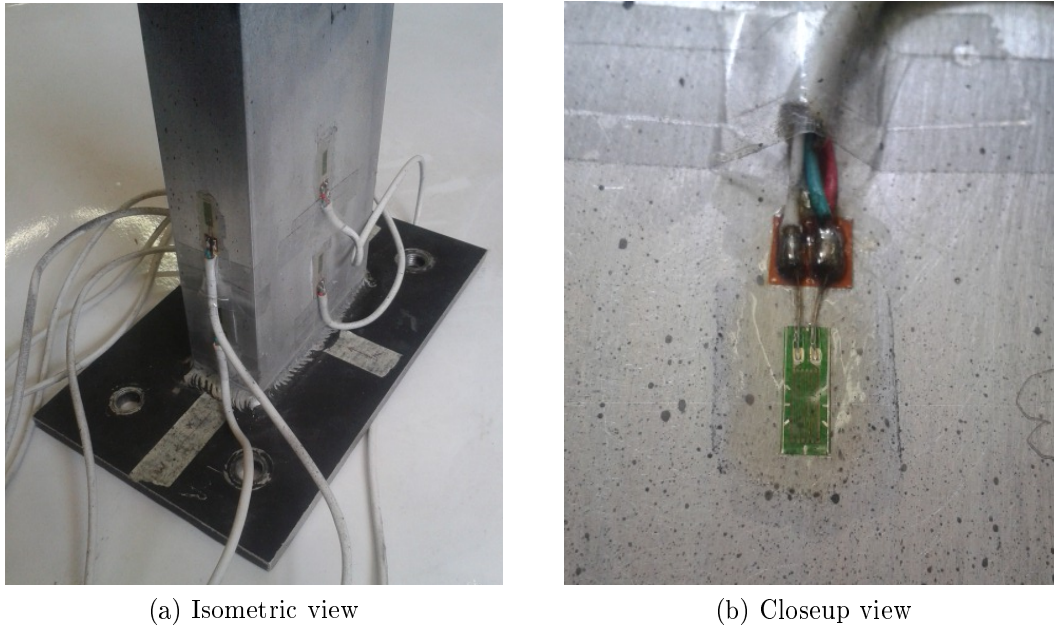


Figure 4.19: Strain gauge photos of the parallel beam

For temperature compensation the following considerations were taken into account:

- Aluminium strain gauges were used to have the same thermal expansion as the beam material.
- Measurements were conducted over a relatively short period of time where the temperature stays constant. The maximum temperature change measured over a test was less than 1 °C.
- Strain gauges were located in areas of the beam where temperature effects have little effect.

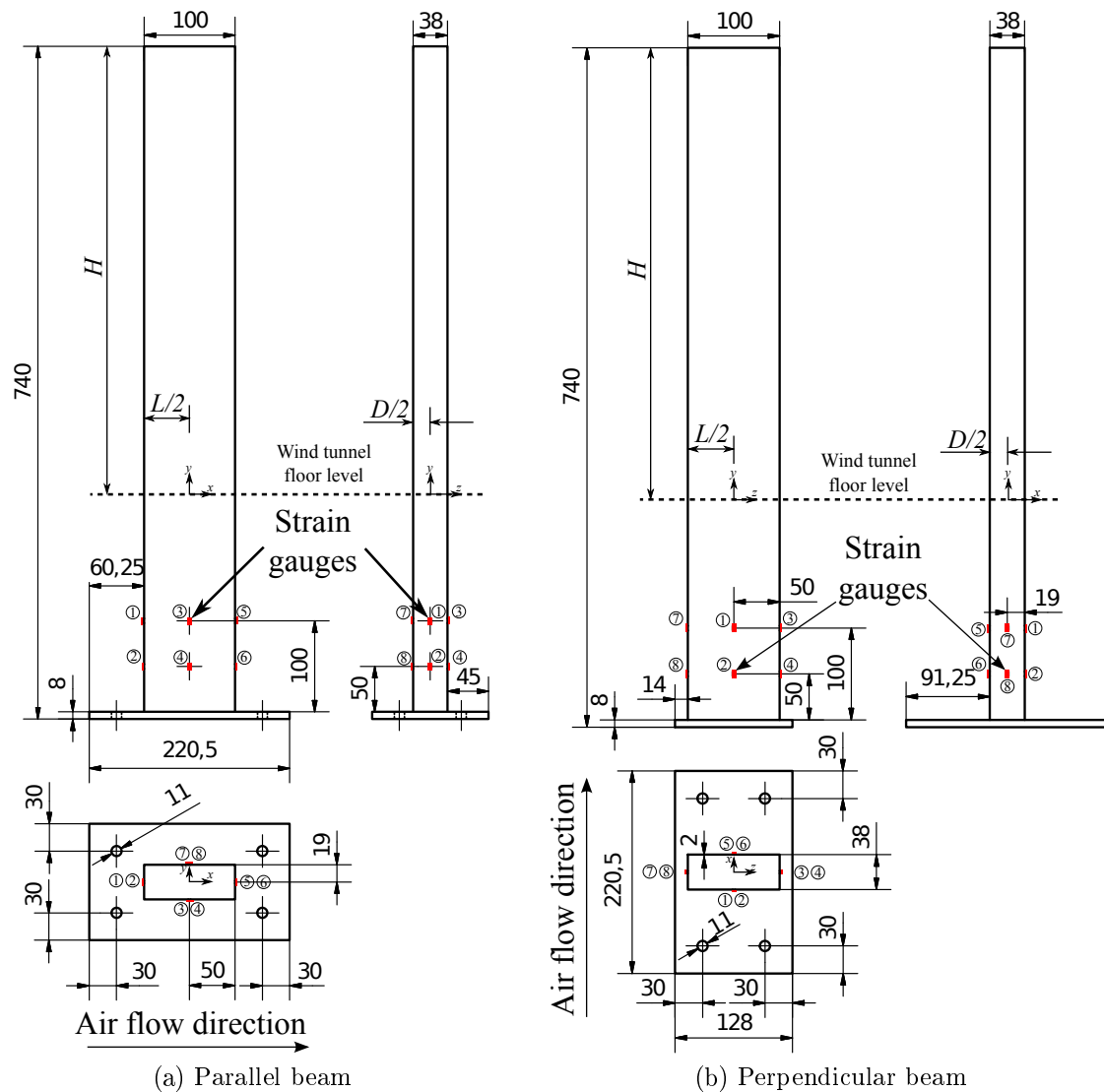


Figure 4.20: Strain gauge measurement locations (units are mm)

- Data analysis and post-processing exclude the initial transient in results which may be affected by small temperature changes during start-up of tests.

Measurements were taken for approximately 5 minute intervals sampling at 600 Hz. This sampling frequency is more than 10 times the expected vortex shedding frequency (approximately 40 Hz at 30 m/s) ensuring sufficient resolution for measuring air flow loading.

#### 4.8.4 Vibration measurement set-up

Vibration measurements were carried out to determine a) the natural frequencies of the beams through modal tests and b) the frequency response of the mounted beams when subjected to wind loading. PCB ICP 333B32 accelerometers were used for the vibration measurements and modal analysis. These accelerometers can only measure in one direction so special care was taken to position them in places where maximum displacement will occur as well as in the correct orientation.

The accelerometers are 10.2 mm cubes weighing 4 g each. These masses were taken into account in the finite element model for simulations as point masses. Accelerometers were placed on the outer surface of the beam for the modal analysis and positioned on two of the faces as shown in figure 4.21. For the wind loading measurements only two accelerometers were used. These were placed on the inside of the beam, at the top, off centre and on two of the faces with the intention of capturing the first three natural frequencies. During the wind loading cases accelerometers were also placed on the channel to measure vertical movement and on the sub-structure to confirm the stiffness.

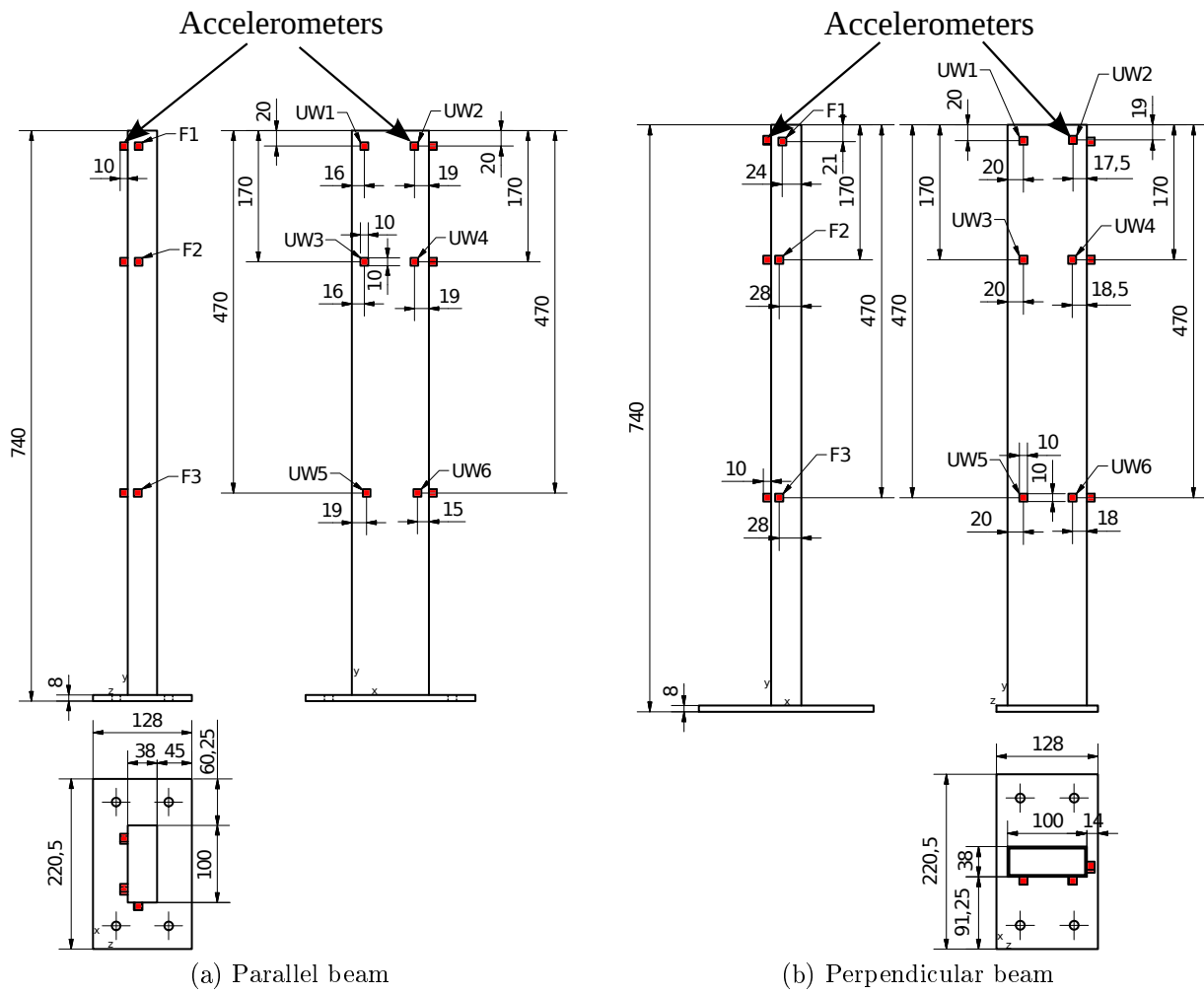


Figure 4.21: Modal tests accelerometer locations

# Chapter 5

## Sensitivity Studies

In this chapter the various modelling sensitivity studies are discussed. These studies were done to determine the effects of various parameters on the results, to test for grid-independence and to provide a degree of confidence in the results. Not all sensitivity studies and results are presented here, only the ones that answered the most important questions. The majority of this chapter is focussed on the parallel beam,  $U = 30$  m/s but similar procedures were followed for the other cases as well.

### 5.1 Convergence Considerations

In computational fluid dynamics (CFD) convergence is important because it means that the final simulation results represent the solution of the underlying discretized partial differential equations given the current mesh and boundary conditions. The solution of underlying differential equations emerges through the systematic process of sequentially refining the mesh until mesh independence achieved. If convergence is not reached it is impossible to make a decision on the modelling accuracy since the solver has not reached the final solution yet.

The convergence is assessed in various ways. One way is to consider the residuals of a solution which represents the changes in variables between iterations or time steps. In OpenFOAM using the PISO solver there are residuals for internal iterations within a time step and residuals between time steps. Within each time step the internal iterations continue until the residuals reach values of less than  $1 \times 10^{-5}$ . The residuals between time steps can be extracted



from the log file and investigated as shown in figure 5.1. It is desirable to have the residuals reduce over time to as small as possible which would mean that the variable values between time steps become more equal. Furthermore, it is also expected that at convergence the residuals will reach an equilibrium.

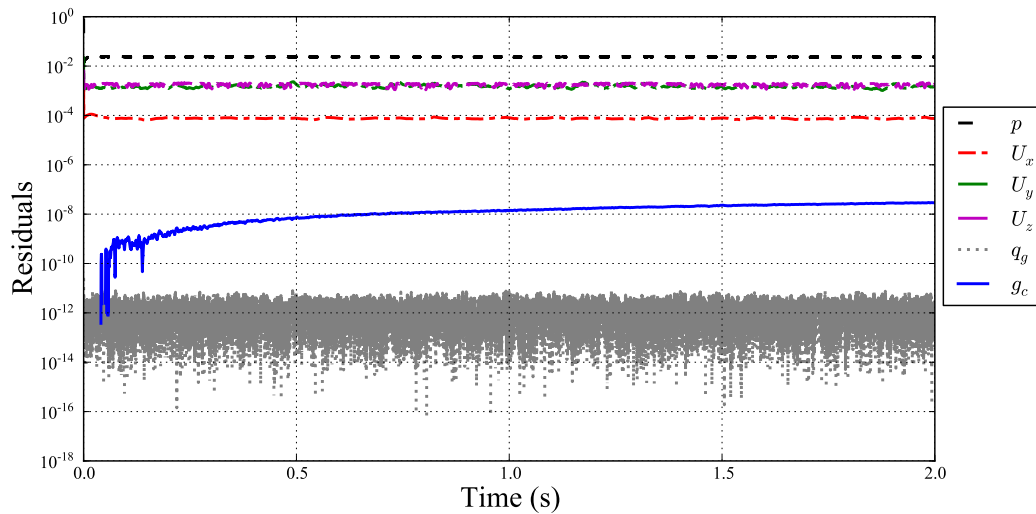


Figure 5.1: Time step residuals for the parallel beam and  $U = 30$  m/s

Looking at the residuals it is only possible to determine if mathematical convergence has occurred at the point where the residuals are determined. This seems to be the case in figure 5.1. Additionally, it is also important to monitor the values of relevant global flow variables to see if convergence has been reached. In this study various variables were monitored over time. In figure 5.2 the lift coefficient for the parallel beam at mid height can be seen. The lift shows oscillations due to the time-dependent pressure loading on the beam but the mean value stays constant. Furthermore, the maximum lift remains relatively constant over time indicating that an equilibrium point has been reached.

## 5.2 Fluid Domain Boundary Distance Effects

Boundary distance sensitivity simulations were carried out to find a mesh set-up that is computationally efficient but also where the flow in the immediate vicinity of the beam is not incorrectly affected by the boundaries. The fluid computational domain, representing the wind tunnel test section, is bounded

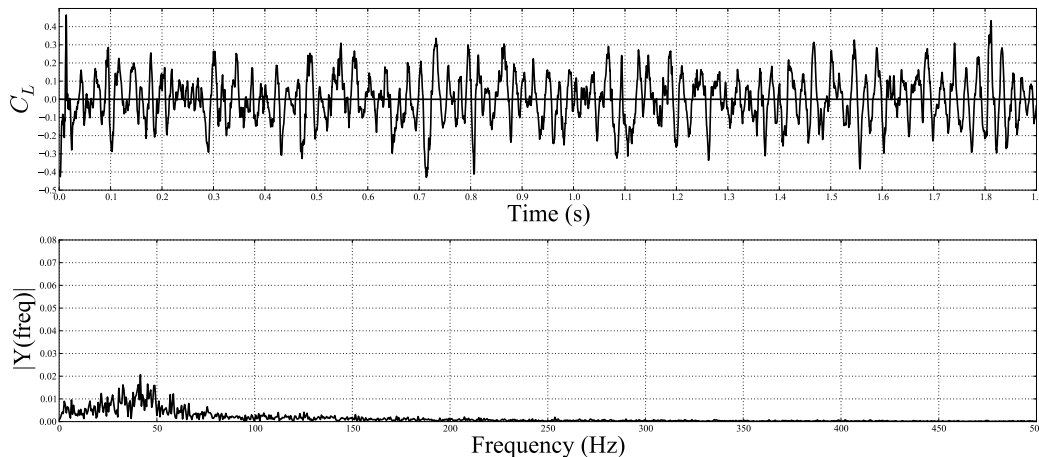


Figure 5.2: Lift coefficient over time at height  $y = H/2$

by the wind tunnel top, bottom and side-walls and, therefore, these were not changed in the sensitivity study since their effects are required. The upstream and downstream parts of the computational domain, on the other hand, have an influence on the stability and accuracy of the simulations and, therefore, these dimensions were changed in the boundary sensitivity study. The upstream part of the computational domain was set at three different distances from the beam namely  $H/2$ ,  $H$  and  $2H$ . The length of the downstream part of the computational domain, accommodating the complex flow in the wake, needed to be longer and was set as  $H$ ,  $2H$  and  $4H$  for the different meshes.

The effects of the inlet and outlet distances were investigated simultaneously. This means that only 3 meshes were constructed for the boundary sensitivity study by increasing the distances of the in- and outlet boundaries from the beam. These meshes is referred to as the short, medium and long meshes. Although the boundary sensitivity study does not highlight the effect of individual boundary movements on the flow, it serves the purpose of identifying a mesh set-up where the resulting flow is independent of the boundary distances which is deemed sufficient considering the time and resources it takes to complete one simulation.

To see if the flow around the beam was affected by the boundary, the pressure along the cross-section half perimeter of the beam at  $y = H/2$  for the short and medium meshes were compared with the long mesh. Only the maximum difference in the time-averaged pressure was considered resulting in an error =  $|(C_{pi} - C_{pL})/C_{pL})|_{max}$  where  $C_{pi}$  is the pressure coefficient ( $Cp =$

$(p - P_\infty)/(\frac{1}{2}\rho_\infty U_\infty^2)$  on the mesh under investigation and  $C_{pL}$  is the pressure coefficient on the long mesh for the same point on the beam. The investigation showed that the maximum difference in the pressure was 1.25% for the short mesh and a negligible maximum difference of 0.08 % for the medium mesh. Even though the short mesh showed insignificant changes, it was decided to continue the investigations using the medium mesh set-up.

### 5.3 Fluid Mesh Refinement Sensitivity

A grid sensitivity study was done which included comparing results from meshes of various levels of refinement. The mesh details are shown in table 5.1. The mesh study was limited by the computational resources available. This is because of the exponential growth in mesh size due to grid refinement (see table 5.1). For example, the last refinement increased the mesh size to more than 14 million cells, even with only local refinement, making it impossible to complete this simulation and analysis with sufficient statistical data.

Table 5.1: Mesh sensitivity study refinement levels and mesh sizes

Name	Refinement levels	Wall normal spacing	Cells
Rough	4	$D/8$	1 222 242
Medium	5	$D/16$	1 695 330
Fine	6	$D/32$	3 490 444
Finest	7	$D/64$	14 585 206

The mesh sensitivity results are shown in figure 5.3 using the simulated and measured pressure data along the half perimeter of the beam cross-section at various heights. All the meshes predict the upstream stagnation and downstream recirculation pressures accurately. On the side-wall the fine mesh is accurate for the bottom and middle positions but it still under-predicts the suction pressure on the side-wall at the top of the beam. The results show that the numerical model is sensitive to mesh refinement. It also shows that the finest mesh produced worse results around the base of the beam, similar results around the mid-height and more accurate results around the tip. However, the mesh refinement from the fine to finest meshes does not improve the

accuracy enough to justify the substantial additional computational requirements. The reduced accuracy of the finest mesh at the base is attributed to local refinement changes incorporated to limit excessive mesh size. The fine mesh is used for further investigations.

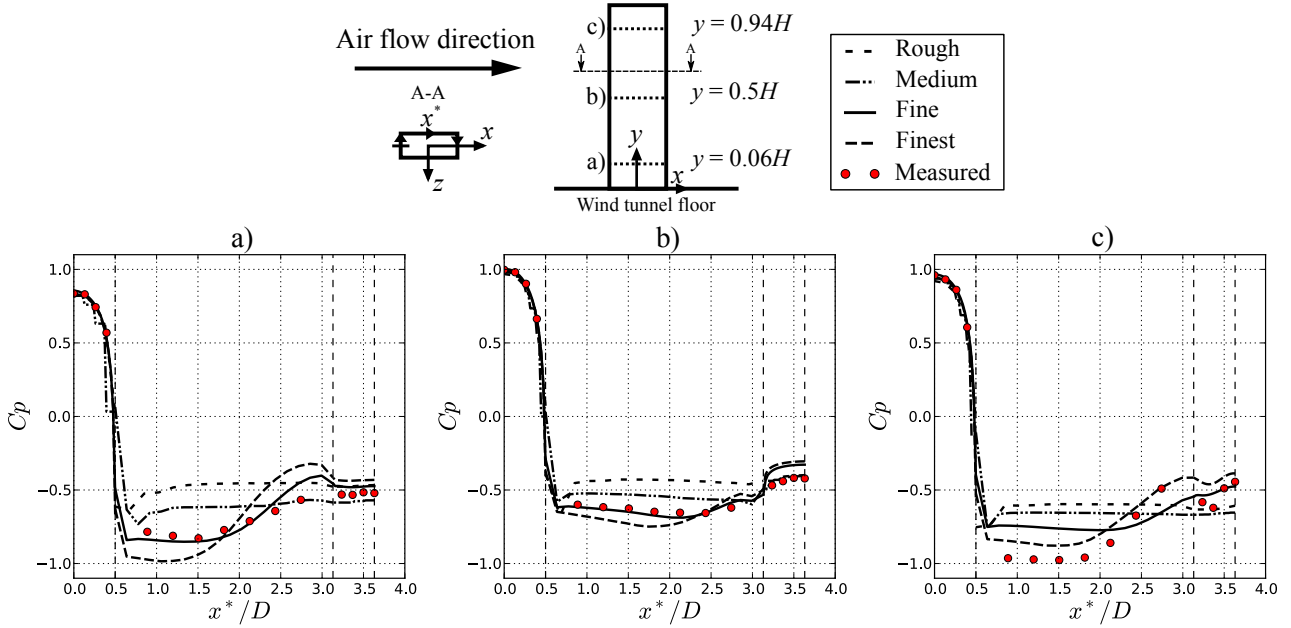


Figure 5.3: Grid sensitivity comparison for the parallel beam with  $U = 30$  m/s using the time-averaged pressure on the beam surface ( $x^*$  is the distance along the half perimeter of the beam cross-section)

To investigate the effect of mesh refinement on the vortex structures the second invariant of the velocity gradient tensor,  $Q$ , defined by equation 5.3.1 (Hunt *et al.*, 1988), is used. The iso-contours of  $Q$  for various mesh refinements are shown in figure 5.4. The most prominent difference between the results is the reduction in size of the attached overarching vortex due to increasing grid densities. For the finer meshes vortices are generally smaller, higher in number and are shed closer to the upstream edge.

$$Q = -1/2(\partial U_i/\partial x_j)(\partial U_j/\partial x_i) = -1/2(S_{ij}S_{ij} - \Omega_{ij}\Omega_{ij}) \quad (5.3.1)$$

Initially the near beam mesh refinement zones were rectangular shaped as shown in figure 5.5 a. However, during the mesh sensitivity analysis it was difficult to accurately reproduce the low pressures measured on the beam side

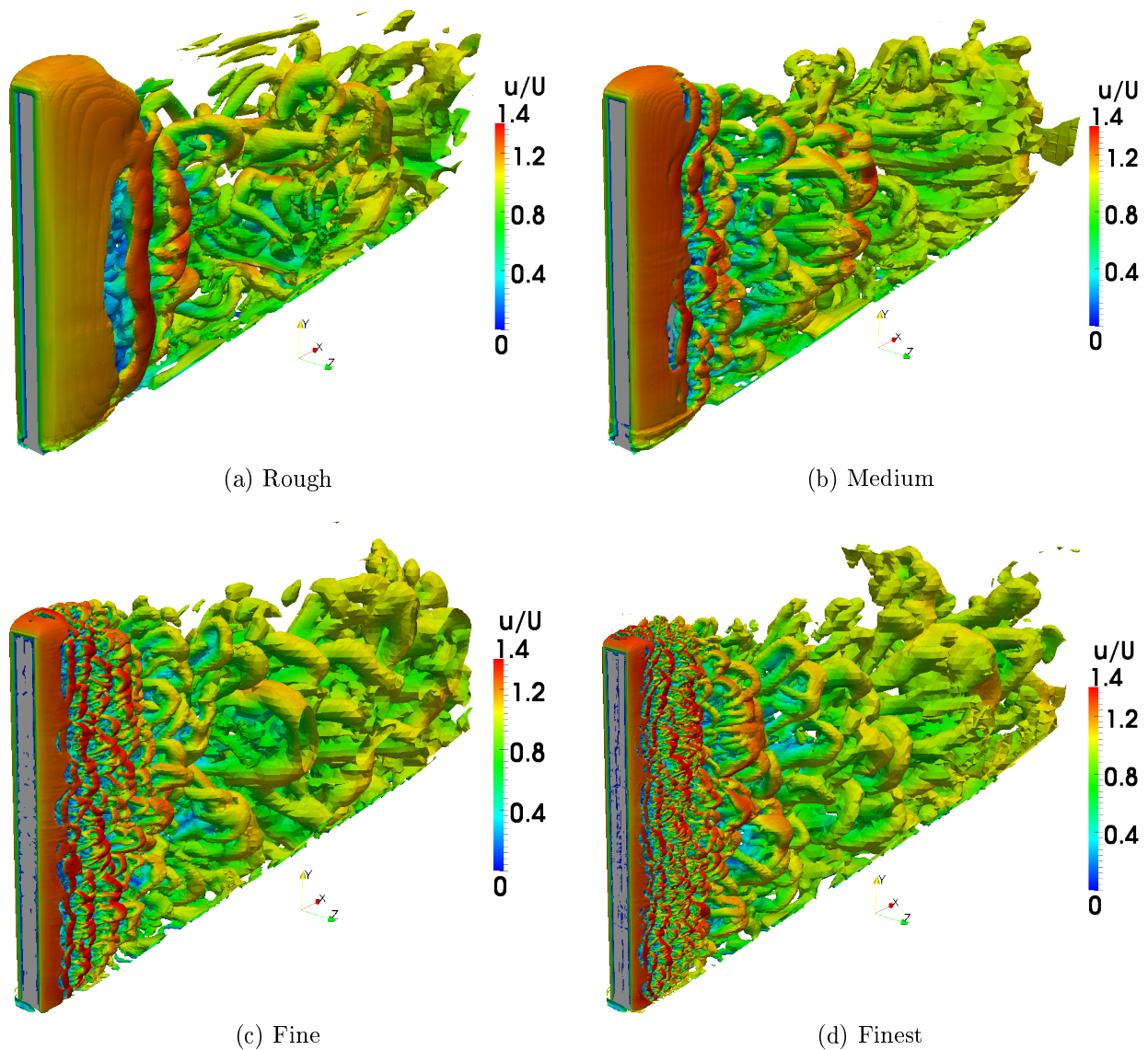


Figure 5.4: Effect of mesh refinement on vortex structures for  $Q = 1.5 \times 10^{-5}$  (see table 5.1 for mesh details)

wall without increasing the mesh size beyond the computational capabilities available using this zoning strategy. In order to address this limitation without increasing the entire mesh the first step was to identify the underlying mechanism and then to come up with a more appropriate refinement zone strategy. It was determined that the low pressure on the side walls occur as a result of fluid being dragged away by viscous stresses at the recirculation boundary with the bulk flow. The first attempt was to refine only the mesh in the area of the high velocity gradient between the bulk flow and side wall recirculation

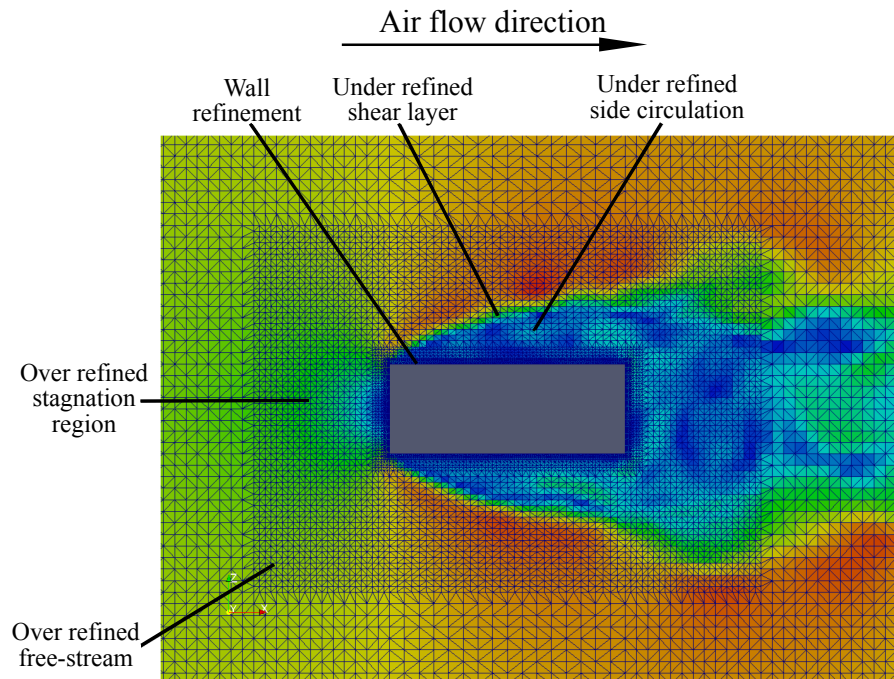
region. Although this improved the results it was determined that it is equally important to have a fine resolution between the velocity gradient and the side wall so the effects of the shear stresses are transported to the wall. The new meshing strategy is shown in figure 5.5 b. Although this image shows no refinement in the wake for the smallest cells the zone was extended into the wake for later simulations but this showed negligible changes in results.

One of the questions raised during this project was if the wall-normal refinement was fine enough. To investigate the sensitivity of the solution on the wall-normal refinement boundary layers were added to one simulation reducing the wall normal spacing from  $D/32$  to  $D/64$  and  $D/442$ . The wall normal refinement is shown in figures 5.6 a and b for the  $D/64$  and  $D/442$  refinement cases. The effect on the wall pressures is shown in figure 5.7. The results show that the solution is not sensitive to changes in the wall-normal mesh refinement. It should be noted that this sensitivity study was done on a slightly different mesh than the final simulations which means that the results will differ slightly from that shown in figure 5.3.

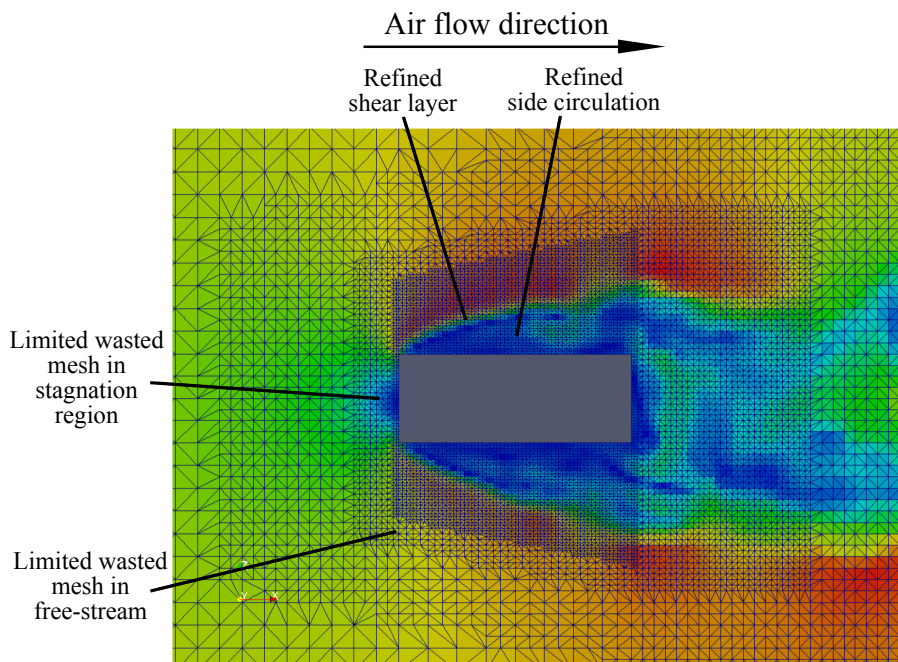
Most of the sensitivity study simulations were conducted prior to the final simulations and, therefore, the results may differ slightly (see figure 5.3 compared to figure 5.7).

## 5.4 Near-wall Treatment Effects

The sensitivity of the results to different wall treatments was also investigated. For this investigation Spalding's "all- $y^+$ " wall function (high-Re approach) was compared to a low-Re approach. When considering the wall treatment two aspects must be taken into account. Firstly, the correct wall boundary values have to be assigned which will differ for various wall treatments. For a low-Re model the values are specifically fixed while for the high-Re model, on the other hand, a wall function is assigned to determine the wall values depending on the first cell location within the boundary layer. Secondly, wall treatments are usually only applicable to a specific range of  $y^+$  values (distance of the first cell centre from the wall). Thirdly, if the mesh is fine enough so that the first grid node falls within the viscous sub-layer or buffer layer the turbulence model must have built in wall damping terms. Models containing the wall damping terms will usually have a "low-Re" addition to the name. The IDDES turbu-



(a) Rectangular refinement



(b) Angled refinement

Figure 5.5: Near beam meshing strategies ( $y = H/2$ )

lence model in OpenFOAM has built in wall damping terms and additionally has the capability to use wall functions of which Spalding's "all- $y^+$ " wall function was chosen for its applicability to a wide range of  $y^+$  values. The results

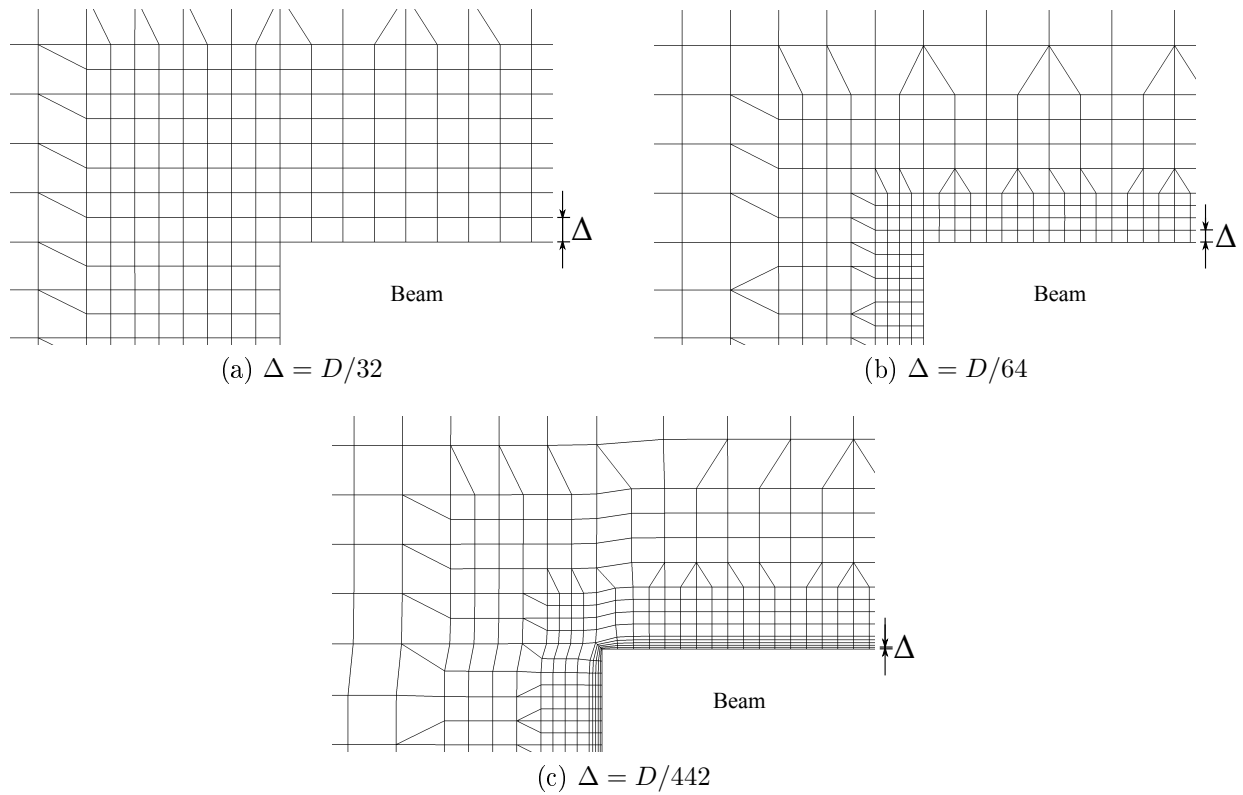


Figure 5.6: Wall-normal refinement sensitivity study meshes ( $z = 0, y = H/2$ )

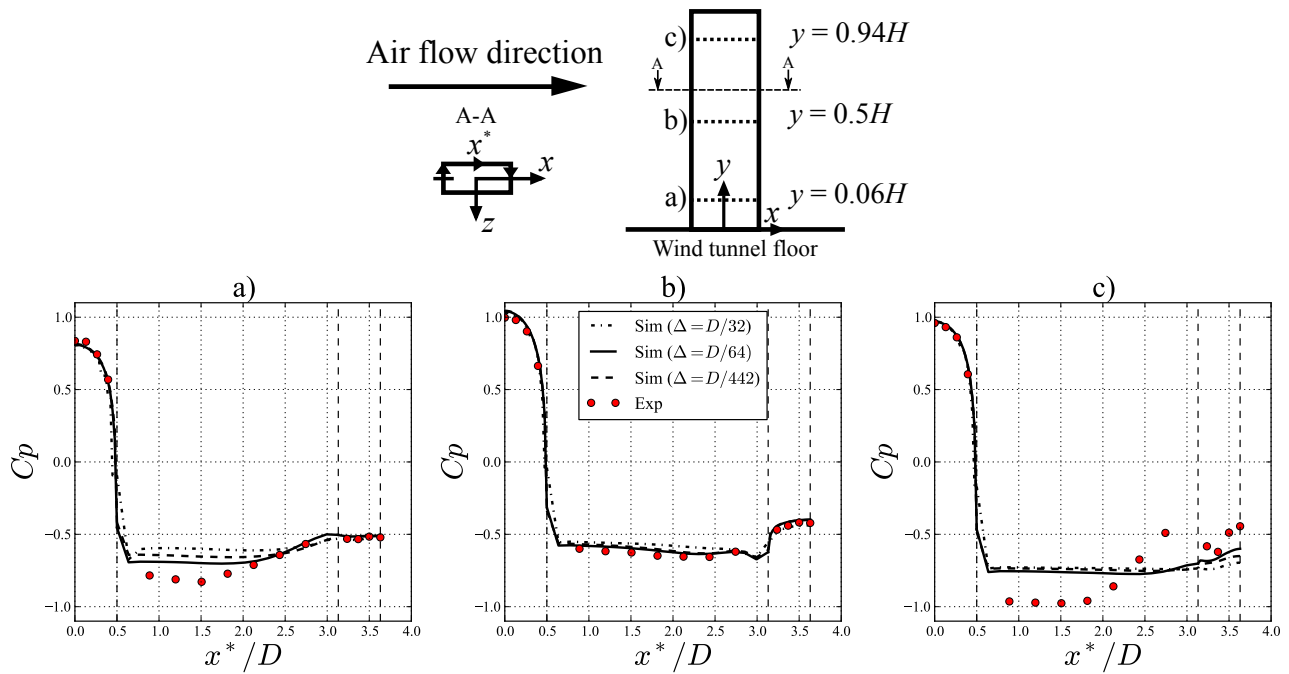


Figure 5.7: Wall-normal refinement pressure results



showed that the high-Re approach provides the same time-averaged pressure on the beam as the low-Re wall treatment but at a lower cost in computational requirements. The high-Re approach is, therefore, considered sufficient in this case.

## 5.5 Boundary Layer Development Investigation

Boundary layer development was also investigated to see if the numerical method produced a horizontally homogeneous velocity profile or if the boundary layer changed as it approached the beam. If the inlet conditions, mesh, near-wall treatment or turbulence modelling is inaccurate the boundary layer will change to reach a new equilibrium different from what the beam experiences in the wind tunnel and so reduce the accuracy of the simulations.

Figure 5.8 shows the velocity profiles measured at various points of the inlet section of the simulation domain. The inlet velocity profile undergoes negligible change until it comes to within  $0.25H$  distance of the beam. It can, therefore, be considered horizontally homogeneous. The difference in the profile at  $x = 0.75H$  is attributed to the high pressure of the stagnation region at the beam upstream face which slows the oncoming flow. Since the horizontally homogeneous boundary layer has been achieved it supports the boundary distance placement, near-wall treatment, turbulence modelling, and mesh strategy.

## 5.6 Load Confirmation

For the fluid structure interaction (FSI) simulations it is important to confirm that the actual load experienced by the beam in the wind tunnel is reproduced by the CFD and applied correctly to the structural model. In figure 5.9 the fully loaded beam is displayed with the nodal forces visible. This was inspected to make sure the applied loads are correct in direction and magnitude. Firstly, it is possible to see that the correct area of the structure is loaded. Secondly, in a closer inspection it was confirmed that the applied forces are in the correct direction and magnitude. The upstream face of the beam is subjected to forces in the flow direction corresponding to the stagnation pressure while all other

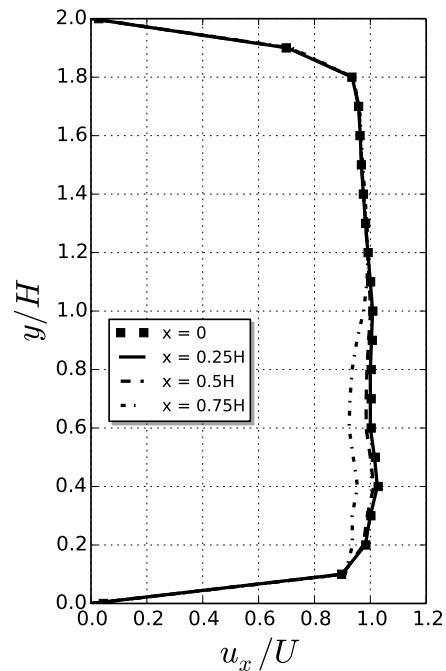


Figure 5.8: Upstream domain velocity profile comparisons (Joubert *et al.*, 2015)

walls are subjected to outward forces corresponding to low pressure on the side and downstream walls.

One way to confirm that the actual load is applied to the structural model is to compare the drag. This was done as shown in table 5.2. From the pressure measurements at  $y = 0.06H$ ,  $0.5H$  and  $0.94H$  the drag is determined to be 12.9 N (equivalent to 1.3 kg in the flow direction). In comparison the CFD simulations produces a 12.7 N drag force and the coupling method produces a 12.8 N drag force on the structural mesh. This means that the CFD is accurately reproducing the overall loading condition and that the coupling method is working correctly. The slight difference between the drag produced by the CFD simulations and the load applied to the structural mesh is attributed to coupling method simplifications which could be reduced through mesh refinement.

The stagnation drag is provided as a reference. It is calculated considering only the stagnation pressure on the upstream surface. If only the stagnation pressure is considered, the drag force is underestimated by 20 %.

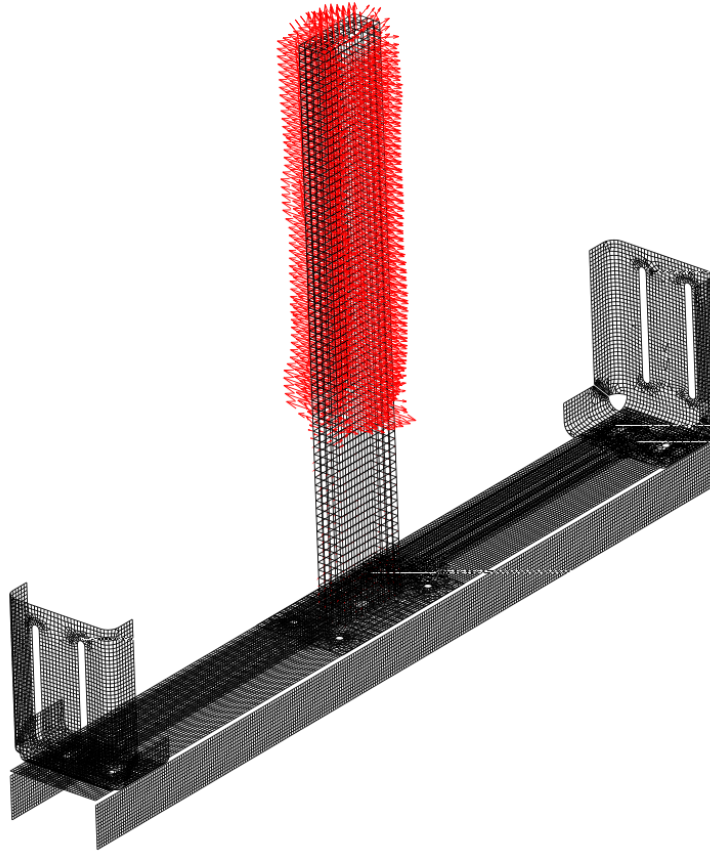


Figure 5.9: Forces at nodes at fully loaded condition

Table 5.2: Comparison of drag measured, reproduced by CFD and applied to the structure for the parallel beam and  $U = 30$  m/s

Source	Description	Drag [N]	Deviation
Measured	Measured pressure load	12.9	n/a
OpenFOAM	Simulated flow-induced load	12.7	1.6 %
Code-Aster	Applied structural load	12.8	0.8 %
Stagnation	Upstream face stagnation pressure only	10.3	20.2 %

## 5.7 Structural Model Parameters Sensitivity

The sensitivity of the solution to changes in various parameters of the structural model was also investigated (see appendix B). This was done by varying parameters such as material properties, point masses and shell plate offsets and considering the changes in the first three natural frequencies (NF). From this investigation it was found that the model is not sensitive to these changes.

The greatest impact on the NF's occurs with changes in the geometry lengths and boundary conditions.

## 5.8 Structural Mesh Resolution Effects

The structural mesh sensitivity was investigated for the parallel beam set-up and inlet flow velocity of  $U = 30$  m/s. The time-averaged distributed load (as produced by the CFD results) is applied to the beam and the strain and displacements are then compared for two different mesh resolutions. The strain is sampled at gauge 2 which is located on the upstream, lower part of the parallel beam as shown in figure 4.20 and the displacement was measured at the top of the beam. The structural mesh refinement comparison is shown in table 5.3. The first three lines show the mesh elements and resulting number of equations for the two refinements. The last two lines show the changes in strain and displacement due to the changes in structural mesh resolution.

Table 5.3: Structure mesh refinement sensitivity

Parameters	Medium mesh	Fine mesh	Difference
Quad4	$2.5 \times 10^4$	$3.23 \times 10^4$	29.2 %
Tria3	676	712	5.3 %
Equations	$1.74 \times 10^5$	$2.15 \times 10^5$	23.6 %
Strain $\epsilon_y$ [ $\mu\text{m}/\text{m}$ ]	5.91	5.54	6.7 %
Displacement $dx$ [mm]	$5.61 \times 10^{-2}$	$5.41 \times 10^{-2}$	3.7 %

It can be seen that the structural mesh refinement only produces a 3.7 % change in tip displacement and a 6.7 % change in the base strain. Although there is a change in the results with mesh refinement the error is considered acceptable considering the additional computational requirements that would be needed by the finer mesh for the transient FSI simulations. This is because each new structural node introduced needs a load function definition over time which increases the memory requirements and simulation time. For example, with the transient FSI simulations it was found that for the medium mesh and a time step  $dt = 2 \times 10^{-4}$  the structural simulations run out of memory (16 Gb RAM and 16 Gb Swap) if the total simulated time  $T > 1$  s. This means that with the current hardware the simulation capabilities are  $5 \times 10^3$  time steps for

a mesh size of  $1.74 \times 10^5$  equations. In order to increase the simulation time or complexity it will require either greater computing resources or a compromise between mesh size and simulation length. It should be noted that the medium mesh was also compared to lab measurements to further investigate the validity (see section 5.9).

## 5.9 Point Load Strain Verification

To investigate the accuracy of the structural model further it was decided to set-up a verification case where a known point load is applied to the cantilever beam in the lab and then simulated for comparison. Both beams were tested in the lab for various point loads (see appendix A.3) but only the parallel beam and one loading condition is used in this section for verification purposes. The specific load used for the comparison is 12.7 N which is equal to the drag of the parallel beam with an inlet velocity of  $U = 30$  m/s. The load is applied at the centre of the upstream face of the beam (middle of wind loaded surface) to be representative of the average distributed drag force. Additionally this validation also provided the opportunity to compare results with a well known commercial FEM structural analysis software code Genesis (2015). The set-up is shown in figure 5.10.

The results for this verification study are summarised in table 5.4. The measurements are described in appendix A.3 as part of the strain gauge calibrations. According to figure A.4 the measured strain in the  $y$ -axis for a 12.7 N point load is  $6.02 \pm 0.1$   $\mu\text{m}/\text{m}$ . The Code-Aster structural simulations produce strain values of 5.91  $\mu\text{m}/\text{m}$  with an error of 1.8 % compared to measurements. In this case the results are more accurate than the commercial software which produced a 6.5 % error. The structural model is, therefore, considered acceptable for the purpose of this study.

Table 5.4: Comparison of simulated and measured strain for the parallel beam subjected to a drag equivalent point load

Source	Strain $\epsilon_y$ [ $\mu\text{m}/\text{m}$ ]	Deviation
Measured	6.02	n/a
Code-Aster	5.91	1.8 %
Genesis	5.63	6.5 %

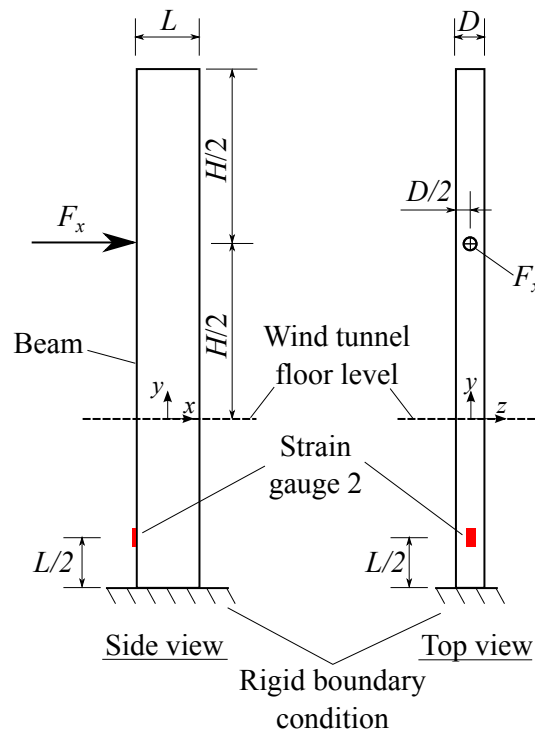


Figure 5.10: Point load strain verification set-up

## 5.10 Modal Analysis and Comparison with Measurements

In the process of configuring the structural simulation model the measured NF were used as reference. The measured values of the first three modes of each of the beams are displayed in figures 5.11 and 5.12. In an iterative process of making small corrections in boundary conditions, connections and mass definitions it was possible to accurately predict the first NF of both beams. To accurately simulate the first NF was the highest priority of this exercise since it will determine the dynamic response of the beam. Also because the aerodynamic loading frequency is expected to be in the range of the first NF. Even so, the model produces reasonable predictions of the 2<sup>nd</sup> and 3<sup>rd</sup> NF's.

In table 5.5 the accuracy of the NF prediction is provided. The results show that both beams accurately predict the first NF as desired. The maximum error for the parallel beam is 8.6 % and the maximum error for the perpendicular beam is 30 % although in both cases these frequencies are far enough from the expected operating range to have negligible effect on the results.

It is also noticed that the measured third NF for the parallel beam (123 Hz)

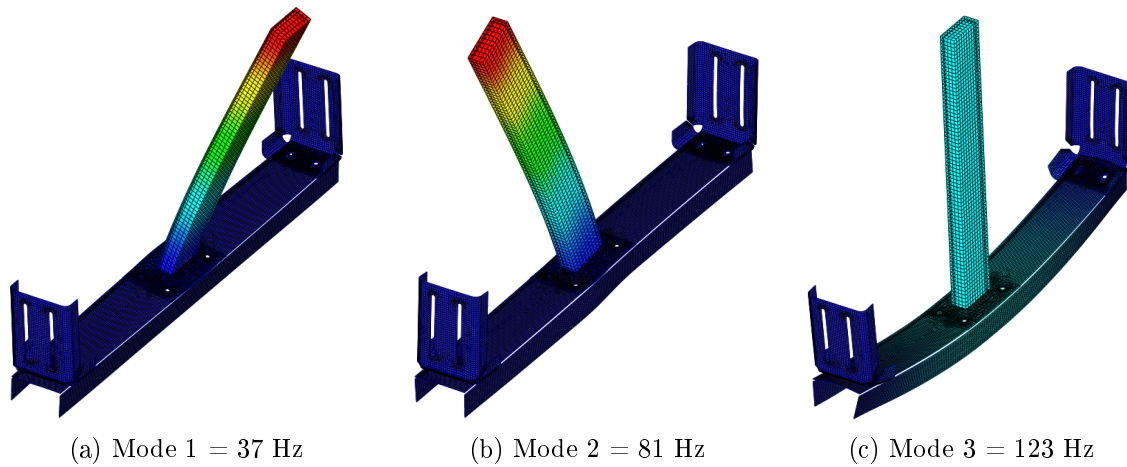


Figure 5.11: First three measured NF's of the parallel beam set-up

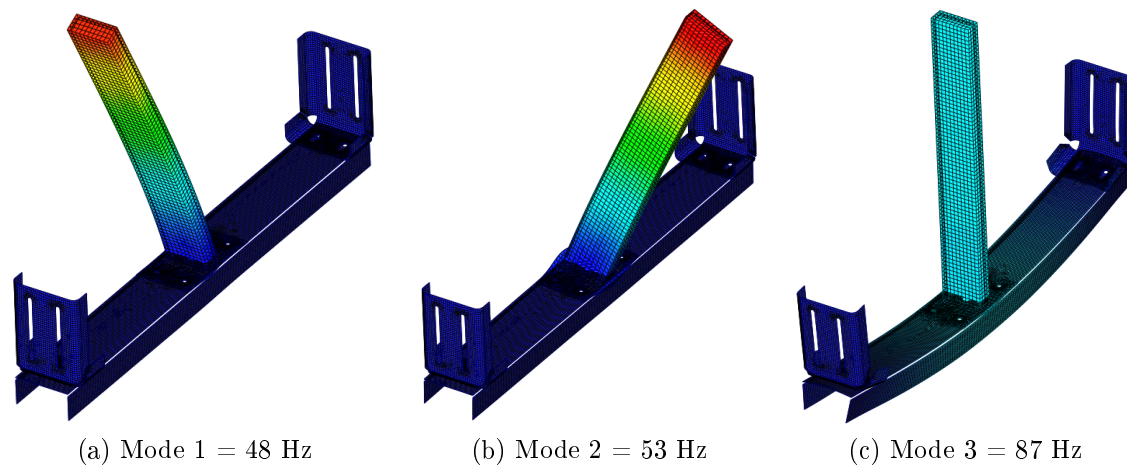


Figure 5.12: First three measured NF's of the perpendicular beam set-up

Table 5.5: Natural frequency prediction accuracy

Beam	Mode	Measured	Simulated	Deviation
Parallel	1	37	37	0 %
	2	81	88	8.6 %
	3	123	116	5.7 %
Perpendicular	1	48	48	0 %
	2	53	53	0 %
	3	87	113	30 %

is higher than that of the perpendicular beam (87 Hz) yet simulations predict almost the same frequency for both beams (116 Hz vs 113 Hz). This is at-

tributed to the linear structural modelling simplification which does not account for the actual non-linearities involved such as contact between the beam and channel. In reality the vertical movement from the third NF is higher for the parallel beam than the perpendicular beam because of the cross-section orientation of the parallel beam and impact of it on the channel preventing downward motion. For the simulations this impact is not accounted for so the parallel beam is allowed to move through the channel which explains why both beam simulations produce similar results.

## 5.11 Ramp Time Sensitivity

As explained in section 4.5 in the structural analysis it is necessary to add a ramp function to smoothly transition the simulation from no load to full load in order to prevent unwanted oscillations. If the ramp function is very short the simulation will experience the loading as a step function and induce unwanted oscillations (similar to an impact). Additionally, if the time step is too big the simulation will see the load as small consecutive steps which could also introduce unwanted oscillations. Since the time-averaged simulation will produce no oscillations from the flow (being constant) it is also possible to use this simulation to see if oscillations are introduced with the ramp function.

For this reason a transient simulation is conducted applying a constant (time-averaged) load with a ramp function of various lengths. The ramp time is varied as shown in figure 5.13 which produces the tip displacements in figure 5.14. For the current flow conditions a ramp time of 0.2 s or more is sufficient for the parallel beam and 0.4 s or more for the perpendicular beam to prevent unwanted oscillations. A time-step of 0.001 s is used in all three cases presented here which also show no oscillations. The data presented is for displacement in the  $z$ -direction since this is the direction of movement for the first NF for the parallel beam. Movement in the  $x$ -direction was also investigated but found negligible.



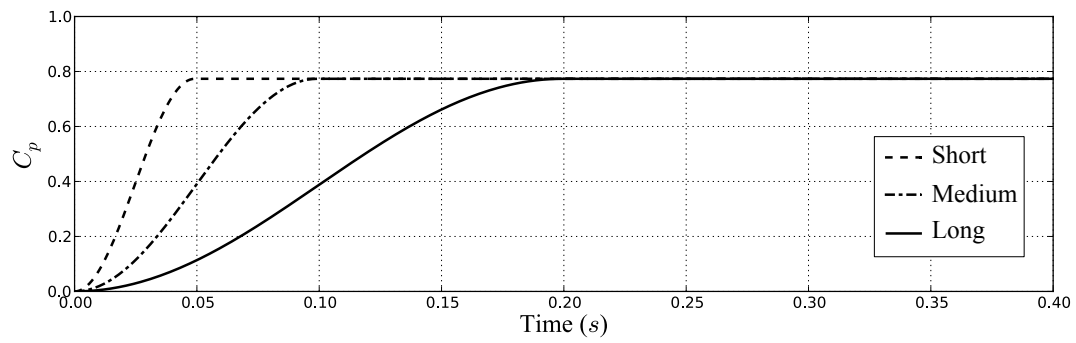


Figure 5.13: Applied loads for different ramp times

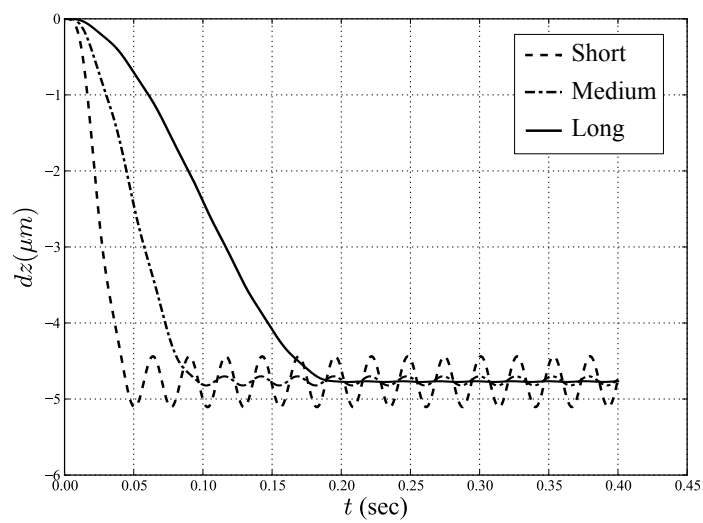


Figure 5.14: Tip displacement response to various ramp times

## Chapter 6

# Turbulence Model Comparisons

In this project one of the questions was: What turbulence model should be used in the fluid simulations for highly separated flows? Through a literature overview (see section 3.5) the improved delayed detached eddy simulation (IDDES) model was selected as the most appropriate model to provide the needed accuracy while limiting computational requirements. Even so it was found necessary to do turbulence model comparison simulations to see just how different the results are and to get a better understanding of the implications of the underlying mathematical modelling simplifications.

For this comparison the measured time-averaged pressure and velocity data are compared with simulation results using the Realizable  $k$ - $\epsilon$ ,  $k$ - $\omega$  SST, Non-linear  $k$ - $\epsilon$  Shih and IDDES turbulence models. All comparisons are done for the parallel beam and  $U = 30$  m/s. The simulations were done using the exact same mesh for all cases. Boundary conditions were also the same apart from slight variations required by different models such as providing the equivalent  $k$ ,  $\epsilon$  or  $\omega$  values at the inlet. All models used a high-Re wall treatment approach by employing wall functions. Furthermore, all cases were done using the same PISO solver implying incompressible unsteady simulation as well as the same interpolation schemes.

Turbulence models have different spacial discretization requirements. This comparative study does not claim to use the perfect mesh for each model but instead provides a simple indication of the different mechanics in the underlying model. Furthermore, in this comparison the IDDES turbulence model has the finest mesh requirements by using LES in the detached eddy regions and RANS on the walls. Therefore, all other models can be applied to this mesh

since it is theoretically more strict than necessary and at a minimum sufficient on the walls.

Considering the comparison of the measured and simulated wall pressure along the half perimeter of the beam cross section in figure 6.1 it can be seen that the IDDES model produces the most accurate results. The IDDES model is especially accurate at  $y = 0.06H$  and  $y = 0.5H$  but fails to produce the low pressures at the top of the beam for  $y = 0.94H$ . All other turbulence models fail to produce the low pressures on the side-wall region with the closest to measurements occurring at  $y = 0.5H$ .

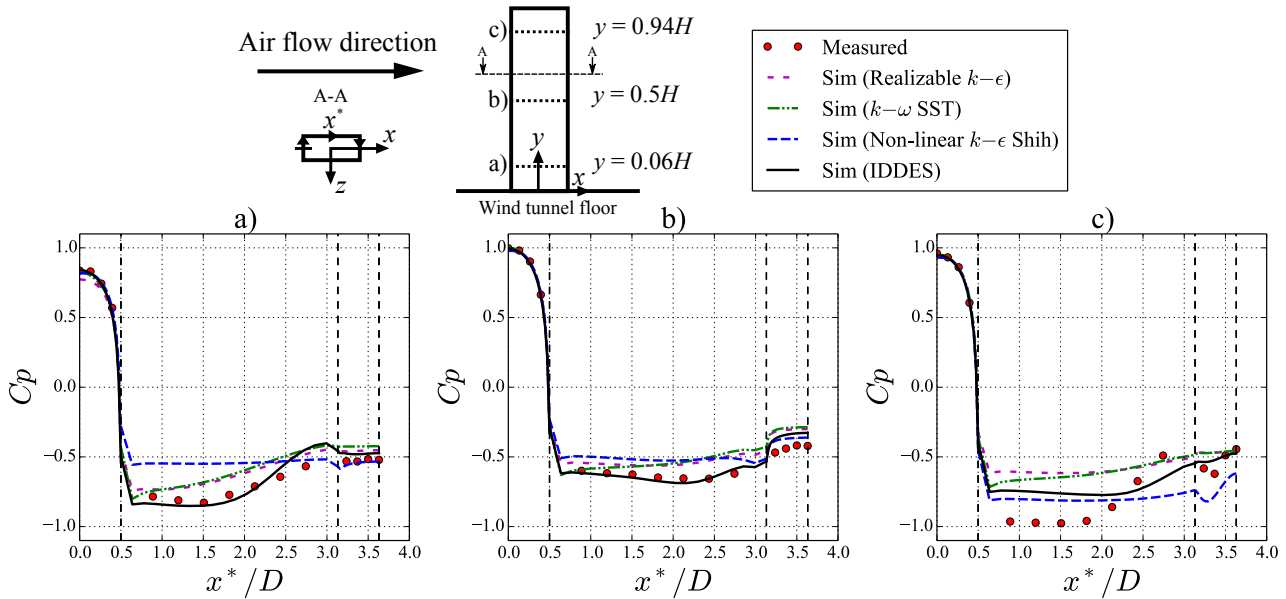


Figure 6.1: Turbulence model comparison of time-averaged pressure along the half perimeter of the beam cross-section at various heights

In figure 6.2 the side-wall velocity profiles of the different turbulence models are compared. All the models produce more or less the same results and can be considered accurate in this region with the most significant errors occurring for the Realizable model at profile  $c$  which is at the top of the beam.

The up- and downstream velocity profiles for the various turbulence models are compared in figure 6.3. It can be seen that all the models perform very well in the stagnation region giving virtually identical results. The stagnation effects are visible  $4D$  upstream of the beam at a height of  $y = 0.5H$  and  $3D$  upstream of the beam at  $y = 0.94H$ . In the downstream wake region, however, the IDDES model produces the most accurate results. This is also evident by

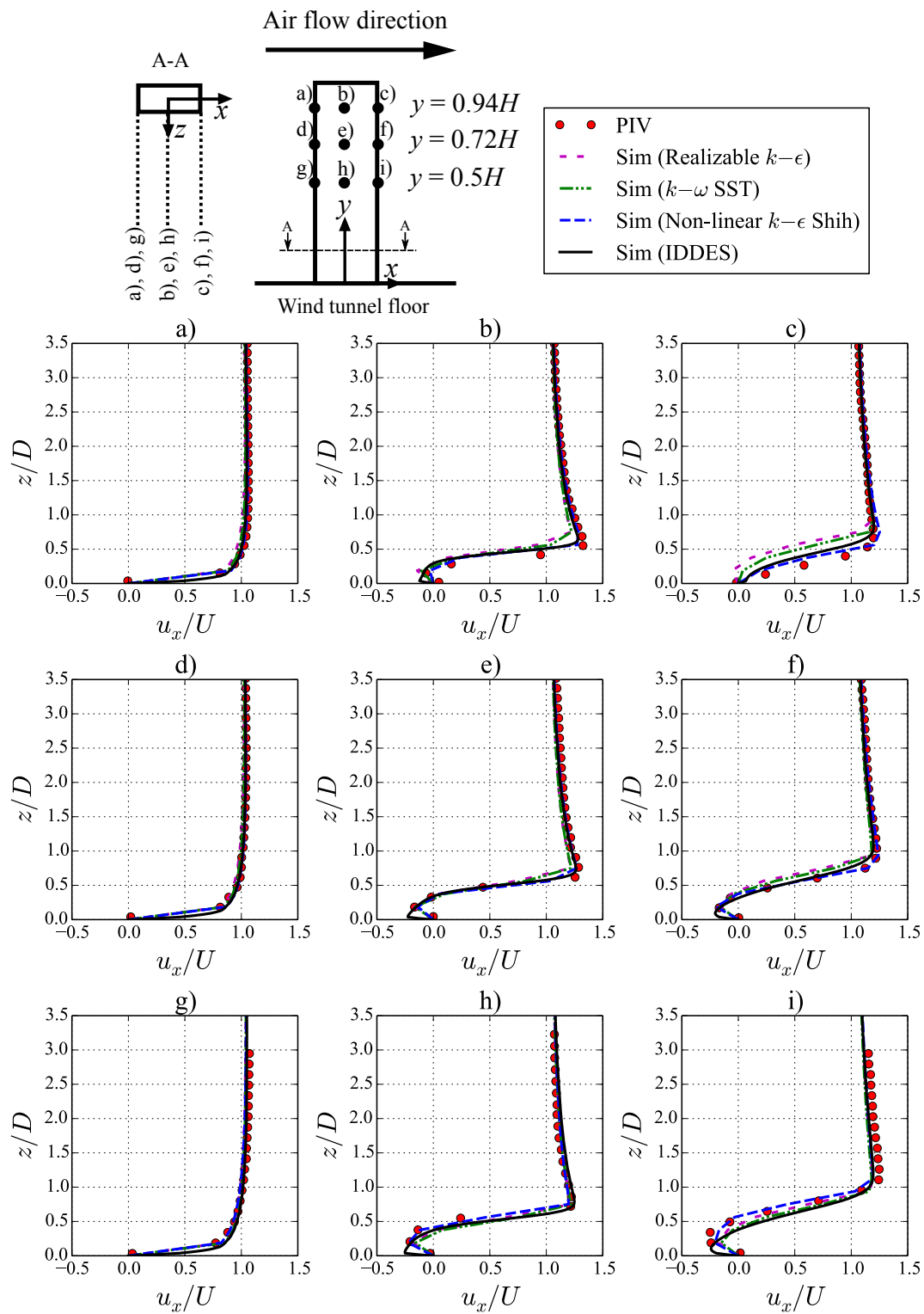


Figure 6.2: Turbulence model comparison of time-averaged velocity profiles of the side-wall recirculation zone

comparing the produced recirculation lengths for the different models as shown in table 6.1. Based on the recirculation lengths the IDDES model performs the best and the Realizable  $k-\epsilon$  model the worst.

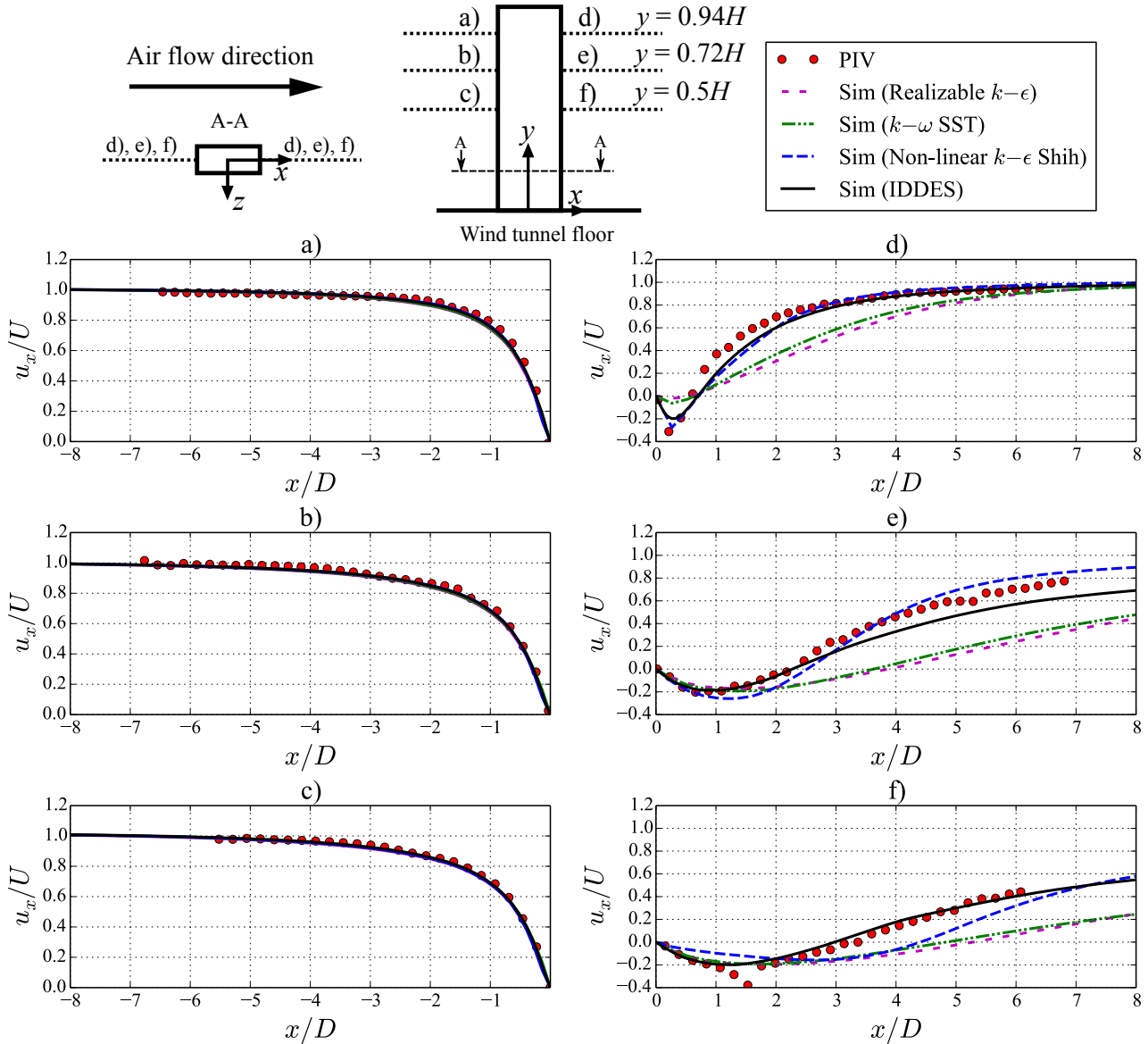


Figure 6.3: Turbulence model comparison of time-averaged velocity profiles of the wake region

It is also of interest to check the accuracy at a greater distance from the beam as shown in figure 6.4. Velocity profiles at a height of  $y = 0.5H$  are compared with PIV measurement data. The profiles start from the mid-width of the beam ( $z = 0$ ) and extend outward perpendicular to the flow to  $z = 5D$ .

Table 6.1: Comparison of performance for various turbulence models (\* = from literature)

Source	Recirculation length			St	Duration [days]
	$y = 0.5H$	$y = 0.72H$	$y = 0.94H$		
Measured	$3.2D$	$2.27D$	$0.6D$	$0.06^*$	-
Realizable $k-\epsilon$	$5.3D$	$3.87D$	$0.72D$	$0.06$	34.8
$k-\omega$ SST	$4.9D$	$3.63D$	$0.72D$	$0.053$	31
Non-linear $k-\epsilon$ Shih	$4.4D$	$2.53D$	$0.72D$	$0.063$	60
IDDES	$3D$	$2.27D$	$0.72D$	$0.053$	32.6

The results show very good agreement for all profiles further confirming the accuracy of the numerical model. The recirculation zone is close to zero at  $3D$  distance away from the beam but the wake extends beyond  $6D$  downstream of the beam. At the  $6D$  downstream profile, the accuracy of the PIV results deteriorate since this was on the edge of the laser field of capture. The wake is seen to diverge slightly outward as you move downstream from the beam due to viscous stresses that smooth out the velocity gradients. Another noticeable feature is the slight flow acceleration occurring between  $z = 1.5D$  and  $2.5D$  as a combined result of the flow obstruction and the recirculation zone.

In figure 6.5 the vortex formations in the wake of the beam are compared for the various turbulence models. Even through the meshes used are exactly the same for all cases the results appear as if the Realizable  $k-\epsilon$  and  $k-\omega$  SST models have less refinement than the Non-linear  $k-\epsilon$  Shih and IDDES models. The Realizable  $k-\epsilon$  and  $k-\omega$  SST models show smooth vortex formations extending the entire height of the beam. In the wake the Realizable  $k-\epsilon$  and  $k-\omega$  SST produce vortices with large distances in-between indicating smaller shedding frequency. On the other hand, the Non-linear  $k-\epsilon$  Shih and IDDES models show much smaller vortices which extend most of the beam height and with higher shedding frequencies. The IDDES model produced the most chaotic turbulent structures in the side separation zone and wake with very small vortices, highly three-dimensional in nature and a high vortex shedding frequencies.

From this comparison it is clear that the turbulence model selection has a significant effect on the time-averaged velocity profiles and time-dependent vortex structures of the wake region. Even so, all models seem to produce more or less the same time-averaged velocity profiles in the upstream and

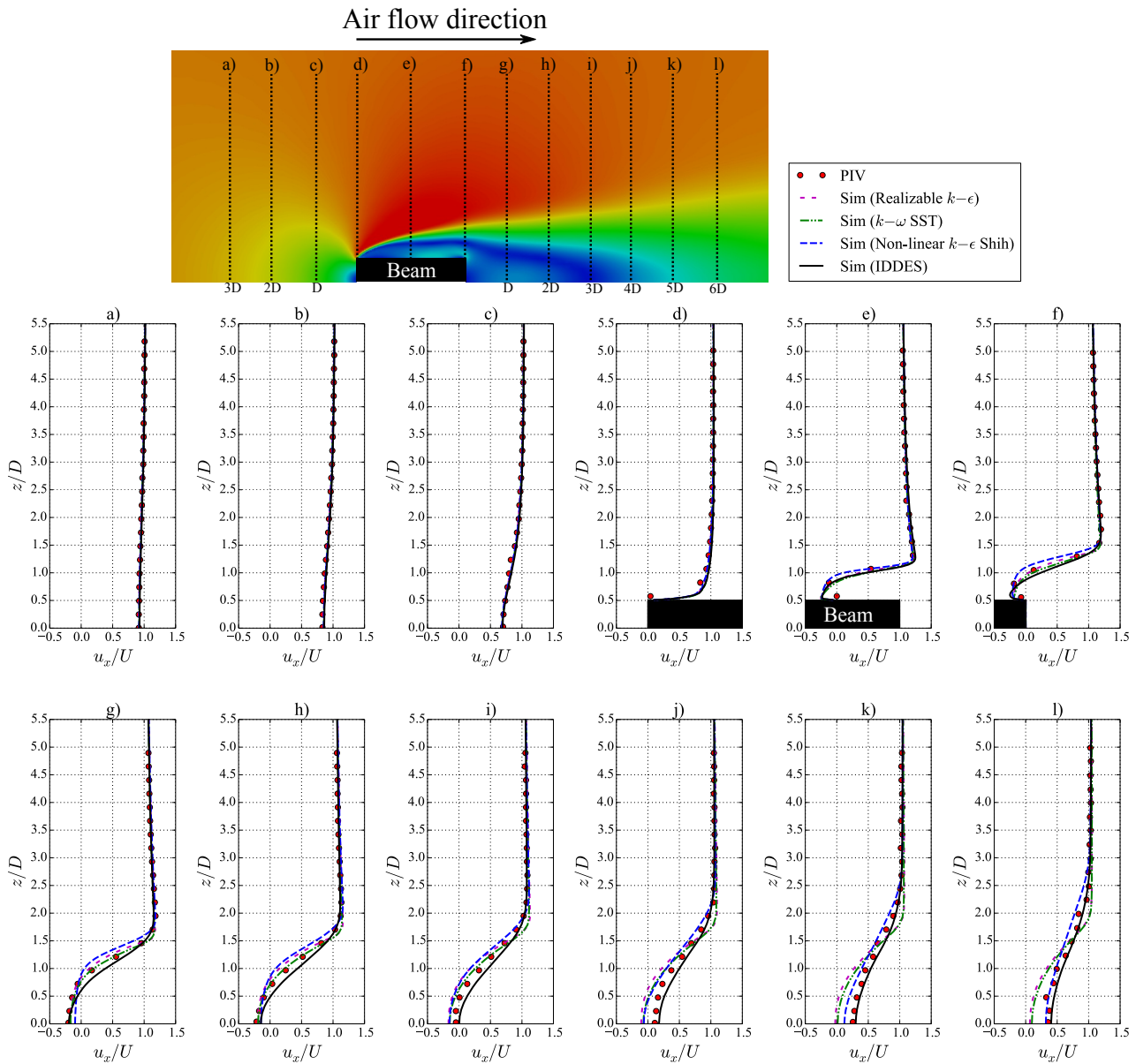


Figure 6.4: Time-averaged velocity profiles at  $y = H/2$

side-wall regions. Therefore, even though RANS models are associated with less computational resources, it lacks the capabilities to reproduce the detail and complexity of the unsteady, highly separated flow and resulting structural loading. The IDDES model is, therefore, favoured not only for accuracy but also for computational efficiency.

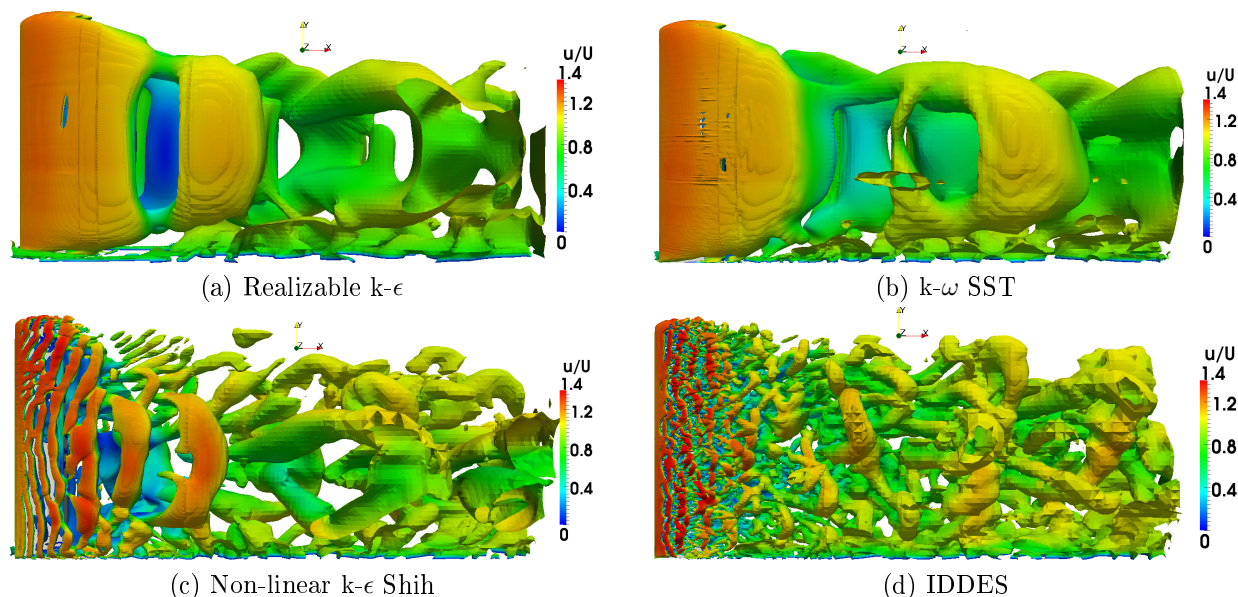


Figure 6.5: Vortex structure comparison for various turbulence models ( $Q = 5 \times 10^{-5}$ )

## 6.1 Vortex Shedding Frequency Compared to Literature Data

In this study it is also important to look at the loading frequency on the beam and how this compares to literature. It is also important because the transient flow patterns are often more difficult to reproduce and, therefore, should be validated. In figure 6.6 the vortex shedding frequency for the simulated cases are displayed against literature data. This is determined at a height of  $y = H/2$  using the lift (difference between the pressure on both sides of the beam).

The parallel beam data compares very well for all cases with the literature data with reported values between  $0.051 < St < 0.064$  for similar  $L/D$  ratios (Deniz and Staubli, 1997; Morgenthal, 2000). The Realizable  $k-\epsilon$ ,  $k-\omega$  SST and IDDES models produce more or less the same frequency at  $St = 0.051$  while the Non-linear  $k-\epsilon$  model produces approximately  $St = 0.63$ . The data is also given in table 6.1.

One important observation is that the reproduced frequencies are very similar despite the significant difference in vortex structures shown in figure 6.5. This means that even though the models produce various degrees of detail of turbulent vortex structures the dominant loading frequencies are very similar. The more complex models will, therefore, produce about the same loading fre-



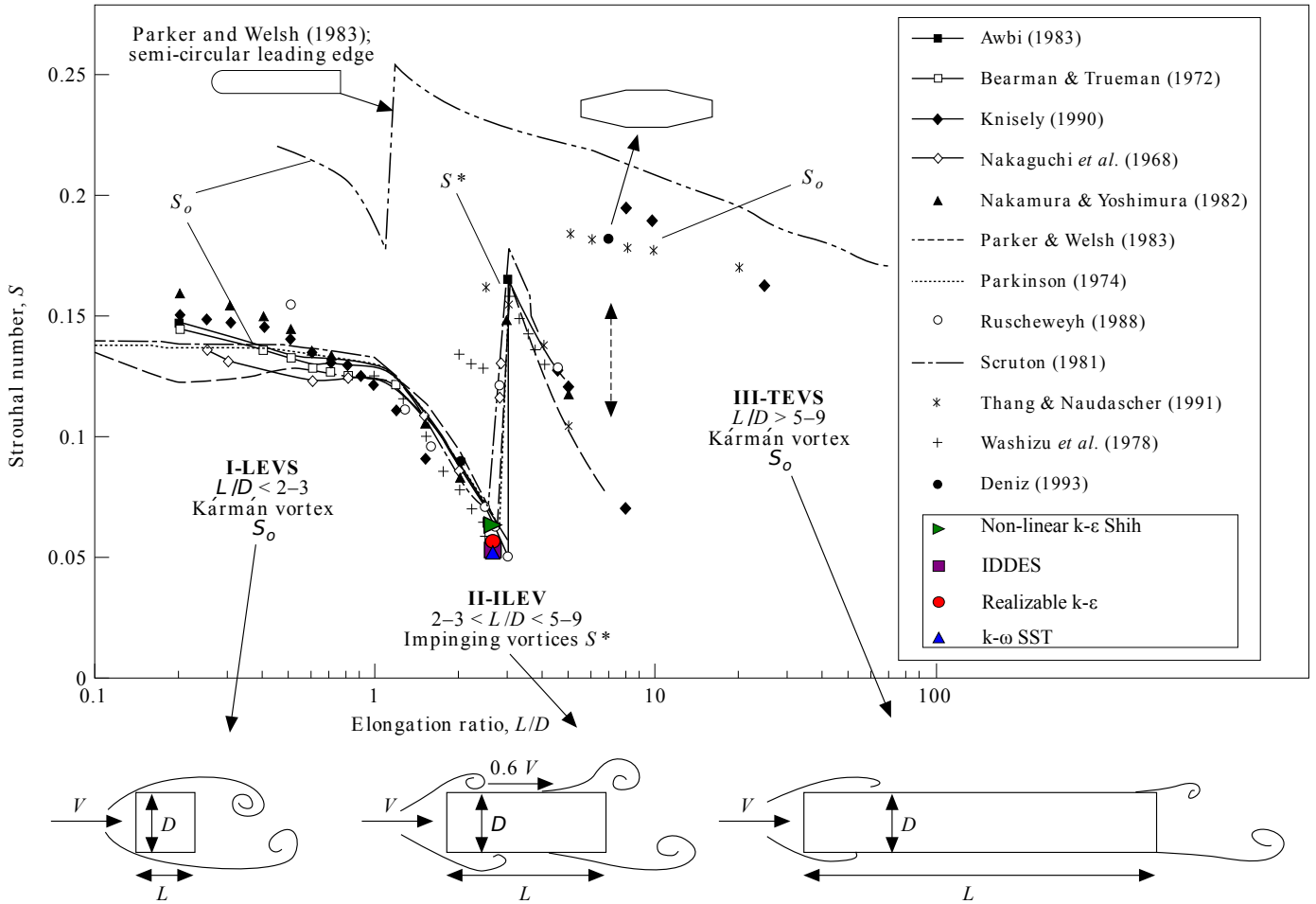


Figure 6.6: Vortex shedding frequency comparison with literature

quency on the beam as the others but additionally higher frequency oscillations with little effect. This, however, does not take into account the magnitude of the loading but only the frequency.

## 6.2 Flow-induced Loading Amplitude Comparison

In figure 6.7 the time dependent lift (or flow-induced loading) at  $y = 0.5H$  is compared for the different turbulence models. It is again observed that the frequency is more or less the same but the magnitudes differ significantly. The Non-linear  $k-\epsilon$  Shih and IDDES turbulence models produce similar magnitudes, followed by the Realizable  $k-\epsilon$  model and lastly the  $k-\omega$  model which have very small lift forces.

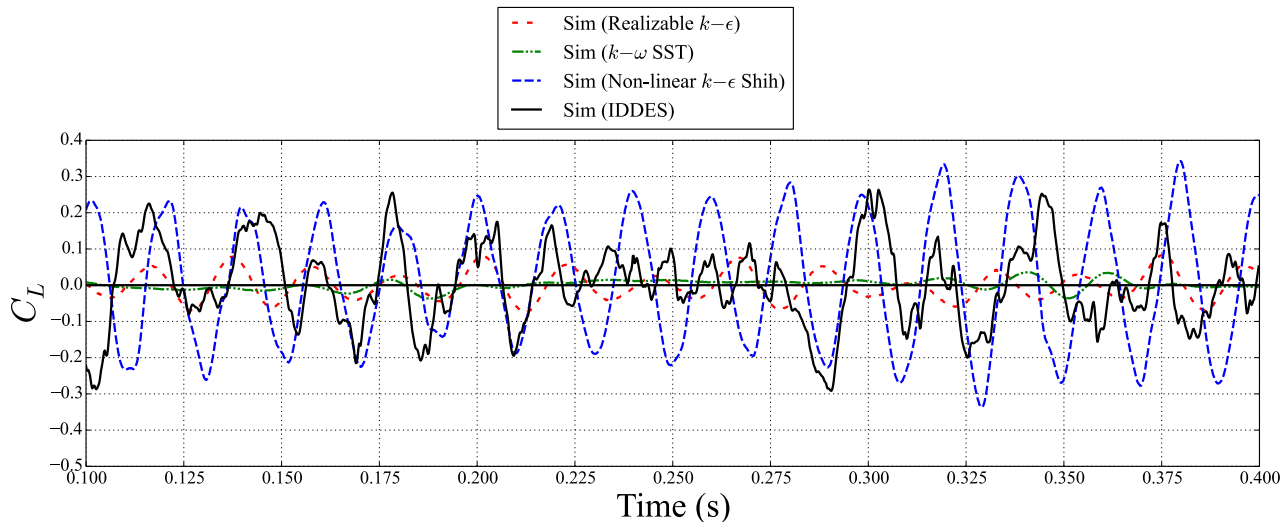


Figure 6.7: Flow-induced loading comparison for various turbulence models

### 6.3 Computational Time

In table 6.1 the turbulence models are compared for the time it takes to simulate 1 second of flow. All simulations were done on the same mesh (approximately 5 million cells) and computational resources which includes 24 cores on a single node of the HPC cluster as described in 4.7. The results show that shortest simulation was by the  $k-\omega$  SST model taking 1 month to complete. Surprisingly the IDDES model does not take much longer and it is more efficient than the Realizable  $k-\epsilon$  and Non-linear  $k-\epsilon$  Shih models. This further motivates the use of this model. The reason for the computational efficiency of the IDDES model may be because the original Spalart-Allmaras RANS model it is based on has a single equation where the other RANS models have two or more.

# Chapter 7

## Data Comparison

A total of four cases were run using the IDDES turbulence model. This includes the two beam orientations, parallel and perpendicular, and two flow speeds,  $U = 30$  and  $60$  m/s. In this chapter these results are compared with data from measurements and literature for the purpose of evaluating the accuracy as well as to highlight the flow features.

### 7.1 Parallel Beam Velocity Data Comparison With Measurements

In figure 7.1 the cross-section of the beam is shown with measurement or sampling locations relative to the beam. The sampling lines include two profiles parallel to the flow with one upstream and one downstream of the beam. Additionally, nine profiles are measured perpendicular to the flow of which three are along the beam side wall. PIV data is used in this case to compare time-averaged velocity components. These data comparisons are done at three different heights which are  $y = 0.5H$ ,  $0.72H$  and  $0.94H$ .

In figures 7.2 to 7.4 the normalised velocity  $u_x/U$  component is compared to measured PIV data. The data for both the  $30$  m/s and  $60$  m/s cases is normalised with  $U = 30$  m/s since it shows more clearly the difference in the results. Overall the simulation results match very well with the measured data.

The stagnation region upstream of the beam shows a sharp drop-off in velocity near the beam due to the small flow obstruction which allows more flow to maintain its speed while being redirected around the obstruction or

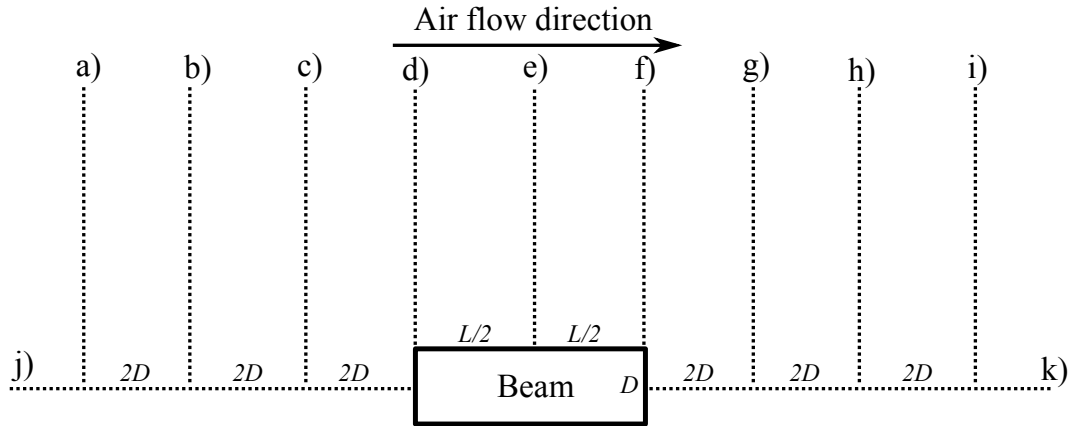


Figure 7.1: Parallel beam velocity profile comparison positions

brought to a halt at the wall (see figures 7.2 to 7.4 j). For all three heights the recirculation lengths produced by the 30 m/s and 60 m/s cases seem to be more or less the same which is not expected. This can be seen on the side wall and wake regions (see figures 7.2 to 7.4 d, e, f and k). The higher velocity case also produces higher recirculation strengths near the beam as expected.

Although the PIV data is accurate it can be seen that the data for the 60 m/s speed has slightly more inaccuracies. This is due to the decreased seeding density as a result of increased mass flow through the wind tunnel at 60 m/s relative to the constraint of a constant mass flow seeding supply, which is always operating at full capacity. As previously mentioned, the camera focus and laser light sheet is focussed near the beam which will also mean that measured inaccuracies are most prevalent far from the beam.

The largest simulation inaccuracies are visible in figure 7.3 k for the 60 m/s case. This is measured in the wake region downstream of the beam at a height of  $y = 0.72H$ . The simulation results perform well in the recirculation region up to approximately  $2.7D$  distance from the beam downstream face. Any further downstream than this the simulations under predict the velocity by up to 20%. The reason for this discrepancy is unclear since the simulations do predict the measured values accurately at the measured positions above and below this point. This is, however, not too alarming for the FSI simulations since the flow around the beam is accurately predicted and these downstream inaccuracies will have little effect on the beam.

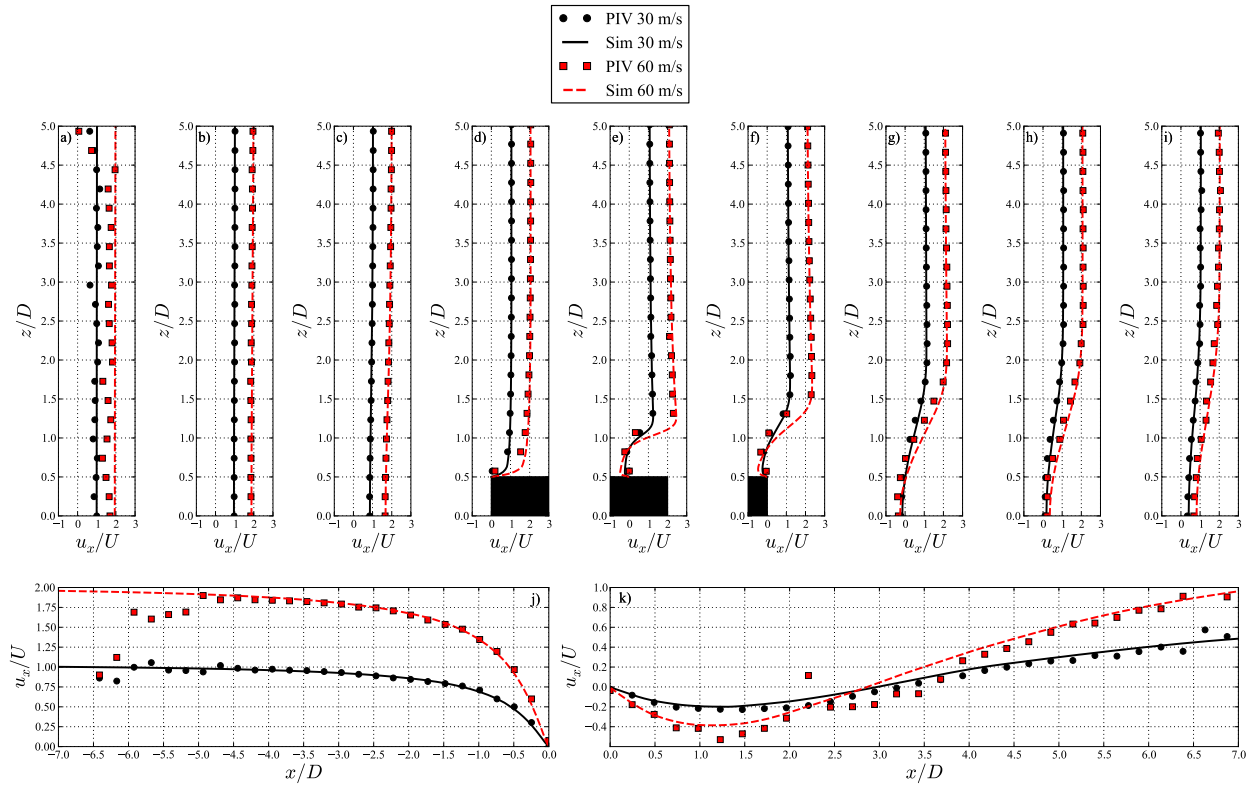


Figure 7.2: Parallel beam validation results at  $y = 0.5H$

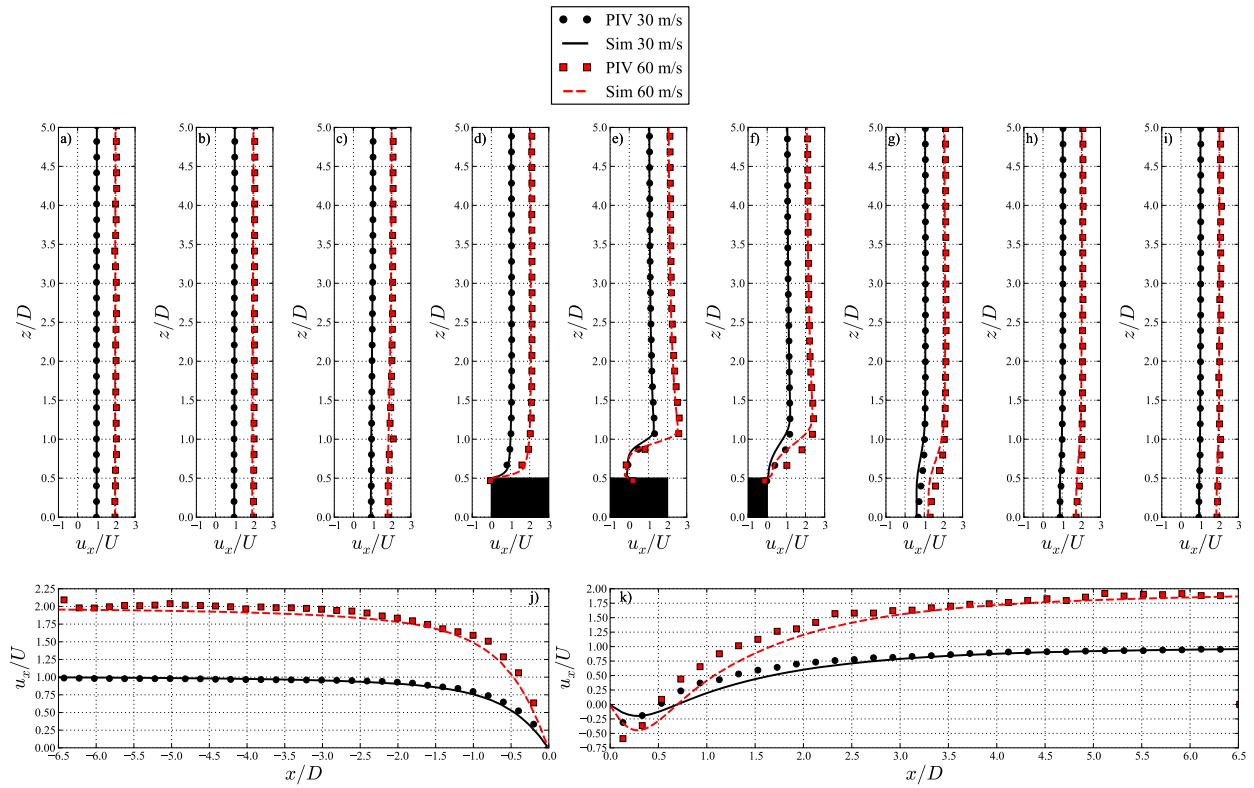
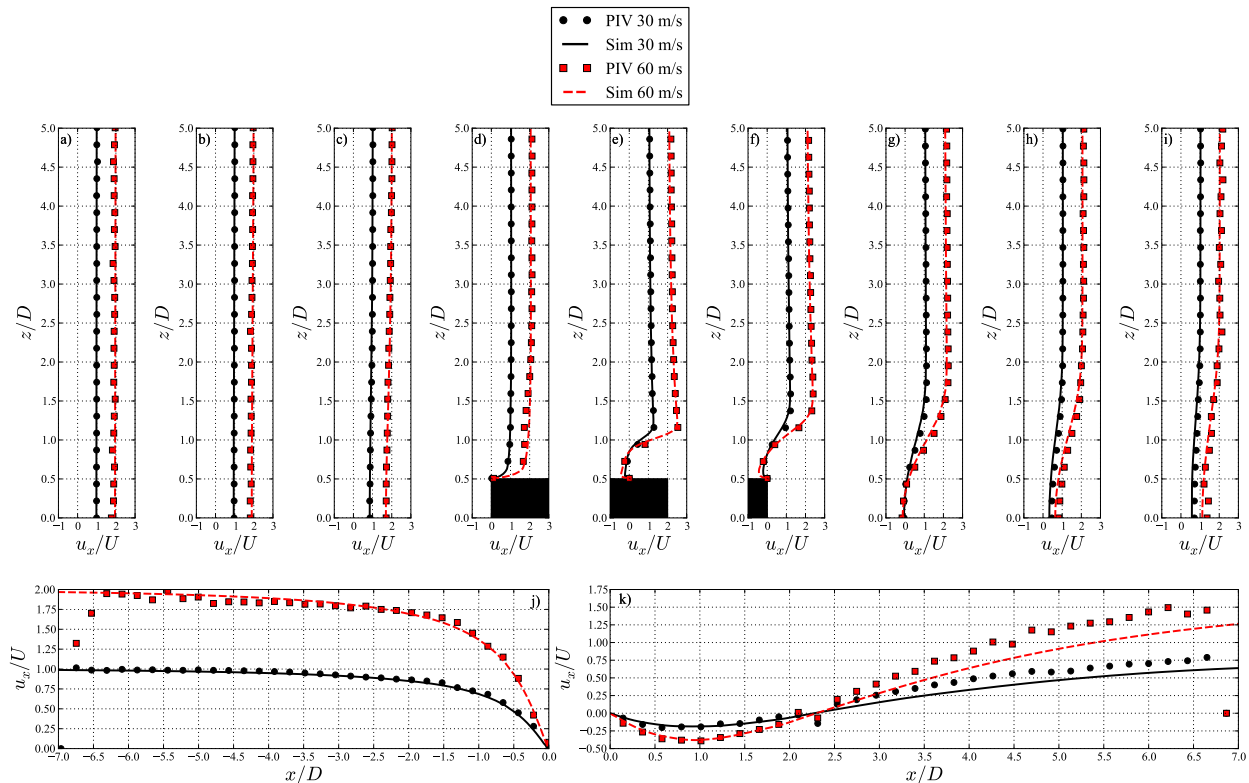


Figure 7.4: Parallel beam validation results at  $y = 0.94H$

Figure 7.3: Parallel beam validation results at  $y = 0.72H$ 

## 7.2 Perpendicular Beam Velocity Data Comparison with Measurements

The perpendicular beam sampling lines are similar to that of the parallel beam except that only two sampling lines are included in the side wall area as shown in figure 7.5. The effect of stagnation is more significant in this case due to the larger flow obstruction which results in lower velocities much further upstream of the beam (see figures 7.6 to 7.8 j). Similarly, the side wall recirculation and wake region is increased.

The wake recirculation length for the parallel beam extends beyond the measurement range of the PIV system. The simulation results compare very well with the measured PIV results in general despite the challenges of highly separated flow and computational limitations. The most significant inaccuracies in this case occurs at the top of the beam ( $y = 0.94H$ ) in the wake (see figure 7.8 j). At the  $y = 0.94H$  the time averaged results show a small recirculation zone close to the beam extending only to  $0.5D$  after which the flow in

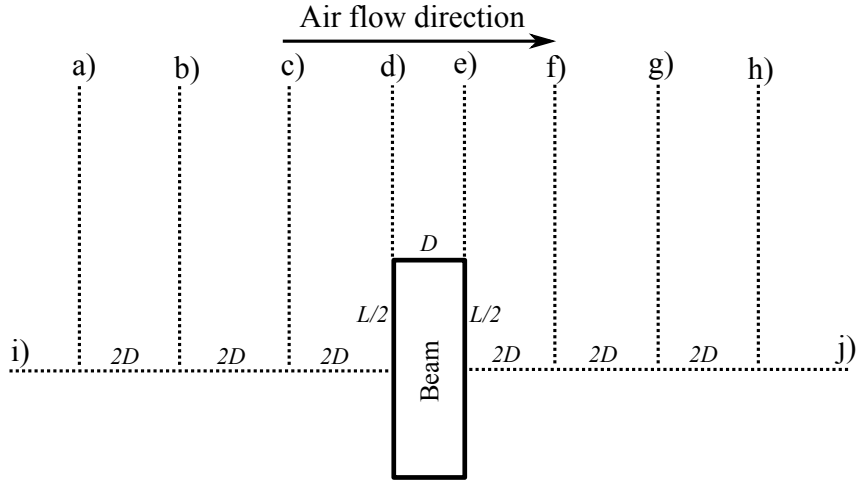


Figure 7.5: Perpendicular beam velocity profile comparison positions

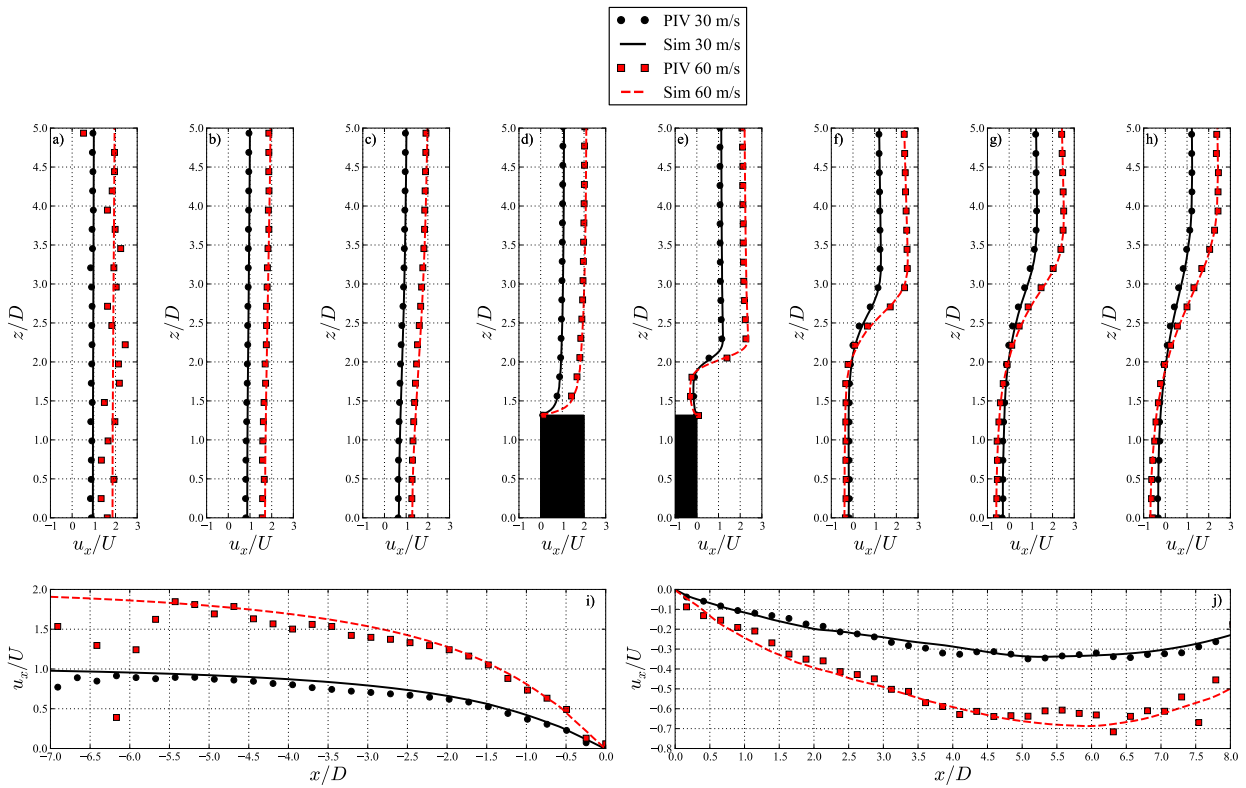


Figure 7.6: Perpendicular beam validation results at  $y = 0.5H$

the  $x$ -direction becomes positive (flow away from the beam) up to  $3.5D$  where it is again negative (flow towards the beam) all the way to  $5.5D$  downstream of the beam.

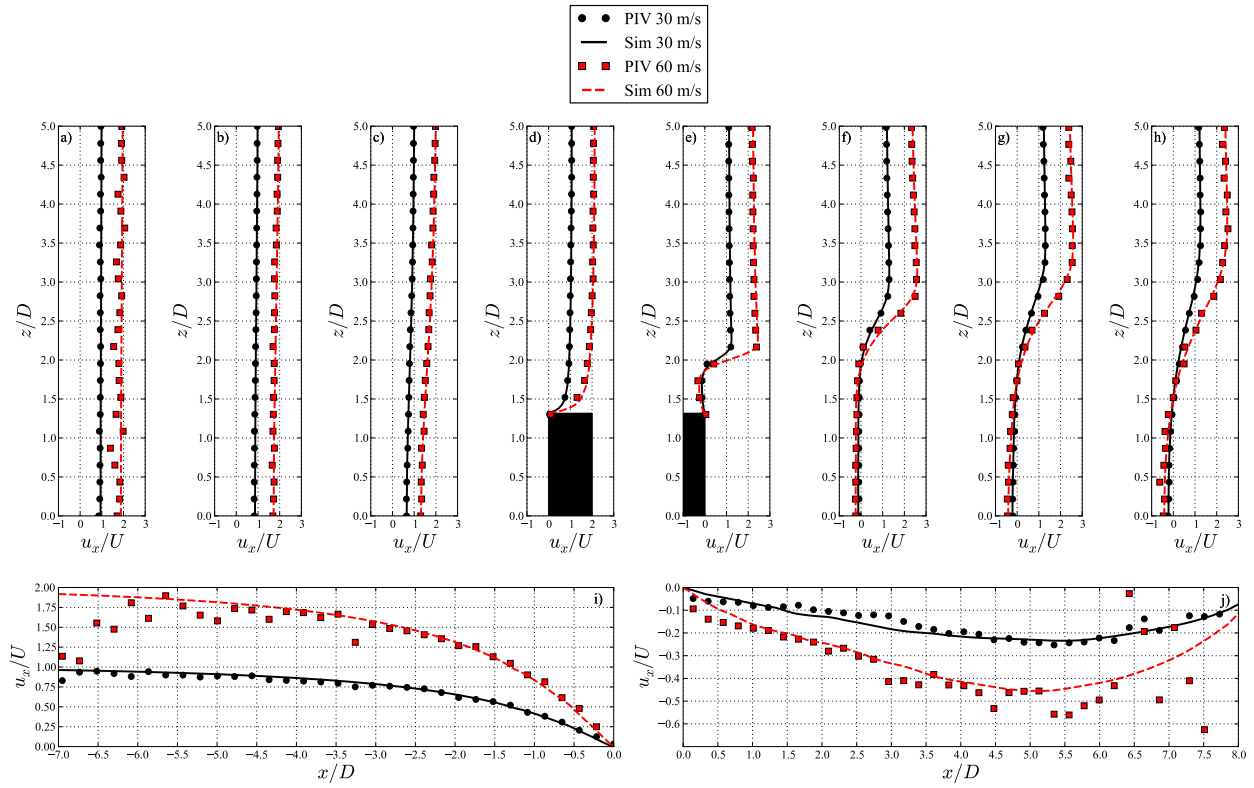


Figure 7.7: Perpendicular beam validation results at  $y = 0.72H$

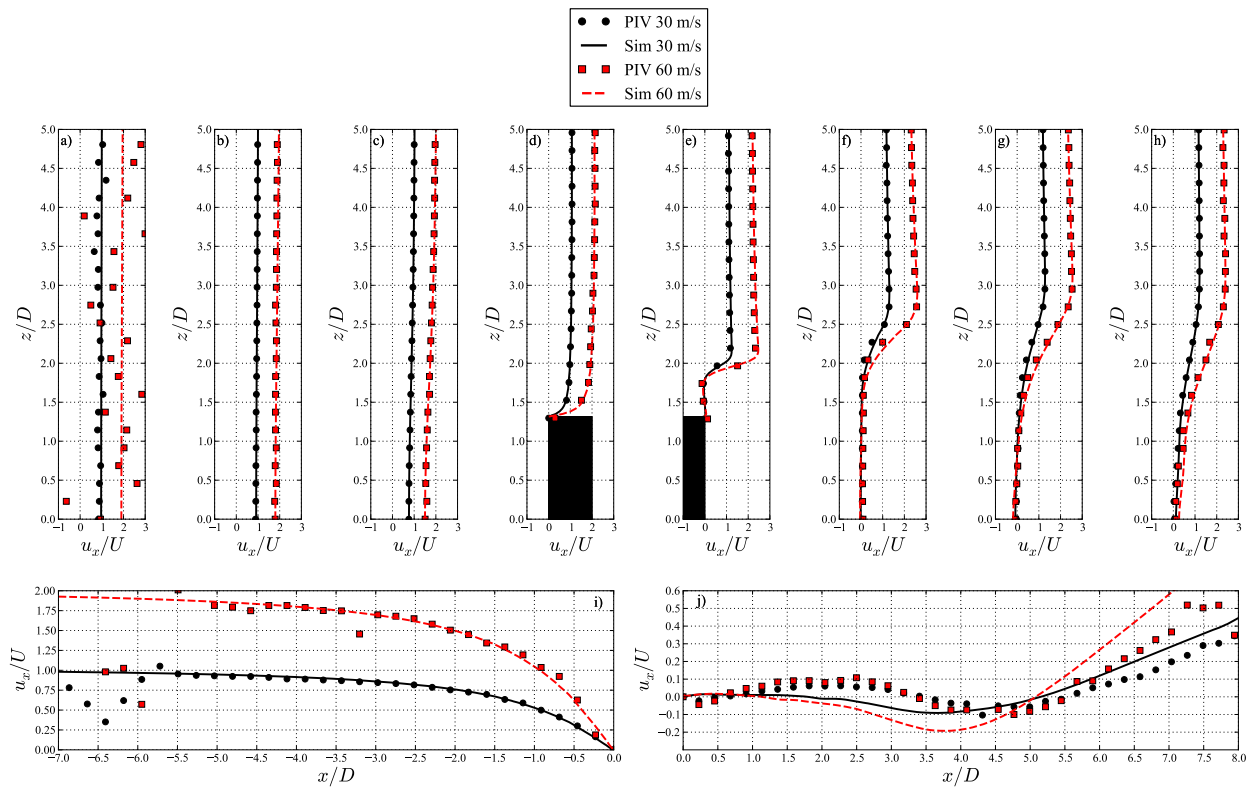


Figure 7.8: Perpendicular beam validation results at  $y = 0.94H$



## 7.3 Fluid Simulation Results Compared to Pressure Data

The pressure results are important since this represents the majority of loading that will be transferred to the structure. For the parallel beam (see figure 7.9) the 30 m/s results have already been presented a few times for validation purposes. The 60 m/s pressure coefficient results are almost identical again showing the under-predicted suction pressure on the side wall near the top of the beam at  $y = 0.94H$ .

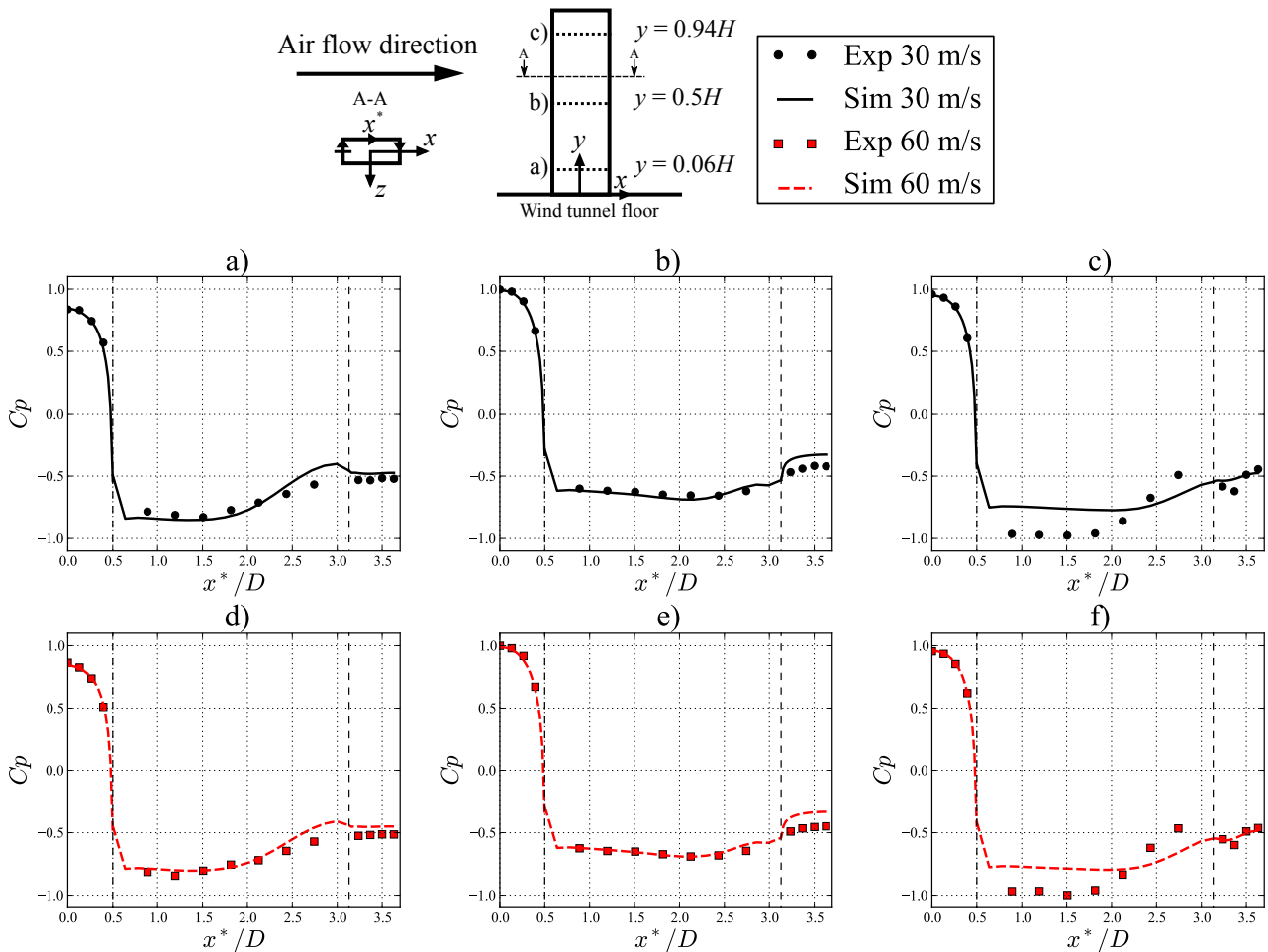


Figure 7.9: Parallel beam pressure validation results

The perpendicular beam results also show very good comparison for both speeds. In this case, however, there is no under-prediction of the suction pressure on the side wall and wake regions.

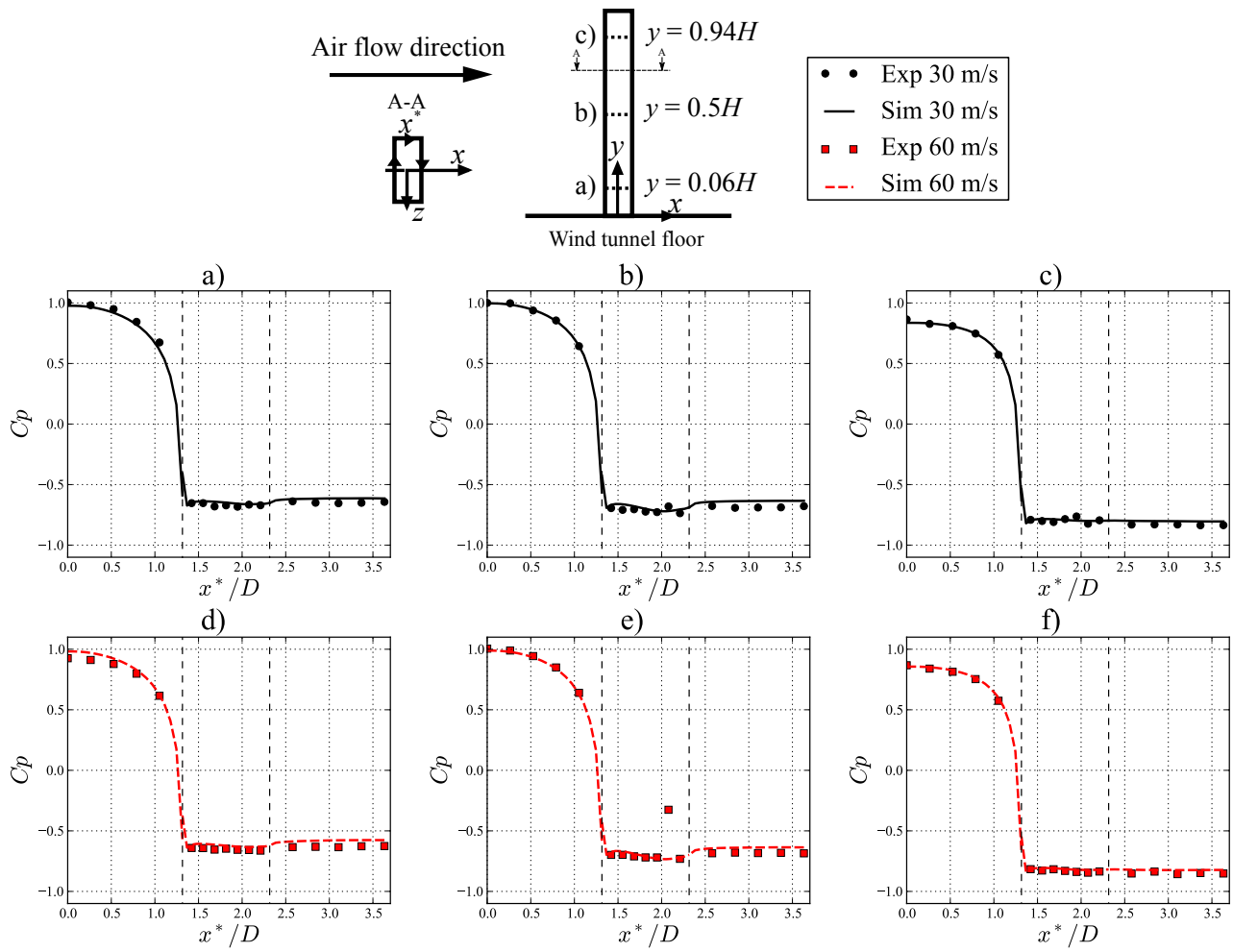


Figure 7.10: Perpendicular beam pressure validation results

# Chapter 8

## General Case Results

In this section an overview of the results for the four case studies are provided. For each case the results are normalised by the inlet velocity or equivalent dynamic.

### 8.1 Global Flow Features

The parallel beam velocity and pressure magnitude results for  $U = 30$  m/s is shown in figure 8.1. The wake region shows the vortex shedding street which results in the cyclic loading on the structure. The velocity shows stagnation at the leading edge, separation around the beam edges, acceleration and recirculation which are the typical flow features of a bluff-body. The pressure is high on the upstream surface showing stagnation with  $C_p = 1$ . On the rest of the beam the pressure shows  $C_p < -0.4$  with only slightly higher pressure on the top surface toward the downstream edge.

The perpendicular beam results for  $U = 30$  m/s is shown in figure 8.2. In this case the downstream wake is wider and shows larger vortex shedding phenomena. The loaded upstream surface is also much larger suggesting increased structural streamwise structural loading but due to the small side wall and increased stiffness in the transverse direction, the impact of the air flow loading cycle will be significantly diminished.

In figure 8.3 the wake vortex structures are compared from a top view perspective. In this comparison it is not possible to identify a clear cyclic motion in the wake of the parallel beam. The perpendicular beam, on the other hand shows significant cyclic motions in the wake.

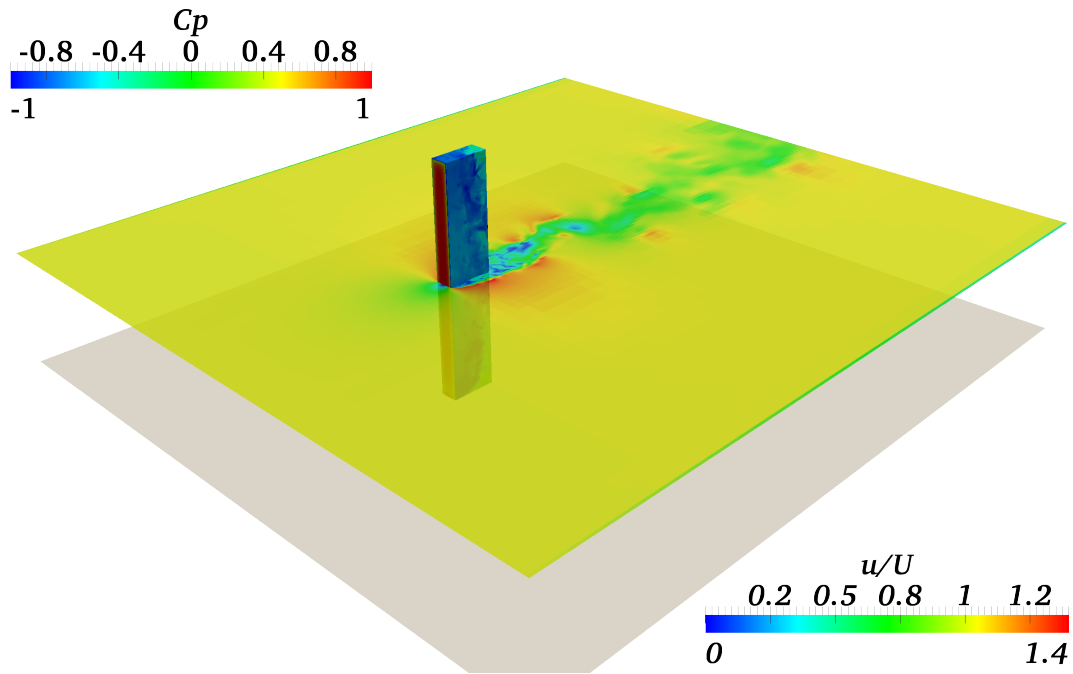


Figure 8.1: Velocity magnitude and pressure coefficient plot of the parallel beam with  $U = 30$  m/s

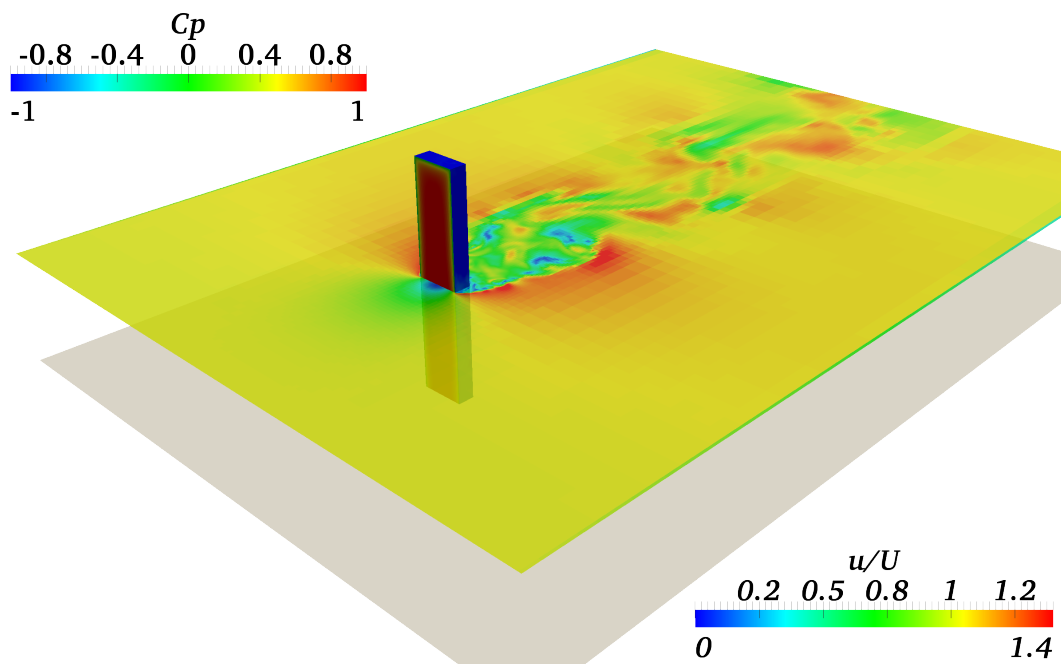


Figure 8.2: Velocity magnitude and pressure coefficient plot of the perpendicular beam with  $U = 30$  m/s

It is also difficult to distinguish any difference in vortex streets between the different speeds of the same orientation.

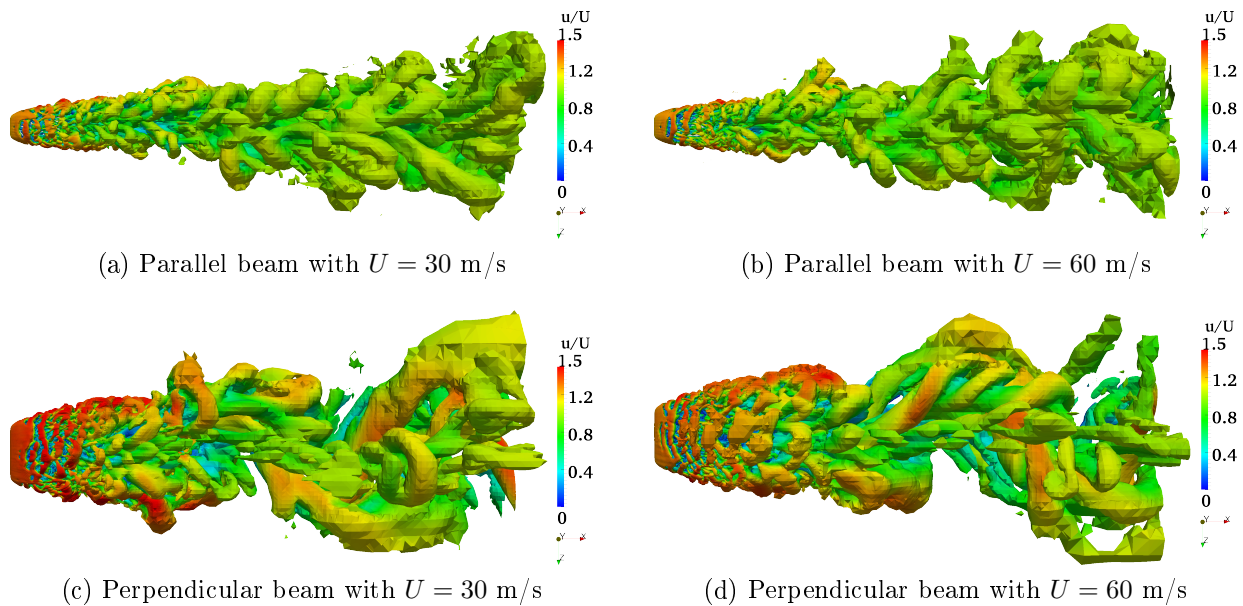


Figure 8.3: Wake vortex structure top view comparison for the four case studies ( $Q = 5 \times 10^{-5}$ )

Looking at the side view in figure 8.4 the perpendicular beam shows more speed-up than the parallel beam. The perpendicular beam seems to have a sharp drop-off compared to the parallel beam wake which is more sustained. The parallel beam wake is not clearly affected by the speed-up but the perpendicular beam wake is slightly larger.

## 8.2 Strain Response

With a good overview of the flow patterns and resulting beam pressure for all four cases now established attention is turned to the structural response due to the flow-induced loading. Strain gauge measurements were carried out as discussed in section 4.8.3. A short section of the results for the strain gauge measurements are presented in figures 8.5 and 8.6. Longer periods, than presented here, were measured to get a good statistical representation of the frequencies and averages.

In figure 8.5 the structure shows clear oscillations on both strain gauges at  $U = 30$  m/s. At this speed the structural oscillation frequency is 37 Hz which is equal to its first natural frequency. The measurements were carried out through consecutive incremental increases in the flow speed and then re-

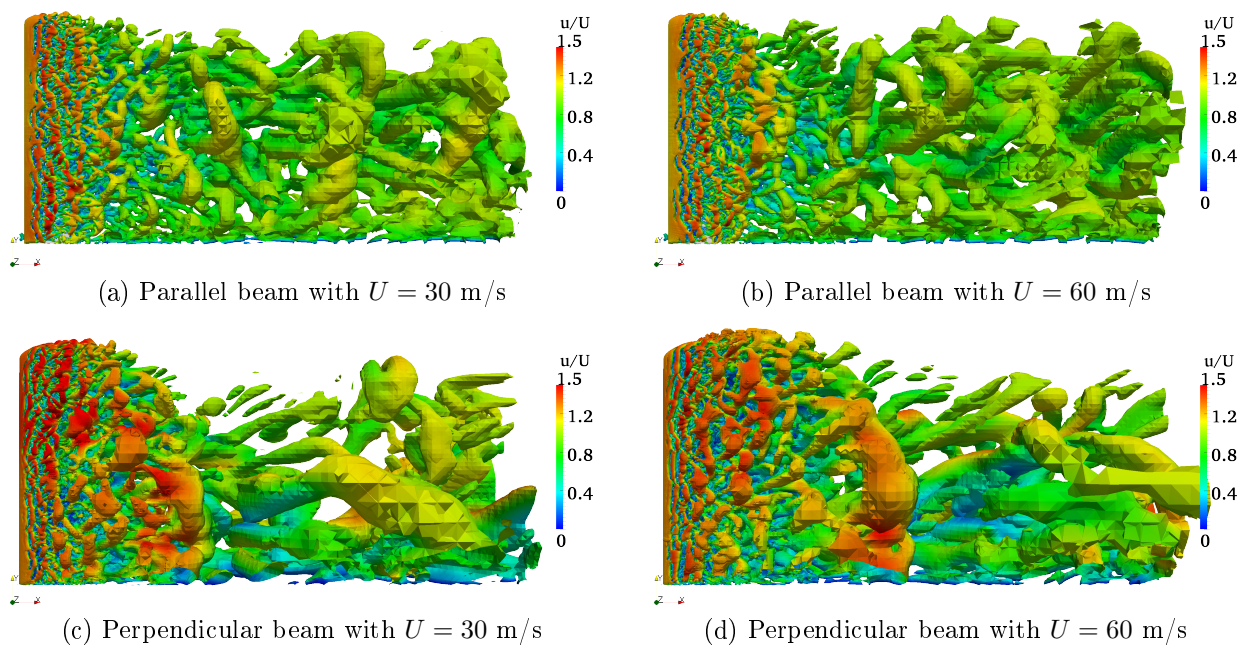


Figure 8.4: Wake vortex structure side view comparison for the four case studies ( $Q = 5 \times 10^{-5}$ )

peated by decreasing the speed and measuring again. This was done to test repeatability and also to eliminate lock-in effects (for a description of the lock-in phenomena see section 2.5). It was observed that lock-in occurs at around  $U = 30$  m/s resulting in severe oscillations if the speed is then increased further without damping the beam once to get it out of the lock-in phenomena. The results presented here do not include the effect of lock-in since the beam was stopped at each speed and released again to respond to the flow-induced oscillations at that speed. The upstream gauge 2 does show time-averaged offsets which increases with the speed as is expected since this is directly related to the dynamic pressure  $P_d = 1/2\rho U^2$ .

The perpendicular beam strain results in figure 8.6 show larger offsets (time-averaged strain or loading) on the upstream face due to the increased surface area. There is, however, no cyclic loading visible on this beam despite its large vortex shedding structures in the wake. This is possibly due to the fact that firstly, the oscillating loading is perpendicular to the flow ( $z$ -direction), secondly, the perpendicular beam has a small afterbody for the pressure to impact on and lastly, the perpendicular beam orientation has an increased stiffness for bending motion perpendicular to the flow direction.

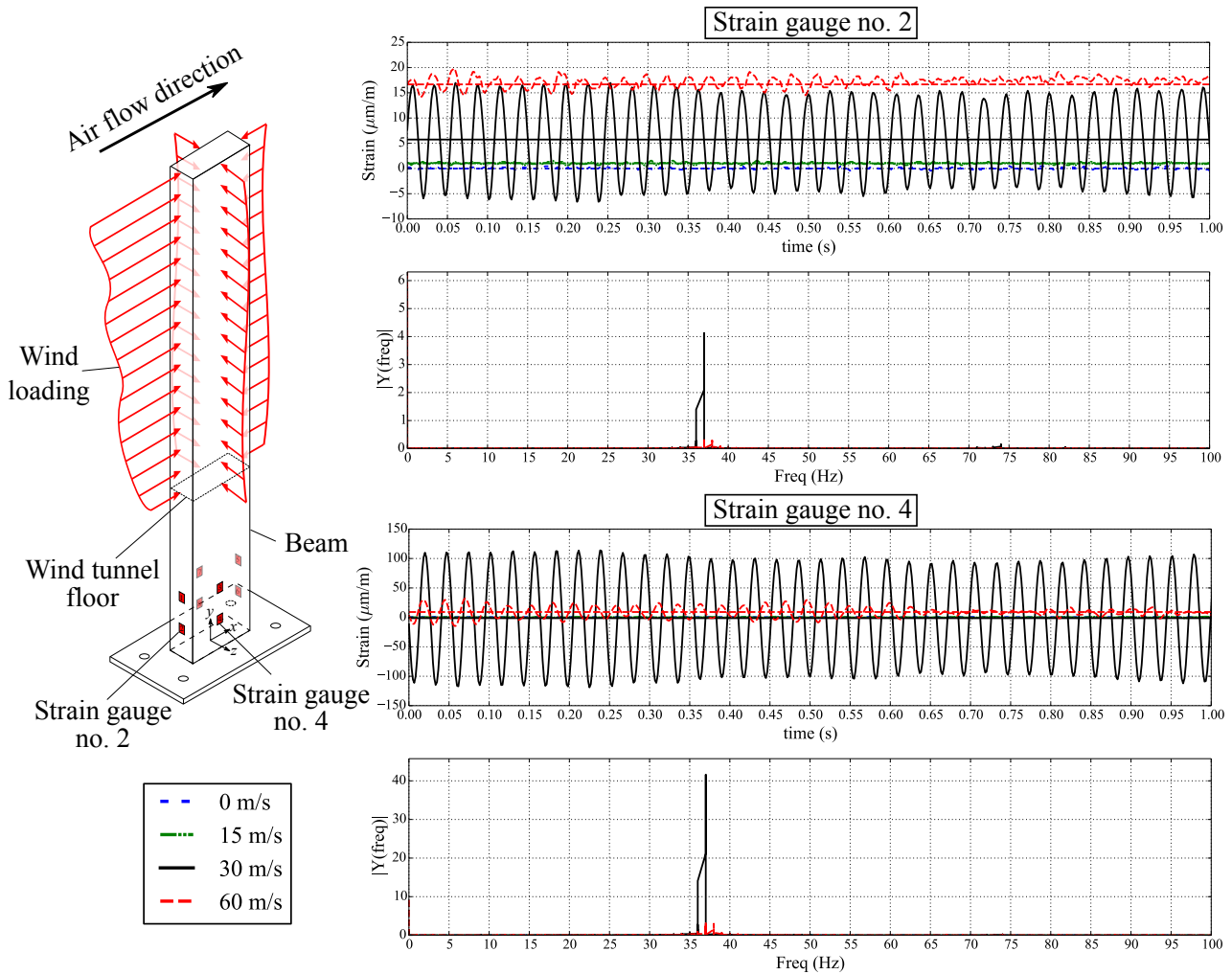


Figure 8.5: Parallel beam strain gauge measurements for various speeds

Since the other cases show very little transient structural response, and also due to the cost of dynamic analysis, only the parallel beam at  $U = 30$  m/s was simulated for time-dependent FSI.

A time-averaged analysis was carried out so that it would be possible to compare the results to measured data. For this analysis the time-averaged flow-induced load is linked to the structural mesh. The results are presented in figures 8.7 and 8.8. From the results it is clear how the increased velocity increases the strain on the beams. The resulting strain is the highest at the corners of the beam mounting positions with some local maximums around the bolt holes and fixing points.

The time-averaged simulated and measured strain for gauge 2 (or 6) are compared in table 8.1. The parallel beam simulations accurately reproduce

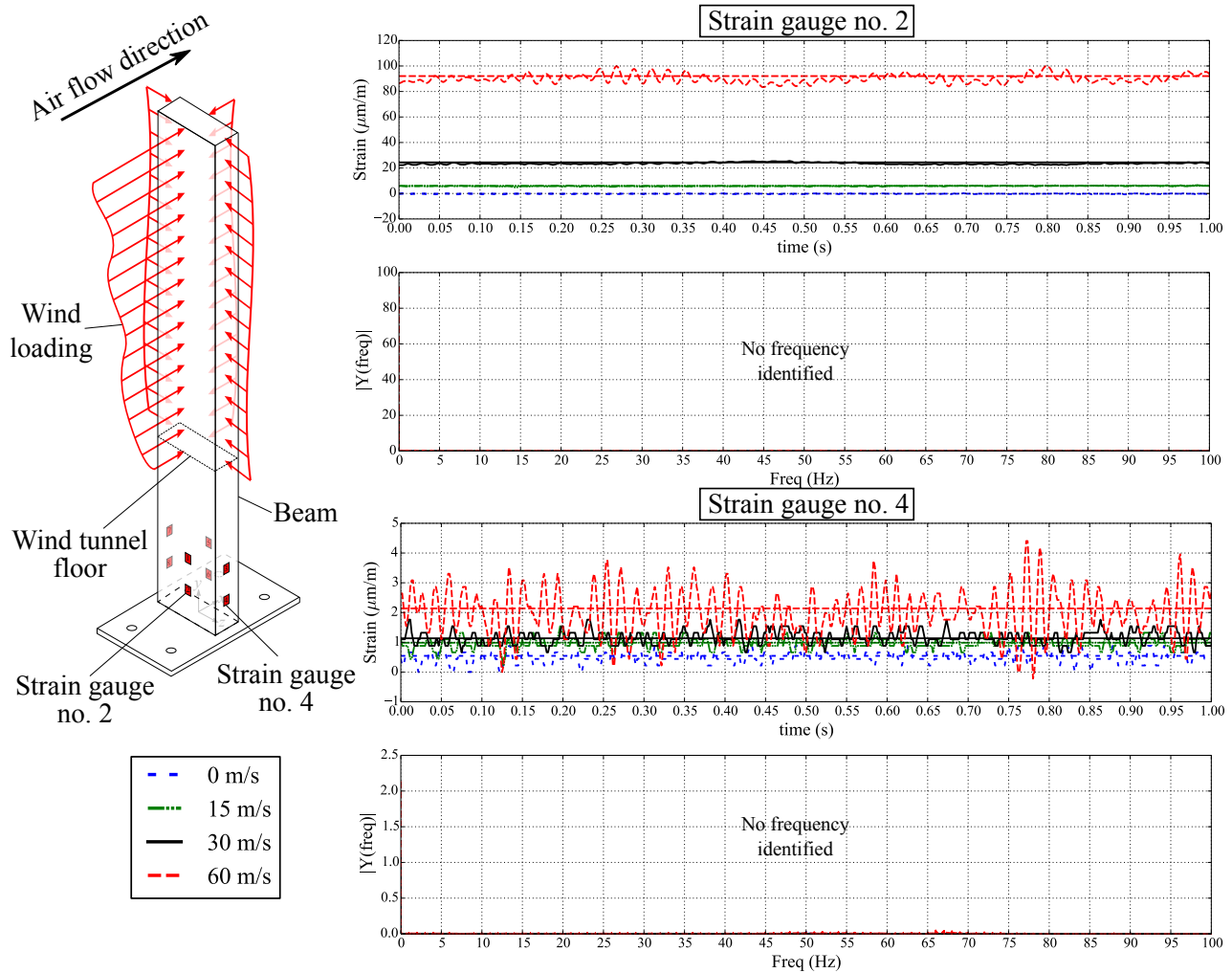


Figure 8.6: Perpendicular beam strain gauge measurements for various speeds

the measured strain in the beam validating the FSI methodology despite the complexity of the structure. The perpendicular beam is less accurate with approximately 16 % error in the strain predicted. This could possibly be reduced by further mesh refinement or more sophisticated linking strategies that would include interpolation methods or even average values from the covered fluid mesh face centres.



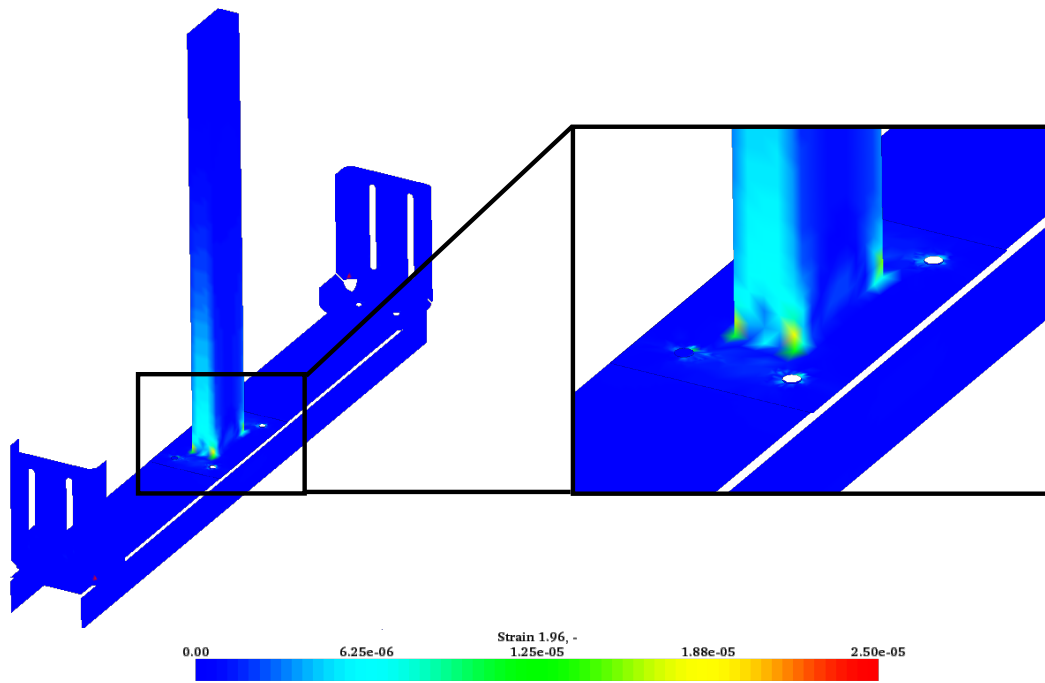
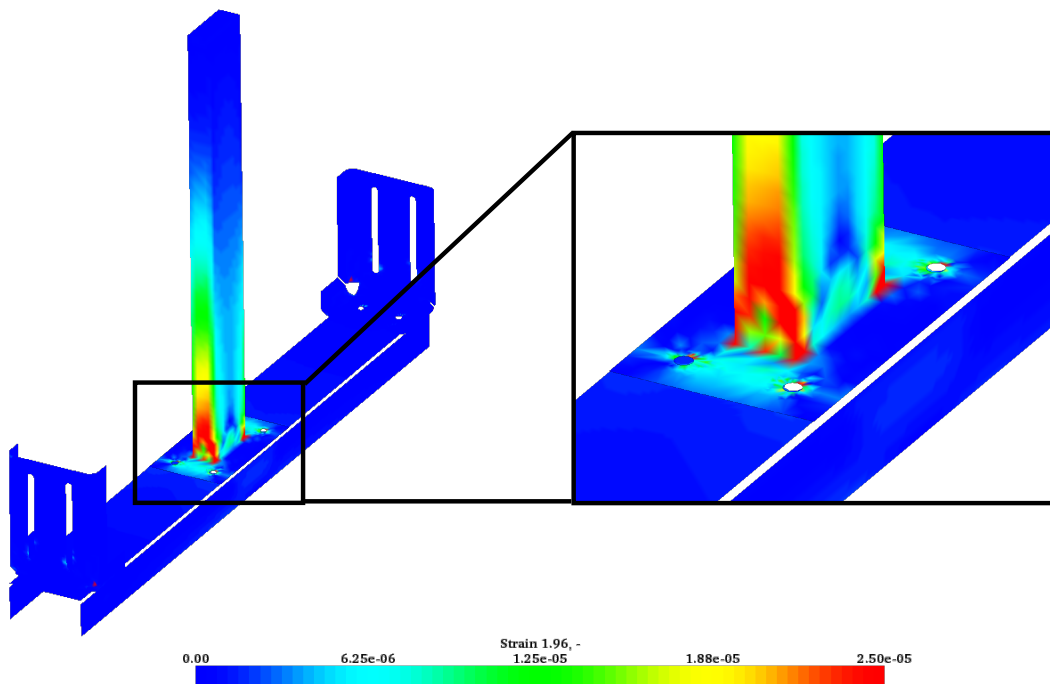
(a) Parallel beam with  $U = 30$  m/s(b) Parallel beam with  $U = 60$  m/s

Figure 8.7: Time-averaged flow-induced strain on the parallel beam at various flow speeds (strain modulus results on the middle plane of the shell elements)

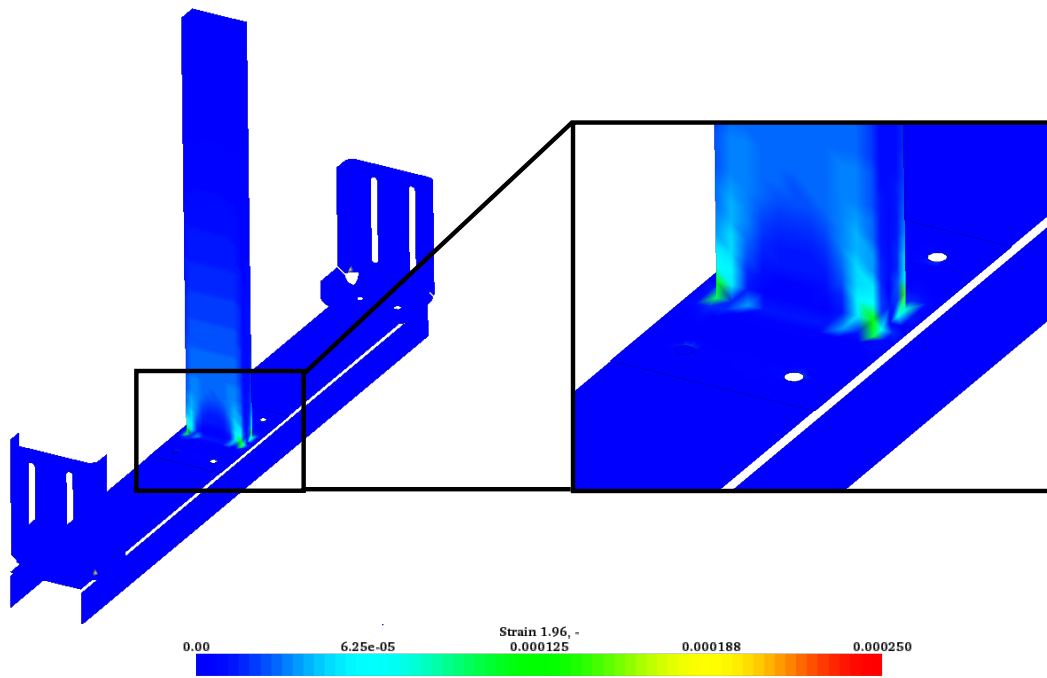
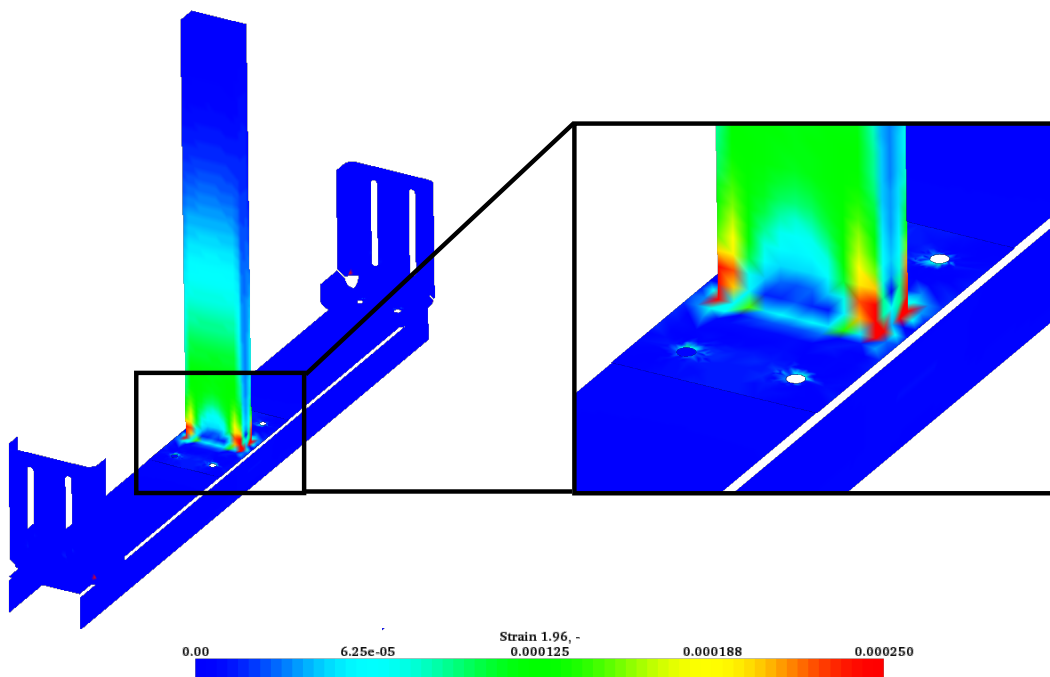
(a) Perpendicular beam with  $U = 30$  m/s(b) Perpendicular beam with  $U = 60$  m/s

Figure 8.8: Time-averaged flow-induced strain on the perpendicular beam at various flow speeds (strain modulus results on the middle plane of the shell elements)

Table 8.1: Comparison of time-averaged simulated and measured strain values (at gauge no. 2 and 6)

Beam	30 m/s		60 m/s	
	Exp	Sim	Exp	Sim
Parallel	5.8	5.8	21.9	22.7
Perpendicular	24.6	20.7	94.3	81.4

# Chapter 9

## Detailed Case Analysis

In chapter 8 the parallel beam with  $U = 30$  m/s is identified as the only case with significant transient oscillating behaviour. For this reason a detailed analysis of fluid dynamics and time-dependent structural behaviour for this case study is the focus of this chapter. The first part looks in detail at the bluff-body aerodynamics to shed light on this topic which continues to challenge research in this field. The second part presents the results from the time-dependent structural loading. The majority of the fluid dynamics analysis in this chapter forms part of a published paper (Joubert *et al.*, 2015).

### 9.1 Global Flow Features

In figure 9.1 the streamlines for the mean flow is displayed. As the flow approaches the beam it slows down in the upstream stagnation region and then accelerates as it moves around the obstacle. In the wake regions, vertical flow movement is visible which forms a funnel shape where streamlines converge. It is possible to see that the side-wall recirculation region is larger at mid-height than at the base and tip of the beam. There is also a small recirculation present near the base upstream of the beam. This recirculation is expected to be related to the upstream near-wall horseshoe vortex noticed in numerous studies such as surface mounted cubes (see for example Rodi (1997); Paterson and Apelt (1990)) although in this case it is far less pronounced most probably due to the reduced flow obstruction.

In figure 9.2 the time-averaged flow field around the beam can be seen expressed in velocity magnitude and superimposed streamlines. Results are

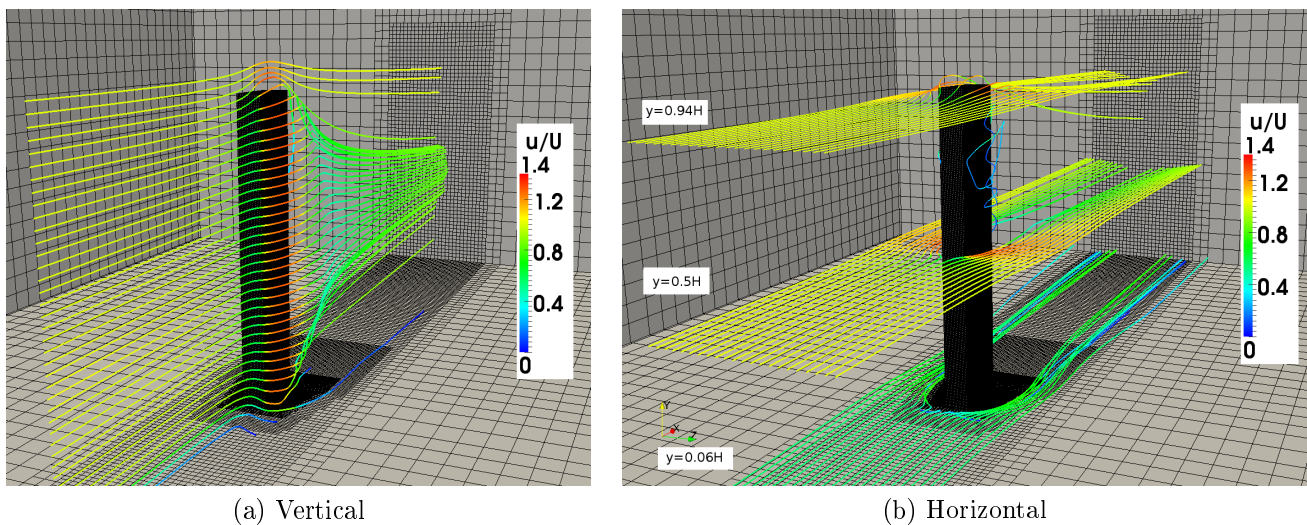
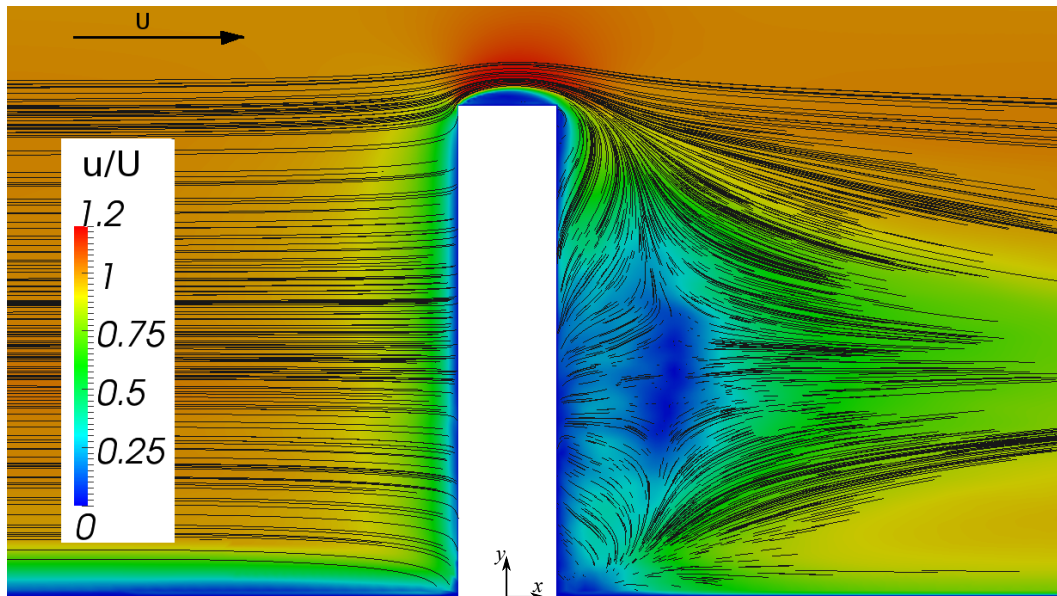
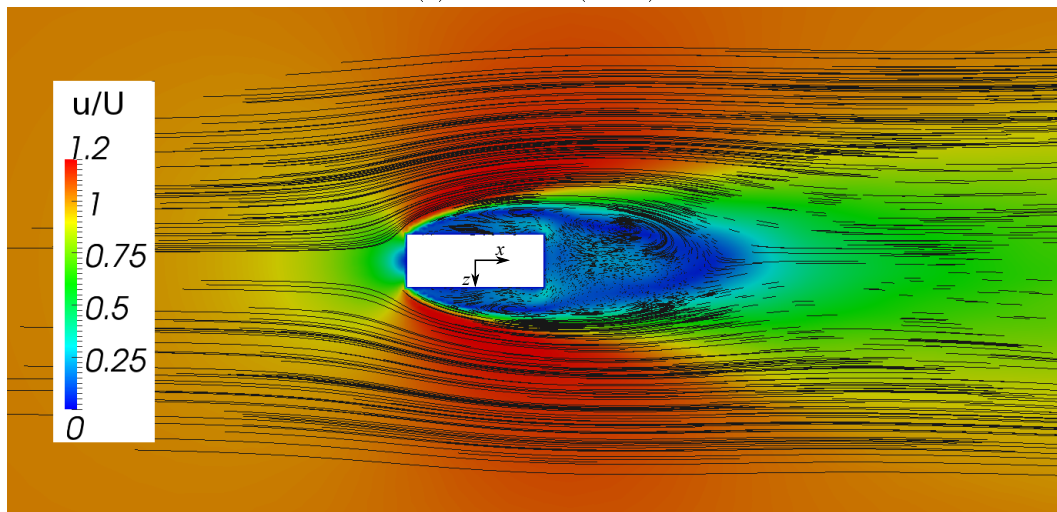


Figure 9.1: Time-averaged three-dimensional global flow features represented by the streamlines (Joubert *et al.*, 2015)

shown for a vertical cross-section through the middle of the beam width (see figure 9.2 a, as well as a horizontal cross-section through the middle of the beam height (see figure 9.2 b).

The flow approaching the beam decelerates to full stagnation due to the obstruction and produces a high pressure zone at the upstream edge. The flow accelerates around the upstream edges and side-wall recirculation region reaching a maximum of  $1.3U$  at  $0.6D$  from the side-wall. Separation occurs at the upstream edge on the side-wall as a result of the sharp edge. At the upstream edge of the side-wall a sudden drop in the pressure occurs which can be seen in figure 5.3 at  $x^*/D = 0.5$  (which represents the edge between the upstream face and the side-wall).

The side-wall recirculation region does not reattach to the side-wall but extends to form part of the greater wake recirculation region (see figure 9.1 a). This suggests that upstream edge vortex shedding still dominates, corresponding to what was reported by Deniz and Staubli (1997). In figure 9.2 b, two distinct counter rotating vortices in the wake can be identified which recirculates flow back toward the beam downstream surface. The recirculation zone on top of the beam (as shown in figure 9.2 a) does reattach just prior to the downstream edge of the beam. This reattachment at the top surface seems to be facilitated by the strong downward movement of flow in the wake region which is observed in figure 9.2 a. In figure 9.2 a, the wake recirculation

(a) Side view ( $z = 0$ )(b) Top view ( $y = H/2$ )Figure 9.2: Time-averaged cross-section flow features (Joubert *et al.*, 2015)

zone can be seen to grow from the bottom of the beam to a maximum length of  $3.2D$  which occurs at height  $y = 0.5H$  and then reduces again to zero near the top surface (see also figure 9.3 a).

To quantify the wake recirculation region is not an easy task. In this case it was decided to present the results for the mean velocity components at a number of vertical cross sections. This makes it possible to measure, for example, the recirculation length at the given heights and interpolate between them (see figure 9.3 a). The vertical movement of the flow around the beam

in figure 9.3 b, shows a strong downward movement just below the top of the beam (height of  $y = 0.94H$ ) in the wake with a maximum value of  $0.6U$  at distance  $1D$  from the beam. This downward flow is more dispersed at a height of  $0.72H$  and reduced to approximately zero at  $y = 0.5H$ . Lower down a less pronounced upward flow movement is visible with a maximum of  $0.1U$  at a distance  $1.8D$  from the beam at height  $0.06H$ .

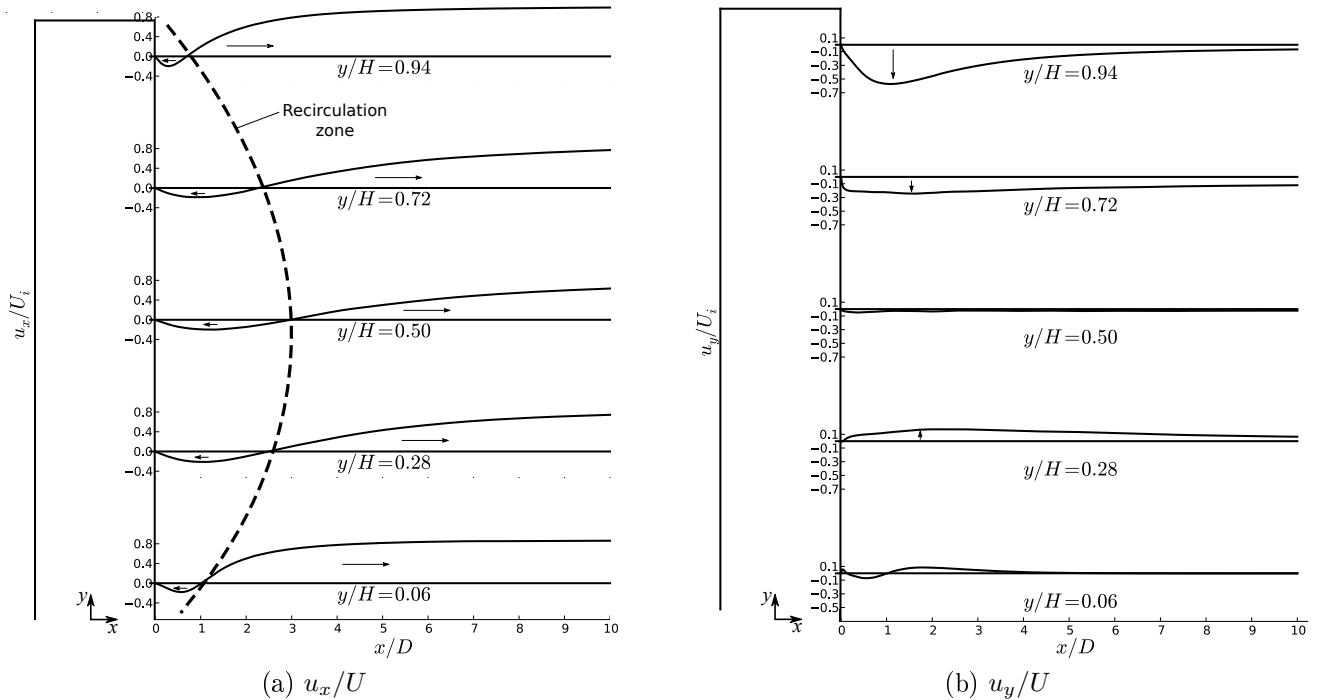


Figure 9.3: Time-averaged velocity profiles in the wake for  $u_x$  and  $u_y$  (Joubert *et al.*, 2015)

Considering the side-wall recirculation velocity profiles in figure 9.4 a, it can be seen that the flow tends to move down for  $y < H/2$  and up for  $y > H/2$ . Close to the base an inversion of the flow direction is observed as well as a large velocity gradient indicating the presence of a vortex structure. This flow pattern corresponds with the base vortex reported by Uffinger *et al.* (2013) and Wang (2004) in position and flow direction. An upward flow is observed at height  $0.94H$  with maximum value of  $0.15U$  at distance  $0.5D$  from the beam. Near the base ( $y = 0.06H$ ), on the other hand, a downward flow is noticed of magnitude  $0.22U$  at distance  $0.5D$  from the beam. The vertical

velocity component is approximately zero at mid-height ( $y = H/2$ ) indicating the vertical position on the beam best representative of infinite cylinder flow.

The horizontal component of the flow (figure 9.4 b) shows strong movement away from the beam similar to what was seen in figure 9.1. The maximum flow movement away from the beam occurs at height  $H/2$  of which the magnitude is  $0.21U$  at a distance of  $0.7D$  from the beam side-wall. Again the flow direction inversion is visible at the base, characteristic of the base vortex.

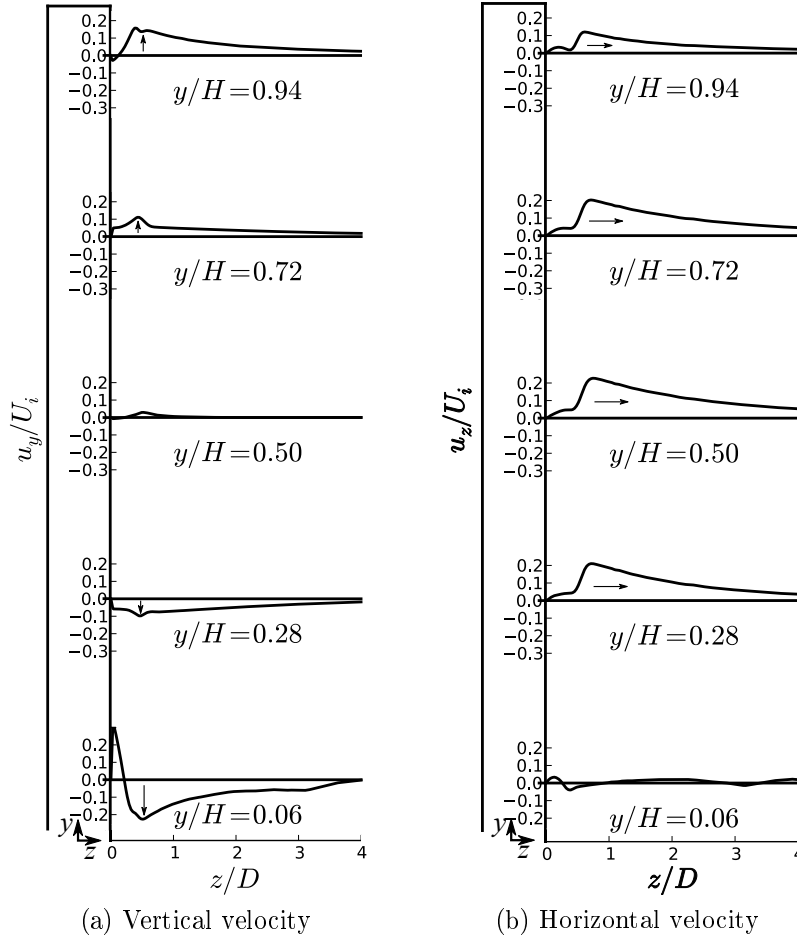


Figure 9.4: Time-averaged horizontal velocity profiles on the side-wall region for  $u_y$  and  $u_z$  (Joubert *et al.*, 2015)

## 9.2 Flow-induced Loading

In figure 9.5 the dimensionless pressure and velocity magnitudes are displayed at the beam mid-height ( $y = H/2$ ) for times of maximum and minimum lift



during the vortex shedding cycle. Low pressures points are related to the centres of vortices. In general a clear stagnation point is visible at the upwind side of the beam where velocity is reduced to zero and translated to pressure.

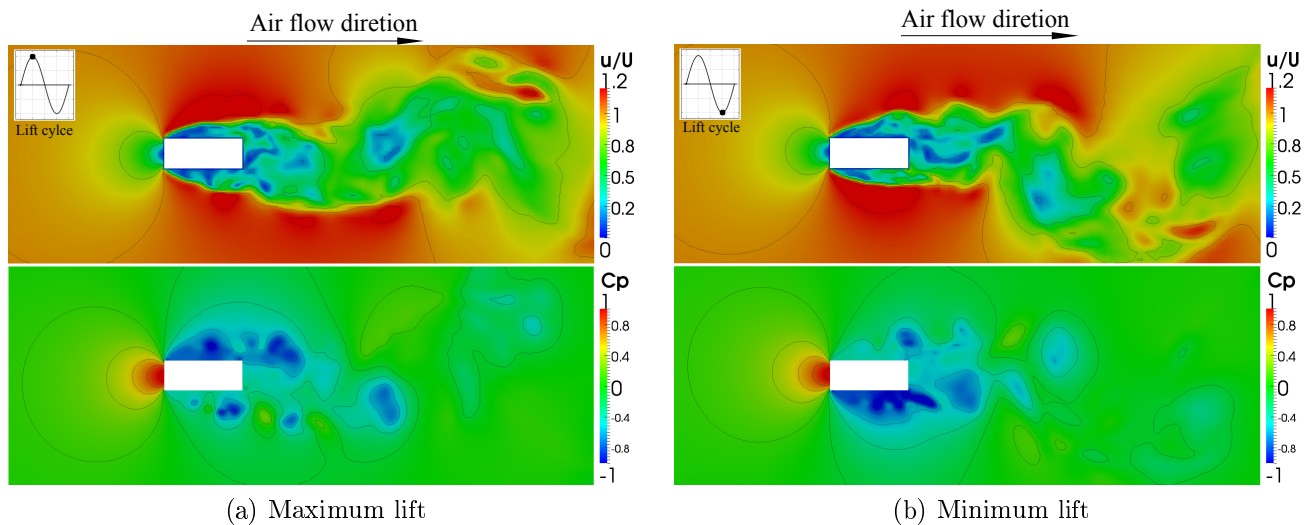


Figure 9.5: Instantaneous velocity and pressure for the points of maximum and minimum lift during the vortex shedding cycle (Joubert *et al.*, 2015)

The pressure difference between the upstream and downstream faces of the beam is greater than the difference between the side-walls but loading in the stream-wise direction acts on a smaller surface and remains steady where, on the other hand, the transverse loading is time-dependent and acts on a larger surface (see figures 9.5). This pressure difference between the side-wall surfaces can be used to construct the lift coefficient ( $C_L = \Delta P / (1/2\rho U^2)$ ). Shear forces were not included in the calculation of the lift coefficient since these were deemed negligible and irrelevant for the purpose of this investigation. The lift coefficient was used to identify the vortex shedding frequency as shown in figure 9.6 for  $y = H/2$  (showing only small portion of the total simulated time). This lift coefficient also characterises the time-dependent transverse vortex-induced structural loading.

Although time-dependent, vortex-induced loading is present, a clear vortex shedding frequency is difficult to identify since the flow pattern seem to change randomly. The interruption of the vortex shedding cycle may be due to the three-dimensional flow features produced by the base and tip.

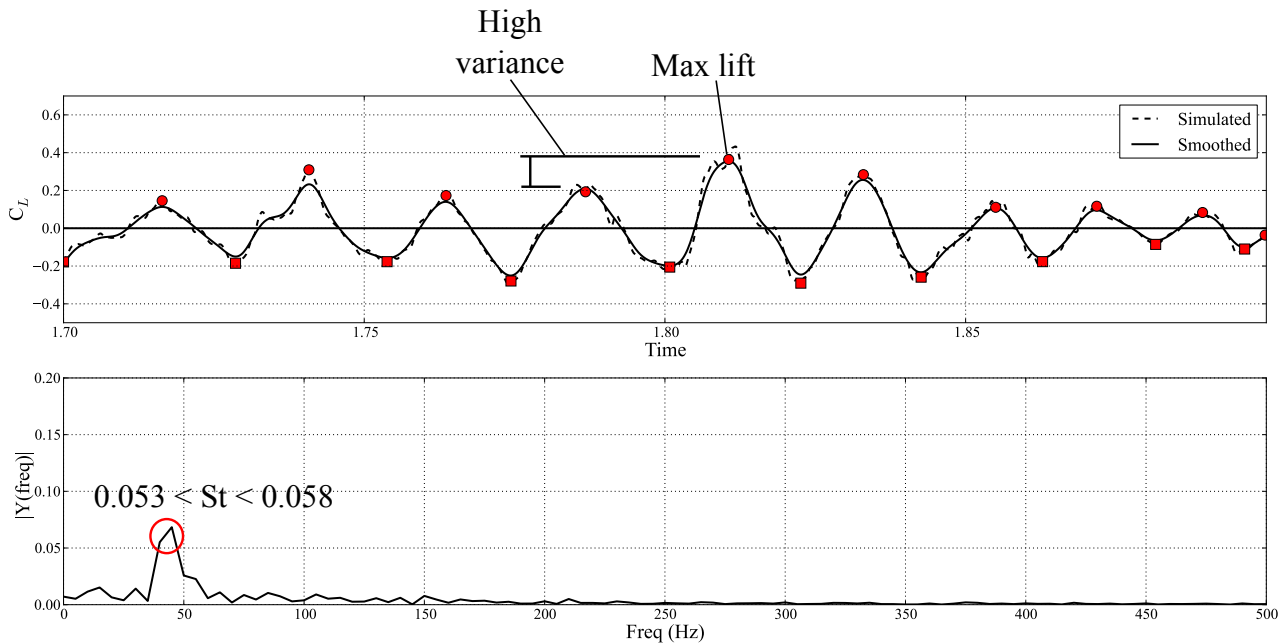


Figure 9.6: Identifying key points in the vortex shedding cycle using the lift coefficient (adapted from Joubert *et al.* (2015))

The lift distribution over the height of the beam is shown in figure 9.7 for the points of maximum and minimum lift during the vortex shedding cycle. It can be seen that the loading is not uniform over the beam height. Cyclic loading is the most extreme at mid-height ( $y = H/2$ ) with the average of the lift coefficient extremes varying between  $-0.13 < C_L < 0.13$ . On the other hand, the cyclic loading at the base and tip of the beam seem less severe. It should also be noted that the data shows significant standard deviations indicating that the lift at these extreme points can vary substantially which is also visible in figure 9.6. Furthermore, since the pressure at the top of the beam were under predicted with the simulations (see figure 5.3 c) the lift values at the top of the beam are also not conclusive.

Considering the pressure distribution around the half perimeter of the cross-section of the beam at height  $y = H/2$  shown in figure 9.8, it can be seen that the beam is also uniformly loaded along the side-wall. The downstream part of the side-wall experiences more cyclic loading extremes than the upstream part with a maximum lift of 1.9 occurring at  $2.1D$  (or  $0.8L$ ) from the upstream edge of the beam. This phenomena is attributed to alternating vortex shedding and resulting loading which has a greater effect downstream due to larger vortices in the downstream region of the side-wall.

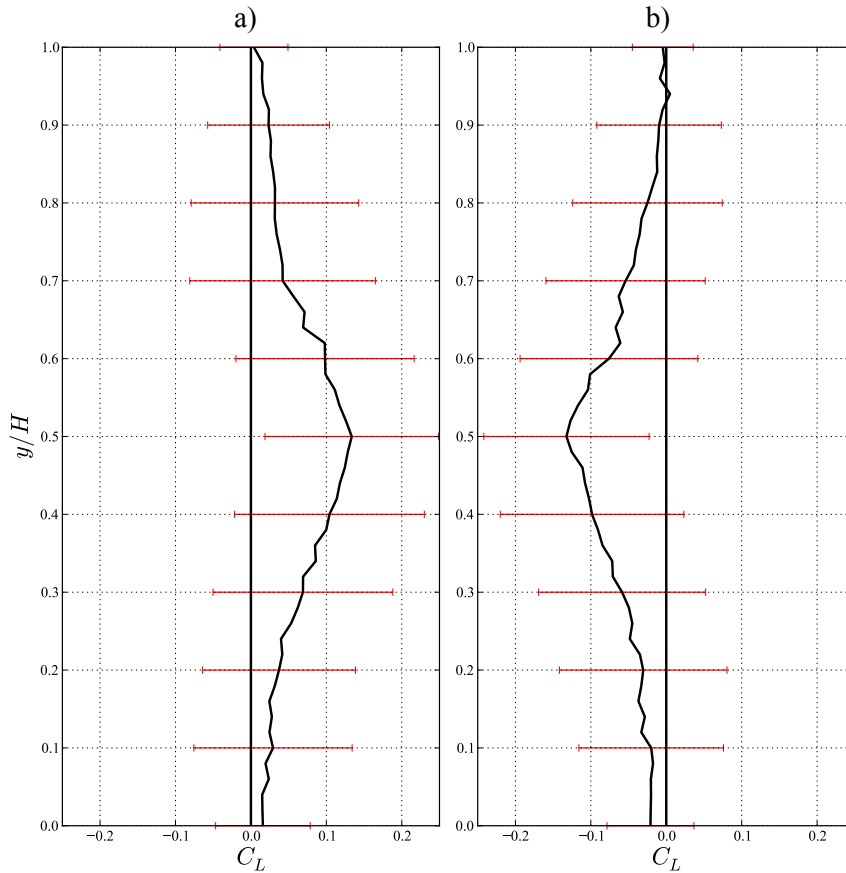


Figure 9.7: The time-averaged lift coefficient distribution over the height of the beam for the point of a) maximum and b) minimum lift during the vortex shedding cycle with standard deviations (Joubert *et al.*, 2015)

### 9.3 Vortex Structures

The instantaneous iso-contours of  $Q$  are displayed in figure 9.9 showing the highly complex vortex flow patterns for the side-wall and wake regions. The following flow features can be identified:

- The height of the wake region decreases downstream (wake funnel effect in figure 9.9 b) corresponding to the downward movement observed for flow in the wake near the top of the beam (see figure 9.2 and 9.1).
- The width of the wake region increases downstream as eddies expand (wake expansion effect in figure 9.9 a).
- The unsymmetrical shape of the wake region from the top view (see figure 9.9 a, suggests a lower frequency oscillation than the vortex shedding

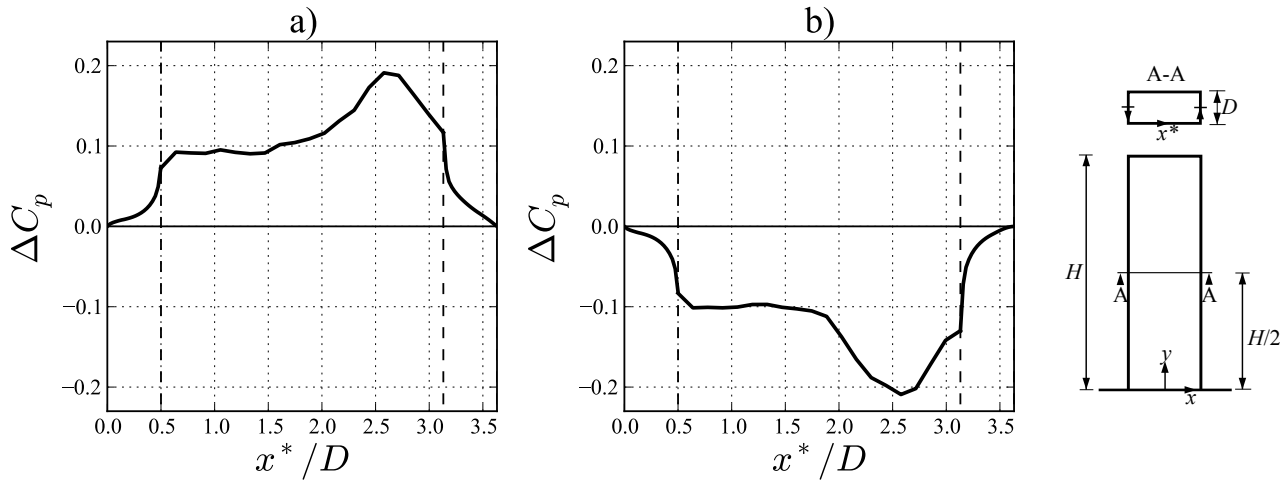


Figure 9.8: The time-averaged pressure coefficient distribution over the half perimeter of the beam cross-section for the point of a) maximum and b) minimum lift during the vortex shedding cycle (Joubert *et al.*, 2015)

which could also translate to the time-dependent transverse loading on the beam.

- An attached vortex overarching the beam is permanently present at the upstream edge of the side-wall and top surfaces. Similar permanent vortex formations have been observed in a number of bluff body studies reported by Uffinger *et al.* (2013), Bruno *et al.* (2010) and Wang (2004).
- At approximately  $L/3$  from the upstream edge vortices shear off of the permanent vortex unevenly and almost immediately start to twist and fold to form hairpin vortices.
- A vortex usually has a part that is driven downstream by the viscous shear forces (velocity gradients) and the free-stream flow along the outer edge of the wake where high velocity gradients are present.
- A vortex usually has a number of parts that is lagging behind due to the slow moving inner wake region.
- The consequence for these driving and lagging parts is vortex stretching producing hairpin vortices that expand as they move downstream.

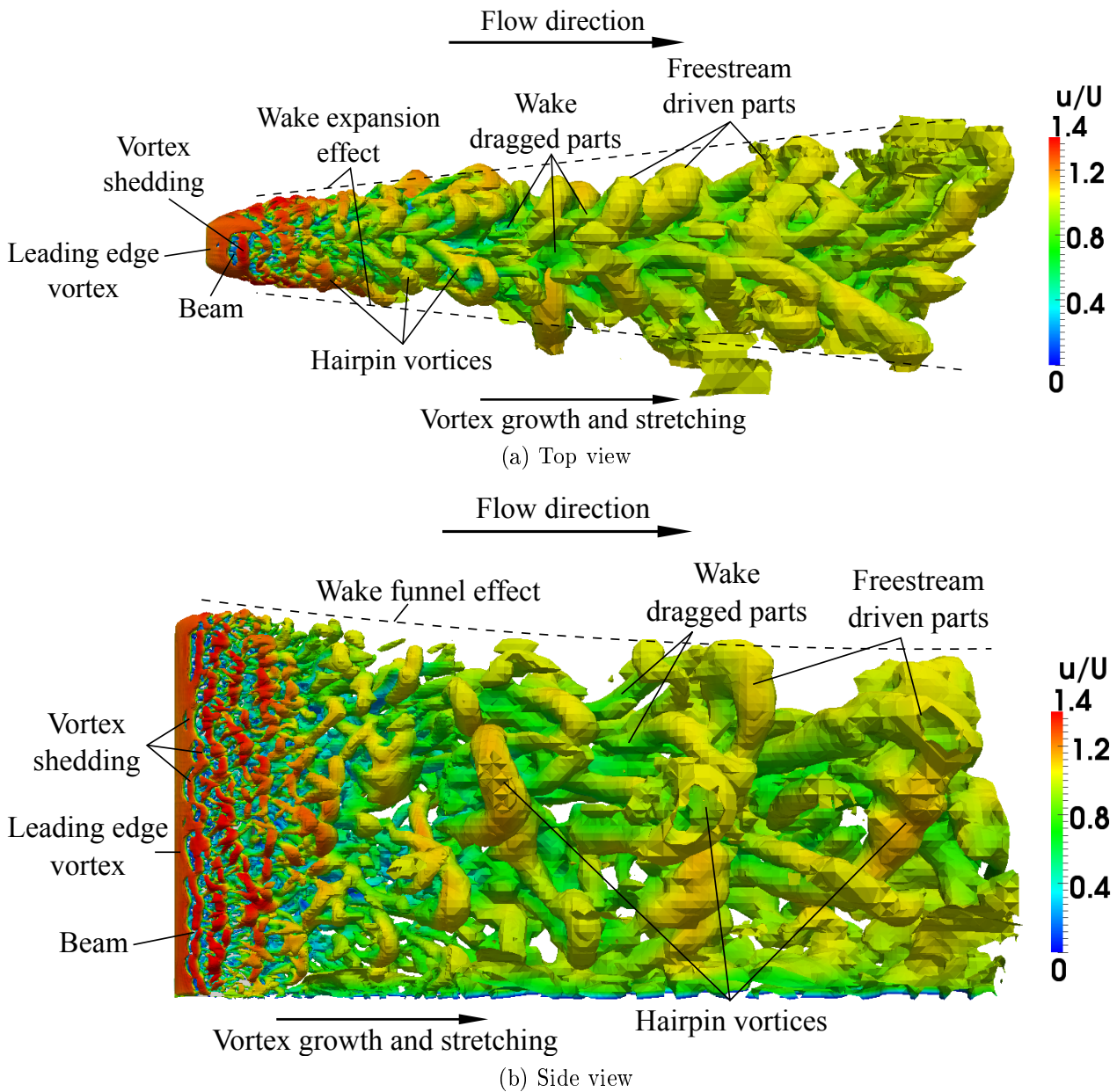


Figure 9.9: Iso-surfaces ( $Q = 5 \times 10^{-5}$ ) (Joubert *et al.*, 2015)

## 9.4 Vortex Stretching

In figure 9.10 three simplified, clear and consecutive vortex formations for the Realizable  $k-\epsilon$  model can be seen. The vortex forms on the side wall of the beam and detaches when reaching the wake. In the wake region the vortex forms a vertical horse shoe shape with end points in the recirculation zone pointing upstream. The middle of the vortex is driven by the free-stream thereby

stretching it downstream. The same phenomena is visible for the other turbulence models used only on smaller scale. The more of these vortices present the more complex the interactions and the resulting vortex entanglement and eventual breakup.

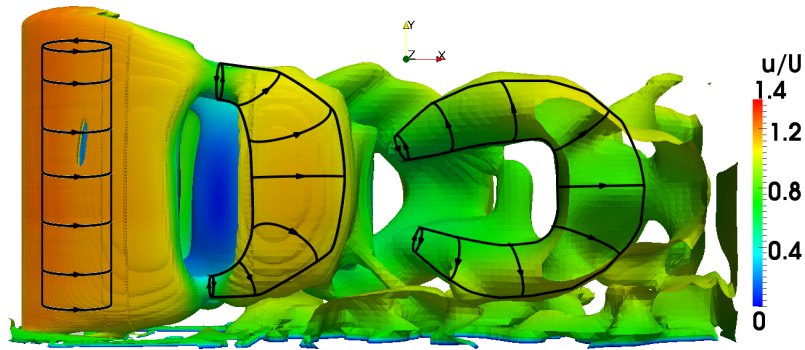


Figure 9.10: Vortex stretching in the wake region

## 9.5 Time-dependent Structural Response

In figure 9.11 a, the time-dependent pressure is shown for two points on the beam surface. One on the front and the other on the back side-wall faces at  $x = 0$  and  $y = H/2$ . The pressures differences on both sides of the beam varies over time. This causes a lift force as shown in figure 9.11 b. Consequently, the beam dynamic response follows the applied load resulting in an oscillation in the  $z$ -direction.

In figure 9.11 c, the beam tip displacement is presented as a result of the flow-induced loading. Since the beam is affected by a large number of nodes, and not only the two represented here, the response is smoother and may also differ slightly from the mid-height side wall nodes. The mesh displacements for points A and B (see figure 9.11 c) are shown in figure 9.12.

The structural response, represented by the beam tip displacement and frequency, for 1 second of simulated time is displayed in figure 9.13. The structure oscillates at a frequency of 40 Hz ( $St = 0.051$ ) which corresponds very well with the applied load and first natural frequency (NF).

In figure 9.14 a trace of the beam tip displacement in the  $x$  and  $z$ -directions is shown for 1 second of simulated time. From rest, the beam tip displaces approximately 0.05 mm downstream ( $x$ -direction) and then starts to oscillate

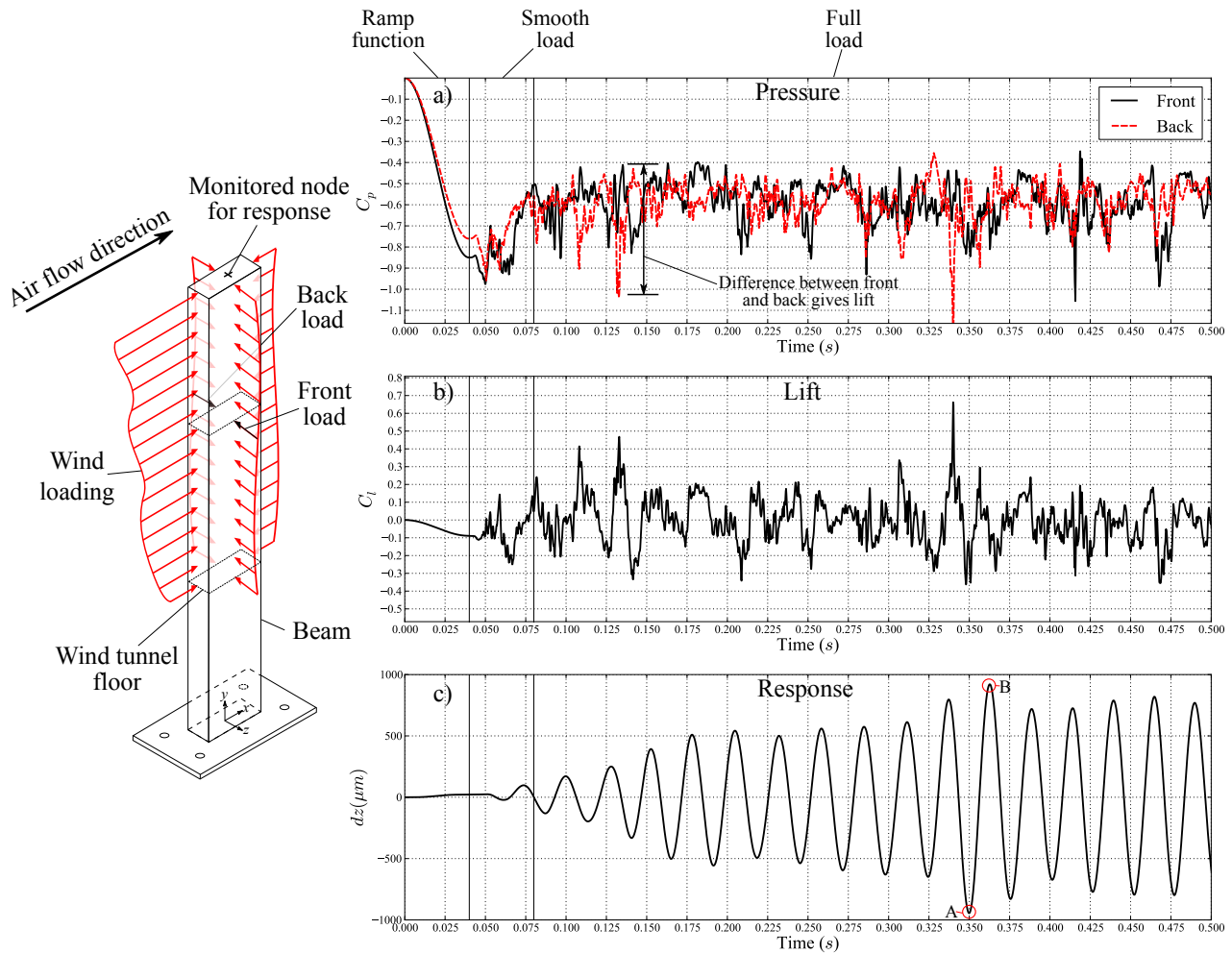


Figure 9.11: Time-dependent a) surface pressure, b) lift and c) tip displacement (where points A and B are the time instances of minimum and maximum tip displacement which used for further discussion)

in the  $z$ -direction to a maximum of 1 mm but mostly less than 0.8 mm. The maximum displacement is 2.6 % of the beam width and 0.1 % of the total beam height (measured from channel). For the purpose of this study this displacement is considered sufficiently small for the one-way coupling approach employed. The beam oscillation also has a streamwise oscillation component although this is much smaller at 0.024 mm and only 0.06 % of the beam width.

In further analysis it was found that the maximum simulated strain reaches only 10 % of the maximum measured strain which occurs during the maximum transverse displacement of the beam tip. This could be due to a number of reasons. Firstly, the turbulence models calculate very different loading amplitudes which was not possible to verify experimentally. If the loading amplitudes are

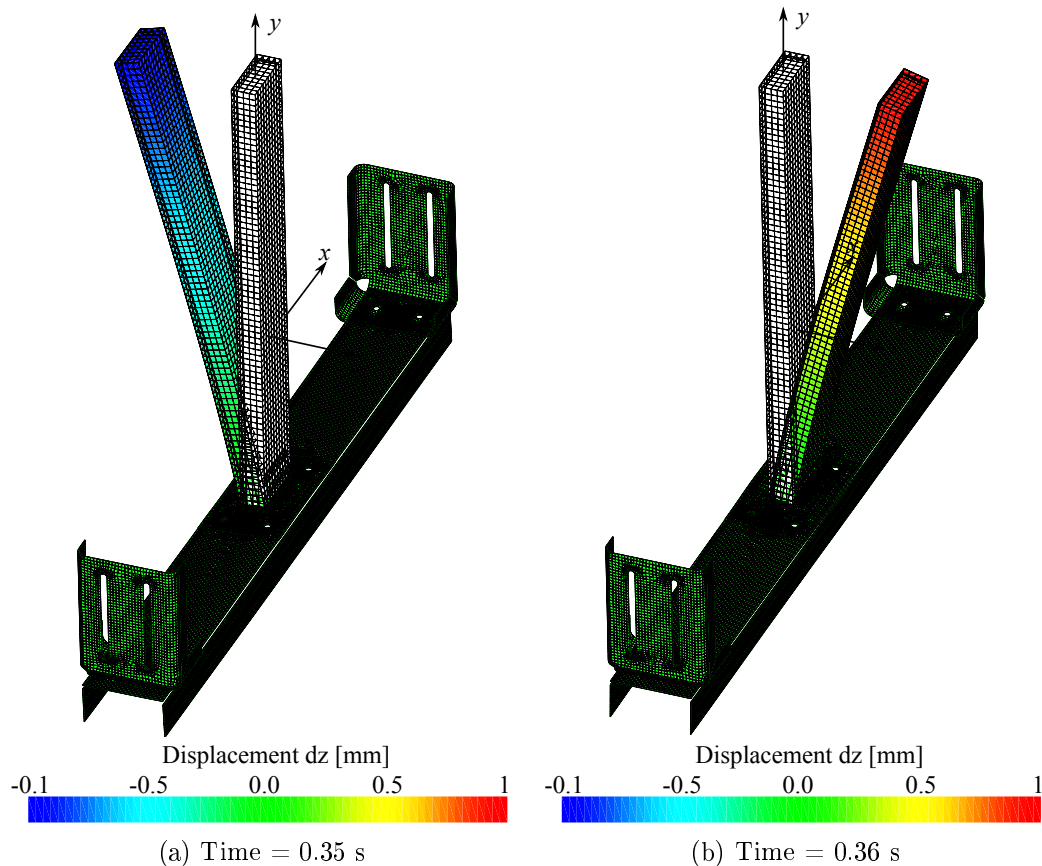


Figure 9.12: Mesh deformation at times of minimum and maximum displacement

under-predicted due to limitations of the turbulence model it would explain the under-predicted strain obtained with the simulations. Even so, the IDDES model provided the most accurate results and computational efficiency. Additionally, most other models produced significantly smaller amplitudes so choosing a different turbulence model would have no clear benefit.

Secondly, this case was chosen specifically because of the transient oscillations observed in the measurements and because the flow simulations produced a loading frequency close to the first NF of the beam. Since the first NF represents the inception of resonance and the lock-in phenomena this case would be at, or very close to, the limits of the proposed methodology's applicability since it was not developed for two-way FSI. This means that the under-predicted strain could be due to the limitation of the one-way coupling method if two-way FSI is present in these conditions.

Thirdly, the linking method does not involve a speed-up process as the



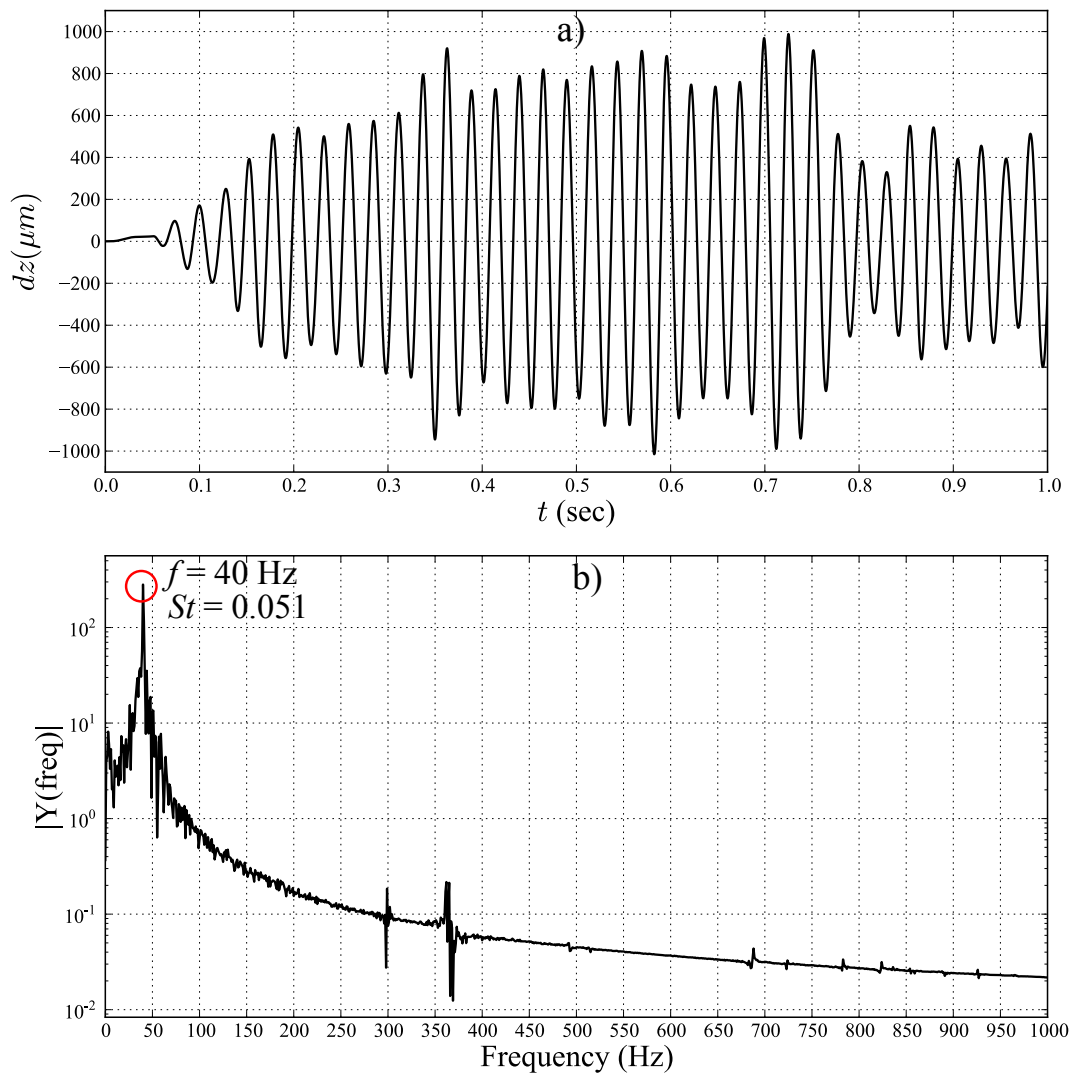


Figure 9.13: Tip displacement frequency

beam would experience in the wind tunnel. Since the CFD at  $U = 30$  m/s produces a loading frequency of 40 Hz which is slightly higher than the first NF of 37 Hz of the parallel beam it means that the high oscillation region might have been bypassed. The results could possibly produce larger oscillations if a speed-up process was included in the linking method.

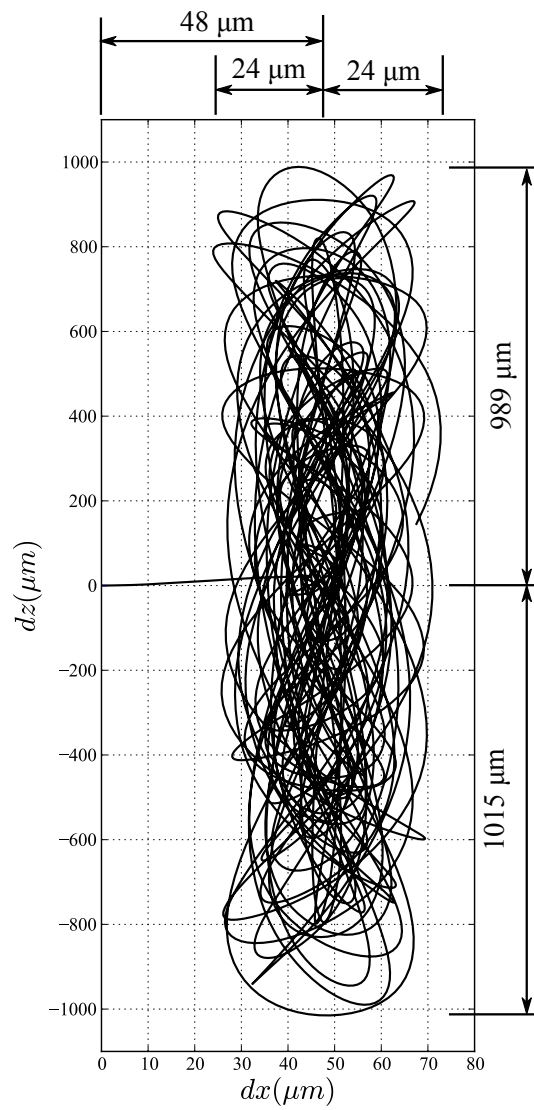


Figure 9.14: Tip displacement trace

# Chapter 10

## Conclusion

### 10.1 Summary of Results

In this study a cantilever beam was selected as a suitable bluff-body structure for the one-way fluid structure interaction (FSI) investigation. Different orientations of the beam made it possible to investigate two different cross-section length to width ratios namely  $L/D = 2.63$  and  $0.38$ . Various lab measurements were done to determine the mechanical properties, aerodynamics and structural response due to the flow-induced loading. This included velocity fields using particle image velocimetry (PIV), pressure on the beam surface, vibration and strain. For these measurements the beam was orientated parallel and perpendicular to the flow and the flow speeds of  $U = 30$  m/s and  $60$  m/s were considered.

OpenFOAM and Code-Aster open source software was used to simulate flow, loading and structural response. A segregated solution was used to solve the one-way FSI and data was transferred between the finite volume computational fluid dynamics (CFD) mesh and the finite element structural mesh using Python software by defining time-dependent, discrete load functions for each structural element according to its nearest fluid mesh neighbour.

For the fluid dynamics the Realizable  $k-\epsilon$ ,  $k-\omega$  SST, Non-linear  $k-\epsilon$  Shih and Spalart Allmaras IDDES turbulence models were compared against measured data. All models performed well in the near-wall region but some errors were observed in the wake where the recirculation length was overestimated. All models produced similar vortex shedding frequencies of  $0.05 < St < 0.06$  which compares very well with literature studies of similar  $L/D$  ratios. Overall, the

IDDES model was found to produce the most accurate results and the second fastest after the  $k-\omega$  SST. The IDDES model was, therefore, further validated for different flow speeds and beam orientations and compares very well with PIV and pressure data. The drag on the beam is measured to be 12.9 N which is under-predicted by 1.6 % using the IDDES model. The results for the IDDES model also support the use of the “all- $y^+$ ” wall treatment and simplified inlet conditions.

The structural model is also validated using strain and vibration measurements. The model accurately predicts the mean strain on the upstream face, at the base of the beam, due to an equivalent drag load, with only 1.8 % error. The first natural frequencies were also accurately predicted to be 37 Hz for the parallel beam and 48 Hz for the perpendicular beam with no error. In the FSI simulations the mean strain in base of the beam was accurately predicted for the parallel beam but a 16 % error was observed for the perpendicular beam results which could possibly be improved with further sensitivity studies and more sophisticated linking schemes. Strain gauge measurements indicates that only the parallel beam orientation subjected to  $U = 30$  m/s produces significant cyclic oscillations which occurs at the 37 Hz, the first natural frequency (NF) of the beam. This is supported by the CFD simulations for the same orientation and speed which predicts oscillating loading at 40 Hz, close to the first NF of the beam. This case was investigated in detail to shed light on the underlying mechanics of bluff-body aerodynamics and structural loading.

The time dependent one-way FSI simulations for this case showed that the beam tip displacement under loading is less than 1 mm supporting the one-way interaction approach. The beam predicted oscillates are in phase with the flow-induced loading and first NF of the beam. However, the maximum strain predicted by the simulations was only 10 % of the measured values which raises the question if this point, at the first NF, is not already within the two-way FSI category which would explain the under-predicted strain. Since the CFD predicts a frequency slightly higher than the first NF of the beam and the linking method does not involve the speed-up as the beam would experience in the wind tunnel it is possible that the results could also be improved by including a speed-up effect in the linking procedure.

Based on the literature study, current wind tunnel measurements and simulations the results from this work provides a number of insights relevant to the

SANAE IV base. It is confirmed that bluff-bodies of similar  $L/D$  ratios induce highly separated flows and wind induced loading in the direction transverse to the wind due to the elongated afterbody. For the SANAE IV base these forces would impact on the top and bottom panels of the base where large oscillations would be experienced when the vortex shedding frequency reaches the NF of the structural elements. Possible remedies might be to modify the aerodynamics by changing the outside structural geometry, to identify the important natural frequencies and modifying these by adding masses or dampers and lastly to isolate the affected panels from the rest of the structure. Should a future study of wind loading on the base be performed it is strongly recommended to make use of the validated methodology provided in the current work.

Large computational requirements were needed especially for the CFD simulations. For example, a typical simulation with 3.5 million cells used approximately 4.6 GB RAM and took 5 weeks to complete 2 seconds of a transient simulation which includes approximately 90 vortex shedding cycles for the parallel beam,  $U = 30$  m/s and  $L/D = 2.63$ . Post-processing and linking of the data for large simulations took approximately 4-5 days and the finite element analysis (FEA) simulation took approximately 1.5 days to complete. Since the CFD simulations contribute the most significant computational time any speed-up in the CFD part would greatly benefit the FSI simulation. However, with the current tools available it seems difficult to achieve any speed-up without sacrificing accuracy unless larger computational resources are utilised. With relatively small modifications it would be possible to do the linking and FEA structural simulation during the CFD simulation thereby saving approximately 1 week. Further speed-up improvements are possible for FSI simulations of larger structures if simpler elements are used.

## 10.2 Future Work

Here are a list of recommended topics for future studies that were highlighted as a direct result of this project:

- Apply the developed one-way method to a large scale structure such as the SANAE IV base for different flow regimes, to highlighting the

most important structural loading concerns and propose modifications to mitigate these loading impacts.

- Identify a ratio of structure characteristic length to displacement length which forms the boundary between one-way FSI and two-way FSI. For example: If a large building undergoes 1 cm displacement this may be considered one-way interaction only since the global flow field will not be affected significantly. However, if a small structure undergoes 1 cm displacement then it might have a significant effect on the global flow features.
- Investigate the lock-in effect on the parallel beam ( $L/D = 2.63$ ) with the current model by considering various flow speeds around the lock-in point which occurs at the first natural frequency. It would be interesting to see how the model responds when approaching the first natural as well as what happens after. It is suspected that the structural displacements would increase around the point of resonance and then decrease thereafter which means that it will still be accurate at resonance but at higher speeds if lock-in has occurred. For this work a speed-up mechanism for the linked loads could also be considered to artificially increase the loading frequency which would save computational resources.
- Develop a strongly coupled FSI model in OpenFOAM and Code-Aster starting from the reported methodology and additionally implement mesh motion and information transfer between time-steps or even internal iterations to make this model applicable to structures with larger displacements. Since the strongly coupled solver would require more computational resources to handle the additional re-meshing and FSI linking convergence, this work should strongly consider ways of reducing the computational resources while maintaining accuracy.
- Investigate the impact of applying the same CFD load but on a simplified structural model as for example using beam elements instead of shell elements. This would require a closer look at the linking procedure to make sure that forces and moments are applied correctly. This work has the potential to reduce the computational time but it will have no effect

on the CFD simulations which require the bulk of the resources and take most of the time.

# Appendices



# Appendix A

## Instrumentation Calibrations and Specifications

### A.1 Particle Image Velocimetry

The PIV requires a calibration grid to determine the direction and magnitude that particle clouds move between two image pairs taken a short time apart. The calibration target is a  $200 \times 200$  mm dotted square that the image recognition software uses to fit the calibration grid to (as shown in figure A.1). Once the grid is set the relative distances and directions to any pixel on the image are known. Additionally it is required to enter the magnitude scaling so that the absolute distance can be determined.

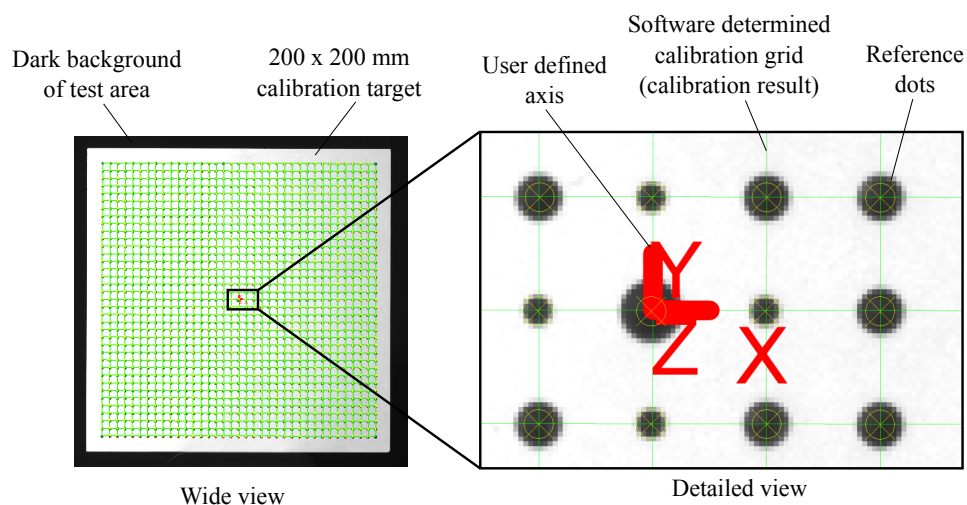


Figure A.1: PIV calibration target

Even when the calibration seems accurate initial results should always be validated to see if the calibration was done correctly. One way to do this is to check the velocity direction and magnitude in the free stream against the set velocities.

## A.2 Pressure Transducers

The pressure transducers were calibrated before and after the tests to check for any changes. The relation of output voltage to pressure is linear and to quadratic to velocity since  $P = \frac{1}{2}\rho V^2$ . The results show that the calibration did not change during the tests. It also indicates that the velocities of 30 m/s and 60 m/s correspond to 2.44 Volts and 3.75 Volts respectively.

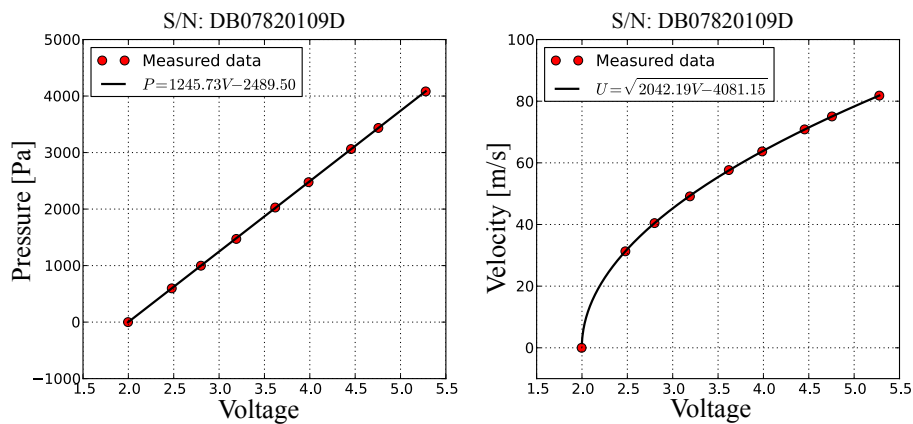


Figure A.2: Pressure transducer calibration curves (S/N: DB07820109D)

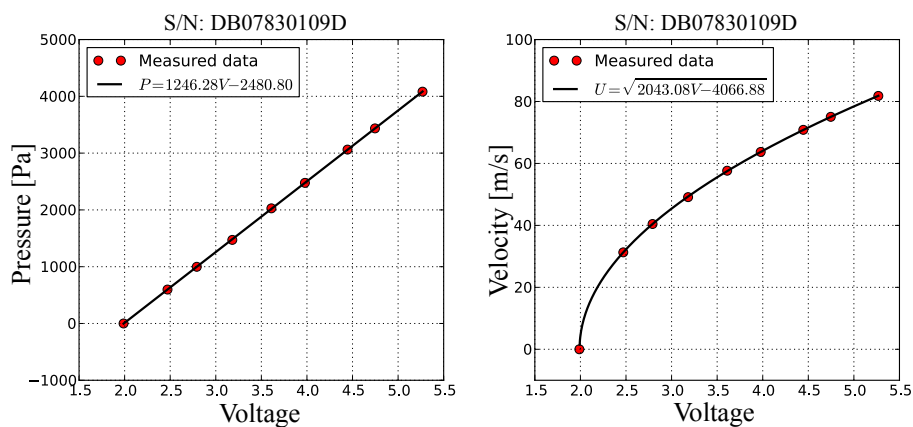


Figure A.3: Pressure transducer calibrations curves (S/N: DB07830109D)

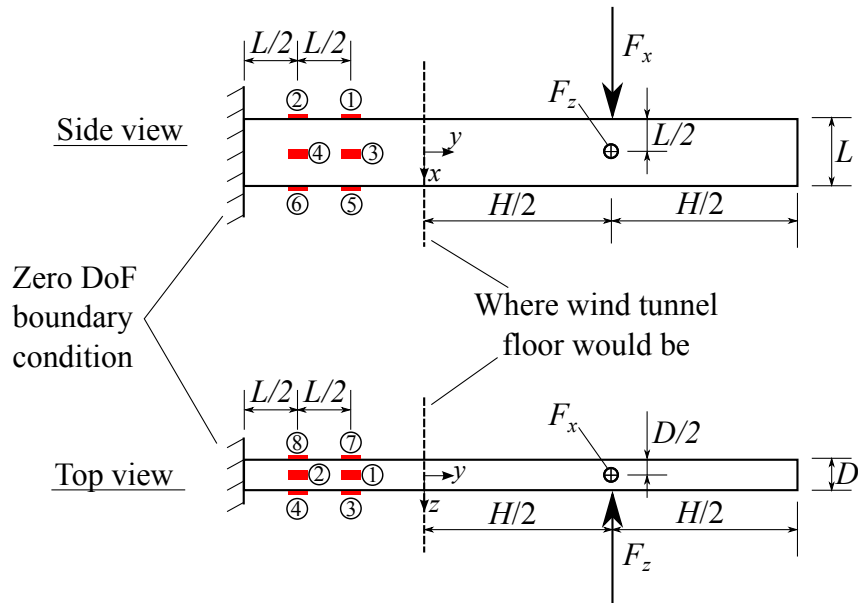
### A.3 Strain Gauge Specifications

The strain gauge specifications are provided in table A.1. These were selected for measuring strain in the aluminium beam near the base. Strain gauges were applied in quarter bridge configuration.

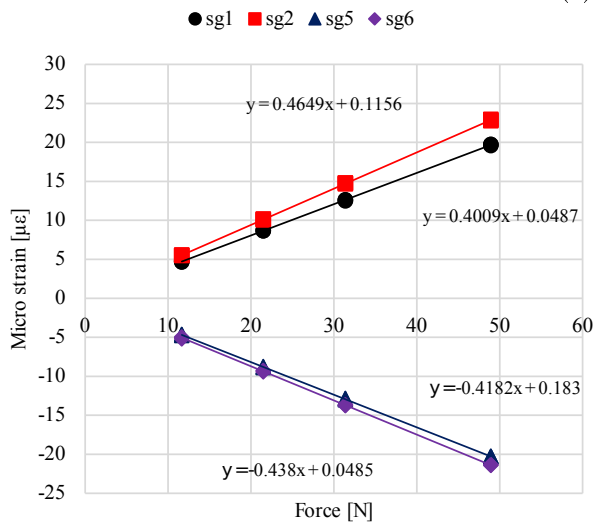
Table A.1: Strain gauge specifications

Parameter	Specification
Manufacturer	Kyowa Electronic Instruments Co., Ltd.
Type	KFC-5-CI-23
Material	Aluminium
Resistance	$120 \pm 0.3 \Omega$
Thermal expansion	23.4 PPM/ $^{\circ}\text{C}$
Gauge length	5 mm
Gauge factor	0.015 %/ $^{\circ}\text{C}$

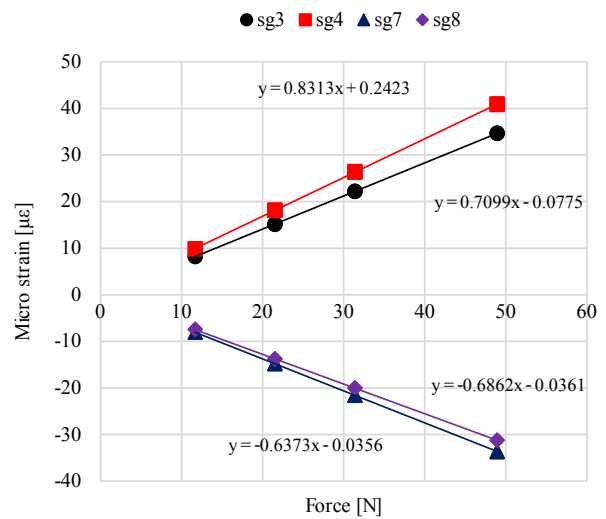
The strain gauges for both beams were calibrated to get a relationship between an applied point load and the resulting strain. The experimental set-up is shown in figures A.4 and A.5 a. Two loading conditions were used, one with a force along the x-axis to calibrate sensors 1, 2, 5 and 6 and one with a force along the z-axis to calibrate the sensors in the 3, 4, 7 and 8. Each sensor's calibration curve is made up of 4 loads and each calibration curve was repeated 3 times. The calibration result for the are shown in figures A.4 and A.5 b and c.



(a) Set-up

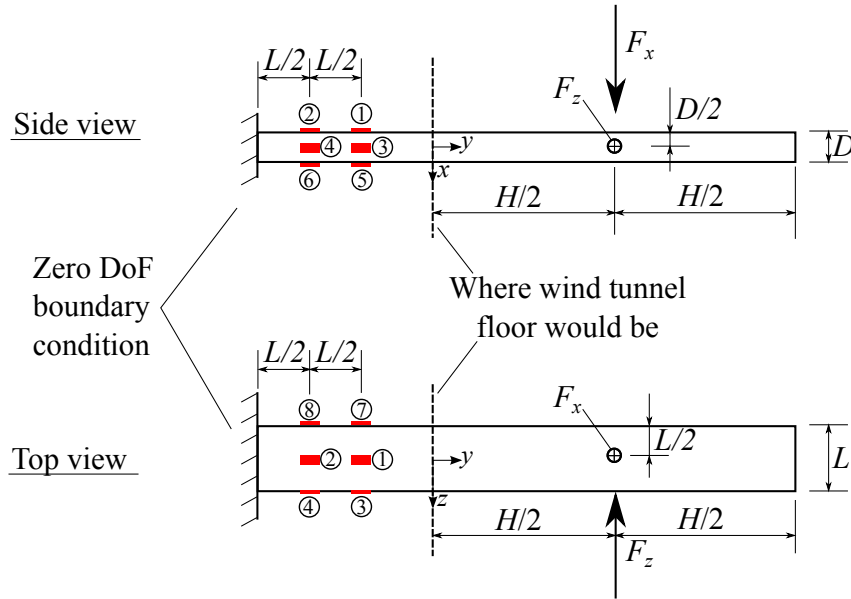


(b) Gauges 1, 2, 5 and 6

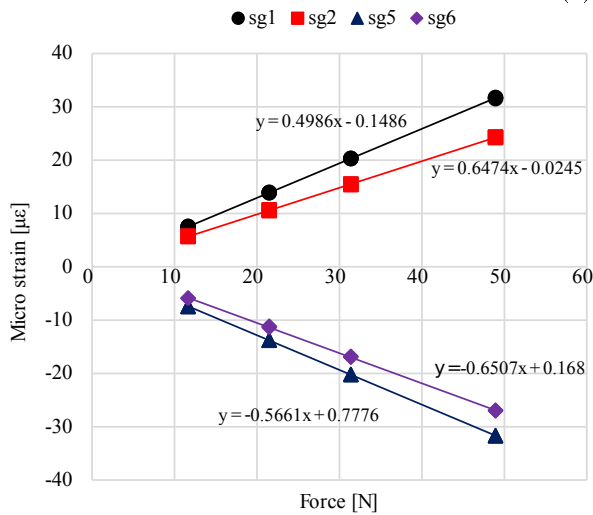


(c) Gauges 3, 4, 7 and 8

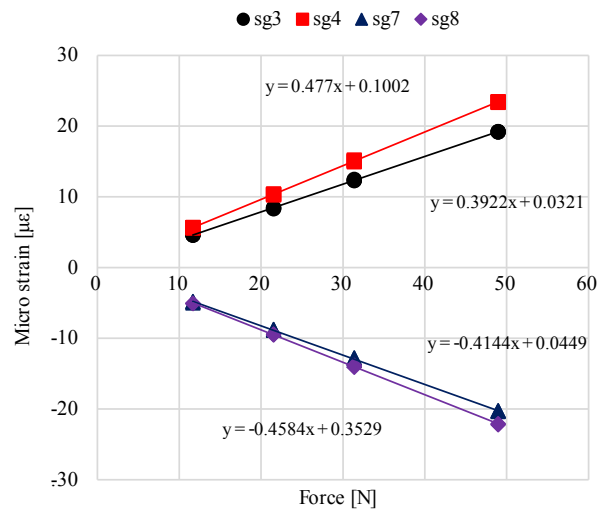
Figure A.4: Parallel beam strain gauge calibration curves



(a) Set-up



(b) Gauges 1, 2, 5 and 6



(c) Gauges 3, 4, 7 and 8

Figure A.5: Perpendicular beam strain gauge calibration curves

## A.4 Displacement Tests

Simple cantilever beam displacement tests were done using strips of the beam material of various lengths to determine the Young's Modulus of the material. This is described in section 4.6 for which one loading condition is shown in figure A.6. These tests were also convenient for testing the validity of the software since it could be compared to analytical results. The results are

compared in table A.2

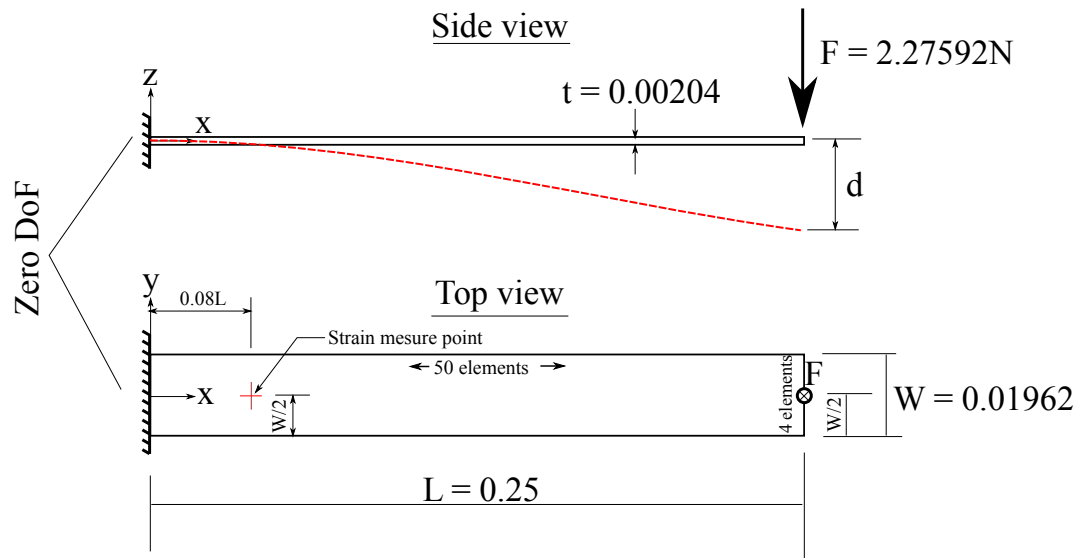


Figure A.6: Displacement test set-up

Table A.2: Displacement test results comparison

Source	Displacement, $d$ [mm]	Error
Analytical	12.04	n/a
Measured	11.92	1 %
Code-Aster	11.92	1 %
Genesis	11.94	0.8 %

## Appendix B

# Structural Model Parameters Sensitivity Analysis

During this study it was desired to establish what the effect was of varying different characteristics of the structure model. In this way it was possible to see where the structural model was the most sensitive to change. This aided in improving the modelling accuracy.

In table B.1 it can be seen that the free beam is not very sensitive to these changes. Even with large changes of 25% (which represent possible errors) in various attributes of the model only small variations in the modelled natural frequencies occur. Even so, considering the above modifications it can be seen that the free beam is most sensitive to changes in the mid-plate thickness since this component has the greatest mass contribution. A greater plate thickness increases the first natural frequency but this is not easy to predict since a higher mass should lower the natural frequencies but the greater stiffness from the thicker plate would increase the natural frequency.

In table B.2 it can be seen that the sensitivity to change increases with the natural frequencies. This means a small error in the model makes a small change to the prediction of the first natural frequency but a large change to the prediction of the third natural frequency which would explain the errors encountered here. The changes in the Young's modulus and density have similar influence in magnitude but of opposite effect. Increase in the Young's modulus (stiffness) generally increases the natural frequencies where, on the other hand, increases in density (mass) decreases the natural frequencies. For the mounted beam it is noted that the beam and channel top plates have the

Table B.1: Free beam sensitivity study

Characteristic	Change	NF 1	NF 2	NF 3
	%	%	%	%
Accelerometer mass	+25	0	-0.1	-0.19
	-25	0.4	0.03	0.15
Top plate thickness	+25	-1.15	0.54	1.05
	-25	0.4	0.03	0.15
Mid plate thickness	+25	3.64	13.8	4.48
	-25	-5.07	-17.62	-12.33
Bottom plate thickness	+25	-1.52	-1.36	-0.33
	-25	2.68	2.11	-2.7
	mm	%	%	%
Top plate offset	-d/2	0	0	0
	0	-0.15	-0.14	0
	+d/2	-0.3	-0.3	0
Mid plate offset	-d/2	0	0	0
	0	0.47	1.3	0
	+d/2	9.3	2.5	0
Bottom plate offset	-d/2	2.1	2.5	-0.67
	0	-3.9	-3.25	-0.67
	+d/2	0	0	0

greatest influence.

To conclude, it can be said that the structure mesh can be fine tuned to compensate for small errors by looking at the above characteristics but in general these changes are insignificant. For more significant other modifications such as boundary conditions or unaccounted masses should be investigated.



## APPENDIX B. STRUCTURAL MODEL PARAMETERS SENSITIVITY ANALYSIS

Table B.2: Mounted beam sensitivity study

Characteristic	Change	NF 1	NF 2	NF 3
	%	%	%	%
Accelerometer mass	+25	-0.45	-0.43	-0.06
	-25	0.45	0.43	0
Top plate thickness	+25	-2.55	-2.45	-0.12
	-25	2.7	2.6	0.12
Mid plate thickness	+25	-0.45	-0.5	-1.4
	-25	-0.9	-0.87	-1.46
Bottom plate thickness	+25	2.5	2.8	-0.12
	-25	3.9	3.97	-0.18
Channel side plate thickness	+25	0.15	0.57	2.43
	-25	-0.15	-0.87	-4.2
Channel top plate thickness	+25	1.95	1.8	-1.89
	-25	-2.4	-2.02	1.89
Bracket plate thickness	+25	0	0	2.3
	-25	0	-0.14	-3.35
Steel Young's Modulus	+25	0.75	1.44	11.5
	-25	-1.05	-2.02	-13.1
Steel density	+25	0	-0.07	-8.89
	-25	0	0.07	12.1
Steel Poisson's Ratio	+25	0.15	0.07	0.24
	-25	-0.03	-0.07	-0.12
	mm	%	%	%
Channel top plate offset	-d/2	ref	ref	ref
	0	0.57	0.5	-2.25
	+d/2	2.1	1.8	-4.5
Channel side plate offsets	-d/2	0.15	0.07	0.12
	0	0.15	0	0.12
	+d/2	ref	ref	ref
Bracket plate offsets	-d/2	0	0	7.98
	0	0	0	2.74
	+d/2	ref	ref	ref

# Appendix C

## Structural Drawings

This section provides supplementary structural drawings which will be needed to reproduce the models.

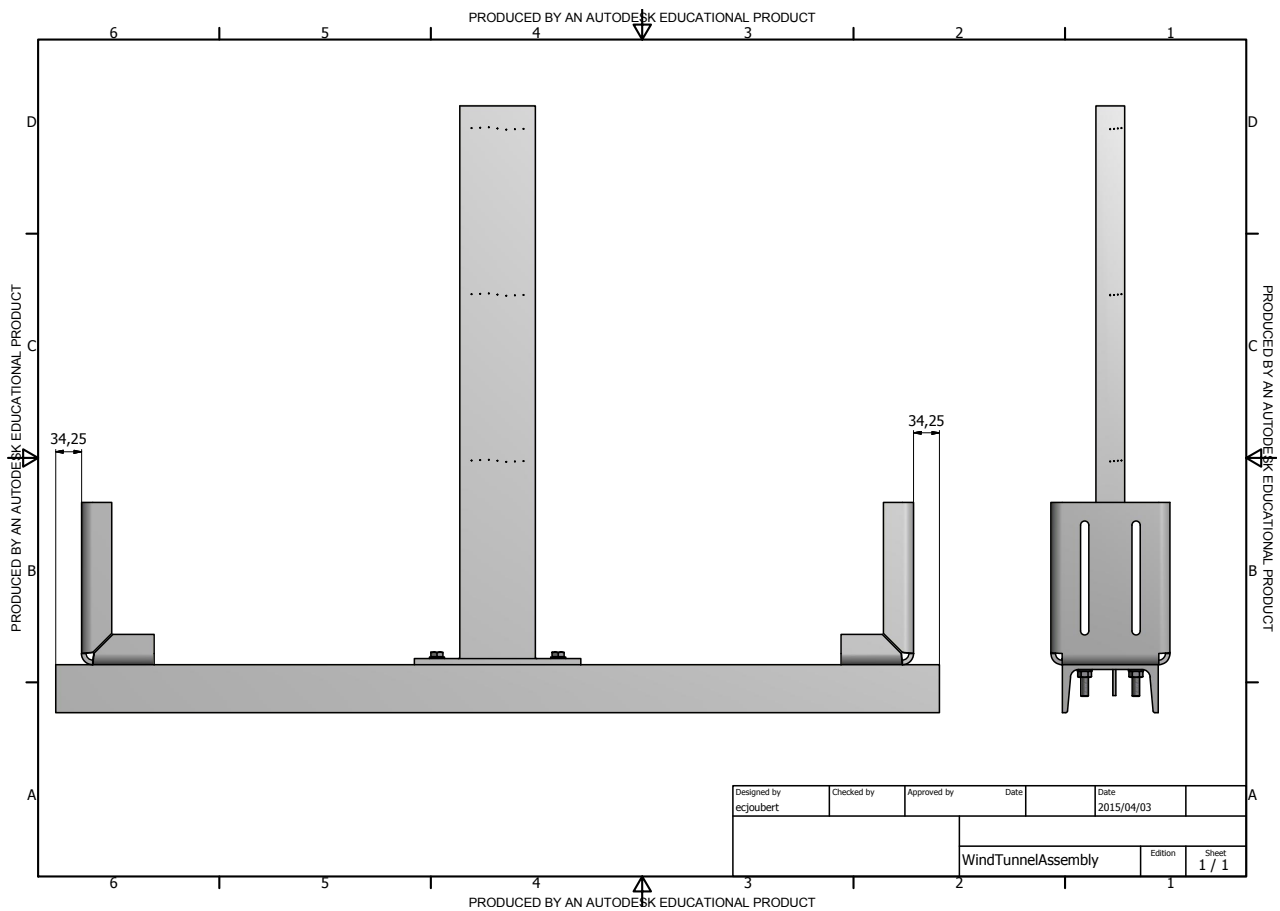


Figure C.1: Mounted beam assembly (showing parallel beam)

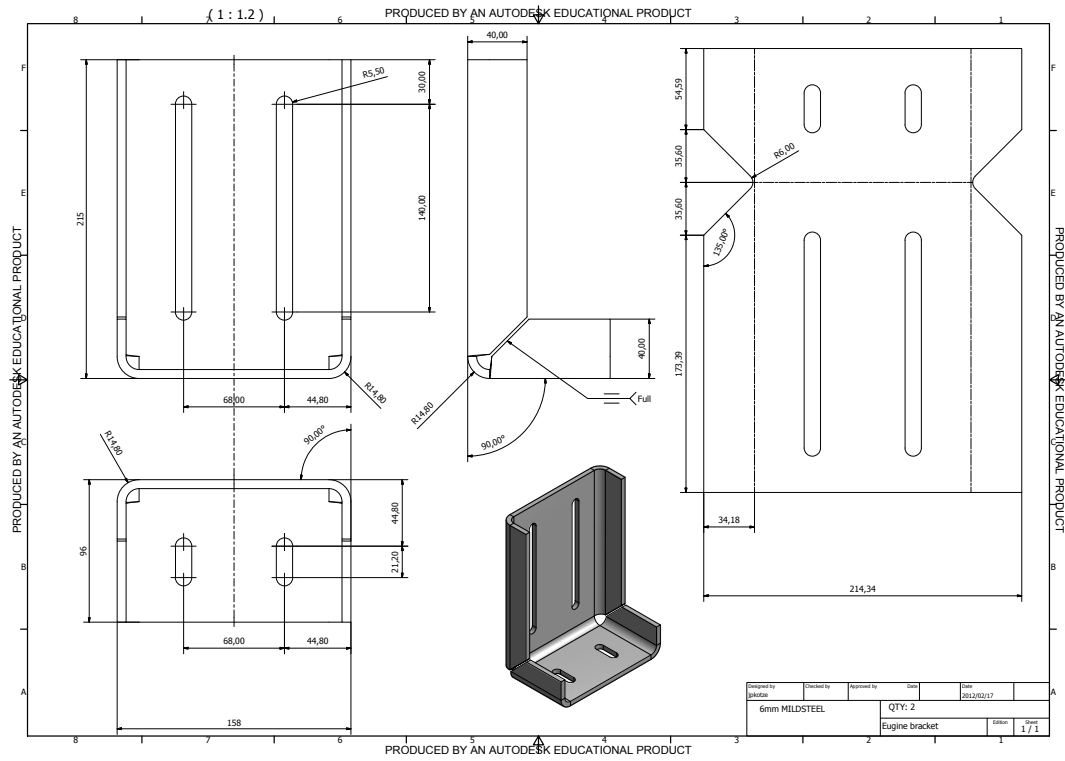


Figure C.2: Brackets dimensions

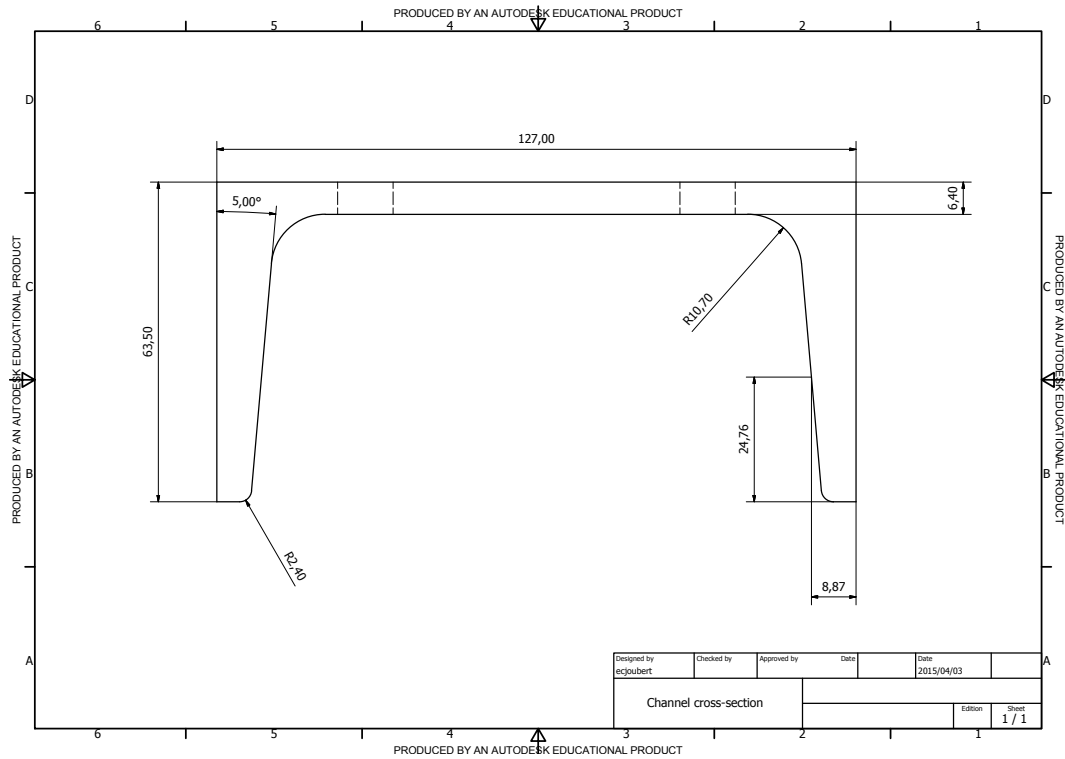


Figure C.3: Channel side view dimensions

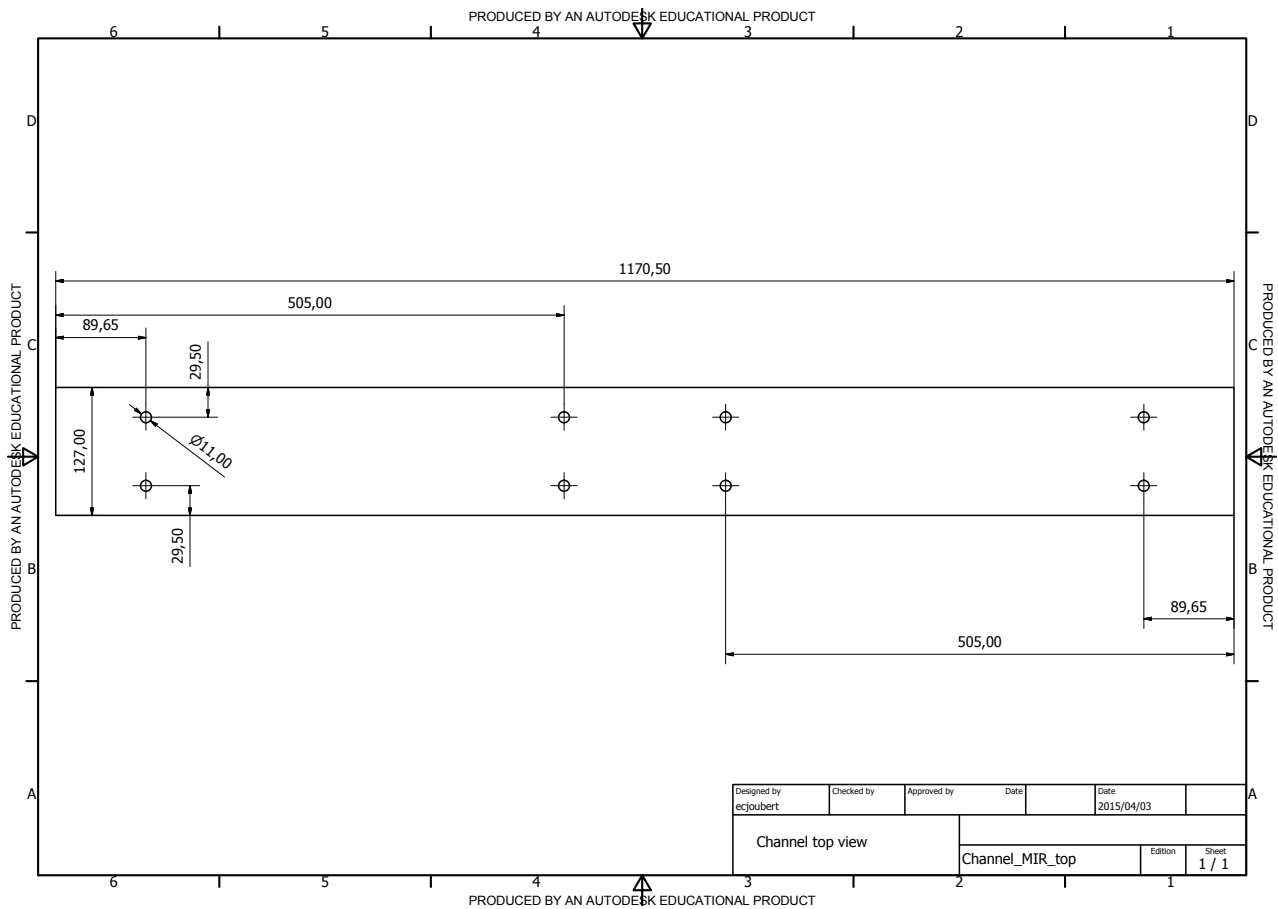


Figure C.4: Channel top view dimensions

# Appendix D

## Code

This appendix contains key code snippets used in the coupling method.

```
forall(patches[patchI], faceI) // loop through faces on patch
{
    point fCenter = mesh.Cf().boundaryField()[patchI][faceI];

    myMeshfile << faceI << "\t"
                << fCenter.x() << "\t"
                << fCenter.y() << "\t"
                << fCenter.z() << "\n";
}
```

Figure D.1: Extract fluid mesh (OpenFOAM utility)

```
forall(patches[patchI], faceI) // loop through faces on patch
{
    scalar fPress = p.boundaryField()[patchI][faceI];
    myPressfile << fPress << "\t";
}
```

Figure D.2: Extract fluid pressure (OpenFOAM utility)

```

forAll(patches[patchI], faceI)    // loop through faces on patch
{
    scalar fShearX = wallShearStressLES.boundaryField()[patchI][faceI].component(vector::X);
    scalar fShearY = wallShearStressLES.boundaryField()[patchI][faceI].component(vector::Y);
    scalar fShearZ = wallShearStressLES.boundaryField()[patchI][faceI].component(vector::Z);
    myShearXfile << fShearX << "\t";
    myShearYfile << fShearY << "\t";
    myShearZfile << fShearZ << "\t";
}

```

Figure D.3: Extract fluid shear stresses (OpenFOAM utility)

```

fileName = "asterMeshCent.txt"
f = open(dirPath + fileName, "w")
for i in range(0, len(FaceCent)):
    if FaceCent[i,1] >= 0:
        f.write('%d\t%f\t%f\t%f\n'%(MyElements[i], FaceCent[i,0], FaceCent[i,1], FaceCent[i,2]))
f.close()

```

Figure D.4: Extract structural mesh (Code-Aster command file)

```

# Function: Get nearest neighbour
# -----

def nearNeighbour(foamMesh, asterMeshCent):
    mytree = scipy.spatial.cKDTree(foamMesh)
    dist, indexes = mytree.query(asterMeshCent)
    return dist, indexes

```

Figure D.5: Find mesh face centre nearest neighbours (Python file)

```

# Periodic load definition
Tlist=DEFI_LIST_REEL(DEBUT=ts,INTERVALLE=_F(JUSQU_A=te,NOMBRE=nt),TITRE='Tlist',INFO=2,);

# Periodic load definition
forcelist=[]; # Initialize empty force list
x = {}
y = {}
z = {}
for j in range(1,len(MyElements)): # Loop through mesh elements
    x["L{0}".format(j)]=LIRE_FONCTION(UNITE=39,INDIC_PARA=(1,1),INDIC_RESU=(1,j),NOM_PARA = 'INST',INFO=2,);
    y["L{0}".format(j)]=LIRE_FONCTION(UNITE=40,INDIC_PARA=(1,1),INDIC_RESU=(1,j),NOM_PARA = 'INST',INFO=2,);
    z["L{0}".format(j)]=LIRE_FONCTION(UNITE=41,INDIC_PARA=(1,1),INDIC_RESU=(1,j),NOM_PARA = 'INST',INFO=2,);
    forcelist.append(_F(MAILLE = 'M%d' %(MyElements[j]),FX=x["L{0}".format(j)],FY=y["L{0}".format(j)],FZ=z["L{0}".format(j)],,))

forcelistP=[]; # Initialize empty force list
p = {} # Initialize empty variable name list
for j in range(1,len(MyElements)): # Loop through mesh elements
    p["L{0}".format(j)]=LIRE_FONCTION(UNITE=38,INDIC_PARA=(1,1),INDIC_RESU=(1,j),NOM_PARA = 'INST',INFO=2,);
    forcelistP.append(_F(MAILLE = 'M%d' %(MyElements[j]),PRES=p["L{0}".format(j)],,))

# Create a boundary condition: Assign periodic load macro (forcelist)
BCShear=AFFE_CHAR_MECA_F(MODELE=Model, FORCE_COQUE=(forcelist),);
BCPress=AFFE_CHAR_MECA_F(MODELE=Model, FORCE_COQUE=(forcelistP),);

```

Figure D.6: Defining time-dependent structural analysis (Code-Aster command file)

# Appendix E

## PIV Guidelines

When conducting PIV experiments it is not always clear how to produce accurate results. Small changes in any of a number of variables may reduce the accuracy substantially and manuals and guidelines do not always cover all the factors to take into account. It is, therefore, considered useful to list some of the factors that influence the accuracy of PIV results that were learned through numerous PIV experiments during the course of this study.

- The closer the camera is to the area of interest the higher the resolution and the more detail and, therefore, particles are visible that produce higher accuracy. It is recommended that the models to be tested with the PIV not only be dimensioned for other factors such as the wind tunnel but also to match the PIV field. It is generally recommended to divide the area of interest into sub regions which can be measured consecutively. Instead of measuring a larger region with less accuracy a number of smaller regions should be measured to produce a higher quality end result.
- The PIV software cannot distinguish between light sourced from particles or other objects. The experiment should be set up so that only the particles can be seen. This means no reflections, overexposure, diffuse light, dirt on the cameras or glass should be visible in the images produced. These can usually effectively be countered by making the room as dark as possible, painting all surfaces in direct or indirect contact with the laser light sheet black, cleaning the glass and cameras etc. Often unexplained data errors can occur. In these cases all image sets and



both images in the set should be investigated under high exposure. The source for any light patterns on the images that correlate to velocity vector errors should be identified and removed.

- The camera, laser and the calibration target must be perfectly positioned in the same plane. If any of these are slightly out of plane it will reduce the accuracy of the results. This can be more easily inspected looking at the particles than just the calibration target. Often during first calibration particles will appear in focus on a line where the beam and camera focus plane intersect. The better these two planes are aligned the wider the line of focus. The calibration should be done so that the particles in most of the camera view of view are in focus.
- The laser light sheet must cover the entire area of interest (currently measured region). If the laser does not illuminate the entire camera field of view there will be no data outside the beam and bad data will be present around the edges. Starting with the entire field of interest it also means that the cameras can be moved closer for better resolution to exclude the areas outside the laser beam.
- The light sheet must be as narrow and thin as possible. The more energy concentrated in a thinner sheet volume the better illumination of particles. This often means that the laser must be as close to the area of interest as possible, but the closer the laser origin is to the target the smaller the measurable area becomes.
- Higher seeding density increases the accuracy in the cross-correlation analysis during post-processing. This has a big effect on the accuracy. Having high seeding density can often produce good results even in areas slightly out of focus or reduced laser intensity. Seeding density should be checked at the beginning and end of each tests and after testing the seeder nozzles should be cleaned. Higher seeding density is possible in closed loop testing conditions such as in a closed room or water tank than in open loop conditions such as the wind tunnel where seeding is lost to the atmosphere.
- Good seeding particle mixing with the fluid also plays a key role. Without proper mixing the particles often come through in streaks, clouds

and empty patches which deteriorate the accuracy of the data. In the ideal set-up the area of interest will be submerged in particles like in the case of a mist bank as opposed to intermittently being hit by individual clouds. When setting up the system these streaks will be clearly visible on the images. Better seeding spread can be achieved by placing the seeder further up-wind, using an injection piping grid or using a fan to agitate the seeding area.

- Measuring the flow in the plane of particle movement increases the accuracy. Fast moving particles that move perpendicular to the laser plane will appear in one image and disappear in the next creating incorrect velocity vectors. This is sometimes impossible to avoid such as in the case of a highly three-dimensional flow. In these cases other measures to increase accuracy are even more important.
- Particle movement distances within the plane of measurement should not be too far or too short between consecutive light pulses. Differently stated, the time between pulses should be adjusted until the best results during cross correlation are achieved. In high speed flows the time between pulses should be short and for slow speed the time between pulses should be larger. A recommended starting value is  $30 \mu s$  for most wind tunnel conditions.

# Appendix F

## Vibration Data

In this section the wind tunnel test's vibration data is provided in figures F.1 to F.4. The results are provided for both the parallel and perpendicular beams at  $U = 30$  m/s and 60 m/s. The most interesting results are from the parallel beam and  $U = 30$  m/s (figure F.1) where the most significant vibrations are observed to occur at 37 Hz which is the beams 1<sup>st</sup> natural frequency. For this experiment harmonics are also observed at intervals of the first natural frequency.

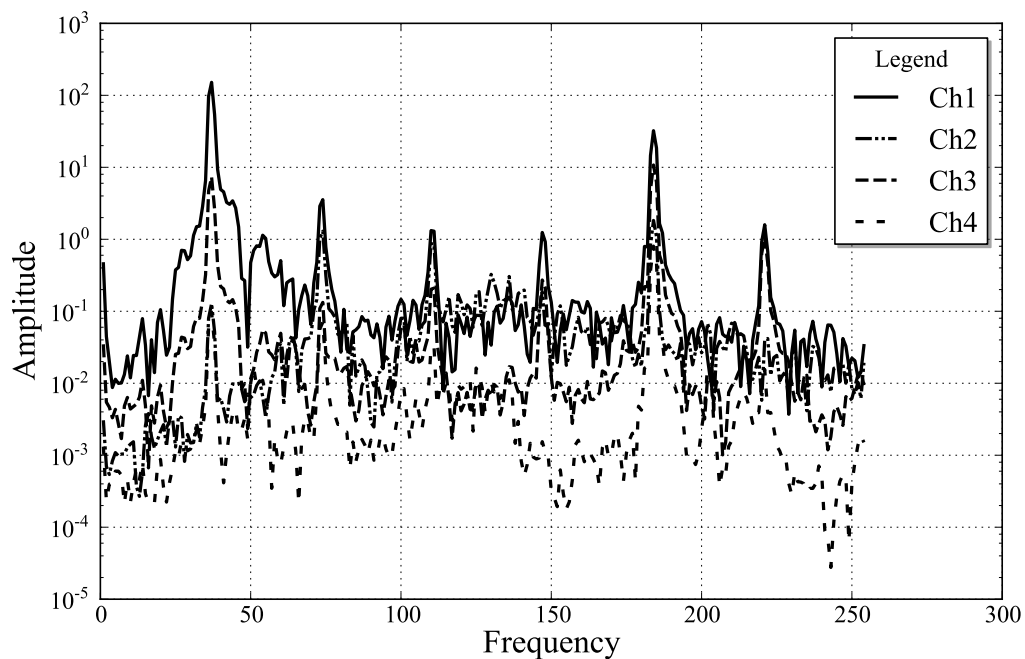


Figure F.1: Vibration results for parallel beam at  $U = 30$  m/s

The parallel beam show lower amplitudes for  $U = 60$  m/s (see figure F.2) although it was necessary to dampen the beam while passing the 30 m/s mark to avoid lock-in. Since this study was not focussed on simulating speed-up or lock-in but rather the impact of vortex-induced loading on the beams at various speeds, it was decided to dampen the beam out of the lock-in condition so that the vortices at 60 m/s will be the only influencing loading.

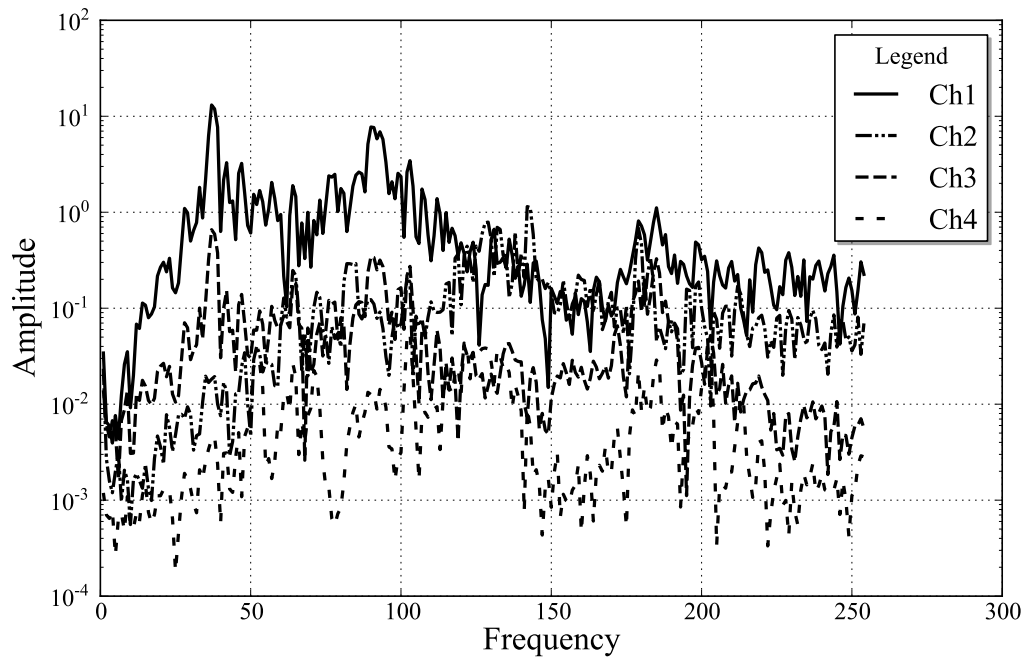
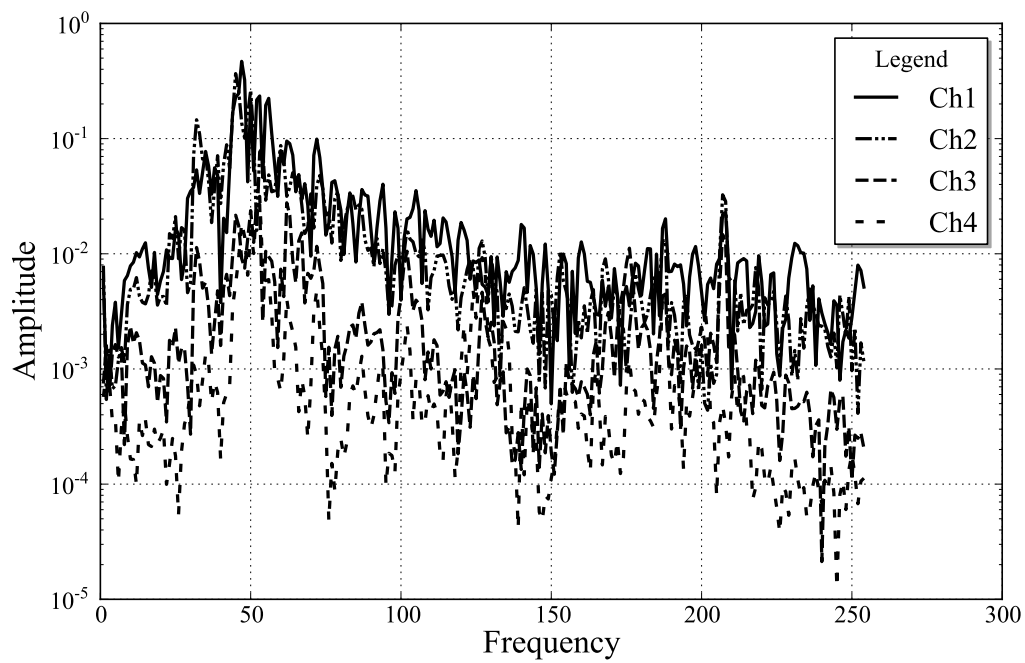
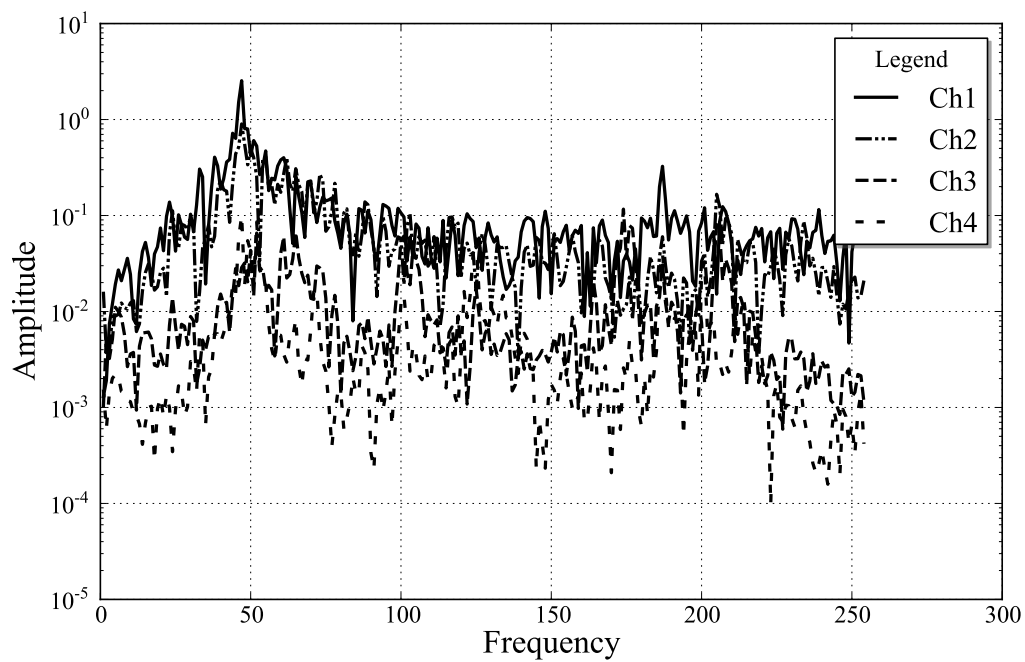


Figure F.2: Vibration results for parallel beam at  $U = 60$  m/s

The perpendicular beam produces significantly lower oscillation amplitudes as shown in figures F.3 to F.4. The highest being at the 1<sup>st</sup> natural frequency of 47 Hz.

Figure F.3: Vibration results for perpendicular beam at  $U = 30$  m/sFigure F.4: Vibration results for perpendicular beam at  $U = 60$  m/s

# List of References

- Bagleito, E. (2009 October). Turbulence and Modelling. CD-Adapco Aerotherm workshop, Johannesburg, South Africa, 13/10/2009.
- Becker, S., Ali, I. and Uffinger, T. (2008 July). Flow Around Wall-mounted Cylinders with Different Geometries: Experiment and Simulation. In: *BBAA VI International Colloquium on: Bluff Bodies Aerodynamics and Applications*, pp. 20–24. Milano, Italy.
- Bloor, M. (1964). The transition to turbulence in the wake of a circular cylinder. *Fluid Mechanics*, vol. 19, pp. 290–304.
- Bourgeois, J.A., Sattari, P. and Martinuzzi, R.J. (2011). Alternating half-loop shedding in the turbulent wake of a finite surface-mounted square cylinder with a thin boundary layer. *Physics of Fluids*, vol. 23, pp. 1–15.
- Bruno, L., Fransos, D., Coste, N. and Bosco, A. (2010). 3D flow around a rectangular cylinder: a computational study. *Journal of Wind Engineering and Industrial Aerodynamics*, vol. 98, pp. 263–276.
- Cardell, G.S. (1993). *Flow past a circular cylinder with a permeable splitter plate*. Ph.D. thesis, Graduate Aeronautical Laboratories, California Institute of Technology.
- Chyu, C.K. and Rockwell, D. (1996). Near-wake structure of an oscillating cylinder: Effect of controlled shear-layer vortices. *Journal of Fluid Mechanics*, vol. 322, pp. 21–49.
- Code-Aster (2011). Accessed March 2011.  
Available at: <http://www.code-aster.org/>
- Dantec Dynamics (2012). Laser optical measurements systems and sensors. Accessed August 2012.  
Available at: <http://www.dantecdynamics.com/>

- De Villiers, E. (2006). *The Potential of Large Eddy Simulation for the Modeling of Wall Bounded Flows*. Ph.D. thesis, Department of Mechanical Engineering, Imperial College of Science, Technology and Medicine.
- Deacon, Q. (2009). Re-Characterization of the Departmental Low Speed Wind Tunnel. Tech. Rep., Department of Mechanical and Mechatronic Engineering, Stellenbosch University. Obtainable through [meganies@sun.ac.za](mailto:meganies@sun.ac.za).
- Deniz, S. and Staubli, T. (1997). Oscillating rectangular and octagonal profiles: Interaction of leading- and trailing-edge vortex formation. *Journal of Fluids and Structures*, vol. 11, pp. 3–31.
- Elliott, B. (1940 November). Collapse of the tacoma narrows bridge as caught on film.
- Etzold, F. and Fiedler, H. (1976). The near-wake structure of a cantilevered cylinder in a cross-flow. *Zeitschrift Für Flugwissenschaften*, vol. 24, pp. 77–82.
- Gatski, T.B. and Speziale, C.G. (1993). On explicit algebraic stress models for complex turbulent flows. *Journal of Fluid Mechanics*, vol. 254, pp. 47–83.
- Genesis (2015). Software for Structural Analysis and Optimisation. Accessed August 2015.  
Available at: [www.vrand.com/Genesis](http://www.vrand.com/Genesis)
- Haase, W., Braza, M. and Revell, A. (2009). *DESider – A European Effort on Hybrid RANS-LES Modelling: Results of the European-Union Funded Project, 2004 - 2007*. Springer.
- Hofmeyr, R. (2015). 2008 expedition team leader and doctor. Accessed April 2015.  
Available at: <http://www.doctorross.co.za/sanae-iv-physical-environment/>
- Huang, S., Li, Q.S. and Xu, S. (2007). Numerical evaluation of wind effects on a tall steel building by CFD. *Journal of Constructional Steel Research*, vol. 63, pp. 612–627.
- Hunt, J.C.R., Wray, A.A. and Moin, P. (1988). Eddies, stream, and convergence zones in turbulent flows. Tech. Rep., Center for Turbulence Research. Report CTR S88, 193.
- Iaccarino, G., Ooi, A., Durbin, P.A. and Behnia, M. (2003). Reynolds averaged simulation of unsteady separated flow. *International Journal of Heat and Fluid Flow*, vol. 24, pp. 147–156.

- iMechanica (2014). Open Source Software. Accessed September 2014.  
Available at: <http://imechanica.org/node/1394>
- Issa, R.I. (1986). Solution of the implicitly discretized fluid flow equations by operator-splitting. *Journal of Computational Physics*, vol. 62, pp. 40–65.
- Jasak, H., Weller, H.G. and Gosman, A.D. (1998). High resolution NVD differencing scheme for arbitrarily unstructured meshes. *International Journal for Numerical Methods in Fluids*, vol. 31, pp. 431–449.
- Joubert, E.C., Harms, T.M. and Venter, G. (2014). One-way FSI in a Vertical Cantilever Beam. In: *SACAM Conference*.
- Joubert, E.C., Harms, T.M. and Venter, G. (2015 July). Computational simulation of the turbulent flow around a surface mounted rectangular prism. *Journal of Wind Engineering and Industrial Aerodynamics*, vol. 142, pp. 173–187.
- Kato, M. and Launder, B.E. (1993). The modelling of turbulent flow around stationary and vibrating square cylinders. In: *Proceedings of 9th Symposium of Turbulent Shear Flows*, pp. 10.4.1–10.4.6. Kyoto, Japan.
- Kawai, H., Okuda, Y. and Ohashi, M. (2009 November). Three dimensional structures of flow behind a square prism. In: *The Seventh Asia-Pacific Conference on Wind Engineering*. Taipei, Taiwan.
- Kawamura, T., Hiwada, M., Hibino, T., Mabuchi, I. and Kumada, M. (1984). Flow around a finite circular cylinder on a flat plate. *Bulletin of the Japan Society of Mechanical Engineers*, vol. 27, pp. 2142–2151.
- Kim, S. and Boysan, F. (1999). Application of CFD to environmental flows. *Journal of Wind Engineering and Industrial Aerodynamics*, vol. 81, pp. 145–158.
- Kolmogorov, A.N. (1991 July). The local structure of turbulence in incompressible viscous fluid for very large Reynolds numbers. In: *Mathematical and Physical Sciences: Turbulence and Stochastic Process: Kolmogorov's Ideas 50 Years On*, vol. 434, pp. 9–13. The Royal Society.
- Kravchenko, A.G. and Moin, P. (2000). Numerical studies of flow over a circular cylinder at  $re = 3900$ . *Physics of Fluids*, vol. 12, no. 2, pp. 403–417.



- Kretzschmar, H. (2010). Flow Measurement On Two-dimensional Model Profiles Of South African Research Base (SANAE IV). Tech. Rep., Department of Mechanical And Mechatronic Engineering, Stellenbosch University. Obtainable through [meganies@sun.ac.za](mailto:meganies@sun.ac.za).
- Launder, B.E. and Kato, M. (1993). Modeling flow-induced oscillations in turbulent flow around a square cylinder. In: *Proceedings of Forum on Unsteady Flows*, vol. 157, pp. 189–199. ASME FED.
- Launder, B.E. and Spalding, D.B. (1974). The numerical computation of turbulent flows. *Computer Methods in Applied Mechanics and Engineering*, vol. 3, pp. 269–289.
- Lee, S. (1997). Unsteady aerodynamic force prediction on a square cylinder using  $k-\varepsilon$  turbulence models. *Journal of Wind Engineering and Industrial Aerodynamics*, vol. 67-68, pp. 79–90.
- Leonard, P.B. (1988). Simple high-accuracy resolution program for convective modelling of discontinuities. *International Journal for Numerical Methods in Fluids*, vol. 8, pp. 1291–1318.
- Li, Q.S., Fang, J.Q., Jeary, A.P. and Paterson, D.A. (1998). Computation of wind loading on buildings by CFD. Transactions. Hong Kong Institution of Engineers.
- Lien, F.S. and Leschziner, M.A. (1993). Upstream monotonic interpolation for scalar transport with application to complex turbulent flows. *International Journal for Numerical Methods in Fluids*, vol. 19, pp. 527–548.
- Lienhard, J. (1966). Synopsis of lift, drag and vortex frequency data for rigid circular cylinders. Research Division Bulletin 300, Washington State University, College of Engineering.
- Lim, H.C., Thomas, T.G. and Castro, I.P. (2009). Flow around a cube in turbulent boundary layer: LES and experiment. *Journal of Wind Engineering and Industrial Aerodynamics*, vol. 97, pp. 96–109.
- Lübcke, H., Schmidt, S., Rung, T. and Thiele, F. (2001). Comparison of LES and RANS in bluff-body flows. *Journal of Wind Engineering and Industrial Aerodynamics*, vol. 89, pp. 1471–1485.
- Mannini, C., Soda, A. and Schewe, G. (2010a). Unsteady RANS modelling of flow past a rectangular cylinder: investigation of Reynolds number effects. *Computers and Fluids*, vol. 39, pp. 1609–1624.

- Mannini, C., Soda, A. and Schewe, G. (2010*b*). Unsteady RANS simulations of flow around a bridge section. *Journal of Wind Engineering and Industrial Aerodynamics*, vol. 98, pp. 742–753.
- Matsumoto, M. (1999). Vortex shedding of bluff bodies: a review. *Journal of Fluids and Structures*, vol. 13, pp. 791–811.
- Mockett, C. (2009). *A Comprehensive Study of Detached-eddy Simulation*. Ph.D. thesis, Technische Universität Berlin.
- Mockett, C., Fuchs, M. and Thiele, F. (2012). Progress of DES for wall-modelled LES of complex internal flows. *Computers and Fluids*, vol. 65, pp. 44–55.
- Morgenthal, G. (2000). Fluid-Structure Interaction in Bluff-Body Aerodynamics and Long-Span Bridge Design: Phenomena en Mehtods. Tech. Rep., Department of Engineering, University of Cambridge.
- Murakami, S., Mochida, A., Hayashi, Y. and Sakamoto, S. (1992). Numerical study of velocity-pressure field and wind forces for bluff bodies by  $k-\epsilon$ , ASM and LES. *Journal of Wind Engineering and Industrial Aerodynamics*, vol. 41-44, pp. 2841–2852.
- Murakami, S., Mochida, A., Kondo, K., Ishida, Y. and Tsuchiya, M. (1998). Development of new  $k-\epsilon$  model for flow and pressure fields arround bluff body. *Journal of Wind Engineering and Industrial Aerodynamics*, vol. 67-68, pp. 169–82.
- NASA (2015). Turbulence Modeling Resource The Spalart-Allmaras Turbulence Model. Accessed April 2015.  
Available at: <http://turbmodels.larc.nasa.gov/spalart.html>
- Naudascher, E. and Rockwell, D. (2005). *Flow-induced vibration - An engineering guide*. Dover Publications Incorporated. First published in 1994 by A A Balkema Publishers, Rotterdam.
- Nikitin, N., Nicoud, F., Wasistho, B., Squires, K. and Spalart, P. (2000). An approach to wall modeling in large-eddy simulations. *Physics of Fluids*, vol. 12(7), pp. 1629–1632.
- Norberg, C. (1994). An experimental investigation of the flow around a circular cylinder: Influence of aspect ratio. *Fluid Mechanics*, vol. 258, p. 287.
- OpenFOAM (2015). The open source CFD toolbox. Accessed April 2015.  
Available at: <http://www.openfoam.com/>

- Parkinson, G.V. (1974). *Mathematical models of flow induced vibrations of bluff bodies*. In: *Flow-Induced Structural Vibrations*. Springer, Berlin, Germany.
- Parkinson, G.V. (1989 January). Phenomena and modelling of flow-induced vibrations of bluff bodies. *Progress in Aerospace Science*, vol. 26, pp. 169–224.
- Paterson, D.A. and Apelt, C.J. (1990). Simulation of flow past a cube in turbulent boundary layer. *Journal of Wind Engineering and Industrial Aerodynamics*, vol. 35, pp. 149–179.
- Prasad, A. and Williamson, C.H.K. (1996). The instability of the separated shear layer from a bluff body. *Physics and Fluids*, vol. 8, p. 1347.
- Prasad, A. and Williamson, C.H.K. (1997). The instability of the shear layer separating from a bluff body. *Journal of Fluid Mechanics*, vol. 333, pp. 375–402.
- Ramesh, V., Vengadesan, S. and Narasimhan, J.L. (2006). 3D unsteady RANS simulation of turbulent flow over bluff body by non-linear model. *International Journal of Numerical Methods for Heat and Fluid Flow*, vol. 16, pp. 660–673.
- Ratnam, G.S. and Vengadesan, S. (2008). Performance of two equation turbulence models for prediction of flow and heat transfer over wall mounted cube. *International Journal of Heat and Mass Transfer*, vol. 51, pp. 2834–2846.
- Rodi, W. (1997). Comparison of LES and RANS calculations of the flow around bluff bodies. *Journal of Wind Engineering and Industrial Aerodynamics*, vol. 69-71, pp. 55–75.
- Roe, P.L. (1985). Some Contributions to the Modelling of Discontinuous Flows. In: *Large-scale computations in fluid mechanics*, vol. 1, pp. 163–193.
- Rung, T. (2000). *Entwicklung anisotroper Wirbelzähigkeitsbeziehungen mit Hilfe von Projektionstechniken*. Ph.D. thesis, Institute for Fluid Mechanics and Engineering Acoustics, Technische Universität Berlin.
- Sakamoto, H. and Arie, M. (1983). Vortex shedding from a rectangular prism and a circular cylinder placed vertically in a turbulent boundary layer. *Journal of Fluid Mechanics*, vol. 126, pp. 147–165.
- Sau, A., Hwang, R.R., Sheu, T.W.H. and Yang, W.C. (2003). Interaction of trailing vortices in the wake of a wall-mounted rectangular cylinder. *Physical Review*, vol. 68, no. 056303, pp. 1–15.

- Shih, T.H., Liou, W.W., Shabbir, A., Yang, Z. and Zhu, J. (1995a). A new  $k$ - $\epsilon$  eddy viscosity model for high Reynolds number turbulent flows. *Computers Fluids*, vol. 24, pp. 227–238.
- Shih, T.H., Zhu, J. and Lumely, J.L. (1995b). A new Reynolds stress algebraic equation model. *Computer Methods in Applied Mechanics and Engineering*, vol. 125, pp. 287–302. ICOMP-94-15, GMOTT-94-8.
- Shur, M., Spalart, P., Strelets, M. and Travin, A. (2008). A hybrid RANS-LES approach with delayed DES and wall-modelled LES capabilities. *International Journal of Heat and Fluid Flow*, vol. 29 (6), pp. 1638–1649.
- Simiu, E. and Scanlan, R.H. (1996). *Wind Effects on Structures: Fundamentals and Applications to Design*. 3rd edn. John Wiley and Sons.
- Spalart, P.R. (2000). Trends in turbulence treatments. *AIAA*, , no. 2000-2306.
- Spalart, P.R. (2009). Detached-eddy simulation. *Annual Review Fluid Mechanics*, vol. 41, pp. 181–202.
- Spalart, P.R. and Allmaras, S.R. (1992). A one-equation turbulence model aerodynamic flows. In: *Proceedings of 30th AIAA Aerospace Sciences Meeting and Exhibit*. Reno, Nevada, USA. AIAA Paper 92-0439.
- Spalart, P.R., Deck, S., Shur, M.L., Squires, K.D., Strelets, M.K. and Travin, A. (2006 May). A new version of detached-eddy simulation, resistant to ambiguous grid densities. *Theoretical and Computational Fluid Dynamics*, vol. 20, pp. 181–195.
- Spalart, P.R., Jou, W.H. and Strelets, M. (1997). Comments on the feasibility of LES for wings, and on a hybrid RANS/LES approach. In: Liu, C. and Liu, Z. (eds.), *Advances in LES/DNS, First AFOSR International Conference on DNS/LES*. Louisiana Tech University, Greyden Press.
- Spalding, D.B. (1961). A single formula for the law of the wall. *Applied Mechanics*, vol. 28, pp. 455–458.
- Strelets, M. (2001 January). Detached Eddy Simulation of Massively Separated Flows. In: *Proceedings of 39th AIAA Aerospace Sciences Meeting and Exhibit*. Reno, Nevada, USA.
- Sumner, D., Heseltine, J.L. and Dansereau, O.J.P. (2004). Wake structure of a finite circular cylinder of small aspect ratio. *Experiments in Fluids*, vol. 37, pp. 720–730.

- Sweby, P.K. (1984). High Resolution Schemes Using Flux Limiters for Hyperbolic Conservation Laws. *SIAM Journal on Numerical Analysis*, vol. 21, no. 5, pp. 995–1011.
- Travin, A., Shur, M., Strelets, M. and Spalart, P.R. (2002). Physical and numerical upgrades in the Detached-Eddy Simulation of complex turbulent flows. Fluid mechanics and its applications. In: Friedrich, R. and Rodi, W. (eds.), *Advances in LES of Complex Flows*, vol. 412, pp. 239–254. Kluwer Academic Publishers, Dordrecht. Proceedings of EUROMECH Colloquium.
- Uffinger, T., Ali, I. and Becker, S. (2013). Experimental and numerical investigations of the flow around three different wall-mounted cylinder geometries of finite length. *Journal of Wind Engineering and Industrial Aerodynamics*, vol. 119, pp. 13–27.
- Uffinger, T., Becker, S. and Ali, I. (2010). Vortex dynamics in the wake of wall-mounted cylinders: experiment and simulation. In: *15th International Symposium on Applications of Laser Techniques to Fluid Mechanics*.
- Uffinger, T., Becker, S. and Delgado, A. (2008 July). Investigations of the flow field around different wall-mounted square cylinder stump geometries. In: *14th International Symposium on Applications of Laser Techniques to Fluid Mechanics*. Lisbon, Portugal.
- Van Albada, G.D., Van Leer, B. and Roberts, W.W. (1982). A comparative study of computational methods in cosmic gas dynamics. *Journal of Astronomy and Astrophysics*, vol. 108, pp. 76–84.
- Van Leer, B. (1974). Towards the ultimate conservative differencing scheme II. Monotonicity and conservation combined in second-order scheme. *Journal of Computational Physics*, vol. 14, pp. 361–370.
- Van Zyl, J.M., Joubert, E.C. and Harms, T.M. (2014). Application of Nvidia Cuda Technology to Computational Fluid Dynamics in South African Research. In: *SACAM Conference*. Somerset West, South Africa.
- Versteeg, H.K. and Malalasekera, W. (2007). *An Introduction to Computational Fluid Dynamics: The Finite Volume Method*. 2nd edn. Pearson Prentice Hall, London England.
- Wang, H., Zhou, Y., Chan, C. and Zhou, T. (2009). Momentum and heat transport in a finite-length cylinder wake. *Experiments in Fluids*, vol. 46, pp. 1173–1185.

- Wang, H.F. (2004 September). Flow structure around a finite-length square prism. In: *15th Australasian Fluid Mechanics Conference*. Australia.
- Wang, H.F. and Zhou, Y. (2009). The finite-length square cylinder near wake. *Journal of Fluid Mechanics*, vol. 638, pp. 453–490.
- Wang, M., Catalano, P. and Iaccarino, G. (2001). Prediction of high Reynolds number flow over a circular cylinder using LES with wall modeling. *Center for Turbulence Research Annual Research Briefs*, pp. 45–50.
- White, F.M. (2006). *Viscous Fluid Flow*. 3rd edn. McGraw - Hill.
- Williamson, C.H.K. (1996). Vortex dynamics in the cylinder wake. *Annual Review of Fluid Mechanics*, vol. 28, pp. 477–539.
- Wissink, J.G. and Rodi, W. (2008). Numerical study of the near wake of a circular cylinder. *International Journal of Heat and Fluid Flow*, vol. 29, pp. 1060–1070.
- Yakhot, A., Liu, H. and Nikitin, N. (2006). Turbulent flow around a wall mounted cube: A direct numerical simulation. *International Journal of Heat and Fluid Flow*, vol. 27, pp. 994–1009.
- Yakhot, V., Orszag, S.A., Gatski, S.T.T.B. and Speziale, C.G. (1992). Development of turbulence models for shear flows by double expansion technique. *Physics of Fluids*, vol. 4, pp. 1510–1520.
- Zdravkovich, M.M. (1997). *Flow Around Circular Cylinders*, vol. 1. Oxford University Press. Chapter 6.